Microscopic Dynamic Properties of Monoclonal Antibodies in Solution Studied by Neutron Scattering

Dissertation

der Mathematisch-Naturwissenschaftlichen Fakultät

der Eberhard Karls Universität Tübingen

zur Erlangung des Grades eines

Doktors der Naturwissenschaften

(Dr. rer. nat.)

vorgelegt von

Ilaria Mosca

aus Todi / Italien

Tübingen

2025

Gedruckt mit Genehmigung der Mathematisch-Naturwissenschaftlichen Fakultät der Eberhard Karls Universität Tübingen.

Tag der mündlichen Qualifikation:	13.05.2025
Dekan:	Prof. Dr. Thilo Stehle
1. Berichterstatter:	Prof. Dr. Frank Schreiber
2. Berichterstatter:	Prof. Dr. Martin Oettel

Preamble

The research work for this thesis was carried out within the PhD programme of the Institut Max von Laue - Paul Langevin (ILL), Grenoble, France, jointly with the Institut für Angewandte Physik of the University of Tübingen, Germany, and Lonza AG/Ltd., Basel, Switzerland. The project was cofunded by InnovaXN, a EU MSCA Horizon2020 COFUND doctoral programme (innovaxn.eu, grant agreement No. 847439), the ILL and the University of Tübingen. The work was supervised by Dr. Tilo Seydel and Dr. Olga Matsarskaia at the ILL, Dr. Christoph Grapentin at Lonza and by Prof. Dr. Frank Schreiber and Prof. Dr. Martin Oettel at the Institut für Angewandte Physik of the University of Tübingen.


List of papers being part of the thesis

- **Biophysical Determinants for the Viscosity of Concentrated Monoclonal Antibody Solutions**
  I. Mosca, K. Pounot, C. Beck, L. Colin, O. Matsarskaia, C. Grapentin, T. Seydel and F. Schreiber
  Molecular Pharmaceutics **2023**, 20 (9), 4698-4713

- **Continuity of Short-Time Dynamics Crossing Liquid-Liquid Phase Separation in Charge-Tuned Protein Solutions**
  I. Mosca, C. Beck, N. H. Jalarvo, O. Matsarskaia, F. Roosen-Runge, F. Schreiber and T. Seydel
  Journal of Physical Chemistry Letters **2024**, 15, 12051-12059

- **Multi-Scale Diffusion, Dynamic Cluster Formation and Intermolecular Interactions in Pharmaceutically Relevant Monoclonal Antibody Formulations**
  I. Mosca, C. Beck, L. Mateo-Miñarro, R. Nasro, A. Grundel, I. Hoffmann, K. Pounot, O. Matsarskaia, C. Grapentin,
  T. Seydel and F. Schreiber
  In preparation for publication

- **Biophysics of Monoclonal Antibodies: a Review**
  I. Mosca, C. Beck, L. Mateo-Miñarro, O. Matsarskaia, C. Grapentin, F. Schreiber and T. Seydel
  in preparation

Other papers

- **Notes on Fitting and Analysis Frameworks for QENS Spectra of (Soft) Colloid Suspensions**
  C. Beck, I. Mosca, K. Pounot, N. H. Jalarvo, F. Roosen-Runge, F. Schreiber and T. Seydel
  EPJ Web of Conferences **2022**, 272, 01004 (QENS/WINS conference 2022)

Contents

Abstract **11**

Zusammenfassung **13**

1 Introduction **17**
1.1 Proteins in aqueous solutions and concepts from colloid physics . . . 17
1.2 Diffusive dynamics in the ns timescale and neutron spectroscopy . . . 17
1.3 Dynamic cluster formation and LLPS in protein solutions . . . 18

2 Biophysics of mAb solutions: A review **19**
2.1 Biophysics of crowded protein solutions . . . 20
2.2 Biophysics of antibodies . . . 21
2.2.1 Immunoglobulin classes and functions . . . 21
2.2.2 Structure of immunoglobulin G . . . 22
2.2.3 Polyclonal versus monoclonal antibodies . . . 23
2.3 Monoclonal antibodies in therapeutics . . . 24
2.3.1 Routes of drug administration . . . 24
2.3.2 The role of excipients . . . 26
2.4 General concepts of colloid physics . . . 27
2.4.1 Diffusion tensor, self- and collective diffusion . . . 28
2.4.2 Viscosity, diffusion and cluster formation . . . 29
2.4.3 Simulations, in silico predictions and scattering experiments on mAb solutions . 31
2.4.4 The unique capabilities of spectroscopy . . . 32

3 Neutron scattering **35**
3.1 Theoretical framework . . . 35
3.1.1 Neutron radiation, production and properties . . . 35
3.1.2 Neutron scattering cross-section . . . 38
3.1.3 Born approximation and nuclear potential . . . 43
3.1.4 Coherent and incoherent neutron scattering . . . 46
3.1.5 Correlation and response functions . . . 50
3.2 Quasi-elastic neutron scattering (QENS) . . . 55
3.2.1 Dynamical independence approximation . . . 57
3.2.2 Elastic Incoherent Structure Factor (EISF) . . . 57
3.3 Neutron spectroscopy . . . 58
3.3.1 Neutron backscattering and TOF spectroscopy . . . 58

3.3.2 Neutron spin-echo spectroscopy . . . 62
3.4 Small-angle neutron scattering . . . 65
3.4.1 SANS instrumentation . . . 67

4 Materials and methods 71
4.1 Materials . . . 71
4.1.1 Lonza monoclonal antibodies . . . 71
4.1.2 Bovine serum albumin . . . 72
4.1.3 Solvents . . . 72
4.2 Methods . . . 74
4.2.1 In silico methods: sequence analysis . . . 74
4.2.2 Laboratory methods: buffer exchange, concentration determination, viscometry 76
4.3 In silico protein sequence analysis results . . . 80
4.3.1 Sequence alignment and amino-acidic composition . . . 80
4.3.2 Sequence properties . . . 86

5 Biophysical determinants for mAb solution viscosity 91
5.1 Introduction . . . 92
5.2 Materials and methods . . . 95
5.2.1 Sample preparation . . . 95
5.2.2 Quasi-elastic neutron backscattering spectroscopy . . . 96
5.2.3 Small-angle neutron scattering (SANS) . . . 98
5.2.4 Viscometry . . . 98
5.2.5 Sample characterization by DLS, SLS, and HIC . . . 98
5.2.6 MD simulations . . . 98
5.3 Results and discussion . . . 100
5.3.1 Viscometry . . . 100
5.3.2 Dynamic and static light scattering . . . 101
5.3.3 Quasi-elastic neutron spectroscopy and MD simulations . . . 102
5.3.4 Small-angle neutron scattering . . . 111
5.4 Conclusions . . . 113
5.5 Supplementary Information . . . 115
5.5.1 Biophysical properties of mAbs . . . 115
5.5.2 Viscometry on deuterated antibody solutions . . . 116
5.5.3 Quasi-elastic neutron backscattering spectroscopy . . . 117
5.5.4 Antibodies as soft colloid suspensions . . . 117
5.5.5 Simulations . . . 121
5.5.6 Small angle scattering . . . 122

6 Multi-scale diffusion in mAb formulations 125
6.1 Introduction . . . 126
6.2 Materials and Methods . . . 130
6.2.1 Sample Preparation . . . 130
6.2.2 Viscometry and light scattering . . . 131
6.2.3 Neutron Spin Echo (NSE) Spectroscopy . . . 131
6.2.4 *In situ* fixed-angle DLS . . . 132

6.2.5 Small Angle Neutron Scattering (SANS) . . . 132
6.3 Results and Discussion . . . 133
6.3.1 Viscometry and light scattering . . . 133
6.3.2 Neutron Spin-Echo Spectroscopy . . . 136
6.3.3 Small Angle Neutron Scattering . . . 142
6.4 Conclusions . . . 143
6.5 Supplementary Information . . . 144
6.5.1 Neutron spin-echo spectroscopy (NSE) . . . 144
6.5.2 *In situ* fixed-angle DLS . . . 147
6.5.3 SANS . . . 150
6.5.4 Physico-chemical properties of the mAbs and solution stability . . . 153

7 Short-time dynamics crossing LLPS in proteins 157
7.1 Introduction . . . 158
7.2 BSA-$LaCl_3$ as a model system . . . 161
7.3 Hypothesis and discussion . . . 165
7.4 Experimental Methods . . . 167
7.5 Supplementary Information . . . 169
7.5.1 Sample preparation, testing conditions for LLPS and selected samples . . . 169
7.5.2 Phase diagrams determined by UV-Vis spectroscopy . . . 173
7.5.3 Additional QENS data analysis and additional fit parameters . . . 175
7.5.4 Additional interpretation in terms of absolute volumes . . . 181

8 Summary and outlook 183
8.1 Summary and conclusions . . . 183
8.2 Importance of industrial participation in basic research . . . 184
8.3 Outlook . . . 184

Appendix: List of experiments performed at large scale facilities 185

Glossary 189

List of Symbols 195

List of Figures 197

List of Tables 201

Bibliography 203

Abstract

Proteins are biomolecules crucial for life, present in all organisms. They differ in size, shape, structure and functionality. Proteins *in vivo* are normally in contact with other biomolecules in a naturally crowded milieu or with solvent molecules. In both cases they are immersed in an aqueous environment, which makes the understanding of their behaviour in solution essential in biological, physico-chemical, clinical and pharmaceutical research.

In particular, this thesis focuses on blood serum proteins, which fulfil fundamental bodily functions such as immune response, nutrient transport, osmotic pressure regulation. One of the proteins investigated is bovine serum albumin (BSA), a globular protein responsible of regulating osmotic pressure, transporting fatty acids, bilirubin, minerals and hormones, and functioning as anticoagulant and antioxidant in blood. BSA is a well-established standard model in protein science. Nevertheless, the main focus of the thesis is on monoclonal antibodies (mAbs). Antibodies, or immunoglobulins, are the first line of defence of mammal organisms and thus a fundamental part of the immune system. MAbs are proteins designed and manufactured to bind to specific targets to fight a broad spectrum of diseases, such as cancers, autoimmune disorders and viral infections. The possibility of self-administration motivates the formulation of products for subcutaneous (SC) administration over other delivery routes. The pharmaceutical challenge associated with is to formulate highly concentrated antibody solutions to achieve a significant therapeutic effect with a minimum number of injections, while limiting their viscosity and preserving their colloidal and physico-chemical stability.

The investigation of highly concentrated monoclonal antibody (mAb) solutions is crucial to avoid unwanted behaviour in the formulation, e.g. aggregation, phase separation or high viscosity, which do not permit painless injections. It is known that reversible self-association (RSA) of proteins is the underlying mechanism of high solution viscosity and it is typically driven by electrostatic or hydrophobic interactions between monomers. Protein aggregation starting at a molecular level can irreversibly form growing domains and lead to macroscopic phase separation. This phase transition has been extensively studied by various disciplines, such as physics, chemistry, biology and engineering. In recent years it was discovered that phase separation is ubiquitous in cells, plays an essential role in biological organisms and lies behind protein pathological misfolding and malfunctioning.

In this thesis, protein microscopic diffusion in aqueous solutions is addressed at different time scales, by different points of view and by means of neutron scattering techniques. By interacting with nuclei, neutrons are non-disruptive probes particularly suited to study the matter in general. Cold neutron scattering matches length and time scales in soft and biological systems, such as protein solutions. Concerning immunoglobulin (Ig) proteins, the self- and collective diffusion of an unprecedented series of pharmaceutically relevant mAbs in a formulation-like buffer were investigated for this thesis. The influence of crowding, temperature and antibody variant was monitored.

In the first study, the short-time self-diffusion of 5 mAbs was studied with quasielastic neutron

scattering (QENS) at different protein concentrations, to assess the effects of crowding, observe antibody self-association and how those relate to solution viscosity. Measurements were collected at temperatures varying from fridge-storage to physiological temperature, to monitor cluster dissociation. In the same study, small angle neutron scattering (SANS) was employed to probe structural features and solution organization of the samples at a relatively high concentration. The work is also enriched by molecular dynamics (MD) simulations.

The second study presented focuses instead on the collective dynamics and intermolecular interactions of a larger series of mAbs. To this purpose, neutron spin-echo (NSE), SANS and dynamic light scattering (DLS) experiments were conducted at different concentrations and in the temperature range aforementioned, but in the opposite direction, to monitor self-association almost in real-time. A slowdown in the diffusion is observed in the most viscous mAbs in solution, indicating the presence of a stronger self-association, i.e. formation of bigger clusters. The mechanism is more enhanced at storage temperature, which acts as a upper critical solution temperature (UCST) for two of the most viscous mAbs, leading to liquid-liquid phase separation (LLPS). SANS and computation of antibody normal modes (NM) also helped in assessing the molecular flexibility in the different protein variants and isotypes studied.

Neutron scattering results were enriched with a detailed computational analysis of the mAb sequences and the extraction of useful parameters to predict their solution behaviour. Moreover, several laboratory techniques like dialysis, centrifugation, ultraviolet-visible (UV-Vis) spectroscopy and viscometry were employed as essential supports for sample preparation and biophysical characterization.

The third study reported in this work aims to elucidate the role of short-time dynamics studied via QENS upon entering the LLPS regime for a quite known protein-salt system, that is BSA in solution with different concentrations of $LaCl_3$. This system exhibits a opposite mechanism with respect to antibody proteins within a similar temperature range, with LLPS being driven by a lower critical solution temperature (LCST). The remarkable observation is that the microscopic environment in the nanosecond scale remains highly dynamic, even while crossing the LLPS regime, so even when the solution macroscopically splits in two phases, a protein-rich one and a protein-poor one.

In conclusion, short-time self- and collective diffusion of proteins in solution was accessed by different neutron spectroscopy techniques in order to elucidate its role in protein aggregation and phase separation mechanisms. In the case of mAbs, we observed that protein self-association results in the formation of small oligomers composed by a higher number of monomers for the proteins exhibiting higher viscosities. Those solutions also display a UCST-LLPS behaviour in the temperature range studied. By studying a simpler protein-salt system with a LCST-LLPS behaviour, we reveal a continuity of the short-time dynamics upon entering the phase separation region, despite the macroscopic phase-splitting. Although a lot of questions in protein and formulation science remain still open, we strongly believe that we closed an important knowledge gap in this field and that our results can serve as starting points for future studies.

Zusammenfassung

[1] Proteine sind lebenswichtige Biomoleküle, die in allen Organismen vorhanden sind. Sie unterscheiden sich in Größe, Form, Struktur und Funktionalität. *In vivo* sind Proteine normalerweise in Kontakt mit anderen Biomolekülen in einem natürlich belebten Milieu oder mit Lösungsmittelmolekülen. In beiden Fällen sind sie in eine wässrige Umgebung eingetaucht, was das Verständnis ihres Verhaltens in Lösung in der biologischen, physikalisch-chemischen, klinischen und pharmazeutischen Forschung unerlässlich macht.

Diese Arbeit konzentriert sich insbesondere auf Blutserumproteine, die grundlegende Körperfunktionen wie die Immunantwort, den Nährstofftransport und die Regulierung des osmotischen Drucks erfüllen. Eines der untersuchten Proteine ist Rinderserumalbumin (BSA), ein globuläres Protein, das für die Regulation des osmotischen Drucks, den Transport von Fettsäuren, Bilirubin, Mineralien und Hormonen sowie als Antikoagulans und Antioxidans im Blut verantwortlich ist. BSA ist ein etabliertes Standardmodell in der Proteinforschung. Der Schwerpunkt dieser Arbeit liegt jedoch auf monoklonalen Antikörpern (mAbs). Antikörper oder Immunglobuline sind die erste Verteidigungslinie von Säugetierorganismen und damit ein grundlegender Bestandteil des Immunsystems. MAbs sind Proteine, die so konzipiert und hergestellt sind, dass sie an spezifische Ziele binden, um ein breites Spektrum von Krankheiten wie Krebs, Autoimmunerkrankungen und Virusinfektionen zu bekämpfen. Die Möglichkeit der Selbstverabreichung motiviert die Formulierung von Produkten für die Verabreichung von subkutane (SC) Injektion gegenüber anderen Verabreichungswegen. Die pharmazeutische Herausforderung besteht darin, hochkonzentrierte Antikörperlösungen zu formulieren, um eine signifikante therapeutische Wirkung mit einer minimalen Anzahl von Injektionen zu erzielen und gleichzeitig die Viskosität zu begrenzen und die kolloidal und physikalisch-chemische Stabilität zu erhalten.

Die Untersuchung hochkonzentrierter mAb-Lösungen ist von entscheidender Bedeutung, um unerwünschtes Verhalten in der Formulierung zu vermeiden, wie z.B. Aggregation, Phasentrennung oder hohe Viskosität, die eine schmerzfreie Injektion verhindern. Es ist bekannt, dass die reversible Selbstassoziation von Proteinen der zugrundeliegende Mechanismus für eine hohe Lösungsviskosität ist und in der Regel durch elektrostatische oder hydrophobe Wechselwirkungen zwischen den Monomeren hervorgerufen wird. Eine Proteinaggregation, die auf molekularer Ebene beginnt, kann irreversibel wachsende Domänen bilden und zu einer makroskopischen Phasentrennung führen. Dieser Phasenübergang wurde von verschiedenen Disziplinen wie Physik, Chemie, Biologie und Ingenieurwissenschaften eingehend untersucht. In den letzten Jahren wurde entdeckt, dass Phasentrennung in Zellen allgegenwärtig ist, eine wichtige Rolle in biologischen Organismen spielt und die Grundlage für pathologische Fehlfaltungen und Fehlfunktionen von Proteinen ist.

In dieser Arbeit wird die mikroskopische Diffusion von Proteinen in wässrigen Lösungen auf

[1]The author acknowledges Dr. Tilo Seydel and Dr. Christian Beck for their assistance with the German translation.

verschiedenen Zeitskalen, aus verschiedenen Blickwinkeln und mit Hilfe von Neutronenstreutechniken untersucht. Da Neutronen mit Kernen wechselwirken, sind sie als nicht-störende Sonden für die Untersuchung von Materie im Allgemeinen besonders geeignet. Kalte Neutronenstreuung eignet sich für Längen- und Zeitskalen in weichen und biologischen Systemen, wie z.B. Proteinlösungen. In dieser Arbeit wurde die Selbst- und Kollektivdiffusion einer beispiellosen Reihe pharmazeutisch relevanter mAbs in einem formelähnlichen Puffer für IgG-Proteine untersucht. Der Einfluss von Crowding, Temperatur und Antikörpervariante wurde beobachtet.

In der ersten Studie wurde die Kurzzeit-Selbstdiffusion von 5 mAbs mit QENS bei verschiedenen Proteinkonzentrationen untersucht, um die Auswirkungen des Crowding zu bewerten, die Selbstassoziation der Antikörper zu beobachten und den Zusammenhang mit der Viskosität der Lösung zu untersuchen. Die Messungen wurden bei verschiedenen Temperaturen durchgeführt, von der Lagerung im Kühlschrank bis hin zu physiologischen Temperaturen, um die Dissoziation der Cluster zu beobachten. In der gleichen Studie wurde SANS verwendet, um die strukturellen Eigenschaften und die Lösungsorganisation der Proben bei relativ hohen Konzentrationen zu untersuchen. Die Arbeiten wurden auch durch MD-Simulationen ergänzt.

Die zweite vorgestellte Studie konzentriert sich dagegen auf die kollektive Dynamik und die intermolekularen Wechselwirkungen einer größeren Anzahl von mAbs. Zu diesem Zweck wurden NSE-, SANS- und DLS-Experimente bei verschiedenen Konzentrationen und im oben genannten Temperaturbereich, jedoch in entgegengesetzter Richtung durchgeführt, um die Selbstassoziation nahezu in Echtzeit zu verfolgen. Eine Verlangsamung der Diffusion wird für das viskosere mAbs in Lösung beobachtet, was auf eine stärkere Selbstassoziation, d.h. die Bildung größerer Cluster, hinweist. Der Mechanismus verstärkt sich bei Lagertemperatur, die für zwei der viskosesten mAbs als UCST wirkt und zu LLPS führt. SANS und die Berechnung von Antikörper-Normalmoden (NM) halfen ebenfalls bei der Bewertung der molekularen Flexibilität in den verschiedenen untersuchten Proteinvarianten und Isotypen.

Die Ergebnisse der Neutronenstreuung wurden durch eine detaillierte rechnerische Analyse der Sequenzen und die Extraktion nützlicher Parameter zur Vorhersage ihres Lösungsverhaltens ergänzt. Darüber hinaus wurden verschiedene Labortechniken wie Dialyse, Zentrifugation, UV-Vis-Spektroskopie und Viskosimetrie als wesentliche Hilfsmittel zur Probenvorbereitung und biophysikalischen Charakterisierung eingesetzt.

Die dritte Studie, über die in dieser Arbeit berichtet wird, zielt darauf ab, die Rolle der Kurzzeitdynamik, die mit QENS untersucht wird, beim Eintritt in das LLPS-Regime für ein gut bekanntes Protein-Salz-System, nämlich BSA in Lösung mit verschiedenen Konzentrationen von $LaCl_3$, zu klären. Dieses System zeigt einen umgekehrten Mechanismus in Bezug auf Antikörperproteine, wobei LLPS durch LCST angetrieben wird. Die bemerkenswerte Beobachtung ist, dass die mikroskopische Umgebung im Nanosekundenbereich sehr dynamisch bleibt, auch wenn das LLPS-Regime durchlaufen wird, d.h. auch wenn sich die Lösung makroskopisch in zwei Phasen teilt, eine proteinreiche und eine proteinarme.

Zusammenfassend wurde die kurzzeitige Selbst- und Kollektivdiffusion von Proteinen in Lösung mit verschiedenen neutronenspektroskopischen Techniken untersucht, um ihre Rolle bei der Proteinaggregation und den Phasentrennungsmechanismen zu klären. Im Fall von mAbs haben wir beobachtet, dass die Selbstassoziation von Proteinen zur Bildung kleiner Oligomere führt, die aus einer größeren Anzahl von Monomeren bestehen, wenn die Proteine eine höhere Viskosität aufweisen. Diese Lösungen zeigen auch ein UCSTLLPS-Verhalten. Bei der Untersuchung eines einfacheren Protein-Salz-Systems mit LCST-LLPS-Verhalten zeigen wir eine Kontinuität der Kurzzeitdynamik

beim Eintritt in den Bereich der Phasentrennung trotz makroskopischer Phasentrennung. Obwohl es noch viele offene Fragen in der Protein- und Formulierungswissenschaft gibt, sind wir fest davon überzeugt, dass wir eine wichtige Wissenslücke auf diesem Gebiet geschlossen haben und dass unsere Ergebnisse als Ausgangspunkt für zukünftige Studien dienen können.

Chapter 1

Introduction

1.1 Proteins in aqueous solutions and concepts from colloid physics

The dynamics of proteins in solution includes a variety of processes, such as backbone and side-chain fluctuations, interdomain motions, as well as global rotational and translational (i.e. center of mass) diffusion. Since protein dynamics is related to protein function and essential transport and signalling processes, a detailed mechanistic understanding and monitoring of protein dynamics in solution is highly desirable. A quantitative characterization of protein dynamics is also essential to unveil life at a molecular level and identify mechanisms leading to protein malfunction. In addition, protein internal dynamics allows for molecular flexibility and plays a role in the protein binding affinity with other molecules, e.g. potential drugs. The hierarchical character of protein dynamics requires several experimental tools addressing a broad range of time- and length scales [1].

The synergy between experiments and simulations or a theoretical interpretation of experimental observations are often required. A common and useful framework to describe the global center-of-mass protein diffusion in solutions is provided by colloid physics, which predicts a short-time regime on which only hydrodynamic interactions induce a simple diffusive behavior [2–4].

The present work focuses in particular on neutron spectroscopy and the reasons why it is important to investigate soft and biological matter, e.g. protein solutions. The results are interpreted in terms of a colloid physics framework, for which a detailed description is provided. In the following chapters, the mathematical framework of neutron scattering, the principles of neutron spectroscopy and the instruments employed are presented in detail. Furthermore, the research on monoclonal antibody solutions for therapeutic purposes is reviewed. The final chapters describe the results of the experimental work done on the systems, along with the data analysis performed.

1.2 Diffusive dynamics in the nanosecond timescale and neutron spectroscopy

Neutron spectroscopy offers a powerful tool to explore nanosecond and sub-nanosecond diffusive dynamics in soft matter, and more specifically, in protein solutions. Neutron spectroscopy translates into several techniques, which differ in the instrumental setup used and consequently in the experimental quantity measured. For instance, neutron backscattering spectroscopy (NBS) is an energy-resolved technique that measures the protein self-diffusion; thanks to the Stokes-Einstein relation, it is possi-

ble to retrieve the hydrodynamic size of the observed particles and thus gaining information on the potential clustering of proteins. Neutron spin echo (NSE) spectroscopy is instead a time-resolved technique that further complements the picture rendered by NBS, by accessing the collective diffusion function. This quantity connects to the hydrodynamic function via the static structure factor of the system.

These insights help elucidate how short-lived protein clusters form and evolve under different conditions, e.g. pH and temperature variations, impacting solution stability and therapeutic efficacy. It should be noted that these clusters are dynamic/transient, meaning that the proteins are kept assembled in an oligomer for a short time, which is basically the time window accessed by the instrument. The cluster formation is therefore reversible and dynamic, meaning that the proteins can associate, dissociate and re-assemble in different ways. The mechanism is driven by protein mutual interactions, caused by the vicinity of charged or hydrophobic patches.

1.3 Dynamic cluster formation and liquid-liquid phase separation in protein solutions

Dynamic cluster formation in protein solutions, particularly for monoclonal antibodies, is a critical area of research for the developability and manufacturability of pharmaceutical products. This phenomenon could also be a precursor of liquid-liquid phase separation (LLPS), another significant process in protein solution phase-behavior. LLPS, which has been observed in both general protein systems and mAbs specifically, is driven by electrostatic interactions and can be tuned and adjusted by charge modulation. The microscopic onset of this phenomenon leads to an increase in the correlation length, until it becomes macroscopically visible in terms of increased solution turbidity and opalescence.

The protein BSA is commonly used as model system in protein science in general, but also studied as reference in LLPS studies due to its availability and relevance as a serum protein. BSA also shares conceptual similarities with mAbs, as both exhibit charge-driven interactions that can lead to LLPS under certain conditions. One remarking difference between these proteins is their opposite mechanism driving LLPS in the temperature range explored in this thesis. In fact, while BSA shows a LCST of ≈ 40°C above which the onset of phase-separation can be observed, the IgG antibodies studied in this thesis are typically characterized by a UCST falling in the range (7-15)°C, below which the system de-mixes in a protein-rich phase and a protein-poor one.

Nevertheless, studying LLPS in a BSA model system aids in understanding protein-protein interactions and aggregation processes that are universal in protein science in general and that are critical for biopharmaceutical formulation.

Chapter 2

Biophysics of monoclonal antibody solutions: A review

Chapter 2 is the basis for the following publication:

Biophysics of monoclonal antibody solutions: A review
(in preparation)

Authors: ILARIA MOSCA[1,2], CHRISTIAN BECK[1,2], LAURA MATEO-MIÑARRO[4], CHRISTOPH GRAPENTIN[3], OLGA MATSARSKAIA[2], FRANK SCHREIBER[1], AND TILO SEYDEL[2]

[1]*Institut für Angewandte Physik, Universität Tübingen*, Germany
[2]*Institut Max von Laue-Paul Langevin*, Grenoble, France
[3]*Lonza AG/Ltd.*, Basel, Switzerland
[4]*Université Grenoble-Alpes*, Saint-Martin d'Hères, France

Author contribution: I. M. wrote the first draft. T. S., L. M. M., C. B., L. M. M., O. M., and F. S. revised the manuscript.

2.1 Biophysics of crowded protein solutions

Inside living cells, macromolecules are densely packed, often occupying 25-40% of the cellular volume with concentrations in the range 90-450 g/L. This state, referred to as macromolecular crowding, was described for the first time by Minton [5–7] and it is still a very hot topic for interdisciplinary research [8–12]. The limited amount of free water and the reduced amount of unoccupied space deeply influence the physical and chemical behaviors of molecules in crowded media, altering protein folding, stability [13, 14], aging [15], viscosity, diffusion [16, 17], and reaction kinetics [6, 18, 19].

Expanding the microscopic knowledge on the crowding of macromolecules, especially of protein solutions, is crucial for a complete understanding of how cellular environments differ from dilute laboratory settings. Unlike dilute solutions where molecules interact mostly through brief and stochastic collisions, crowded solutions mimic the highly interactive environment inside cells, where space is limited, and molecular encounters are frequent and prolonged. As already stated, one significant effect of crowding is on protein stability. In a crowded environment, proteins are more likely to adopt and maintain their folded states due to the excluded volume effect [5, 20]. The high concentration of molecules in close proximity reduces the available free volume for proteins to unfold, thereby favouring compact, stable configurations over extended or denatured states. This effect enhances protein stability and can influence the balance between folded and misfolded forms, potentially leading to pathological protein aggregation [21]. Besides volume exclusion, soft interactions and solvation contribute to macromolecular crowding [22–24]. The crowded cellular environment is not a passive "bag full of macromolecules", but an active participant in biochemical processes essential for life [9].

Crowding also affects protein-protein interactions (PPIs), favouring the formation of molecular complexes and assemblies [25]. When proteins are surrounded by many other macromolecules, they are more likely to encounter one another and form transient or stable complexes, a process crucial for signaling and metabolic pathways. Crowded environments can enhance the likelihood of specific interactions and change binding affinity [26]. This aspect is particularly relevant for understanding cellular processes such as the formation of protein complexes, multi-protein signaling pathways, and even the assembly of intracellular structures, such as ribosomes [27]. Macromolecular crowding has also been identified as the driving force for liquid-liquid phase separation (LLPS) [28], itself considered as the mechanism behind the formation of membraneless organelles in the cellular medium [29, 30] and its consequent microcompartmentation [31].

Besides influencing steady-state properties, crowding also significantly affects the diffusion and transport of macromolecules. Protein diffusion in a crowded milieu is generally slower and less predictable [32, 33], with some exceptions that concern short-time diffusion [11, 34]. Its complexity arises from the interplay of several factors, including the size and shape of the macromolecules [35, 36], the nature of the crowding agents [37] and the resulting mutual interactions [35]. For instance, smaller proteins may diffuse faster in heterogeneous and poly-disperse mixtures compared to self-crowded solutions, while larger proteins exhibit the opposite behavior [38, 39]. Crowding-induced sub-diffusive regime [17, 40], anomalous diffusion [41–43] and microviscosity [44] can alter reaction kinetics, sometimes increasing reaction rates by keeping molecules close together [44], sometimes slowing them down with consequent "noise" reduction in some processes, e.g. gene expression [45]. Again, some biological processes are triggered by crowding and enhanced at very specific crowding conditions depending on the size of the macromolecules involved [46].

Investigating macromolecular crowding is also essential for improving drug delivery technologies, as it impacts drug behavior within densely packed cellular environments. It is often the case that

highly concentrated biopharmaceuticals, with special consideration of mAbs, are required for specific routes of administration. In such instances, changes in viscosity and diffusion may occur as a result of crowding, which can have a significant impact on drug transport, release, and pharmacokinetics. In a recent review, Singh et al. provide a comprehensive overview of the latest experimental findings and theoretical models in the field, along with application opportunities and open challenges [47].

2.2 Biophysics of antibodies

The immune system in vertebrates is subject of continuous evolution in order to protect itself from a range of intruding pathogens. The immune response arises from a number of innate and adaptive mechanisms representing the body's first line of defence [48]. The most significant process is the production of antibody molecules that are capable of recognizing harmful pathogens (bacteria, viruses, fungi, and other parasites) with exquisite specificity, neutralizing them and remembering them for faster response in future infections [48, 49].

2.2.1 Immunoglobulin classes and functions

Antibodies are antigen-reactive proteins produced by B-cells present in the plasma and in extracellular fluids, referred to as immunoglobulins (Igs). They represent the main component of immune serum obtained after exposure of the host to a given antigen. In humans, five classes of immunoglobulins, also referred to as isotypes (IgG, IgM, IgA, IgD and IgE), have been identified. They differ in terms of their physicochemical and serological properties, as well as in the amino acid sequence of their constant regions [50].

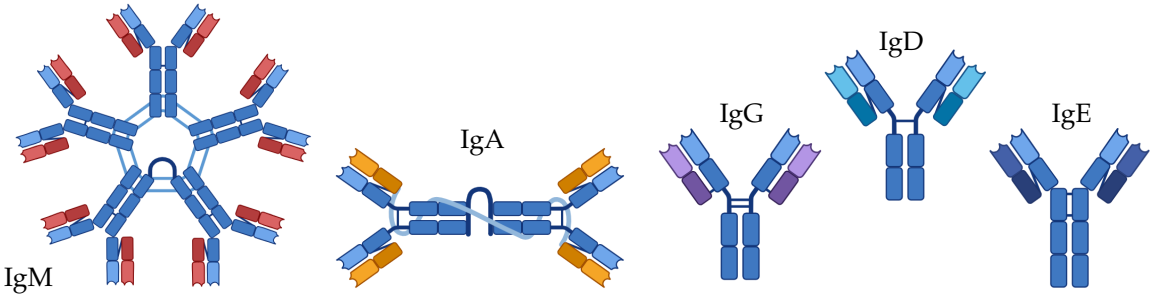

Fig. 2.1. Different classes or isotypes of human Igs. From left to right: IgM, in which monomers associate to form pentamers; IgA, characterised by its dimeric form and shown here with its secretory component (light blue filament); IgG, IgD and IgE, consisting in single monomeric units. Figure created using Biorender.

Figure 2.1 depicts the structure of the different human Ig isotypes. While IgG, IgD and IgE consist of a single monomeric unit, the IgM and IgA classes are composed of monomers that associate to form pentamers and dimers, respectively. Their structural organization translates into different functions. For instance, IgM is the first antibody produced in response to an infection and is primarily found in blood and lymphatic fluid. In fact, due to its pentameric structure, IgM is highly effective at binding antigens and initiating complement activation [50, 51]. The second phase of the immune response is managed by IgG, the most abundant antibody in blood and extracellular fluids and the only antibody

that can cross the placenta, providing passive immunity to the fetus [52]. In this context, IgA is instead present in breast milk and therefore provides passive immunity to newborns. IgA is mainly found in mucosal areas and secretions and defends against pathogens by preventing their attachment to and invasion of mucosal cells [53,54]. IgE is instead associated with protection against parasitic infections and allergic responses, due to its binding to allergens that triggers histamine release and eventually causes inflammation [50, 55]. IgE is also responsible for mast-cell and basophil function [56]. The least abundant antibody in blood is IgD, mainly present on the surface of immature B cells (or B lymphocytes) and potentially involved in the initiation of immune response and in the regulation of B cell function. The role of IgD still has to be fully defined [57].

Regardless of their isotype, antibody specificity, adaptability, and versatility make them foundational in both natural immunity and important applications in medicine, including diagnostics and targeted therapies for diseases such as cancer, autoimmune disorders, and infectious diseases. A recent review by Daëron provides a comprehensive overview of the diverse range of antibody functions from an immunological perspective [58].

2.2.2 Structure of immunoglobulin G

In their monomeric form, all Ig classes exhibit the same basic Y-shaped structure composed of two heavy chain (HC) and two light chain (LC) units, held together by covalent (disulphide) and non-covalent bonds [59–61]. While IgE and IgD monomers have a molecular-weight (MW) of $\sim$ 188 kDa and $\sim$ 184 kDa, respectively [50], IgG has a lower MW of $\sim$ 150 kDa. In this latter case, the molecular weight of each HC and LC is 50 kDa and 25 kDa, respectively. Given that the majority of mAb therapies are predominantly based on IgGs, the focus of this work will be entirely on these antibodies.

A detailed representation of an IgG antibody with its domains and relevant regions is reported in Figure 2.2. The basis of this Y-shaped protein is the so-called crystallisable fragment/domain (Fc), formed by two CH_2 and two CH_3 subdomains. The Fc region is essential in immune response modulation, pathogen elimination, determination of antibody class and function, prolongation of antibody half-life thanks to the binding to the neonatal Fc receptor (FcRn). This makes the Fc region essential for both natural immunity and therapeutic antibody development [62,63].

The hinge region is a flexible linker between the Fc and two "arms" of the protein are called antigen-binding fragment (Fab). It allows antibodies to adjust their binding sites to an antigen or receptor. The hinge is typically formed by 12 to 15 residues, depending on the Ig class and isotype; for further details, see paragraph 6.1 - 'IgG1 and IgG4 antibodies' in Chapter 6.

The lower part of the Fab, next to the hinge region, is formed by CH_1 and CL subdomains. The upper part of Fab domain is instead the antibody variable fragment/domain (Fv), as opposite to the constant part of the molecule (C-domains). Fv is in turn formed by VH and VL domains (where V stands for variable). The loop structures located on the Fv upper part are called hypervariable or complementarity determining regions (CDRs), which form the antigen-binding surface. The complementarity determining region (CDR) loops are normally six: CDR loop 1/2/3 in the heavy chain (CDR-H1/H2/H3) and CDR loop 1/2/3 in the light chain (CDR-L1/L2/L3).

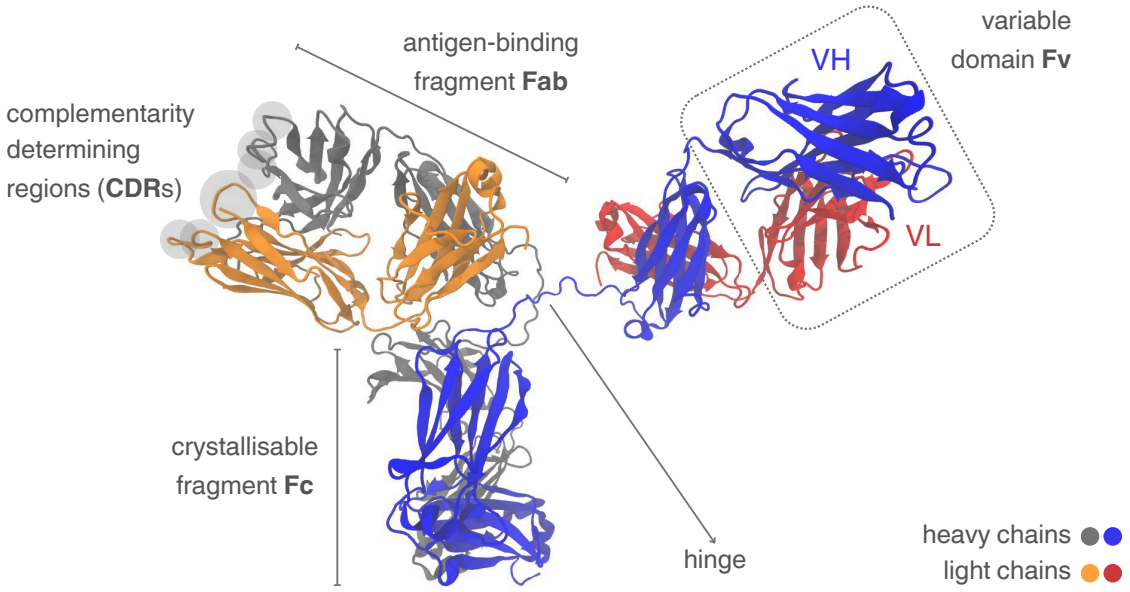

Fig. 2.2. Structure of an IgG1 antibody monomer with its domains and subdomains. The protein is formed by four polypeptide chains, two heavy ones (HC, depicted in grey and blue) of $\sim$ 50 kDa each, and light ones (LC, depicted in orange and red) of $\sim$ 25 kDa each. The two heavy chains are held together by disulphide bonds forming the so-called hinge region. The "stem" of the Y-shaped molecule is the Fc, while the two "arms" of the protein are called antigen-binding fragments (Fabs). The upper part of Fab domains is referred to as Fv, since it is the part where differences between antibody variants are generally located. Fv is formed by two subdomains VH and VL. The upper loop structures are called hypervariable or CDRs, which form the antigen-binding surface.

2.2.3 Polyclonal versus monoclonal antibodies

Polyclonal antibodies (pAbs) are a heterogeneous mix of antibodies (of the same class, mostly IgG) produced by multiple B cell clones in response to an antigen [64–66]. Each type in the mixture targets a specific epitope on the same antigen. This multiple-epitope binding is useful for broad target recognition, e.g. to identify complex antigens, such as proteins with several structural variations. Moreover, it ensures a high sensitivity, especially in applications like diagnostic assays, where pAbs can yield stronger signals and adapt to variations in antigen structure, making them useful for detecting pathogens or antigens with slight mutations.

Conversely, monoclonal antibodies (mAbs) are produced by a single B cell clone and recognize only a single epitope [64–66]. They are generated using specialized techniques, such as hybridoma technology, in which a single antibody-producing B cell is fused with a cancer cell to create a cell line that continuously produces identical antibodies [67]. The extremely high specificity of mAbs is a widely exploited feature in targeted therapies. In fact, they allow for precise intervention with minimized off-target effects. They typically address particular molecules, e.g. receptors, enzymes or proteins responsible for diseases like cancer, autoimmune disorders and inflammatory conditions. Unlike polyclonals, monoclonals provide uniform results across different batches, thus ensuring consistency and reproducibility [66]. Although pAbs may still be a useful tool for specific applications

and not easily replaceable by mAbs [68], the latter are undoubtedly a valuable asset in research and clinical applications where consistent dosing and targeted effects are paramount.

2.3 Monoclonal antibodies in therapeutics

After Köhler and Milstein developed the Nobel prize-winning hybridoma technology in the '70s [67, 69], monoclonal antibodies (mAbs) started to become the most popular class of biopharmaceuticals. This technology was employed to develop Orthoclone OKT3® (muromonab-CD3), which became the first monoclonal antibody approved by the U.S. Food and Drug Administration (FDA) [70]. Since that time, antibody therapeutics research and development have experienced a surprising growth, especially in the last two decades. Moreover, antibody-based products far exceed small-molecule drugs in terms of approval success rates. Until the end of 2023, nearly 200 mAbs in total have received approval in the U.S. or other countries, with 13 new ones in 2023 [71], 21 in 2024 [72, 73], and more were forecast to be either approved or to enter regulatory reviews by the end of 2025 [73]. The already broad spectrum of clinical applications of these biopharmaceuticals is currently expanding and includes several types of cancers [74–76], infectious and autoimmune diseases [77, 78], multiple sclerosis [79], kidney diseases [80] and migraine [81, 82]. In the last two decades, the development of mAbs for the treatment of neurodegenerative pathologies such as Alzheimer's disease has been the object of an extensive research [83–85], but still a lot of work has to be done for substantial steps forward in this field [86, 87].

Antibody-based drug products are mostly administered via intravenous (IV) or SC injections. A more detailed examination of the different administration routes for mAb-based drug products will be provided in Section 2.3.1. In the last years, pharmaceutical research has been focused in engineering antibody formulations for SC injection [88, 89], so that patients could benefit from self-administration and flexibility [90–92].

Since the amount of antibody needed is around hundreds of mg and the injectable volume in the subcutaneous space is in the range 0.5-2 mL, this administration route requires high concentrations, potentially leading to viscosities exceeding a tolerance threshold of $\sim$ 15-20 mPa·s [93, 94] and translating into high injection forces or long injection times [88,95]. Besides rendering the drug administration difficult (and sometimes impossible), high viscosity may also compromise the physicochemical stability and manufacturability of these pharmaceuticals [96, 97]. To this end, lots of studies on the microscopic origin of macroscopic viscosity of highly concentrated mAb solutions have been conducted to optimize their design and manufacturability [98, 99] by attempting to reach a fundamental understanding of this phenomenon.

One of the main reasons for high viscosity [100, 101] in mAb solutions is RSA, which can be influenced by multiple parameters, including concentration, pH, ionic strength [100], or specific interactions between domains of monomers [102, 103]. Both electrostatic and hydrophobic interactions seem to play a role in driving this mechanism [104] and affecting solution viscosity. Moreover, the peculiar shape and structure of antibodies – non-globular, multi-domain and flexible proteins – significantly influences their viscosity in solution [105].

2.3.1 Routes of drug administration

Regarding the administration of mAb-based drugs, it is important to choose the most appropriate route in terms of drug absorption, onset, and comfort of administration. The unique properties of

mAbs – large, complex and sensitive proteins – make this choice quite challenging. Although typically convenient, oral administration is not suitable for mAbs . In fact, the acidic environment of the digestive system can denature mAbs , and yet their large size prevents absorption [106].

Parenteral administration, referring to any non-oral method of delivering drugs directly into the body, bypasses the gastrointestinal tract being the most preferred delivery route for mAbs . This category includes intravenous (IV), subcutaneous (SC), intramuscular (IM), intradermal (ID), intrathecal, and intravitreal injections. Intrathecal and intravitreal routes are specialized methods for delivering mAbs to specific areas, like the central nervous system and the eye, respectively. While effective, these routes are invasive, generally reserved for severe conditions related to the targeted area and therefore require skilled administration [107, 108]. Injections entering the body via the skin barrier are referred to as percutaneous and are depicted in Figure 2.3. IV, IM, ID and SC are part of this subgroup and differ in terms of injection area and angle. Intravenous (IV) administration delivers drugs directly into the bloodstream and allows precise control and a fast drug release and absorption. However, it requires specific clinical settings with skilled personnel, often complicating long-term treatment. Intramuscular (IM) and intradermal (ID) routes are less common for mAbs due to issues with injection volume and the viscosity of mAb formulations. Still, research is exploring ways to make these methods more feasible for biologics, e.g. with micro-needling and transdermal patches [109–111].

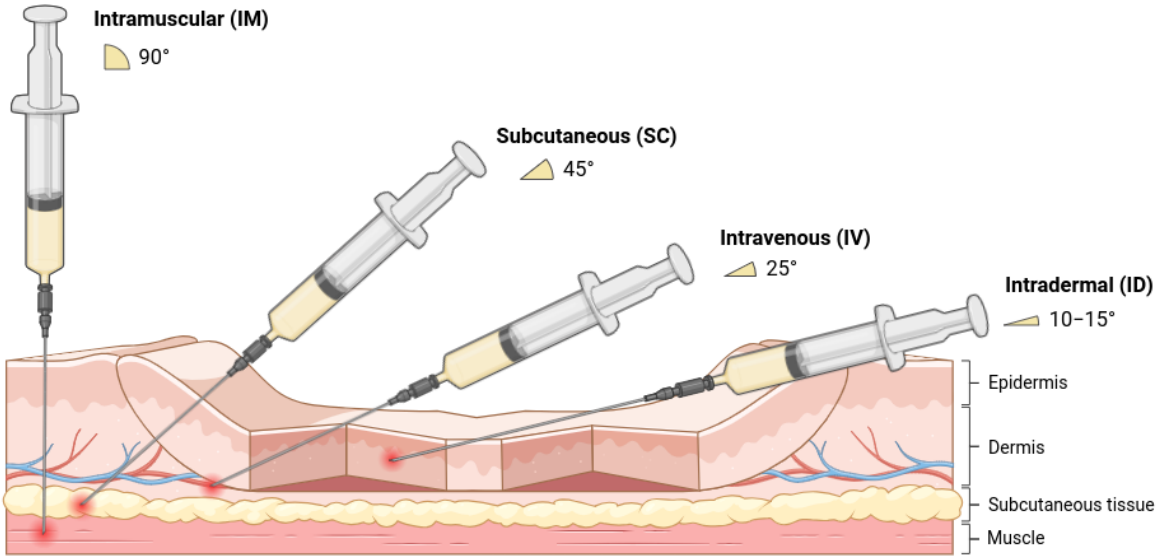

Fig. 2.3. Percutaneous routes of drug administration with specific injection angles, suited for the targeted area. For intramuscular delivery, the drugs are injected directly into the muscular tissue with the needle entering the skin barrier at 90°. For subcutaneous injections, the needle penetrates the skin at 45° and injects the drug in the fatty subcutaneous tissue – or hypodermis. For intradermal ones, the injection angle is 10-15° and the drug goes straight in the dermis. In intravenous administration, the drug is injected in a blood vessel with an angle of 25° and enters the bloodstream, ensuring a faster release. Figure adapted from template [112] and modified using Biorender.

The SC route, involving injection into the fatty tissue just beneath the skin, provides a middle ground between the rapid onset of IV delivery and the slower absorption of some other methods. Since SC injections are typically administered in areas with a layer of subcutaneous fat, such as the

abdomen, thigh, or upper arm, this route is very popular for mAbs due to the convenience of self-administration. Many mAbs for autoimmune diseases, such as adalimumab for rheumatoid arthritis, utilize this route [113]. Formulations for SC use must minimize injection site reactions while controlling absorption and especially minimize the viscosity of these highly concentrated protein solutions. To optimize delivery, manufacturers may adjust the formulation by adding stabilizers or altering the injection volume and concentration to reduce injection pain and control the absorption rate [114].

The preferred administration route for mAbs depends on the treatment needs, patient comfort, and logistical feasibility. Nevertheless, IV and SC administration remain the most common delivery routes. The substantial difference between the two lays in their pharmacokinetics; IV typically reaches peak blood levels immediately, thus being beneficial for high doses, rapid action, and high bioavailability and widely used in oncology or acute-care settings [115]. On the other hand, SC injections ensure a more controlled release and are thus commonly used for chronic conditions that require long-term management, where convenience and reduced frequency of clinic visits are important for patient adherence [114]. Of course, both routes of administration present advantages and disadvantages depending on the patient condition [116–118]. However, when SC formulations are optimized, no remarkable differences were observed between the two delivery methods in terms of drug efficacy [115, 119–121].

Ultimately, there is no definitive criterion for preferring SC over IV injection. However, the potential for self-administration undoubtedly makes the first option more appealing and patient-friendly, which is the reason why research in recent decades has been so focused on this goal. In this direction, the SC Drug Development & Delivery Consortium, recognising the factors creating pain or discomfort, is working to advance the development of patient-focused and well-tolerated high-dose/high-volume SC drug delivery solutions [122].

2.3.2 The role of excipients

As introduced in Section 2.3, counteracting the mechanism of RSA is of crucial importance in the manufacturability of mAb-based drug products. Since the pH of these formulations must remain in the physiological range and the temperature at which they must be stabilised is body temperature, the only way to tune intermolecular interactions is through the use of excipients.

Excipients are typically small molecules included in protein biotherapeutic formulations in solution to improve colloidal and conformational stability without compromising their injectability and pharmacokinetics [123]. Although they are not generally designed for the specific purpose of preventing aggregation, this function is fulfilled by the majority of them due to the reduction of the solvent accessible area on the surface of proteins in the presence of these other molecules. Based on their chemical structure, they can modify inter-protein interactions by shielding hydrophobic or charged patches, thus preventing self-association and aggregation and thereby reducing the solution viscosity [124]. A recent work by Kumar et al. [123] reviews all the excipients approved by U.S. FDA used in parenteral peptide and protein formulations from an industrial perspective, explaining in details their general purposes and disadvantages.

Among the most employed excipients in mAb formulations with the purpose of reducing their viscosity, one can find salts (NaCl, Na_2SO_4, NaOAc) [125], amino acids (proline or its analog forms [126]) or their salt forms (arginine-HCl, histidine-HCl, lysine-HCl, ornithine-HCl) [125, 127–131], and also in combination, e.g. Arg/Cl and Na/Glu [132]. Arg and its salts have been successfully employed in > 20 approved protein injectables, as viscosity reducers and protein stabilizers in high concentration

formulations [133]. Other molecules with analogous effects are hydrophobic salts [134], caffeine [135], amino acid derivatives [136] and even aminoacid polymers [137]. Moreover, the combination of some viscosity-reducing agents (e.g. amino acid + anionic excipient) has also been observed to enhance the performance of the excipients alone [131]. Although the addition of viscosity-reducing excipients to mAb formulations is by now a common practice in pharmaceutics, it is also the subject of continuous research [122, 138–141]. In order to prevent surface-adsorption and denaturation, polyoxyethylene-based surfactants such as polysorbates and poloxamers [142, 143], amphiphilic copolymers [144] and surfactants like Tween20® and Tween80® are used [123]. Excipients are also widely used as cryo- or lyoprotectants to preserve the proteins in freeze-dried and lyophylized products, which is the case of sugars and carbohydrates like sucrose, glucose, lactose, fructose, trehalose, sorbitol, mannitol, also acting as general stabilizers again temperature and tonicity adjusters [123]. Some of these sugars, along with glycine and succinic acid, have been studied with nuclear magnetic resonance (NMR) spectroscopy and computational methods to rank their interactions with mAbs in biologics formulations [145]. Sucrose is the only one displaying a specific binding site on the mAb surface, making it a better stabilizer than the others [145].

Of all the excipients mentioned, histidine certainly stands out for its versatility. In fact, due to its unique physicochemical properties among amino acids, histidine has been widely used as an effective excipient in protein-based biopharmaceutical formulations for its multi-faceted effect [146]. With a pKa of ~ 6.0 at the side chain, histidine has been primarily employed as a buffering agent, especially in the pH range 5.5–6.5. Since it displays properties analogous to those of carbohydrates (such as sucrose or trehalose), it can substitute them in stabilizing the formulations. It may also serve as a cryo-/lyo-protectant, antioxidant, viscosity and aggregation reducer via shielding hydrophobic regions [147, 148], and solubilising agent. More details on the importance of this excipient and on its specific use in the experiment described in this work are reported in Chapter 4.

2.4 General concepts of colloid physics

While inertia plays a crucial role in the macroscopic world, its effects become essentially negligible in the microscopic world of molecules. The opposite applies instead to friction and viscous forces arising from it. Indeed, whereas friction has far less impact than inertia in the macroscopic world, it assumes a pivotal role in the microscopic one. Each molecule, with particular focus on proteins, is subjected to friction due to the solvent and other neighbours, giving rise to a very diverse dynamics. To explain this concept, Callaway et al. produced a very powerful image stating that "the environment of a protein has more in common with playing badminton at the bottom of a swimming pool full of molasses than a cruise ship crossing the Atlantic Ocean" [149].

A central concept in both macroscopic and microscopic world of molecules moving in a medium is diffusion. Diffusion governs the transport of molecules through fluids and plays a fundamental role in pharmaceutical sciences [150], e.g. in formulation stability of drug products and in drug release mechanisms driven by concentration gradients. Although mAbs are complex proteins with a high degree of shape and diffusion anisotropy, they can be treated as (soft) colloidal suspensions in order to evaluate their diffusion behaviour and molecular interactions in solution in a simpler way. Despite its limits, a colloid approach to protein solutions still has an enormous potential in many areas [151], in particular providing a useful framework for understanding the dynamic, thermodynamic, and stability properties of mAb solutions.

Diffusion of charge-stabilized colloid suspensions has been extensively studied by theoretical ap-

proaches [3, 4, 152–155]. Due to the large size and mass disparity between colloidal particles and solvent molecules, diffusion can be understood by treating its simpler limit cases, namely the short-time and long-time diffusion [4]. A threshold is set by the time τ_B, above which the particles and solvent basically move inertia-free. The time $t \gg \tau_B$ characterizes the so-called Brownian dynamics regime. Following the random walker formalism, the mean squared displacement (MSD) of each particle experiencing Brownian motion – measuring how it explores its surroundings over time t – can be expressed as:

$$r^2(t) = 2n\,D\,t = 6\,D\,t\,,\ \text{if}\ n = 3\,. \tag{2.1}$$

n is the dimensionality of the system – in this case, $n = 3$. So, for Brownian/free diffusion, the MSD increases linearly with time. Within this regime, which is the one accessed by all the experimental techniques employed in this work, one can distinguish between *short-time dynamics*, characterized by $\tau_B \ll t \ll \tau_I$ and *long-time dynamics*, instead defined by $t \gg \tau_I$. Short-time diffusion thus occurs before hydrodynamic interactions and long-range collective effects dominate, while long-time diffusion describes hydrodynamic, electrostatic and direct interactions with other particles [4].

The diffusive behaviour of the system under study therefore depends entirely on which regime is accessed by the instrument used and on the measurement time.

2.4.1 Diffusion tensor, self- and collective diffusion

The study of particle diffusion in many-body colloid suspensions spans multiple scales and requires descriptions of both individual and collective particle dynamics. At the heart of these descriptions is the diffusion tensor $\mathbf{D}$, a fundamental quantity that encodes the anisotropic nature of particle motion. The diffusion tensor is a mathematical representation of the microscopic, directional and complex diffusion of particles under the influence of thermal motion and interactions with the surrounding medium and serves as the starting point for deriving macroscopic diffusion properties.

From the generalized diffusion described by $\mathbf{D}$, two specific cases can be derived [3, 34]:

- the *self-diffusion* or *tracer diffusion*, describing the motion of individual particles over time;
- the *collective diffusion*, representing the time-evolution of density fluctuations in a system.

These quantities are interrelated and form a coherent framework for understanding particle behaviour in complex systems. More details on these two distinct concepts and how the quantities can be probed with neutron scattering techniques are presented in the next paragraph and further discussed in Chapter 3, Section 3.1.4.

In 1905, Einstein [156] demonstrated that the diffusion of non-interacting particles in a viscous medium can be well described by the following Fick's law [157] and is denoted as "free diffusion":

$$\mathbf{J} = -\mathbf{D} \cdot \nabla\rho\,. \tag{2.2}$$

Here, $\mathbf{J}$ is the diffusion flux vector (amount of substance per unit area per unit time, $\mathrm{mol} \cdot \mathrm{m}^{-2} \cdot \mathrm{s}^{-1}$), $\nabla\rho$ is the concentration gradient (spatial rate of change of concentration, $\mathrm{mol} \cdot \mathrm{m}^{-4}$), and $\mathbf{D}$ is the aforementioned diffusion tensor, defined as a symmetric, positive-definite 3×3 matrix. Diffusion is thus mathematically described as the tendency of the system to return to an equilibrium state characterized by a uniform concentration of particles, also being the state of maximum entropy and a thermal equilibrium [158]. The direction of the diffusion is from high to low concentrations, hence the negative sign in 2.2. From equation 2.2 and the following principle of mass conservation

$$\frac{\partial\rho(\vec{r},t)}{\partial t} + \vec{\nabla} \cdot \vec{\mathrm{J}}(\vec{r},t) = 0\,, \tag{2.3}$$

the diffusion equation or second Fick's law can be obtained [157]:

$$\frac{\partial \rho(\vec{r},t)}{\partial t} = \mathbf{D} \cdot \nabla^2 \rho(\vec{r},t)\,, \tag{2.4}$$

In isotropic systems, $\mathbf{D}$ instead simplifies to:

$$\mathbf{D} = D_{ij} = D\,\delta_{ij}\,, \tag{2.5}$$

where D is a scalar diffusion coefficient, and δ_{ij} is the Kronecker delta. In this case, the Fick's law therefore reads as follows:

$$\frac{\partial \rho(x,t)}{\partial t} = D\frac{\partial^2 \rho(x,t)}{\partial x^2}\,. \tag{2.6}$$

The solution of equation 2.6 can be written as

$$G_s(\vec{r},t) = \frac{1}{(4\pi D|t|)^{3/2}} \exp\left(-\frac{r^2}{4D|t|}\right), \tag{2.7}$$

a correlation function describing the correlation of a particle with itself over time, also referred to as *self-correlation*. This solution in the reciprocal space reads as

$$I_s(\vec{q},t) = \int G_s(\vec{r},t)\exp(i\vec{q}\cdot\vec{r})\,\mathrm{d}^3\vec{r} = \exp(-i\,q^2 D\,|t|) \tag{2.8}$$

and it is defined as the self- (or incoherent) intermediate scattering function. Writing this in the $(\vec{q},\omega)$-space, it gives the incoherent dynamic structure factor

$$S_s(\vec{q},\omega) = \frac{1}{2\pi\hbar}\int I_s(\vec{q},t)\exp(-i\omega t)\,\mathrm{d}t = \frac{1}{\pi\hbar}\frac{Dq^2}{(Dq^2)^2+\omega^2} = \frac{1}{\pi\hbar}\frac{\gamma}{\gamma^2+\omega^2} = \mathcal{L}_\gamma(\omega)\,. \tag{2.9}$$

So, in a system of many non-interacting particles diffusing freely, the scattering function can be essentially described by a Lorentzian function with a half width at half maximum (HWHM) $\gamma(q) = Dq^2$.

In anisotropic systems, the diffusion tensor contains off-diagonal terms, reflecting coupled motion along different axes, e.g. when a concentration gradient along the x-axis induces a flux on the z-axis. Being the most general descriptor of how particles diffuse microscopically, $\mathbf{D}$ contains both translational and rotational contributions coupled together. To calculate $\mathbf{D}$ for known biomolecules, the software HYDROPRO [159, 160] can be employed. It requires the Protein Data Bank (PDB) structure as input, which is assumed to be rigid, and accounts for the full shape anisotropy [159, 160].

2.4.2 Viscosity, diffusion and cluster formation

As already mentioned, years later after Fick's laws, Einstein found the link between the diffusion coefficient of non-interacting spherical particles performing the so-called "Brownian molecular motion" with the medium viscosity and the size of the suspended particles [156]:

$$D = \frac{k_B T}{6\pi\eta R_H}\,. \tag{2.10}$$

The diffusion coefficient D is directly proportional to the temperature T and inversely proportional to the viscosity of the surrounding medium and the the hydrodynamic radius of the particles R_H. The validity conditions of the Stokes-Einstein (SE) relation 2.10 are that the medium is homogeneous and isotropic, the system is at thermal equilibrium, the particles are large compared to solvent molecules

and the particle concentration is in the dilute limit. Equation 2.10 thus holds for the translational diffusion coefficient at the dilute limit D_{t0}:

$$D_{t0} = \frac{k_B T}{6\pi\eta R_H} \,. \tag{2.11}$$

A particle with a radius R_H can also rotate around its origin generating a rotational component contributing to the scattering function. This rotational component can be described by a rotational diffusion coefficient D_{r0} that can be linked to the hydrodynamic radius at the dilute limit, leading to the Stokes-Einstein-Debye (SED) relation:

$$D_{r0} = \frac{k_B T}{8\pi\eta R_H^3} \,. \tag{2.12}$$

Both translational and rotational components of the diffusion D_t and D_r slow down as long as the particle concentration increases. For hard spheres, the volume fraction scaling can be written as:

$$D_t(\varphi) = D_{t0} \cdot f_t(\varphi) \tag{2.13}$$

$$D_r(\varphi) = D_{r0} \cdot f_r(\varphi) \tag{2.14}$$

for translational and rotational diffusion, respectively. The scaling factors $f_t(\varphi)$, $f_r(\varphi)$ are described by expressions given in refs. [4, 161] and can further change if the particle shape varies or any interaction is taken into account [4, 162].

If the translational diffusion contribution to the scattering function is a single Lorentzian function (Equation 2.9), the incoherent scattering function for rotations is an infinite sum of Lorentzians:

$$S_s(q,\omega) = \sum_{l=0}^{\infty} B_l(q)\mathcal{L}_{\gamma r}(\omega) \,, \tag{2.15}$$

$$\gamma_r = l(l+1)\, D_r \;;\; B_l(q) = (2l+1) \int \rho_H(r) j_l^2(qr) \mathrm{d}r \,, \tag{2.16}$$

with $\rho_H(r)$ and $j_l(qr)$ being the hydrogen distribution of the particles investigated and the l-th order spherical Bessel functions. When both translations and rotations are taken into account, as in real samples, the QENS spectra obtained can be perfectly fitted with one or a sum of Lorentzian functions, based on the different motions occurring in the system. Nevertheless, the signal contains coupled information on both translations and rotations. Assuming to fit a QENS spectrum with a single Lorentzian, its HWHM would be linked to an apparent global diffusion coefficient D_{app} fulfilling the condition [163]

$$\sum_{l=0}^{\infty} B_l(q) \frac{l(l+1)D_r + q^2(D_t - D_{app})}{l(l+1)D_r + q^2(D_t + D_{app})} = 0 \,. \tag{2.17}$$

Furthermore, the classical relation 2.10 could be extended to more complex systems, e. g. non-Newtonian fluids, crowded or non-homogeneous or out-of-equilibrium systems, leading to several generalized forms. In real – non-model – systems, the viscosity is and hence the diffusion coefficient changes with the applied shear rate:

$$D(\omega) = \frac{k_B T}{6\pi\eta(\omega) R} \tag{2.18}$$

Banchio et al. derived the viscoelasticity and generalized Stokes-Einstein (GSE) relations in hard-sphere and charge-stabilized colloidal suspensions [164]. Moreover, there is a close connection between the SE relation and the more general fluctuation-dissipation theorem (FDT), proven by Callen and Welton in 1951 [165] and expanded in the following decade by Kubo [166]. The FDT states that

the response of a system to an external perturbation is the same as that of its spontaneous thermodynamical fluctuations. It follows that in a system at its equilibrium the ratio of the correlation and response functions is constant, with (inverse) temperature being the proportionality constant. In this sense, the Stokes relation $B = 1/6\pi\eta R$ – related to the SE one $D = B\,k_B T$ (with B being the particle mobility) [167] – can be interpreted as a manifestation of the FDT in colloidal particles [167,168]. Any deviations from the SE in nonequilibrium systems can therefore be described in terms of an effective thermodynamic temperature in the FDT framework [167]. The limits of the validity of the SED relation for the rotational diffusion in colloid suspensions were discussed by Könderink et al. [169].

In the specific case of protein solutions, the condition that most compromises the validity of SE is the high concentration/crowding and this is particularly relevant for the scientific case presented in this work. Rothe et al. used pulsed-field gradient (PFG)-NMR to demonstrate apparent violation of GSE in crowded protein solutions and linked it to transient binding [170].

2.4.3 Simulations, in silico predictions and scattering experiments on mAb solutions

In the last decades antibody solutions have been the subject of a huge number of studies, which in most cases tend to combine experimental and computational/predictive approaches. In the following paragraphs an overview of a few significant works on the topic will be given. This excursus is not intended to be completely exhaustive on the subject.

Several studies have successfully investigated the link between viscosity, RSA and cluster formation using small angle X-ray scattering (SAXS), microrheology and coarse-grained simulations, and employed cluster theory to predict structure factors of highly concentrated mAb solutions [171,172]. The same systems have also been investigated using again SAXS, viscometry, static light scattering (SLS) and DLS, in combination with other analytical techniques [173] and again coarse-grained modeling [174]. Kumar et al. unveiled the underlying mechanism of anomalous diffusion [43] in bulk of highly-concentrated mAb solutions using coarse-grained simulations. The same computational method was applied to investigate the adsorption of mAb fragments at the oil-water interface [175], to shed light on the molecular mechanism behind the stabilizing effect of histidine in mAb solutions [148], and again to investigate the effect of glycosylation on PPIs in these systems.

Atomistic simulations have been widely employed to predict the viscosity of high-concentration mAb solutions [176]. Molecular simulations can significantly contribute in fitting small angle scattering data for a comprehensive biophysical characterization of these samples [177]. Both atomistic and coarse-grained simulations are essential to assess mAb colloidal stability on a multi-scale level [178] and can quantitatively predict protein-protein interactions [179].

The complementary approach to viscosity reduction via mAb formulation optimization is protein engineering. This method consists in predicting how viscosity is affected by small modifications in the primary sequence, especially in the Fv of the antibody [180]. Different viscosity trends depend on how the mAb Fab and Fc contribute to aggregation, so PPIs and viscosity are perfectly tunable by modifying specific sites or patches of the protein [181]. Viscosity prediction and minimization can be done via machine learning (ML) or deep-learning algorithms [182, 183], and also using artificial neural networks (ANNs) based on experimental and simulation-derived parameters for rational drug design [184]. For instance, antibody sequence mutations aiming to reduce hydrophobic patches seem to reduce significantly mAb solution viscosity, whereas mutations altering only electrostatic patches were insufficient to influence viscosity [185].

Beyond computational studies, experimental techniques based on scattering are extremely useful for a biophysical characterisation of mAbs in solution on multiple length and time scales. Light scattering is undoubtedly one of the first analytical approaches to monitor aggregation, often along with size-exclusion chromatography (SEC) [186]. Using DLS, the long-time diffusion of the particles can be measured and the presence and the size of potential aggregates can be assessed [187]. Colloidal interactions and formulation stability [102, 188–190] can also be investigated. In some cases, DLS can be used to study antibody-antigen dynamics [191]. The useful parameter that can be extracted from DLS is the diffusion-interaction parameter $\mathrm{k_D}$, defined as the slope of the linear fit performed on $D_\mathrm{c}^\mathrm{long}$ *vs* protein concentration/volume fraction. Analogously, the second virial coefficient $\mathrm{A_2}$, can be extracted from the slope of a linear fit of the scattered intensity obtained from SLS plotted *vs* protein concentration (source: Malvern Panalytical). These two parameters arising from the combination between DLS and SLS information are typically very important to establish the formulation stability of mAb solutions [184, 192–194]. Moreover, their behaviour at high concentrations can be predicted from the conditions of the dilute solutions [195–197].

Besides light scattering, higher energy photons and neutrons are effective probes for the study of soft and biological matter. For example, SAXS is a classical tool to study proteins in solution [198–201], often combined to atomistic and coarse-grained simulations [202, 203]. In antibody solutions it is essential to link macroscopic viscosity to biophysical and structural properties like the size of potential aggregates, the intensity of their PPIs and their flexibility [204–210]. This enables the assessment of their formulation stability upon variation of environmental conditions like pH, temperature, and buffer composition [128, 211–215].

The neutron analogue for this technique is SANS, which will be presented in detail in Chapter 3. This experimental tool can benefit from the intrinsic non-disruptiveness and isotopic sensitivity of neutrons to carry out contrast variation studies in biological systems [216, 217] – and specifically for mAbs [216] – and measure hydrogen-deuterium exchange (HDX) [218]. In order to study mAb solution, SANS is often used in combination with SAXS [219–222], light scattering [192, 223], chromatography [224–226], rheology [223, 227–230], atomistic and coarse-grained modeling [224, 230], colloid theory descriptions [231, 232] and dynamic techniques like NBS [194] and NSE [233–235], which will be further explained in the next paragraph. A comprehensive overview of the utilisation of neutron scattering in general for the investigation of mAb solutions can be found in the review by Wang et al. [236].

2.4.4 The unique capabilities of spectroscopy

Spectroscopy is a powerful and versatile analytical technique that involves the interaction of a probe, e.g. electromagnetic radiation, neutrons, electrons, with matter to study its properties. By analysing the energy and momentum variation of the probe after its interaction with matter, spectroscopic techniques based on scattering typically offer simultaneous access to spatial and time correlations. This is the reason why spectroscopy in general represents a fundamental pillar of scientific research, offering unparalleled insights into the structure, dynamics, and interactions of matter.

For instance, NMR spectroscopy detects the spin relaxations of nuclei subjected to a magnetic field. This non-destructive technique is able to access solid-state and biological materials. In contrast to scattering techniques, which access spatial correlations, NMR provides information on angular correlations [237]. It can probe molecular dynamics over a wide time window (from nanoseconds to second) and it allows real-time monitoring of specific chemical reactions and precise location of

their sites, e.g. bonding between two molecules. The numerous possibilities in designing the magnetic fields and their time dependencies for NMR are beyond the scope of this paragraph. Antibody pharmaceutical formulations have been extensively studied via NMR spectroscopy for a comprehensive biophysical characterization [238], e.g. to assess their viscosity [239–241], protein-protein interactions [242], and excipient-driven LLPS [243].

Another powerful technique that gained interest and success in the last decades is X-ray photon correlation spectroscopy (X-ray photon-correlation spectroscopy (XPCS)), which employs a transversely coherent X-ray synchrotron or free-electron laser (FEL) beam to measure the slow dynamics of matter, in particular of soft and disordered systems with dynamics on timescales ranging from microseconds to seconds [244]. XPCS is the X-ray equivalent of dynamic light scattering (DLS), the latter using visible photons. As DLS, XPCS probes long-time collective diffusion. Protein solutions have been the subject of numerous experiments using this technique. For instance, XPCS was employed to probe molecular dynamics and aggregation of concentrated mAb solutions [245]. Two model proteins, e.g. BSA and lysozyme (LYS) were also investigated upon entering LLPS triggered by charge-decoration or pressure [246, 247]. This technique is also useful to access long-time cage relaxations and anomalous diffusion [248,249]. Although very powerful, XPCS on biological samples can be potentially destructive due to radiation damage. It is thus necessary to find strategies to obtain analysable speckles, without altering the sample structure and chemical composition [250, 251].

Of the various spectroscopic techniques available, neutron spectroscopy is undoubtedly central to the study of soft and biological matter. With its wide range of possible configurations and the intrinsic property of neutrons as a non-invasive probe, neutron spectroscopy is a versatile tool for the investigation of dynamic and structural properties of matter, with a special mention for biological systems like pharmaceutically relevant mAb solutions. Its ability to probe protein-protein interactions, hydration dynamics, and conformational motions under various conditions makes it invaluable for optimizing formulation stability, reducing aggregation, and improving the overall design of therapeutic proteins. In the simplest case, diffusion results in overdamped harmonic oscillations or Debye-relaxations that gives rise to a so called quasi-elastic scattering (QENS) [252,253]. These diffusive motions can be probed using spectrometers with different energy resolutions and hence different configurations. The design concept for spectrometers always constitutes a compromise between neutron beam intensity on the sample and the coherence volume V_c of the interaction of this beam with the sample [254–256].

For example, NBS is an energy-resolved technique that measures the dynamic structure factor (or scattering function) $S(q, \omega)$ of the sample (cf. Section 3.1.4 in Chapter 3). In this case, the QENS signal shows itself as a broadening around the elastic peak, signature of the presence of one or diffusive motions/relaxations. On the other hand, NSE spectroscopy is time-resolved counterpart measuring the sample intermediate scattering function (ISF) $I(q, t)$, which is basically a correlation function in the reciprocal space. In this other case, diffusive motions with different rates result in slower or faster exponential decays and their coexistence gives rise to non-single or stretched exponentials. Both techniques can access the center-of-mass (COM) dynamics of potential protein aggregates and also their internal and sub-domain motions. For this reason, both NBS and NSE have been extensively employed in protein solutions. The main difference between these two spectroscopic techniques is that while NSE mainly probes short-time collective diffusion, NBS accesses the short-time self-diffusion of the particles in the sample.

General reference works on protein solutions studied with NSE are the ones by Liu [257,258] and Callaway et al. [149,259], but also pivotal studies on several proteins, e.g Taq-polymerase [260], fer-

ritin [261], hemoglobin and myoglobin [262, 263], mammalian Na^+/H^+ exchange regulatory factor 1 (NHERF1) [264], β-lactoglobulin (BLG) [265], phosphoglycerate kinase (PGK) [266], alcol dehydrogenase (ADH) [267, 268], multi-domain flexible proteins [269, 270], intrinsically disordered proteins (IDPs) and unfolded proteins [271]. Recently, Callaway et al. [272] used NSE to reveal the activation of nanoscale dynamics in the cell–cell adhesion cadherin–catenin complex upon binding to vinculin, relevant for adherens junction functioning. NSE is also confirmed as an essential technique to investigate nanoscale dynamics of antibodies [233,235,273,274], in order to access their internal and domain dynamics in aqueous solutions [235, 274] and to probe them in an arrested phase, e.g. in the presence of PEG [273]. A milestone work employing NSE on two National Institute of Standards and Technology (NIST) mAbs is the one conducted by Yearley et al. [234], where they revealed formation of small clusters of few monomers as the underlying mechanism of high solution viscosity.

A richer body of literature on NBS applied in protein solutions is available and provided by an excellent review by Grimaldo et al. [1]. More recent works on this topic involve model proteins like BSA alone [275, 276] and in a bidisperse solution with Ig [38], hemoglobin [277], myelin basic protein (MBP) [278], LYS and tau protein and their pathological aggregation [279, 280], and histatin5 as an intrinsically disordered protein (IDP) model [281]. The sub-ns diffusive dynamics of other proteins like the core domain of the cardiac protein troponin (Tn-CD) [282, 283] and Lv18 (squid-inspired protein from Loligo vulgaris) [284] was also studied, along with the effect of the solvent or other molecules on protein solution behaviour [285, 286]. NBS is also an excellent technique to access short-lived clusters and their behaviour upon temperature variation [194, 287] and the microscopic picture of proteins when the enter the LLPS regime [273, 288]. The significant use of this technique for the systems under consideration has led to the development of increasingly advanced frameworks for data collection, interpretation and analysis [289–292].

We note that our work [194], presented in detail in Chapter 5, is to our knowledge the first application of NBS to a series of mAbs. The NSE-SANS study in Chapter 6 is instead the first study employing those techniques on an unprecedented set of pharmaceutically relevant antibodies.

Chapter 3

Neutron scattering

In the present chapter, the theory of neutron scattering is presented starting from the basics – neutron radiation and production – , building the mathematical framework behind it step by step, ultimately focusing on the physical quantities that are actually probed in the experiments conducted, on the techniques employed and, eventually, on the specific instruments. The main sources of this chapter are: "Theory of neutron scattering from condensed matter" by S. W. Lovesey (1984) [293], "Introduction to the Theory of Thermal Neutron Scattering" by G. L. Squires (3rd ed. Cambridge University Press - 2012) [294] and "Neutron Scattering" by F. Fernandez-Alonso and D. Price [295]. The content is shaped from Ref. [296] and expanded.

3.1 Theoretical framework

3.1.1 Neutron radiation, production and properties

When the physicist Sir James Chadwick discovered the neutron in 1932, no one could imagine that this groundbreaking achievement, for which he was awarded the Nobel prize in 1935, would have a high significance even beyond the understanding of atomic and nuclear structure. The neutron is a subatomic particle with no electrical charge, with a mass $m = 1.67492735 \times 10^{-27}$ kg (1839 times the electron mass) or analogously $m = 939.565$ MeV and spin-parity $J^{\pi} = \frac{1}{2}^{+}$. The neutron decays via β-decay as it follows:

$$n \rightarrow e^{+} + e^{-} + \overline{\nu}_{e}\,, \tag{3.1}$$

so to a proton e^{+} by emitting an electron e^{-} and an electron anti-neutrino $\overline{\nu}_{e}$, with a mean lifetime $\tau = (881.5 \pm 1.5)$ s. Having no electrical charge, neutrons have a low interaction probability with matter and a high level of penetration in matter. For this reason, they are a good probe for bulk properties of condensed matter. Since the neutron possesses a magnetic moment $\mu_N = -1.913\ \mu_B$, it is also useful to probe magnetic features.

Neutrons can be produced using either spallation or nuclear fission. Spallation reaction is an inelastic nuclear interaction induced by incident high-energy particles, like accelerated protons, hitting target nuclei, e.g. mercury and tungsten. The impact causes the disintegration of the target nuclei, which produces several secondary particles, including neutrons [297]. These neutrons can be collected, moderated in energy and delivered to different instruments. The importance of spallation sources for the design of specific instruments, e.g. operating on time-of-flight (TOF) technique, has been widely discussed in numerous works [298, 299]. Since each proton impact causes a spallation

event localized in time, neutrons are ejected from the target in bursts. Using a continuous beam of protons could compromise the synchronization between neutron production and experimental detection. If a pulsed proton beam is employed instead, neutron bursts are well-defined in time, which is essential for many measurements. Some sources operating on this principle are the Spallation Neutron Source (SNS) at Oak Ridge National Laboratory (ORNL) and Los Alamos Neutron Science Center (LANSCE) in the US, ISIS at the Rutherford Appleton Laboratory in the UK, China Spallation Neutron Source (CSNS), Japan Proton Accelerator Research Complex (JPARC), Swiss Spallation Neutron Source (SINQ) at Paul Scherrer Institute (PSI) in Switzerland and the European Spallation Source (ESS) in Sweden (currently under construction).

Attention should now be directed towards the other mode of neutron production: nuclear fission. In simple words, nuclear fission is the process by which an unstable heavy atomic nucleus divides into two or three fragments – lighter nuclei – with a massive energy emission in the form of heat and radiation. This exothermic reaction can occur spontaneously in nature, but it can also be artificially triggered by the collision with other particles, like neutrons. This is the case of all nuclear power plants and research reactors in the world. The commonly used fuel elements are uranium-235 (^{235}U, with 143 neutrons in its nucleus) and plutonium-239 (^{239}Pu, with 145 neutrons), with the first being the most employed one. After an initial collision with a thermal neutron (see Table 3.1), ^{235}U absorbs it becoming ^{236}U and then splits into lighter nuclei by releasing neutrons. The reason why thermal neutrons are preferred to trigger this reaction in ^{235}U lies in their fission cross section of 584.1 ± 3 bn, significantly higher than the one for fast neutrons being ≈ 1 bn. One of the many fission reactions that ^{235}U can undergo is the following:

$$n + {}^{235}_{92}\mathrm{U} \rightarrow {}^{236}_{92}\mathrm{U} \rightarrow {}^{146}_{56}\mathrm{Ba} + {}^{92}_{36}\mathrm{Kr} + 3\,n \tag{3.2}$$

In this specific case, with a neutron absorption process (left side of reaction 3.2), ^{235}U becomes ^{236}U, which then splits into barium $^{146}_{56}$Ba and krypton $^{92}_{36}$Kr, emitting 3 neutrons. Neutrons are thus the final products of this reaction and can trigger further processes in a so-called "nuclear chain reaction". Several research facilities are operating based on this principle, including the high flux isotope reactor (HFIR) at ORNL and the National Center for Neutron Research (NCNR) at NIST in the US, Forschungsreaktor München II (FRM-II) in Germany and the high-flux research reactor at the Institut Laue-Langevin (ILL) in Grenoble, where the majority of the experiments presented in this work was conducted. At present, the ILLcan provide the most intense continuous neutron flux in the world, namely up to 1.5×10^{15} neutrons per second per cm^2, with a maximum thermal power of 58.3 MW. Its core is formed by a single highly enriched uranium fuel element (10 kg) that is cooled by heavy water. The high-energy neutrons produced are slowed down by the heavy water both to trigger further fission events in order to sustain the chain reaction and to supply neutrons to the different instruments.

For a better understanding of how the neutron speed can affect its properties and its consequent scientific relevance, one can start by considering the kinetic energy E of a free neutron of mass m travelling with velocity v, which can be written as it follows:

$$E = \frac{1}{2} m v^2 \,. \tag{3.3}$$

Note that the formula just written is valid in the classical approximation, which applies in the case of cold neutrons [300]. In agreement with the wave-particle picture, neutrons are also plane waves with a wavevector

$$\vec{k} = \frac{m}{\hbar}\vec{v} \tag{3.4}$$

and a De-Broglie wavelength

$$\lambda = \frac{2\pi}{|\vec{k}|} = \frac{h}{mv}\,, \tag{3.5}$$

with h and $\hbar$ being the normal and the reduced form of Planck's constant, respectively. So, for a given kinetic energy E of the neutron, there is a De-Broglie wavelength λ obeying the following relation:

$$E = \frac{\hbar^2 k^2}{2m} = \frac{h^2}{2m\lambda^2} = k_B T\,. \tag{3.6}$$

According to equation 3.6, a thermal neutron with $T \sim 300$ K, corresponding to an energy $E = 25$ meV, has a wavelength $\lambda = 1.81$ Å, which is compatible with atomic spacings in condensed matter. This fact suggests that one can probe structure and dynamics in matter at different levels through changing the incident neutron energy. At the facilities mentioned above, neutrons can be produced at various energies, depending on the moderator used (Table 3.1). Depending on the temperature T of the moderator, the flux velocity density distribution $\phi(v)$ of the moderated neutrons is sufficiently well described by a Maxwell distribution:

$$\phi(v) \propto v^3 \exp\left(-\frac{mv^2}{2k_B T}\right), \tag{3.7}$$

with k_B being the Boltzmann constant and m the mass of the neutron. In particular, cold neutrons match the energies encountered in proteins and nucleic acids, providing access to both spatial and temporal information. Cold neutrons also have the advantage of preserving chemical bonds due to their low energy, spanning from 0.1 to 10 meV (see Table 3.1). In reactors, a first moderator is typically used to cool down the neutrons until thermal energies and temperatures. To obtain cold neutrons, one has to shift the energy of the thermalized reactor-neutrons to even lower temperatures. Therein the need of a second moderator, consisting of 2.5 l of liquid deuterium at a temperature of 25 K. The liquid deuterium is confined in an aluminium sphere immersed in the D_2O of the first moderator near the uranium core. Subsequently, the cold neutrons are delivered to the instrument by zigzagging through the neutron guide by means of total external reflections on nickel-titanium multilayers. In an actual scattering experiment the key variables are the change in neutron energy $\hbar\omega$ and the corresponding change in neutron momentum $\vec{Q}$. Being E, $\vec{k}$ the energy and the momentum of the incident neutron and E', $\vec{k'}$ the ones of the scattered neutron, the energy transfer between the probe and the sample reads as:

$$\hbar\omega = E - E' = \frac{\hbar^2}{2m}(k^2 - k'^2)\,, \tag{3.8}$$

while the momentum transfer (or scattering vector) is

$$\vec{Q} = \vec{k} - \vec{k'}\,. \tag{3.9}$$

Source	Energy [meV]	Temperature [K]	Wavelength [Å]	Velocity [m/s]
Ultra-cold	$< 3 \times 10^{-4}$	$\sim 3.5 \times 10^{-3}$	> 500	< 7.575
Cold	$0.1 - 10$	$1 - 120$	$30 - 4$	$138.3 - 1383$
Thermal	$25 - 100$	$60 - 1000$	$4 - 1$	$2185 - 4373$
Hot	$100 - 500$	$1000 - 6000$	$1 - 0.4$	$4373 - 9779$
Epithermal	$500 - 10^7$	> 6000	$0.4 - 0.03$	$9779 - 1.38 \times 10^6$

Table 3.1. Energy, temperature, wavelength and velocity for five types of neutron sources [293, 301].

The spectrum of the scattered neutrons is solely a function of $\vec{Q}$ and no other functions of $\vec{k}$ and $\vec{k'}$, because the scattering of low-energy neutrons is a weak process and can can be described using quantum mechanical perturbation theory, as further explained in Sec. 3.1.2.

The motion of atoms and their spatial correlations are revealed in a neutron scattering experiment when the energy and momentum transfer $\hbar\omega$, $Q = |\vec{Q}|$ accessible by the instrumental setup match the corresponding energies and momenta involved in the sample structure and dynamics. The $\vec{Q}$ and ω-dependence of the scattered intensity can often be ascribed to the conservation of energy and wave-vector in the scattering process; for example, scattering from a lattice vibration with a long lifetime occurs only when the neutron energy and wave-vector coincide with the energy and the wave-vector of the vibration.

Furthermore, Equations 3.8 and 3.9 show that ω and $\vec{Q}$ are related and this relation imposes kinematic constraints on the scattering experiments. Therefore, not the entire $(\vec{Q}, \omega)$-space is accessible in a neutron scattering experiment. The kinematically allowed region is a function of the neutron incident energy E and lies between the $(\vec{Q}, \omega)$-loci corresponding to forward and back-scattering configurations. For example, in order to access the domain of large ω and modest $\vec{Q}$ it is necessary to use incident neutrons with high energies and to measure at small scattering angles.

3.1.2 Neutron scattering cross-section

In the following paragraph, a mathematical description of the neutron scattering cross-section will be presented. Please note that magnetic scattering will be neglected and only nuclear scattering will be taken into account in the following calculations.

When a neutron passes near a nucleus there are two possibilities translating into two different neutron-nucleus interactions. One option is *neutron absorption* by the nucleus. A compound nucleus in an excited state is formed and it decays into its ground state. In most cases this decay occurs by γ-emission or α-emission, which is used for instance in ^{3}He neutron detectors. Finally, the compound nucleus can decay by fission, like uranium in a reactor core. The other possible scenario is *neutron scattering* by the nucleus, therefore its direction as well as its energy and momentum may change after the collision with the target. The energy of thermal neutrons is too small to create internal excitations in the nucleus or in its outer electronic shell. However, the atomic motions that the nucleus experiences and which correspond to much smaller energies can be "felt" by the neutron and give rise to inelastic scattering. Assuming a flux of incident neutrons Φ on a sample, the quantities I_a and I_s, which are the number of absorption and scattering events occurring per second per squared centimetre, read as:

$$I_a = \sigma_a \, \Phi \,, \tag{3.10}$$

$$I_s = \sigma_s \, \Phi \,, \tag{3.11}$$

where σ_a and σ_s are the *absorption cross-section* and the *scattering cross-section*, respectively. Both σ_a and σ_s have the dimension of a surface and their usual unit is the barn (bn), defined as it follows:

$$1\,\mathrm{bn} = 10^{-24}\,\mathrm{cm}^2 \,. \tag{3.12}$$

At low energies, such as few meV, σ_a is a smooth function of the incident neutron energy, so

$$\sigma_a \sim \lambda \sim \frac{1}{v} \,. \tag{3.13}$$

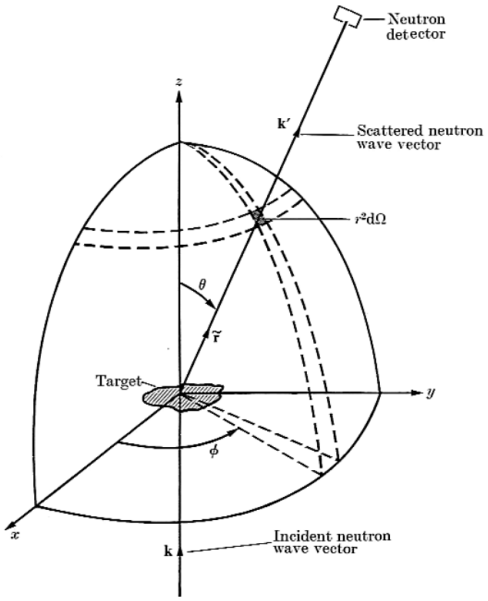

Fig. 3.1. Geometry of a neutron scattering experiment. The incoming neutron with scattering vector **k** aligned along the z-axis hits the target sample. It is then scattered along the direction $\tilde{r}$ (at an angle θ with the z-axis and an angle ϕ in the (x, y)-plane) with a scattering vector $\mathbf{k}'$ and falls onto the detector. The two angles θ and ϕ define the scattering geometry and determine the solid angle $r^2\,\mathrm{d}\Omega$. Image from Ref. [293].

Having now established the role of absorption cross-section, the scope of next paragraph will be to evaluate the neutron scattering cross-section σ_s. Figure 3.1 depicts the geometry of a neutron scattering experiment. An incoming neutron with wave-vector $\vec{k}$ and energy $E = \hbar\omega$ is scattered into a state with wave-vector $\vec{k'}$ and energy $E' = \hbar\omega'$ after hitting the target sample; the neutron exchanges energy and momentum with the sample, as defined in Equations 3.8 and 3.9. The quantity measured in a neutron scattering experiment is the double differential cross-section, which represents the fraction of neutrons with incident energy E scattered into an element of solid angle $d\Omega = sin\theta\, d\theta'\, d\phi$ with a final energy between E' and $E' + dE'$. The cross-section is denoted by $\frac{d^2\sigma}{d\Omega dE'}$ and has the dimension of [area/energy*solid angle].

For simplicity, an expression for the differential cross-section is first obtained for the special case of elastic scattering, namely when no energy is exchanged between the neutron and the sample. The expression will be then generalized to the partial differential cross-section that includes inelastic events. The free incident neutron is well described by a wave function $\psi_{\vec{k}}$, while the scattered one is represented by $\psi_{\vec{k'}}$. The direction of propagation of the scattered neutron with respect to the incident one is defined by the polar angle θ and the azimuthal angle ϕ. If the flux of incident neutrons (number of neutrons per unit area per unit time) is N, then the number of the scattered neutrons per unit time into an element of solid angle $d\Omega$ is

$$N\Big(\frac{d\sigma}{d\Omega}\Big)d\Omega\,, \tag{3.14}$$

with $d\sigma/d\Omega$ being the differential cross-section. It follows that $d\sigma/d\Omega$ and the total cross-section σ have the dimensions of an area. If the kinetic energy of the incident neutron is conserved after the interaction with the sample, it means that the neutron does not transfer any of its energy to the sample;

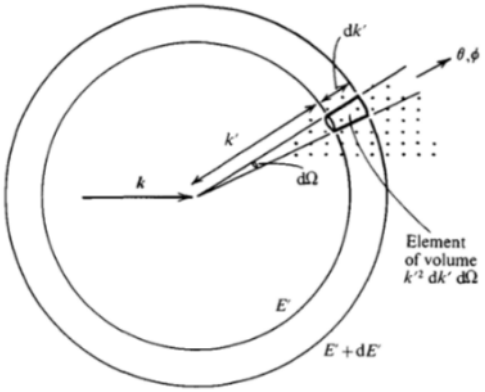

Fig. 3.2. Visual aid for the calculation of the density of final scattering states per unit energy range $\rho_{\vec{k'}}(E)$. The small dots represent the values of the final momentum transfer $\vec{k'}$ permitted by box normalisation. The two spheres delimited by solid lines with radii k' and $k' + dk'$ correspond to neutron energies E' and $E' + dE'$, respectively. Among all the accessible $\vec{k'}$ values, the interest is in the ones falling into the element of volume $k'^2 dk' d\Omega$. Image from Ref. [293].

instead, it is merely deflected by the nuclei within the sample without causing any internal excitations or changes in the internal energy states of the nuclei. The scattering process is therefore elastic. For simplicity, this special case can be considered to evaluate the scattering cross-section. The transition probability $W_{k\to k'}$ – from $\psi_{\vec{k}}$ to $\psi_{\vec{k'}}$ – is needed and it is given by Fermi's golden rule:

$$W_{k\to k'} = \frac{2\pi}{\hbar}\left|\int d\vec{r}\psi^*_{\vec{k'}}\hat{V}\psi_{\vec{k}}\right|^2 \rho_{k'}(E)\,, \tag{3.15}$$

where $\hat{V}$ is the interaction potential that leads the transition and $\rho_{k'}(E)$ is the density of final states with momentum $\vec{k'}$ and energy $E' = E$. $\psi_{\vec{k}}$ and $\psi_{\vec{k'}}$ are plane waves which describe the incident and the scattered neutron, respectively. Assuming to delimit the scattering geometry in a large box of volume L^3, the normalized incident and scattered wave functions can be written as:

$$\psi_{\vec{k}} = \frac{1}{L^{3/2}}e^{i\vec{k}\cdot\vec{r}}\ ,\ \psi_{\vec{k'}} = \frac{1}{L^{3/2}}e^{i\vec{k'}\cdot\vec{r}}\,. \tag{3.16}$$

At this point, the density of final scattering states per unit energy range $\rho_{\vec{k'}}(E)$ can be evaluated as it follows:

$$\rho_{\vec{k'}}(E) = \left(\frac{L}{2\pi}\right)^3 \frac{d\vec{k'}}{dE}\,, \tag{3.17}$$

where the two momentum and energy differentials $d\vec{k'}$, dE are:

$$d\vec{k'} = k'^2 dk' d\Omega = k^2 dk d\Omega\ ,\ dE = \frac{\hbar^2 k}{m}dk\,. \tag{3.18}$$

The density of final scattering states per unit energy range is therefore

$$\rho_{\vec{k'}}(E) = \left(\frac{L}{2\pi}\right)^3 \frac{mk}{\hbar^2}d\Omega\,. \tag{3.19}$$

A visual representation of the calculation in Equations 3.17, 3.18, 3.19 is reported in Figure 3.2 as aid for the reader. To obtain the cross-section we have to determine the incident flux of neutrons

classically:

$$\Phi = \frac{\upsilon_0}{L^3} = \frac{\hbar}{mL^3}\,, \tag{3.20}$$

where υ_0 is the velocity of the incident neutrons; the following quantum mechanical expression for the probability current density $\vec{\jmath}$ can also be used:

$$\vec{\jmath} = -\frac{i\hbar}{2m}\Big(\psi^*\nabla\psi - \psi\nabla\psi^*\Big)\,. \tag{3.21}$$

Both expressions lead to the same results. Hence, from Equations 3.15, 3.19 and 3.20:

$$\mathrm{d}\sigma = \frac{W_{k\to k'}}{\Phi} = L^6\Big(\frac{m}{2\pi\hbar^2}\Big)^2\Big|\int d\vec{r}\psi^*_{\tilde{\mathrm{k}}'}\hat{\mathrm{V}}\psi_{\tilde{\mathrm{k}}}\Big|^2\mathrm{d}\Omega\,. \tag{3.22}$$

One can use the Dirac (or "bra-ket") notation, namely:

$$\frac{L^3m}{2\pi\hbar^2}\int d\vec{r}\psi^*_{\vec{k}'}\hat{V}\psi_{\vec{k}} = \langle\tilde{\mathrm{k}}'|\hat{\mathrm{V}}|\tilde{\mathrm{k}}\rangle\,, \tag{3.23}$$

to have the following expression for the differential cross section:

$$\frac{\mathrm{d}\sigma}{\mathrm{d}\Omega} = \Big|\langle\vec{k'}|\hat{\mathrm{V}}|\vec{k}\rangle\Big|^2 = \Big|f(\vec{Q})\Big|^2\,. \tag{3.24}$$

The quantity $f(\vec{Q})$ is defined as *scattering amplitude* and it can be expressed as:

$$f(\vec{Q}) = -\langle\vec{k'}|\hat{\mathrm{V}}|\vec{k}\rangle\,, \tag{3.25}$$

where the negative sign is arbitrarily chosen (so the scattering amplitude has a negative phase) and not determined by the previous expressions; the reasons of this choice are explained in detail in Sec. 3.1.3. Moreover, note that with the definition 3.23, the matrix element $\langle\tilde{\mathrm{k}}'|\hat{\mathrm{V}}|\tilde{\mathrm{k}}\rangle$ has the dimension of a length.

The concept of differential cross-section can now be generalized by including inelastic scattering events and evaluate the partial differential cross-section $\mathrm{d}^2\sigma/\mathrm{dE}'\mathrm{d}\Omega$. In such events the neutron exchanges a finite amount of energy $\hbar\omega$ with the sample, causing a rearrangement of its states. As defined in equation 3.8, the frequency transfer ω is $\omega > 0$ for neutron energy loss and $\omega < 0$ for neutron energy gain.

By labelling the sample initial states with the wavelength index λ, the corresponding eigenvector is $|\lambda\rangle$, so that the initial state of the system, composed of neutron and target, is described by the product function

$$|\vec{k}\rangle|\lambda\rangle \equiv |\vec{k}\lambda\rangle\,. \tag{3.26}$$

The states $|\lambda\rangle$ form a complete set and we assume that they are normalized so that the closure relation is

$$\sum_\lambda |\lambda\rangle\langle\lambda| = 1\,. \tag{3.27}$$

The energy associated with the target state $|\lambda\rangle$ is denoted by E_λ. If the response of the target sample to the neutron interaction is to change from state $|\lambda\rangle$ to the state $|\lambda'\rangle$, then conservation energy requires that

$$\hbar\omega = E_\lambda - E_{\lambda'}\,. \tag{3.28}$$

With the notation in Equations 3.23 and 3.26, the associated cross-section is therefore

$$\Big(\frac{d\sigma}{d\Omega}\Big)^\lambda_{\lambda'} = \frac{k'}{k}\Big|\langle\vec{k'}\lambda'|\hat{V}|\vec{k}\lambda\rangle\Big|^2\,, \tag{3.29}$$

where the factor (k'/k) derives from the ratio between the density of final states and the initial flux of incident neutrons. If inelastic processes are also taken into account, the conservation of energy in equation 3.29 must be incorporated to obtain the partial differential cross-section. This requirement is accomplished with the aid of a δ-function:

$$\delta(E + E_\lambda - E' - E_{\lambda'}) = \delta(\hbar\omega + E_\lambda - E_{\lambda'}) \,, \tag{3.30}$$

which vanishes unless the condition 3.28 is satisfied. Therefore, the partial differential cross-section for specific initial and final target states has the following expression:

$$\Big(\frac{d\sigma}{d\Omega d\omega}\Big)^{\lambda}_{\lambda'} = \frac{k'}{k}\Big|\langle\vec{k}'\lambda'|\hat{V}|\vec{k}\lambda\rangle\Big|^2 \delta(\hbar\omega + E_\lambda - E_{\lambda'}) \,. \tag{3.31}$$

In general, instead of having a unique couple of accessible initial and final states $(|\lambda\rangle, |\lambda'\rangle)$, there would be a range of accessible initial and final target states $|\lambda\rangle_i$ and $|\lambda'\rangle_i$. The probability to reach an initial state $|\lambda\rangle$ can be described with a weight p_λ that can be the product of a thermo-dynamical factor $e^{-E_\lambda/k_B T}$ (where T is the sample temperature) and a degeneracy factor; a normalization for p_λ is also chosen:

$$\sum_\lambda p_\lambda = 1 \,. \tag{3.32}$$

Conversely, if the final target states are not selected by some sort of constraint, they can all be observed and accessible. So, the partial differential cross-section must contain the sum upon final states and the average of the initial ones:

$$\Big(\frac{d\sigma}{d\Omega d\omega}\Big)^{\lambda}_{\lambda'} = \frac{k'}{k}\overline{\sum_{\lambda\lambda'} p_\lambda |\langle\vec{k}'\lambda'|\hat{V}|\vec{k}\lambda\rangle|^2 \delta(\hbar\omega + E_\lambda - E_{\lambda'})} \,. \tag{3.33}$$

The horizontal bar in equation 3.33 stands for any other relevant averages not included in the weights p_λ, e.g. the distribution of isotopes, the nuclear spin orientations, the precise positions of the nuclei in the sample. So, the cross-section in equation 3.33 is clearly spin indipendent. In addition, the reader may observe that, since expression 3.15 for the transition probability is derived from perturbation theory, the expression for the neutron scattering cross-section including inelastic events derived above and reported in equation 3.33 is approximate; the nature of this approximation will be exhaustively discussed in Sec. 3.1.3.

The final step of this section is to introduce spin dependence in scattering cross-section calculations. Assuming that the spin states are labelled by an index σ, the corresponding eigenvector will be $|\sigma\rangle$. A complete initial state of the neutron-target system is described by the product function

$$|\vec{k}\lambda\rangle|\sigma\rangle \tag{3.34}$$

and a complete final state is described by

$$|\vec{k}'\lambda'\rangle|\sigma'\rangle \,. \tag{3.35}$$

If the initial spin state $|\sigma\rangle$ occurs with a weight p_σ, when the neutron spin is incorporated in the cross-section formula, the squared matrix element is replaced as it follows:

$$\Big|\langle\vec{k}'\lambda'|\hat{V}|\vec{k}\lambda\rangle\Big|^2 \Rightarrow \sum_{\sigma\sigma'} p_\sigma \Big|\langle\sigma'|\langle\vec{k}'\lambda'|\hat{V}|\vec{k}\lambda\rangle|\sigma\rangle\Big|^2 \,. \tag{3.36}$$

Whether and when the interaction potential $\hat{V}$ is completely independent of the neutron spin:

$$\langle\sigma'|\hat{V}|\sigma\rangle = \langle\sigma'|\sigma\rangle\hat{V} = \delta_{\sigma\sigma'}\hat{V} \,, \tag{3.37}$$

where the δ-function is a consequence of the orthogonality of the spin states. Thus, the expression in 3.33 is valid when $\hat{V}$ is independent of the neutron spin. For the opposite case in which $\hat{V}$ is a function of the neutron spin, it is useful to simplify the right hand side of equation 3.36 by using the closure relation for the spin states $|\sigma\rangle$:

$$\sum_{\sigma} |\sigma\rangle\langle\sigma| = 1\,. \tag{3.38}$$

For example, for a non polarized incident neutron beam $p_\sigma = \frac{1}{2}$, since there is 50% possibility for the incident neutron to hit the sample with a spin up or a spin down.

3.1.3 Born approximation and nuclear potential

The expression for the differential cross-section is derived using Fermi's golden rule 3.15, which is equivalent to the Born approximation in the quantum theory of scattering. A simple system consisting of an incident neutron and a target nucleus can be analyzed by separating its dynamics into two components: center of mass motion and relative motion. Assuming that the scattering arises from an interaction potential $\hat{V}$, which depends solely on the coordinate of the relative motion and is non-vanishing only within a limited spatial region $|\vec{r}| \leq d$, the Schrödinger equation for the neutron-nucleus system in the center of mass frame reads as:

$$(\nabla^2 + k^2)\psi_{sc}(\vec{r}) = \frac{2\mu\hat{V}(\vec{r})}{\hbar^2}\psi_{sc}(\vec{r})\,, \tag{3.39}$$

where μ is the reduced mass of neutron-nucleus system, namely

$$\mu = \frac{m_n m_N}{m_n + m_N} \tag{3.40}$$

and

$$k^2 = \frac{2\mu E}{\hbar^2}\,. \tag{3.41}$$

The asymptotic solution for equation 3.39 corresponding to an outgoing wave can be expressed as:

$$\psi_{sc}(\vec{r}) = e^{i\vec{k}\cdot\vec{r}} - \frac{\mu}{2\pi\hbar^2}\int d\vec{r}\,\frac{e^{ikr}}{r}\,e^{-i\vec{k'}\cdot\vec{r}}\hat{V}(\vec{r})\psi_{sc}(\vec{r})\;, r \gg d\,. \tag{3.42}$$

The expression for ψ_{sc} has been formulated in its integro-differential form, and the resolution of equation 3.42 is iterative, referred to as the Born series. The process can be approximated by stopping at the first order of the expansion, substituting the plane wave into ψ_{sc}. This is known as the *Born approximation*:

$$\psi_{sc}(\vec{r}) = e^{i\vec{k}\cdot\vec{r}} - \frac{\mu}{2\pi\hbar^2}\int d\vec{r}\,\frac{e^{ikr}}{r}\,e^{-i\vec{k'}\cdot\vec{r}}\hat{V}(\vec{r})e^{i\vec{k}\cdot\vec{r}}\;, r \gg d\,. \tag{3.43}$$

The Born approximation is a method of perturbation theory applicable when the interaction potential $\hat{V}$ causing the diffusion process is weak. In this context, the potential coupling the incident neutron and the nucleus is the nuclear potential, which is known for its high intensity. However, the range of this interaction is extremely small ($\simeq 10^{-15}$ m) compared to the wavelength of the incident neutron, resulting in the neutron perceiving the nucleus as a point. The scattered wave in equation 3.43 can therefore be written as a superposition of the incident wave and an outgoing spherical wave (Figure 3.3):

$$\psi_{sc}(\vec{r}) = e^{i\vec{k}\cdot\vec{r}} + f(\vec{Q})\frac{e^{ikr}}{r}\,, \tag{3.44}$$

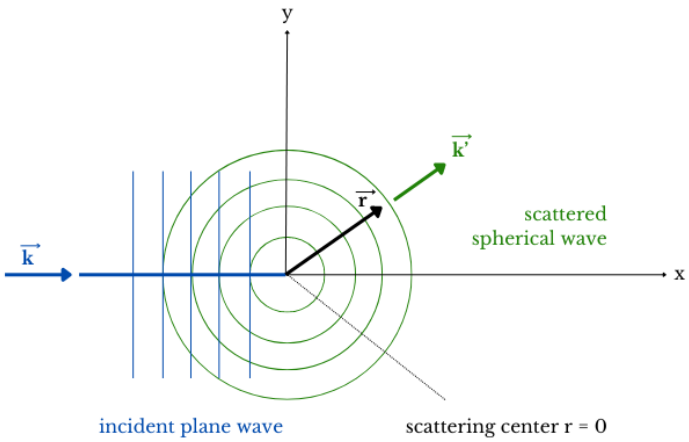

Fig. 3.3. Two-dimensional graphical representation of equation 3.44, showcasing the scattered wave in the (x,y)-plane as a superposition of the incident plane wave with momentum $\vec{k}$ and an outgoing spherical wave with momentum $\vec{k'}$. Figure adapted from Ref. [302] and rendered with Canva.

where $f(\vec{Q})$ is the scattering amplitude which modulates the outgoing spherical wave. The expression for this quantity in Born approximation can be obtained by comparing (3.43) and (3.44):

$$f(\vec{Q})\Big|_{\text{Born}} = -\frac{\mu}{2\pi\hbar^2}\int d\vec{r}\, e^{-i\vec{k'}\cdot\vec{r}}\hat{V}(\vec{r})e^{i\vec{k}\cdot\vec{r}} = -\frac{\mu}{2\pi\hbar^2}\int d\vec{r}\,\hat{V}\, e^{i\vec{Q}\cdot\vec{r}}\,. \tag{3.45}$$

This formulation is identical to that in equation 3.25, where f only depends on the scattering vector $\vec{Q} = \vec{k} - \vec{k'}$. That expression for $f(\vec{Q})$ with an arbitrary negative sign introduced in Sec. 3.1.2 has thus been justified.

Assuming $\hat{V}$ as a spherically symmetric potential, the angular momentum $\vec{L}$ becomes an integral of motion and allows the Schördinger equation to be written in spherical coordinates, with a framework chosen such as the $\hat{z}$-axis lies along the momentum of the incoming plane wave $\vec{k}$. Then the incoming plane wave can be written as a superposition of an infinite number of states with a defined angular momentum:

$$\psi_{sc}(\vec{r}) = e^{i\vec{k}\cdot\vec{r}} = \frac{1}{kr}\sum_{\ell=0}^{\infty}(2\ell+1)i^{\ell}R_{\ell}(r)P_{\ell}(\cos\theta)\,, \tag{3.46}$$

where the spherical harmonics do not depend on the anomaly ϕ, so they are proportional to Legendre polynomials $P_{\ell}(\cos\theta)$, and $R_{\ell}(r)$ are the radial functions which satisfy the equation that follows:

$$R''_{\ell}(r) + \frac{2}{r}R'_{\ell}(r) + \left[k^2 - \frac{2\mu\hat{V}(r)}{\hbar^2} - \frac{\ell(\ell+1)}{r^2}\right]R_{\ell}(r) = 0\,. \tag{3.47}$$

It can be observed that the centrifugal barrier depends on the scattering channel. At distances larger than the interaction range ($r \gg d$) the potential effects can be neglected and one obtains the asymptotic equation:

$$R''_{\ell}(r) + \frac{2}{r}R'_{\ell}(r) + \left[k^2 - \frac{\ell(\ell+1)}{r^2}\right]R_{\ell}(r) = 0\,, \tag{3.48}$$

whose asymptotic solution reads as:

$$R_{\ell}(r) = j_{\ell}(r) \sim \frac{A_{\ell}}{kr}\sin\left(kr - \frac{\ell\pi}{2} + \delta_{\ell}\right),\ kr \to \infty\,. \tag{3.49}$$

In fact, for very large distances ($r \to \infty$) the centrifugal term can also be neglected and the radial function $R_\ell(r)$ reduces to its asymptotic form, that is the zero-order Bessel spherical function. The expression for $R_\ell(r)$ can now be entered in equation 3.46 and the latter be compared with relation 3.44, leading thus to the following expression for the scattering amplitude:

$$f(\theta) = \frac{1}{k}\sum_{\ell=0}^{\infty}(2\ell+1)\, e^{i\delta_\ell}\sin\delta_\ell\, P_\ell(\cos\theta)\,, \tag{3.50}$$

where $P_\ell(\cos\theta)$ are Legendre polynomials and δ_ℓ is the phase-shift between scattered and incident wave. The reader may have noticed that the scattering amplitude now solely depends on the scattering angle θ, more specifically on its cosine function.

For distances $r > d$ the centrifugal force is the only force acting upon the neutron and therefore the motion is restricted to a region of space such that:

$$\frac{\hbar^2 k^2}{2\mu} \geqslant \frac{\hbar^2\ell(\ell+1)}{2\mu r^2}\,, \tag{3.51}$$

which also gives the condition to have a scattered wave. At this point, a distance of closest approach can be defined by considering equation 3.51:

$$r_{0\ell} = \frac{\sqrt{\ell(\ell+1)}}{k}\,. \tag{3.52}$$

This distance changes as long as the scattering channel – and so the angular momentum ℓ – does. An outgoing scattered wave is only present only when

$$r > r_{0\ell} \;\Rightarrow\; kr > \sqrt{\ell(\ell+1)}\,, \tag{3.53}$$

which becomes $kr > 0$ for $\ell = 0$. In the interesting case of slow neutrons, since $k \sim 10^{10}\, m^{-1}$ and $d \sim 10^{-15}\, m$, $kd \ll 1$ which is still > 0. Therefore

$$r_{0\ell} > d\ ,\ \forall \ell \neq 0\,, \tag{3.54}$$

which means that merely s-waves participate to the scattering and that the latter is isotropic and well describable by a single parameter b, the *scattering length*. b can be a complex parameter, whose real part can be positive or negative depending on the incident neutron energy and the type of nucleus involved. The imaginary part of b represents absorption (mostly radiative capture of slow neutrons) and in most cases it is small compared to the real counterpart. In general we can have different scattering lengths not only for each atomic type, but also for each isotope. Furthermore b can also depend on the relative orientations of the neutron spin and the nuclear spin.

The only expression for the potential $\hat{V}(r)$ giving rise to isotropic scattering in Born approximation is a δ-function. Therefore, assuming the nucleus is in a position defined by $\vec{R}$, the following potential can be introduced:

$$\hat{V}(\vec{r}) = \frac{2\pi\hbar^2}{m} b\,\delta(\vec{r}-\vec{R})\,, \tag{3.55}$$

which is referred to as *Fermi pseudo-potential*. It should be noted that this is not a real potential, but rather a formal artifice that yields the correct result for scattering in the s-wave; in fact, perturbation theory is inapplicable to the scattering of a neutron by a nucleus because, although the interaction potential has a very short range, it is very strong. The Fermi pseudo-potential 3.55 can be substituted in equation 3.23 with $\vec{R} = 0$ to find the scattering amplitude:

$$f(\vec{Q}) = \langle\vec{k}'|\hat{V}|\vec{k}\rangle = \frac{m}{2\pi\hbar^2}\frac{2\pi\hbar^2}{m} b\int d\vec{r}\, e^{-i\vec{k}'\cdot\vec{r}}\delta(\vec{r})e^{i\vec{k}\cdot\vec{r}} = b \tag{3.56}$$

So, the differential cross-section from equation 3.24 is

$$\frac{d\sigma}{d\Omega} = |b|^2 \,, \tag{3.57}$$

and hence the total cross-section is:

$$\sigma = 4\pi|b|^2 \,. \tag{3.58}$$

3.1.4 Coherent and incoherent neutron scattering

In this section, the specific case of neutron scattering from a rigid array of N nuclei neutron scattering is discussed. In the laboratory frame each nucleus is labeled with an index ℓ, its position is denoted by $\vec{R}_\ell$ and it has a scattering length b_ℓ. The incident neutron therefore encounters this potential:

$$\hat{V}(\vec{r}) = \frac{2\pi\hbar^2}{m} \sum_\ell b_\ell \delta(\vec{r} - \vec{R}_\ell) \,. \tag{3.59}$$

Thus, the matrix element in the cross-section formula 3.33 becomes:

$$\langle \vec{k'}|\hat{V}|\vec{k}\rangle = \sum_\ell b_\ell \int d\vec{r}\, e^{-i\vec{k'}\cdot\vec{r}} \delta(\vec{r} - \vec{R}_\ell) e^{i\vec{k}\cdot\vec{r}} = \sum_\ell b_\ell e^{i\vec{Q}\cdot\vec{R}_\ell} \,, \tag{3.60}$$

and the partial differential cross-section reads as:

$$\frac{d^2\sigma}{d\Omega dE'} = \frac{k'}{k} \sum_{\lambda,\sigma} p_\lambda p_\sigma \sum_{\lambda',\sigma'} \overline{\left|\left\langle \sigma'\lambda' \middle| \sum_\ell b_\ell e^{i\vec{Q}\cdot\vec{R}_\ell} \middle| \lambda\sigma \right\rangle\right|^2} \delta(\hbar\omega + E_\lambda - E_{\lambda'}) \,, \tag{3.61}$$

where $\vec{Q} = \vec{k} - \vec{k'}$. Since the nuclei are rigidly bound, $e^{i\vec{Q}\cdot\vec{R}_\ell}$ is not an operator, so it follows that the matrix element in equation 3.61 is proportional to

$$\langle \lambda|\lambda'\rangle = \delta_{\lambda,\lambda'} \,, \tag{3.62}$$

which means that there is only one term in the sum over $\lambda = \lambda'$. Moreover, the sum over p_λ is unity by definition and the result in equation 3.62 implies that $E_\lambda = E_{\lambda'}$ and the scattering is therefore elastic. Considering all of these results, the expression of the neutron scattering cross-section for a rigid array of N nuclei reduces to:

$$\frac{d\sigma}{d\Omega} = \sum_\sigma p_\sigma \sum_{\ell\ell'} e^{i\vec{Q}\cdot(\vec{R}_\ell - \vec{R_{\ell'}})} \langle \sigma|\overline{b^*_{\ell'} b_\ell}|\sigma\rangle \,, \tag{3.63}$$

where the quantity $\overline{b^*_{\ell'} b_\ell}$ is the product $b^*_{\ell'} b_\ell$ averaged over random nuclear spin orientations and random isotope distributions, so every σ-dependence must disappear:

$$\frac{d\sigma}{d\Omega} = \sum_{\ell\ell'} e^{i\vec{Q}\cdot(\vec{R}_\ell - \vec{R_{\ell'}})} \overline{b^*_{\ell'} b_\ell} \,. \tag{3.64}$$

The scattering length density b_ℓ depends on which isotope is at site $\vec{R}_\ell$ and what nuclear spin is associated with it; assuming there is no correlation between site ℓ and site ℓ', it is clear that:

$$\overline{b^*_{\ell'} b_\ell} = \overline{b^*_{\ell'}}\,\overline{b_\ell} = |\overline{b}|^2 \text{ , if } \ell \neq \ell' \tag{3.65}$$

$$\overline{b^*_{\ell'} b_\ell} = \overline{b^*_\ell b_\ell} = \overline{|b_\ell|^2} = \overline{|b|^2} \text{ , if } \ell = \ell' \tag{3.66}$$

In general, the two cases in Equations 3.65, 3.66 can be summarized in the following expression:

$$\overline{b^*_{\ell'} b_\ell} = |\bar{b}|^2 + \delta_{\ell\ell'}(\overline{|b|^2} - |\bar{b}|^2)\,. \tag{3.67}$$

Now, substituting expression 3.67 into equation 3.61 yields:

$$\frac{d\sigma}{d\Omega} = \sum_{\ell\ell'} e^{i\vec{Q}\cdot(\vec{R}_\ell - \vec{R}_{\ell'})}|\bar{b}|^2 + \sum_{\ell\ell'} e^{i\vec{Q}\cdot(\vec{R}_\ell - \vec{R}_{\ell'})}\delta_{\ell\ell'}(\overline{|b|^2} - |\bar{b}|^2)\,. \tag{3.68}$$

The scattering cross-section for a rigid array of N nuclei has thus two components:

$$\frac{d\sigma}{d\Omega} = \left(\frac{d\sigma}{d\Omega}\right)_{coh} + \left(\frac{d\sigma}{d\Omega}\right)_{inc}, \tag{3.69}$$

where the *coherent cross-section* is

$$\left(\frac{d\sigma}{d\Omega}\right)_{\text{coh}} = |\bar{b}|^2 \left|\sum_\ell e^{i\vec{Q}\cdot\vec{R}_\ell}\right|^2 \tag{3.70}$$

and the *incoherent cross-section* is

$$\left(\frac{d\sigma}{d\Omega}\right)_{inc} = N(\overline{|b|^2} - |\bar{b}|^2) = N\overline{|b - \bar{b}|^2}\,. \tag{3.71}$$

These two formulas differ fundamentally. Coherent scattering involves significant interference between waves scattered by each nucleus. This interference is so pronounced that coherent scattering from a crystal occurs only under strict geometrical conditions. Conversely, incoherent scattering lacks interference entirely, resulting in a completely isotropic cross-section. In essence, incoherent scattering examines correlations between the positions of the same atom at different times (self-motion), while coherent scattering investigates correlations between the positions of different atoms at different times (collective motion). [303] A visual representation of the two processes in a group of randomly distributed particles is reported in Figure 3.4.

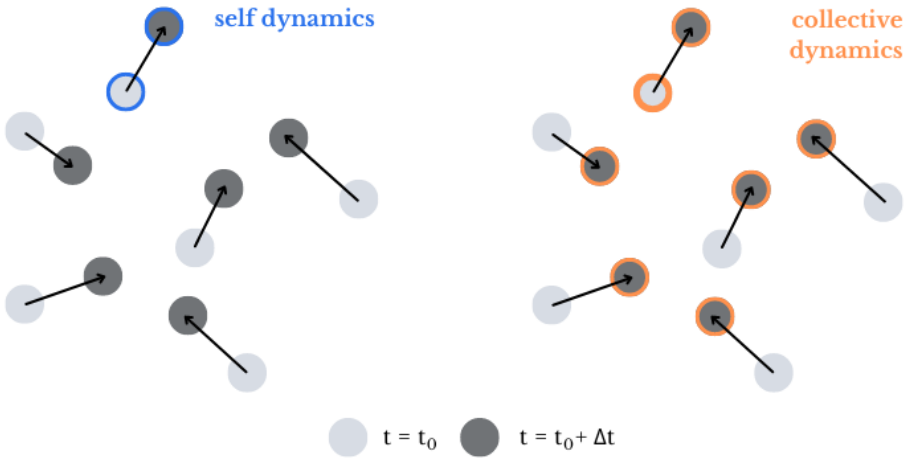

Fig. 3.4. Graphic representation of the difference between self and collective dynamics within the same group of randomly distributed particles from a time $t = t_0$ (light-grey spheres) to a time $t = t_0 + \Delta t$ (dark-grey spheres). Self dynamics refers to the correlation between a single particle at time $t = t_0$ and itself at a later time $t = t_0 + \Delta t$. Collective dynamics defines instead the correlation between a single particle at time $t = t_0$ and all the particles in the system (including itself) at a later time $t = t_0 + \Delta t$. Figure rendered with Canva.

These two types of scattering can be interpreted physically as follows: since b varies between isotopes and depends on nuclear spin orientations, the neutron perceives a crystal with a non-uniform scattering potential, changing from site to site. Only the average scattering potential can produce interference effects, leading to coherent scattering. This average scattering potential is proportional to $\overline{b}$ and the coherent cross-section is proportional to $|\overline{b}|^2$. Deviations from the average scattering potential are randomly distributed and do not produce interference effects; thus, incoherent scattering involves the mean-square deviation, represented by $\overline{|b-\overline{b}|^2}$. To determine the values of $\overline{b}$ and $\overline{|b|^2}$, the mere variation of isotopes is initially taken into account, assuming that $\overline{b}$ and $\overline{|b|^2}$ are independent of spin orientations. Let the isotopic species in the sample be labeled with the index x, with c_x and b_x being the isotopic concentration and the scattering length of isotope x, respectively. It therefore yields:

$$\overline{b} = \sum_x c_x b_x \tag{3.72}$$

and

$$\overline{|b|^2} = \sum_x c_x |b_x|^2 \,. \tag{3.73}$$

The problem can be oppositely approached by assuming that $\overline{b}$ and $\overline{|b|^2}$ depend on the relative spin orientations of the neutron and the nucleus, without considering the target isotopic distribution. When an incident neutron interacts with a nuclear spin i it can create states of spin $(i+\frac{1}{2})$ with multiplicity $2(i+\frac{1}{2})+1 = (2i+2)$ and states of spin $(i-\frac{1}{2})$ with multiplicity $2(i-\frac{1}{2})+1 = 2i$. Accordingly, the scattering lengths $b^{(+)}$ and $b^{(-)}$ are associated with these two states. The probability of forming states with parallel or anti-parallel spins ($p_{\uparrow\uparrow,\downarrow\downarrow}$ and $p_{\uparrow\downarrow,\downarrow\uparrow}$, respectively) is given by the ratio of the multiplicity of these states to the total number of states:

$$\left(i+\frac{1}{2}\right) \rightarrow \; p_{\uparrow\uparrow,\downarrow\downarrow} = \frac{2i+2}{4i+2} = \frac{i+1}{2i+1} \,, \tag{3.74}$$

$$\left(i-\frac{1}{2}\right) \rightarrow \; p_{\uparrow\downarrow,\downarrow\uparrow} = \frac{2i}{4i+2} = \frac{i}{2i+1} \,. \tag{3.75}$$

$\overline{b}$ is thus a linear combination of $b^{(+)}$ and $b^{(-)}$ weighted with the their probabilities:

$$\overline{b} = \left(\frac{i+1}{2i+1}\right) b^{(+)} + \left(\frac{i}{2i+1}\right) b^{(-)} \tag{3.76}$$

and the same applies to $\overline{|b|^2}$:

$$\overline{|b|^2} = \left(\frac{i+1}{2i+1}\right) |b^{(+)}|^2 + \left(\frac{i}{2i+1}\right) |b^{(-)}|^2 \,. \tag{3.77}$$

Moreover, accounting for the presence of various isotopic species leads to the more general expressions:

$$\overline{b} = \sum_x \frac{c_x}{2i_x+1} \Big[(i_x+1) b^{(+)} + i_x b^{(-)} \Big] \,, \tag{3.78}$$

$$\overline{|b|^2} = \sum_x \frac{c_x}{2i_x+1} \Big[(i_x+1) |b^{(+)}|^2 + i_x |b^{(-)}|^2 \Big] \,. \tag{3.79}$$

By inserting these two expression in Equations 3.70, 3.71, the coherent and the incoherent scattering cross-sections are obtained.

The very same result can be achieved by introducing a *scattering length operator* $\hat{b}$ acting on the spin state of the system; for a single neutron the above-mentioned operator can be written as:

$$\hat{b} = A + \frac{1}{2} B (\hat{\sigma} \cdot \hat{i}) \,, \tag{3.80}$$

where $\hat{i}$ is the nuclear spin, $\hat{\sigma}/2$ is the neutron spin and A and B can be obtained by imposing that $\hat{b}$ has eigenvalues $b^{(\pm)}$ for the two possible states of the total spin $(i \pm \frac{1}{2})$. In the end, the following expressions for A and B are obtained:

$$A = \frac{1}{2i+1}[(i+1)b^{(+)} + ib^{(-)}]\,, \tag{3.81}$$

$$B = \frac{2}{2i+1}(b^{(+)} - b^{(-)})\,. \tag{3.82}$$

The particular case of hydrogen should be mentioned. For neutron-proton scattering, specifically a neutron hitting a ^{1}H nucleus, the following scattering lengths are measured:

$$b^{(+)} = 1.04 \times 10^{-12}\,\mathrm{cm}\ (\text{triplet})\,, \tag{3.83}$$

$$b^{(-)} = -4.74 \times 10^{-12}\,\mathrm{cm}\ (\text{singlet})\,, \tag{3.84}$$

which give average values:

$$\overline{b} = \frac{3}{4}b^{(+)} + \frac{1}{4}b^{(-)} = -0.38 \times 10^{-12}\,\mathrm{cm}\,, \tag{3.85}$$

$$\overline{|b|}^2 = \frac{3}{4}|b^{(+)}|^2 + \frac{1}{4}|b^{(-)}|^2 = 6.49\,\mathrm{bn}\,. \tag{3.86}$$

In terms of cross-section, it yields:

$$\sigma_{\mathrm{coh}} = 4\pi|\overline{b}|^2 = 1.8\,\mathrm{bn}\,, \tag{3.87}$$

$$\sigma_{inc} = 4\pi(\overline{|b|^2} - |\overline{b}|^2) = \sigma - \sigma_{\mathrm{coh}} = (81.7 - 1.8)\,\mathrm{bn} = 79.8\,\mathrm{bn}\,. \tag{3.88}$$

It is recalled that $b^{(+)}$ and $b^{(-)}$ typically have opposite signs, so their average $\overline{b}$ is small, while their fluctuation around it, namely the quantity $(\overline{|b|^2} - |\overline{b}|^2)$, is higher; it translates into a poor σ_{coh} and a considerable σ_{inc}, as seen in Equations 3.87, 3.88.

However, the situation is completely different for deuterium D (^{2}H), which has spin $i = 1$; for neutron-deuterium scattering process the following scattering lengths were measured:

$$b^{(+)} = 0.95 \times 10^{-12}\,\mathrm{cm}\ ,\ b^{(-)} = 0.10 \times 10^{-12}\,\mathrm{cm}\,. \tag{3.89}$$

These values are used to obtain $\overline{b}$ e $\overline{|b|}^2$:

$$\overline{b} = \frac{2}{3}b^{(+)} + \frac{1}{3}b^{(-)} = 0.67 \times 10^{-12}\,\mathrm{cm}\,, \tag{3.90}$$

$$\overline{|b|}^2 = \frac{2}{3}|b^{(+)}|^2 + \frac{1}{3}|b^{(-)}|^2 = 0.61\,\mathrm{bn} \tag{3.91}$$

and then to evaluate the coherent and incoherent contributions to the cross-section:

$$\sigma_{\mathrm{coh}} = 4\pi\,|\overline{b}|^2 = 5.6\,\mathrm{bn}\,, \tag{3.92}$$

$$\sigma_{inc} = \sigma - \sigma_{\mathrm{coh}} = (7.6 - 5.6)\,\mathrm{bn} = 2\,\mathrm{bn}\,. \tag{3.93}$$

This substantial difference between the two hydrogen isotopes can be exploited in the investigation of biological samples, which are particularly rich in hydrogen and thus they mainly experience incoherent neutron scattering; this topic will be further discussed in following chapters.

It is also useful to remind neutron scattering and absorption cross-sections (see Table 3.2) for other constituting elements in biomolecules, such as carbon (C), nitrogen (N), oxygen (O) and phosphorus (P). Other interesting elements when neutron scattering is concerned are aluminium (Al) and vanadium (V). The former has a small neutron cross-section and it is commonly used to produce sample holders for neutron spectroscopy, while the latter has a quite intense neutron cross-section and it is therefore used for calibration scopes.

Element	σ_{coh} [bn]	$\sigma_{\mathbf{inc}}$ [bn]	$\sigma_{\mathbf{tot}}$ [bn]	$\sigma_{\mathbf{abs}}$ [bn]
Hydrogen **H**	1.7568	80.26	82.02	0.3326
Deuterium **D**	5.592	2.05	7.64	0.000519
Nitrogen **N**	11.01	0.5	11.51	1.9
Oxygen **O**	4.232	0.0008	4.232	0.00019
Carbon **C**	5.551	0.001	5.551	0.0035
Phosphorus **P**	3.307	0.007	1.026	0.172
Aluminum **Al**	1.495	0.0082	1.503	0.231
Vanadium **V**	0.0184	5.08	5.1	5.08

Table 3.2. Coherent and incoherent neutron scattering cross-sections σ_{coh}, σ_{inc}, total scattering cross-section σ_{tot} and absorption cross-section σ_{abs} for 2200 m/s (300 K) incident neutrons of the most common elements in biomolecules (H, N, O, C, P) and of other relevant elements in neutron scattering (D, Al, Va). Cross-section are commonly measured in barn (bn), defined as it follows: 1 bn = 10^{-24} cm^2. Source: NIST Center for Neutron Research (NCNR).

3.1.5 Correlation and response functions

The general form for the interaction potential between the neutrons and the target for purely nuclear scattering is:

$$\frac{m}{2\pi\hbar^2}\hat{V}(\vec{r}) = \sum_i \hat{V}_i(\vec{r} - \vec{R}_i)\,, \tag{3.94}$$

where $\vec{R}_i$ is the position vector for the i-th scattering nucleus. Substituting this potential in the cross-section formula for non-polarised neutrons 3.33 yields:

$$\Big(\frac{d\sigma}{d\Omega d\omega}\Big)^{\lambda}_{\lambda'} = \frac{k'}{k}\overline{\sum_{\lambda\lambda'} p_\lambda |\langle\lambda'|\sum_i \hat{V}_i(\vec{Q})e^{i\vec{Q}\cdot\vec{R}_i}|\lambda\rangle|^2 \delta(\hbar\omega + E_\lambda - E_{\lambda'})}\,, \tag{3.95}$$

where

$$\hat{V}_i(\vec{Q}) = \int d\vec{r}\, e^{i\vec{Q}\cdot\vec{r}}\hat{V}_i(\vec{r})\,, \tag{3.96}$$

so that

$$\langle\vec{k'}|\hat{V}|\vec{k}\rangle = \sum_i \hat{V}_i(\vec{Q})e^{i\vec{Q}\cdot\vec{R}_i}\,. \tag{3.97}$$

The δ-function in equation 3.95 can be thus expressed as it follows:

$$\delta(\hbar\omega + E_\lambda - E_{\lambda'}) = \frac{1}{2\pi\hbar}\int dt\, e^{-\frac{it}{\hbar}(\hbar\omega + E_\lambda - E_{\lambda'})}\,, \tag{3.98}$$

where t has obviously the dimension of time. In the end, the calculations lead to the form

$$\Big(\frac{d^2\sigma}{d\Omega d\omega}\Big)^{\lambda}_{\lambda'} = \frac{k'}{k}\frac{1}{2\pi\hbar}\int_{-\infty}^{+\infty} dt\, e^{-i\omega t}\overline{\sum_{jj'}\Big\langle e^{-i\vec{Q}\cdot\hat{\vec{R}}_i(0)}\hat{V}_i^\dagger(\vec{Q})\hat{V}_j(\vec{Q},t)e^{i\vec{Q}\cdot\hat{\vec{R}}_j(t)}\Big\rangle}\,, \tag{3.99}$$

with the following notation representing the thermal average:

$$\langle(...)\rangle = \sum_\lambda p_\lambda\langle\lambda|(...)|\lambda\rangle\,. \tag{3.100}$$

The development now proceeds for the case where the average over spin orientations and isotopic distributions (represented by the horizontal bar) is independent of the thermal averaging. In this instance:

$$\Big(\frac{d^2\sigma}{d\Omega d\omega}\Big)^{\lambda}_{\lambda'} = \frac{k'}{k}\frac{1}{2\pi\hbar}\int_{-\infty}^{+\infty} dt\, e^{-i\omega t}\sum_{ij}\overline{\hat{V}_i^{\dagger}(\vec{Q})\hat{V}_j(\vec{Q})}Y_{ij}(\vec{Q},t)\,, \tag{3.101}$$

where the quantity

$$Y_{ij}(\vec{Q},t) = \Big\langle e^{-i\vec{Q}\cdot\hat{\vec{R}}_i(0)} e^{i\vec{Q}\cdot\hat{\vec{R}}_j(t)}\Big\rangle \tag{3.102}$$

can be referred to as *correlation function* in the $(\vec{Q},t)$-space.

From equation 3.67 it follows that the average of the product of the potentials in equation 3.101 for a monoatomic sample can be written as:

$$\overline{\hat{V}_i^{\dagger}(\vec{Q})\hat{V}_j(\vec{Q})} = |\bar{b}|^2 + \delta_{ij}(\overline{|b|^2} - |\bar{b}|^2) = \frac{\sigma_{\rm coh}}{4\pi} + \delta_{ij}\frac{\sigma_{inc}}{4\pi}\,. \tag{3.103}$$

It could be now useful to introduce the *intermediate scattering function*

$$I(\vec{Q},t) = \frac{1}{N}\sum_{ij} Y_{ij}(\vec{Q},t) = \frac{1}{N}\sum_{i=1}\sum_{j=1}^{N}\Big\langle e^{-i\vec{Q}\cdot\hat{\vec{R}}_i(0)} e^{i\vec{Q}\cdot\hat{\vec{R}}_j(t)}\Big\rangle \tag{3.104}$$

and the corresponding "self" component

$$I_s(\vec{Q},t) = \frac{1}{N}\sum_{i=1}\Big\langle e^{-i\vec{Q}\cdot\hat{\vec{R}}_i(0)} e^{i\vec{Q}\cdot\hat{\vec{R}}_i(t)}\Big\rangle = \Big\langle e^{-i\vec{Q}\cdot\hat{\vec{R}}(0)} e^{i\vec{Q}\cdot\hat{\vec{R}}(t)}\Big\rangle\,, \tag{3.105}$$

which refers to incoherent scattering. Operating the time Fourier transform on Equations 3.104, 3.105 leads to the so called *dynamic structure factor*, which separates into a coherent component

$$S_{\rm coh}(\vec{Q},\omega) = S(\vec{Q},\omega) = \frac{1}{2\pi\hbar}\int_{-\infty}^{+\infty} dt\, e^{-i\omega t} I(\vec{Q},t) \tag{3.106}$$

and an incoherent component

$$S_{inc}(\vec{Q},\omega) = S_s(\vec{Q},\omega) = \frac{1}{2\pi\hbar}\int_{-\infty}^{+\infty} dt\, e^{-i\omega t} I_s(\vec{Q},t)\,. \tag{3.107}$$

These quantities are thus the coherent and the incoherent *response functions* of the system and have the dimension of (energy)$^{-1}$. At this point, the partial differential cross-section can be expressed by taking into account Equations 3.103, 3.106 3.107:

$$\frac{d^2\sigma}{d\Omega d\omega} = \frac{k'}{k}\Big[\frac{\sigma_{\rm coh}}{4\pi}S(\vec{Q},\omega) + \frac{\sigma_{inc}}{4\pi}S_s(\vec{Q},\omega)\Big]\,. \tag{3.108}$$

The terminology used for $S(\vec{Q},\omega)$ deserves some explanations. Since $S(\vec{Q},\omega)$ is also called response function, it contains information on the spontaneous dynamical fluctuations in the target sample. The intimate relation between the response and the spectrum of spontaneous fluctuations arises from the fact that neutron scattering is a weak process; the response of the sample to an external solicitation is linear and can thus be described using perturbation theory. It follows that the cross-section, which is a measure of the response of the sample, is determined by the spectrum of the spontaneous fluctuations, as reported in equation 3.108. It can therefore be stated that the neutron cross-section measures the undistorted properties of the sample. The formal theory that relates linear response to spontaneous fluctuations of the sample is embodied in the *fluctuation-dissipation theorem*, for the first time presented

by H. Callen and T. Welton in 1951 [165] and later expanded by R. Kubo. The derivation of the aforementioned theorem will not be presented in this work.

In order to complete this scenery, another physical quantity is now introduced: the *pair correlation function* $G(\vec{r},t)$. It is defined as the space and time Fourier transform of the response function $S(\vec{Q},\omega)$:

$$G(\vec{r},t) = \frac{1}{(2\pi)^3}\int_{-\infty}^{+\infty}\int_{-\infty}^{+\infty} d\vec{Q}d\omega\, e^{-i(\vec{Q}\cdot\vec{r}-\omega t)}S(\vec{Q},\omega) \tag{3.109}$$

$$= \frac{1}{(2\pi)^3}\int_{-\infty}^{+\infty} d\vec{Q}\, e^{-i\vec{Q}\cdot\vec{r}}I(\vec{Q},t) \tag{3.110}$$

$$= \frac{1}{(2\pi)^3}\int_{-\infty}^{+\infty} d\vec{Q}\, e^{-i\vec{Q}\cdot\vec{r}}\frac{1}{N}\sum_{ij}Y_{ij} \tag{3.111}$$

$$= \frac{1}{(2\pi)^3}\int_{-\infty}^{+\infty} d\vec{Q}\, e^{-i\vec{Q}\cdot\vec{r}}\frac{1}{N}\sum_{ij}\left\langle e^{-i\vec{Q}\cdot\hat{\vec{R}}_i(0)}e^{i\vec{Q}\cdot\hat{\vec{R}}_j(t)}\right\rangle, \tag{3.112}$$

which can be written in the form

$$G(\vec{r},t) = \frac{1}{N}\sum_{ij}\int d\vec{r'}\langle\delta(\vec{r'}-\vec{r}+\hat{\vec{R}}_i(0))\delta(\vec{r'}-\hat{\vec{R}}_j(t))\rangle\,. \tag{3.113}$$

In order to be able to apply classical statistics, one can assume that the following conditions on the energy and the momentum transferred in the scattering process are true:

$$\hbar\omega \ll \frac{1}{2}k_BT\,,\ \frac{(\hbar Q)^2}{2M} \ll \frac{1}{2}k_BT\,, \tag{3.114}$$

where $M =$ atomic mass, $k_B =$ Boltzmann constant and $T =$ temperature. In fact, the conditions for the validity of the classical approximation are that the energy and momentum transfer must be much smaller than the thermal energy. The pair correlation function is thus related to the probability that, given a particle at the origin at time $t = 0$, any particle is found at the position $\vec{r}$ at time t. In order to better explain this concept, a *microscopic particle density operator* is introduced:

$$\hat{\rho}(\vec{r},t) = \sum_j \delta(\vec{r}-\hat{\vec{R}}_j(t))\,, \tag{3.115}$$

which can be used to express the pair correlation function from equation 3.113:

$$G(\vec{r},t) = \frac{1}{N}\int d\vec{r'}\,\hat{\rho}(\vec{r'}-\vec{r},0)\hat{\rho}(\vec{r'},t)\,. \tag{3.116}$$

The function has the following normalization:

$$\int d\vec{r}\,G(\vec{r},t) = N\,. \tag{3.117}$$

A *self correlation function* can also be defined as the space and time Fourier transform of $S_s(\vec{Q},\omega)$:

$$G_s(\vec{r},t) = \frac{1}{(2\pi)^3}\int_{-\infty}^{+\infty}\int_{-\infty}^{+\infty} d\vec{Q}d\omega\, e^{-i(\vec{Q}\cdot\vec{r}-\omega t)}S_s(\vec{Q},\omega) \tag{3.118}$$

$$= \frac{1}{N}\sum_i\int d\vec{r'}\langle\delta(\vec{r'}-\vec{r}+\hat{\vec{R}}_i(0))\delta(\vec{r'}-\hat{\vec{R}}_i(t))\rangle,\,. \tag{3.119}$$

This function is related to the probability that, given a particle at the origin at time $t = 0$, the same particle is found at the position $\vec{r}$ at time t. In analogy with equation 3.117 for $G(\vec{r}, t)$, $G_s(\vec{r}, t)$ is normalized as it follows:

$$\int d\vec{r} G_s(\vec{r}, t) = 1 \,. \tag{3.120}$$

The information about the sample dynamics can therefore be probed in the frequency domain, through $S(\vec{Q}, \omega)$, and in the time domain, by studying the pair correlation function $G(\vec{r}, t)$. This direct connection between correlation functions and scattered intensities is made crystal-clear by the use of *Van Hove formalism*, namely embodied by the mathematical relations 3.109 and 3.118.

Actually, for many complex systems it is more convenient to deal with the intermediate scattering function $I(\vec{Q}, t)$ introduced in equation 3.104, which is also the spatial Fourier transform of $G(\vec{r}, t)$:

$$I(\vec{Q}, t) = \int d\vec{r} e^{i\vec{Q}\cdot\vec{r}} G(\vec{r}, t) \,. \tag{3.121}$$

At this point, two limit cases that are of particular interest will be considered: $t \to 0$ and $t \to +\infty$. In the first case, since the operators involved in the definition of G and G_s commute at equal time, the pair correlation functions become:

$$G_s(\vec{r}, t = 0) = \delta(\vec{r}) \text{ and } G(\vec{r}, t = 0) = \delta(\vec{r}) + \rho g(\vec{r}) \,, \tag{3.122}$$

where $g(\vec{r})$ is the static pair-distribution function and gives the average particle-density about a given particle.

Another important special case concerns the behaviour of the correlation functions at very long times. In this instance there is no correlation between the two terms on the right-hand sides of Equations. 3.113 and 3.119; considering equation 3.116, the pair correlation function in the limit of $t \to \infty$ becomes:

$$G(\vec{r}, \infty) = \frac{1}{N} \int d\vec{r'} \langle \rho(\vec{r} - \vec{r'}) \rangle \langle \rho(\vec{r'}) \rangle \,. \tag{3.123}$$

For a particle diffusing in a space which is very large if compared to interatomic distances, the self-correlation function reads

$$G_s(\vec{r}, t) = 0 \ , \ t \to +\infty \,, \tag{3.124}$$

whereas, for a particle bound to a finite volume (i.e. as a part of rotating molecule fixed in a crystal), it approaches a finite value:

$$G_s(\vec{r}, t) = G_s(\vec{r}, \infty) \ , \ t \to +\infty \,, \tag{3.125}$$

for $\vec{r}$ varying in the interior of this volume. We shall notice that G and G_s possess a pronounced local structure for $t = 0$, but as t increases it dies away, and in the limit of $t \to +\infty$ the functions are independent of $\vec{r}$. In general, the pair correlation function can be split into its asymptotic value in the long-time limit and a time-dependent term yielding:

$$G(\vec{r}, t) = G(\vec{r}, \infty) + G'(\vec{r}, t) \,, \tag{3.126}$$

so that

$$\lim_{t \to \infty} G'_s(\vec{r}, t) = 0 \,. \tag{3.127}$$

The same form can be used for the self-correlation function

$$G_s(\vec{r}, t) = G_s(\vec{r}, \infty) + G'_s(\vec{r}, t) \,, \tag{3.128}$$

so that

$$\lim_{t\to\infty} G'_s(\vec{r},t) = 0\,. \tag{3.129}$$

By applying the spatial Fourier transform to this expression, the intermediate scattering function can be obtained, which is divided into two contributions:

$$I_s(\vec{Q},t) = I_s(\vec{Q},\infty) + I'_s(\vec{Q},t)\,. \tag{3.130}$$

By operating the time Fourier transform on the intermediate scattering function, the incoherent dynamic structure factor is obtained:

$$S_s(\vec{Q},\omega) = \frac{1}{2\pi}\int_{-\infty}^{+\infty}\int_{-\infty}^{+\infty} e^{i(\vec{Q}\cdot\vec{r}-\omega t)}\Big[G_s(\vec{r},\infty) + G'_S(\vec{r},t)\Big]\,d\vec{r}dt\,, \tag{3.131}$$

which gives

$$S_s(\vec{Q},\omega) = S_s^{el}(\vec{Q})\,\delta(\omega) + S_s^{inel}(\vec{Q},\omega)\,. \tag{3.132}$$

The incoherent scattering function is thus decomposed into a purely elastic line, whose intensity is the integrated dynamic structure factor, and a nonelastic component. The elastic line is the result of the neutron diffraction on the "infinite time" distribution in space of a single nucleus spread over a finite volume by its motion [304]. In terms of cross-section, the decomposition in equation 3.132 translates into:

$$\Big(\frac{d^2\sigma}{d\Omega dE'}\Big)_{incoh} = \Big(\frac{d^2\sigma}{d\Omega dE'}\Big)^{el}_{incoh} + \Big(\frac{d^2\sigma}{d\Omega dE'}\Big)^{inel}_{incoh}\,. \tag{3.133}$$

The elastic contribution to the incoherent cross-section is:

$$\Big(\frac{d^2\sigma}{d\Omega dE'}\Big)_{incoh} = N\frac{\sigma_{inc}}{4\pi}\,\delta(\hbar\omega)I_s(\vec{Q},\infty) = N\frac{\sigma_{inc}}{4\pi}\,\delta(\hbar\omega)\int d\vec{r}\,e^{i\vec{Q}\cdot\vec{r}}\,G_s(\vec{r},\infty)\,. \tag{3.134}$$

Since after an infinite time positions of the same atoms become uncorrelated, the intermediate self-scattering function reads:

$$I_s(\vec{Q},\infty) = \frac{1}{N}\sum_j \langle e^{-i\vec{Q}\cdot\vec{R}_j}\rangle\langle e^{i\vec{Q}\cdot\vec{R}_j}\rangle\,, \tag{3.135}$$

giving the following expression for the incoherent scattering cross-section:

$$\Big(\frac{d\sigma}{d\Omega}\Big)_{incoh} = \frac{\sigma_{inc}}{4\pi}\sum_j |\langle e^{i\vec{Q}\cdot\vec{R}_j}\rangle|^2\,. \tag{3.136}$$

It is crucial to remember that the variables are operators, so this applies to the position $\vec{R}_j$, which is in reality $\hat{\vec{R}}_j$. This operator can be written as the sum of an equilibrium position operator $\hat{\vec{r}}_j^{eq}$ and a displacement (from the equilibrium position) operator $\hat{\vec{u}}_j$:

$$\hat{\vec{R}}_j = \hat{\vec{r}}_j + \hat{\vec{u}}_j\,. \tag{3.137}$$

Assuming that the equilibrium position operator is $\hat{\vec{r}}_j^{eq}$=0, equation 3.136 becomes:

$$\Big(\frac{d\sigma}{d\Omega}\Big)_{incoh} = \frac{\sigma_{inc}}{4\pi}\sum_j |\langle e^{-i\vec{Q}\cdot\vec{u}_j}\rangle|^2\,, \tag{3.138}$$

which can also be written as it follows:

$$\Big(\frac{d\sigma}{d\Omega}\Big)_{incoh} = \frac{\sigma_{inc}}{4\pi}\sum_j |\langle e^{-W(\vec{Q})}\rangle|^2\,. \tag{3.139}$$

The quantity just introduced is referred to as the *Debye-Waller factor (DWF)*

$$e^{-W(\vec{Q})} = e^{-i\hat{\vec{Q}}\cdot\hat{\vec{u}}_j}\,, \tag{3.140}$$

and it represents a fundamental quantity in elastic incoherent neutron scattering that can be evaluated by means of an expansion into a series of powers of $\hat{\vec{Q}}$ with the aid of a parameter x and then making the assumption of an harmonic oscillator motion [293], leading to this expression:

$$W(Q) = \frac{1}{2}\langle(\hat{\vec{Q}}\cdot\hat{\vec{u}}_j)^2\rangle\,. \tag{3.141}$$

Moreover, assuming Gaussian approximation to be valid and after further considerations (see Lovesey, 1984 [293]), the DWF will be given by:

$$W(Q) = \frac{1}{6}Q^2\langle\hat{u}^2\rangle\,, \tag{3.142}$$

allowing us to write the dynamic structure factor in case of elastic scattering as it follows:

$$S_s(Q,\omega=0) \propto 1 - \frac{1}{6}Q^2\langle\hat{u}^2\rangle \simeq \exp\left(-\frac{1}{6}Q^2\langle\hat{u}\rangle^2\right). \tag{3.143}$$

In the equation, $\langle\hat{u}\rangle^2$ are the mean squared displacements (MSDs) of the atoms in the system from their equilibrium positions, due to thermal vibrations. Equation 3.143 clearly shows the departure from elastic behaviour, corresponding to $S_s(Q,\omega=0)=1$, caused by this kind of phenomena. It is important to distinguish between the just introduced vibrational mean-squared displacement contained in the DWF and the diffusive mean-squared displacements arising from different motions of groups of atoms in the sample, also often abbreviated with MSD.

3.2 Quasi-elastic neutron scattering (QENS)

As discussed in previous sections, in a neutron scattering experiment, the neutron intensity scattered into a solid angle is measured after energy exchange with the sample. If the exchanged energy is zero or smaller than the energy resolution of the spectrometer, the scattering event is referred to as elastic; ideally, the scattered intensity would be a delta function. Elastic scattering arises from objects that are immobile in the energy window explored by the instrument, meaning that their motions are too slow to be detected. Conversely, if the exchanged energy is non-zero and leads to an excitation in the sample, the scattering is inelastic and it would correspond to a sharp peak at a specific energy transfer in the measured spectrum. If the scattering arises from a diffusive or overdamped motion, the scattering is denoted *quasi-elastic* and it translates into a broadening of the signal around the elastic line. These scattering events are schematized in Figure 3.5 and will be further explained from a mathematical point of view in the following lines.

In Section 3.1.5, the self-correlation function and its space and time Fourier transforms were decomposed into their constant limit at infinite time and its time-dependent parts. In the quasi-elastic regime, inelastic scattering events are not considered, so equation 3.132 for the incoherent scattering function can be written as follows:

$$S_s(\vec{Q},\omega) = S_s^{el}(\vec{Q})\delta(\omega) + S_s^{qe}(\vec{Q},\omega)\,, \tag{3.144}$$

where

$$S_s^{qe}(\vec{Q},\omega) = \frac{1}{2\pi}\int_{-\infty}^{\infty}\Big[I(\vec{Q},t) - I(\vec{Q},\infty)\Big]e^{-i\omega t}\,dt\,. \tag{3.145}$$

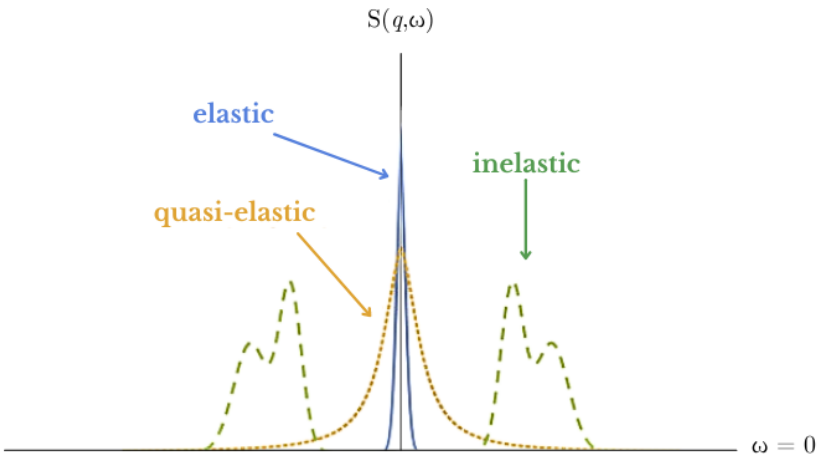

Fig. 3.5. Sketch of the scattering function of elastic, quasi-elastic and inelastic neutron scattering, in the absence of so-called detailed-balance effects. While elastic scattering gives a sharp peak centred at $\omega = 0$, QENS yields a broader peak always centred at $\omega = 0$; inelastic signal is instead characterized by peaks centred at $\omega \neq 0$. Figure adapted from Ref. [1] and rendered with Canva.

The scattering function appears as composed of a purely elastic component superimposed on another, that is $S_s^{qe}(\vec{Q},\omega)$ (equation 3.145), which is the time-Fourier transform of a time-dependent term and then exhibits a non-vanishing broadening [305]. This behaviour of the scattering function is schematized in Figure 3.5, where the quasi-elastic signal manifests as a broadening around the elastic line placed at zero energy transfer and can reflect a variety of motions [303]. First of all, QENS is a uniquely powerful spectroscopy in the investigation of motions with characteristic times in the range 10^{-9}-10^{-13} s and length scales in the range around 1-30 Å, i. e. local scales around inter- and intra-molecular distances. In general, QENS is used to probe self motion, so incoherent scattering is involved. As a consequence, QENS is particularly applicable to hydrogenous systems and, in principle, yields characteristic times and diffusion coefficients processes – determined from the width of the broadened part –, along with the detailed geometry of the dynamical processes underlying in the investigated system [305]. This allows the study of different dynamical processes, from fast modes such as vibrations, rotations and localized motions, to slower modes including segmental relaxations, reorientations and diffusion. However, one cannot precisely define which class of motions contribute to the quasi-elastic component of the spectrum, because it strongly depends on the system under study but mainly on the experimental resolution. In the case of macromolecules in solution or – more generally – of (soft) colloid suspensions, QENS data treatment and analysis can be approached as established in previous works [163, 290, 306, 307].

Secondly, it is noteworthy that the temporal and spatial ranges covered by QENS fully overlap with those currently accessible by MD simulations. QENS is thus perfectly suited as a validation tool for simulations; conversely, MD simulation data aid the interpretation of experimental results. Moreover, it is known that motions in soft matter systems span a wide dynamic range, so to access the whole QENS dynamic range it is necessary to combine results from more than one spectrometer. The comparison and the collaboration with other experimental techniques which show complementary features with QENS can also be extremely useful and such approach is becoming a common methodology [303].

3.2.1 Dynamical independence approximation

In complex systems like biological macromolecules, atomic motion manifests as multiple components operating across various time scales. These motions can exhibit different degrees of coupling: strong, weak, or none at all. When strong coupling exists, the computation of Van Hove correlation functions and scattering functions necessitates consideration of this coupling, while in cases of weak or no coupling, individual motion types can be treated independently. Assuming, for instance, that vibrational, rotational, and translational motions are dynamically independent, simplifies the calculations and greatly facilitates the analysis. Consequently, the total intermediate scattering function can be represented as a product of individual ones:

$$I_s(\vec{Q},t) = I_{vib}(\vec{Q},t)\, I_{rot}(\vec{Q},t)\, I_{trans}(\vec{Q},t)\,, \tag{3.146}$$

while the scattering function will be the convolution of the single contributions, as it follows:

$$S_s(\vec{Q},\omega) = S_{vib}(\vec{Q},\omega) \otimes S_{rot}(\vec{Q},\omega) \otimes S_{trans}(\vec{Q},\omega)\,. \tag{3.147}$$

As long as the study is restricted to the quasi-elastic region, the vibrational term can be represented by a Debye-Waller factor (DWF), indicated with $\beta(\vec{Q})$ in our analysis framework [290].

3.2.2 Elastic Incoherent Structure Factor (EISF)

An accurate investigation of the exact shape of the quasi-elastic component can provide precise information about the geometry of the motion of the scatterers [308]. An extremely useful quantity introduced and defined by Bée, that is the *elastic incoherent structure factor (EISF)*, representing the fraction of the elastically scattered intensity with respect to the total intensity.

$$EISF = \frac{I^{el}}{I^{el} + I^{inel}} = \frac{A\, S_s^{el}(\vec{Q})}{\left[A \int_{-\infty}^{\infty} S_s(\vec{Q},\omega)\, d\omega\right]}\,, \tag{3.148}$$

where I^{el} and I^{inel} are the integrated intensities corresponding to the elastic and inelastic parts of the spectra, respectively. Then, it follows that:

$$EISF = S_s^{el}(\vec{Q})\,, \tag{3.149}$$

so the elastic incoherent structure factor (EISF) is exactly the coefficient multiplying the delta-function in equation 3.132 and so the amplitude of the elastic peak. It should be observed that the EISF in 3.148 is in its most general form and it includes all the possible motions of the diffusing atom. However, the motions contributing to the elastic component of the total scattering function strongly depend on the instrument energy resolution. In fact, only the dynamics of the specific motions occurring within the instrumental energy resolution range are visible, since much slower motions are hidden within the energy resolution function, whereas much faster motions appear only as a flat background [309].

In the analysis framework established in our group and employed in this thesis [290], the EISF is usually indicated with $A_0(\vec{Q})$ and it represents the weighing factor of the first Lorentzian contribution of the scattering function $S(\vec{Q},\omega)$, which also contains the elastic component. According to the diffusive motions occurring in the sample, $A_0(\vec{Q})$ can follow diverse trends in $\vec{Q}$ and can thus be modelled in multiple ways [304]. For further details, see Equation 5.4 in Chapter 5.

3.3 Neutron spectroscopy

The instrumental configurations that can be employed to perform a QENS study on a sample essentially differ in the way the energy of the incident or scattered neutrons is measured. The TOF, backscattering and spin-echo techniques are named after three different ways to do it. In TOF instruments, the energy of the neutrons is measured by determining its speed via its flight time over a known distance, whereas in NBS, it is done by measuring its wavelength via Bragg reflection employing a crystal. In NSE instruments, the neutron energy is measured by inferring the flight time from the number of its spin precessions while travelling through a magnetic field of known dimensions. These spectroscopic techniques, along with many other tools to study matter in general, are reported in Fig. 3.9 in an (energy, wavevector) and (time, length)-plot.

All neutron spectrometers can be divided into two main components: the primary spectrometer, referring to everything placed before the sample, and the secondary spectrometer, defining everything after it. The design of spectrometers is mainly driven by a desired resolution or coherence volume V_c [254–256] and its optimal propagation through the primary and secondary spectrometer – meaning that the primary and secondary resolutions must be identical, i.e. must contribute equally to the Gaussian error propagation [1]. In the following sections, an overview of the instruments employed for this work and their operation principles will be given.

3.3.1 Neutron backscattering and time-of-flight spectroscopy

By operating in the so-called "inverse spectroscopy" or "indirect geometry" mode, backscattering spectrometers achieve particularly high energy resolutions. Inverse spectroscopy, also achievable in TOF spectrometers, consists in fixing the final energy of the neutron E_f, e.g. by a filter or an analyser crystal, while keeping the incident energy E_i variable. E_i can be determined by measuring the neutron TOF or by varying the initial energy via a monochromator. In a nutshell, while the primary spectrometer varies the incoming energy of the neutrons on the sample, the secondary spectrometer analyses the neutron energy and only detects the neutrons with one specified energy at a time. By knowing both E_i and E_f, it is possible to measure the energy transfer $\hbar\omega = E_i - E_f$.

While the layout of secondary spectrometers is very similar among all instruments, the operation principle and configuration of primary spectrometers can be instead quite different. Moreover, in some spectrometers the different operation principles can be combined together; for instance, it is possible to have a TOF primary spectrometer and NBS secondary spectrometer in the same machine (see paragraph 3.3.1). Below are the various technologies used in neutron spectrometers to vary and determine the energy of the probe.

(a) NBS crystal monochromator primary spectrometer. The energy of the incoming neutrons is defined via a monochromator thanks to Bragg reflection from a crystal. The initial neutron beam hits the monochromator crystal and is reflected with a divergence Θ; the energy resolution of the reflected beam will depend on Θ and on the crystal lattice constant a, along with their uncertainties $\Delta\Theta$, Δa:

$$\frac{1}{2}\frac{\Delta E}{E} = \frac{\Delta\lambda}{\lambda} = \frac{\Delta k}{k} = \sqrt{\left(\frac{\Delta a}{a}\right)^2 + (\Delta\Theta \cdot \cot(\Theta))^2}\,. \tag{3.150}$$

At continuous neutron sources, NBS spectrometers use perfect backscattering both in primary and secondary spectrometers, namely in the monochromator and in the analysers (see item

(c)). Deviations from perfect backscattering ($\Theta + \varepsilon$ instead of $\Theta = 90°$) allow to realize simpler geometries at the expense of the energy resolution. Minimizing ε means that the second term in Equation 3.150 vanishes and the resolution basically the one reachable with perfect backscattering (if all the other variables are unchanged); this condition is referred to as "near-backscattering".

Besides the energy resolution achievable with this setup, it is important to tune the incident energy in order to access different energy transfers. When a monochromator crystal is employed, the lattice spacing should be tuned either by varying the crystal material (obviously not convenient), or its temperature (as done on the thermal neutron backscattering spectrometer (IN13) spectrometer at ILL [310]). Another effective option consists in mechanically moving the monochromator along its optical axis to achieve an apparent Doppler shift of the incident energy, therefore realising an "effective Bragg reflection" in a moving reference frame. Further details on this technology are given in the paragraph dedicated to the IN16B spectrometer.

(b) TOF primary spectrometer. To obtain neutrons with a desired energy, a first chopper system is used to obtain a pulsed white neutron beam. Due to the dispersion relation, the neutrons pass the distance to the second chopper with different flight times. Then, an adapted second chopper selects only neutrons with a specified neutron energy. Since no monochromator crystal is used, the energy resolution depends on different flight paths L and different flight times TOF [311,312]:

$$\frac{1}{2}\frac{\Delta E}{E} = \frac{\Delta\lambda}{\lambda} = \frac{\Delta k}{k} = \sqrt{\left(\frac{\Delta L}{L}\right)^2 + \left(\frac{\Delta \mathrm{TOF}}{\mathrm{TOF}}\right)^2}. \tag{3.151}$$

At spallation sources, the first chopper system is not needed because the beam is already pulsed from the start. TOF instruments are the most common for the QENS technique. Their typical energy resolution for cold neutrons at 5 Å is ~ 90 μeV full width at half maximum (FWHM).

(c) Secondary spectrometer. As previously mentioned, the secondary spectrometer detects scattered neutrons with a specified energy at a time, in all angles covered by the optics. To obtain the angular information and hence the q-dependence of the scattering function, analyser crystals are positioned around the sample on a spherical surface, at an average distance of 2 m, covering a large fraction of the solid angle. In this way, the backscattering condition can be achieved. In case of pulsed neutron beams, the backscattering condition can be fulfilled by separating the neutrons being scattered directly into the detector from the analysed ones by the time of flight and then discarding them. For continuous neutron beams the analysers can be positioned in such a way that the neutrons do not pass a second time through the sample. The energy resolution of the secondary spectrometer can also be described with Equation 3.150. At pulsed sources, deviations from exact backscattering are sometimes allowed, with consequent broadening of the resolution with respect to instruments at continuous sources [1].

IN16B: cold neutron high-flux backscattering spectrometer

The cold neutron high-flux backscattering spectrometer (IN16B) at ILL is a sub-μeV energy resolution backscattering spectrometer (~ 0.9 μeV FWHM when employing Si(111) crystals associated with an elastic wavelength of 6.271 Å). The dynamic range of IN16B spans from -30 to $+30$ μeV. Snapshots of the path travelled by neutrons inside IN16B are reported in Figure 3.6. First, from the cold-neutron guide a velocity selector defines a "pink" beam with $\Delta\lambda/\lambda \approx 12\%$ around the elastic wavelength

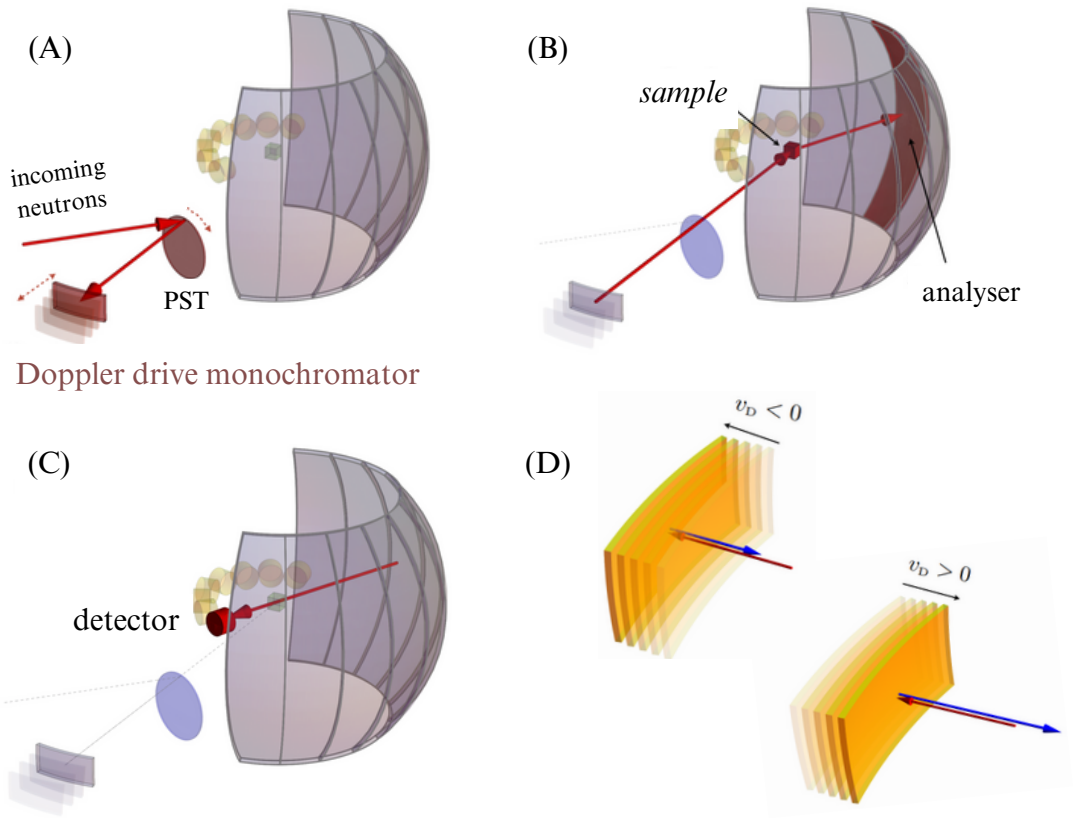

Fig. 3.6. Operation principles of a backscattering spectrometer. **(A)** Incoming neutrons are Bragg reflected by rotating PST disk. A Doppler drive monochromator alters the velocity of the perpendicularly impinging neutrons (red arrow). **(B)** Neutrons are inelastically scattered by the sample (small red cube) and reach the analysers. **(C)** Neutrons fulfilling the Bragg condition at the analysers are back-reflected towards the detectors placed behind the sample position. **(D)** Principle of a Doppler monochromator: An incident neutron beam (red arrow) is backscattered (blue arrow) on a moving single crystal surface (in yellow). The path of the Doppler monochromator is depicted by the superposition of the yellow plates in different time snapshots. When $v_d < 0$: The monochromator velocity is parallel to the incoming beam (red arrow) hence the energy of the reflected neutrons (blue arrow) is decreased. When $v_d > 0$: The monochromator velocity is antiparallel to the incident beam (red arrow) therefore the energy of the reflected neutrons (blue arrow) is increased. Note that the length of the arrows corresponds to the energy of the neutrons. The image is adapted from Ref. [314] and rendered using Canva.

of 6.271 Å. Neutrons are then transmitted through a quasi-elliptical supermirror focus guide, where a background chopper is located. The guide focuses neutrons onto the deflector which is made of PG(002) crystals with a wide mosaic, mounted on a fast rotating phase-space transformation (PST) chopper (brown disk in Subfigure **(A)**, circumferential speed $\sim 230\,\mathrm{m/s}$) at the end-of-guide position: this object aims at increasing the flux to the sample [313]. Moreover, its angular velocity is chosen such that it optimally accelerates the neutrons with an energy $E < E_0$, and decelerates those with $E > E_0$, thus "compressing" the neutron energy distribution around E_0. The pulsed neutron beam is then transmitted to the monochromator, consisting in a Si(111) single crystal ($450 \times 250\ \mathrm{mm}^2$), from which

it is reflected with a 90° angle (Subfigure **(A)**). The energy scan is realized through a Doppler drive where the monochromator crystal is mounted, moving with an oscillating speed v_d (Subfigure **(D)** in Figure 3.6). The resulting energy shift will then be:

$$\frac{\delta E_0}{E_0} = 2\frac{v_d}{v_0}\,, \tag{3.152}$$

which yields an energy window of $\delta E_0 = \pm 30\,\mu eV$ for maximum speed values $v_d = \pm 2.5\,ms^{-1}$. The pulsed beam from the monochromator is thus directed to the sample, from which it is scattered in all directions; all flight path are placed in vacuum. Neutrons scattering from the sample reach the analysers (again Si(111) single crystals) by which they are filtered through backscattering (Subfigure **(B)**), before being focused into a set of 18 ^{3}He tube detectors (Subfigure **(C)**). Each of them corresponds to a certain scattering angle or q-value; the covered solid angle goes from 10° to 142°. The incident beam is also periodically interrupted by the background chopper: it ensures that only those neutrons which have been scattered and analysed in energy are detected, rejecting all the others (background). So the monochromatic neutrons from the oscillating monochromator crystal, falling onto the sample, being scattered, and finally detected, are individually labelled with the corresponding instantaneous speed of the Doppler drive. IN16B can also be used with the Doppler drive at rest, in the so-called elastic fixed window scan (EFWS) mode of operation. In this option, the intensity at $\omega = 0$ for every q-value is collected. These scans can give a quick overview of the onset of motions faster than the time scale corresponding to the energy resolution. Moreover, inelastic fixed window scan (IFWS) can be performed: in this case, the scattered intensity from the sample is recorded at a single energy transfer value (typically 1.3 and 2.6 μeV), in order to better investigate off-peak regions of QENS spectra. Additional information on the instrument, e.g. on its Backscattering Time-of-flight Spectrometer (BATS) option, can be found in Refs. [311, 315, 316] and at the following page: IN16B @ILL.

In this thesis, NBS was employed to investigate the short-time self-diffusion of a series of mAbs in order to establish a connection between their microscopic solution behaviour and their macroscopic viscosity. The experiment carried out on IN16B is described in Chapter 5. The spectrometer was employed with standard Si(111) crystals as analysers, sample heating and cooling were performed by a cryo-furnace and samples were sealed in double-well aluminium cylinder cells.

BASIS: the Backscattering Silicon Spectrometer

BAckscattering SIlicon Spectrometer (BASIS) is an indirect geometry spectrometer located on Beam-Line 2 (BL2) at the SNS at the ORNL. It provides an energy resolution in the range $\approx 3.0 - 3.5\,\mu$eV FWHM, a dynamic range of $-100\,\mu\text{eV} \leq \hbar\omega \leq 100\,\mu\text{eV}$ and a scattering vector range $0.4\ \text{Å}^{-1} \leq q \leq 1.9\ \text{Å}^{-1}$. A long initial guide section of 84 m from moderator to sample is needed in order to achieve the appropriate timing resolution for the aforementioned energy resolution. BASIS is a combined TOF-NBS spectrometer, with Si(311) crystal analysers in the second spectrometer and choppers in the primary spectrometer to select the incident energy based on neutron TOF. Moreover, the backscattering in the analysers is not perfect (near-backscattering condition) [312, 317]. Additional information on the instrument can be found in Refs. [312, 317] and at the following page: BASIS @SNS.

For this thesis, BASIS data were collected on the BSA-$LaCl_3$ model system in order to probe the short-time dynamics upon entering the LLPS regime of the protein phase diagram. Data treatment, analysis and interpretation are reported in Chapter 7. Sample heating and cooling, necessary to emplore the temperature-driven phase transitions, were performed by a cryo-furnace and the samples were sealed in double-well aluminium cylinder cells.

3.3.2 Neutron spin-echo spectroscopy

The main references for this section are Mezei's different works published along the years after his invention of the first NSE spectrometer in 1972, a high resolution instrument employing the neutron spin precession [318–320]. As introduced in Section 3.1.5, in inelastic neutron scattering spectroscopy the spectral response of the sample $S(\vec{Q},\omega)$ corresponds to the probability of a variation of the neutron energy during the scattering process (Equation 3.8), which is in turn determined by a change of the neutron velocity:

$$\hbar\omega = \frac{1}{2}m(v'^2 - v^2) \tag{3.153}$$

with v and v' being the neutron incoming and final velocity, respectively. In conventional spectroscopy, neutron final and initial velocities v' and v have to be determined in two separate steps. The precision of these calculations determines the resolution of the instrumental setup. The idea behind NSE technique is to use the neutron spin as an "internal clock" for the particle, allowing to follow the energy change for each individual neutron in the scattering process. To this purpose, spin manipulation via a magnetic field is necessary. In this way, there is in principle no need of a monochromator and hence no loss in neutron flux. In Figure 3.7, a sketch of a typical setup of an NSE spectrometer is shown. The path followed by a neutron beam inside such a machine is presented below.

- A neutron beam with a wavelength distribution $P_{\Delta\lambda}(\lambda - \lambda_0)$ centred at λ_0 with a typical divergence of $\Delta\lambda/\lambda_0 \approx 15\%$ is polarized by a mirror magnetized along the propagation direction (schematically represented by a gray disk). The neutrons exit the polariser with their spin parallel to the guide field, thus without any spin precessing, which somehow represents their "internal clock" switched off.

- After a short distance the neutron beam hits a $\pi/2$-flipper, a very thin plate with two orthogonal coil windings (flat orange rectangle), causing a $\pi/2$ spin flip with respect to the guide field. The spins are now orthogonal to the homogeneous field $\mathbf{B_1}$ of the first solenoid (yellow cylinder with concentric coil), meaning that the "internal clock" of the neutrons is on. While travelling along the field with a velocity v_1, the neutron spin processes about the field lines with a Larmor frequency $\omega_1 = -\gamma_L \mathbf{B_1}$, where $\gamma_L = 2/\hbar\gamma_n$ is the neutron gyromagnetic ratio – with γ_n being the neutron magnetic dipole moment. γ_L is also called Larmor constant measuring 2.916 kHz/Oe. The $\pi/2$ flip thus initiates Larmor precessions that keep track of the time elapsed since the neutron hit the $\pi/2$ flipper. By multiplying the Larmor frequency for an elapsed time t, the Larmor precession angle ϕ can be obtained: $\phi = -\gamma_L \mathbf{B_1}\, t$. After crossing the first solenoid of length l_1 at speed v_1, the Larmor precession angle is thus $\phi_1 = -\gamma_L \mathbf{B_1}\, l_1/v_1$.

- Neutrons hit the sample and are scattered experiencing energy and momentum transfers (Equations 3.8, 3.9). Scattering changes the divergence and the energy distribution of the neutron beam. For a specific momentum transfer value $\mathbf{q}$, the probability density distribution $P(\mathbf{q},\omega)$ of having an energy transfer $\hbar\omega$ reads

$$P(\mathbf{q},\omega) = \frac{S(\mathbf{q},\omega)}{\int S(\mathbf{q},\omega)\,\mathrm{d}\omega} \tag{3.154}$$

  Soon after the scattering with the sample, neutrons hit a π-flipper resulting in a change in the Larmor precession of $\phi \to -\phi$, meaning that only one of the two components of the neutron spin in the plane of precession is inverted.

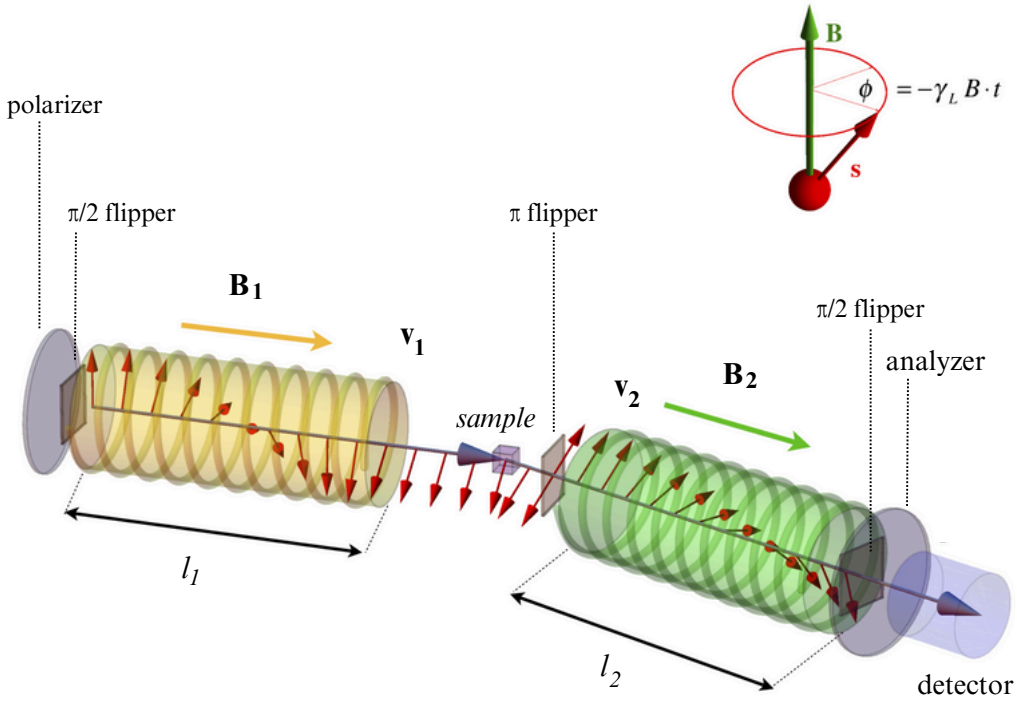

Fig. 3.7. Sketch of a spin-echo spectrometer, divided into the primary spectrometer (in yellow) and the secondary one (in green). An incoming neutron beam (from the left side of the image) with velocity v_1 is polarised by a mirror; the neutron spin is parallel to the magnetic guide field $\mathbf{B_1}$ (gray arrow in the middle of the yellow solenoid). When neutrons cross the $\pi/2$ spin-flipper, their "internal clock" is switched on by flipping the spin so that is orthogonal to $\mathbf{B_1}$ (first red arrow from the left). Due to the magnetic field, neutrons transversing l_1 undergo Larmor spin precessions (precessing red arrows). Before hitting the sample, their spin precession angle is thus $\phi_1 = -\gamma_L B_1 l_1/v_1$. The image inset on the top right visually explains the spin precession due to the presence of a magnetic field B. After scattered from the sample (small purple cube) the neutron velocity is v_2 and the neutron spin is inverted by a π-flipper, so that the spin component parallel to the field remains unchanged. Then, the scattered neutron beam enters a second solenoid (green cylinder) with a homogeneous magnetic field $\mathbf{B_2}$, with consequent spin precessions about the field lines. After travelling a distance l_2, the spins are $\pi/2$-flipped again parallel to the guide-field and the beam crosses the analyzer and finally, its intensity is measured by a detector (right side of the image). Image adapted from Ref. [314] and rendered using Canva.

- After the π-flipper, the neutron beam crosses with a velocity v_2 the secondary spectrometer of length l_2, equipped with a solenoid generating a second magnetic field $\mathbf{B_2}$, causing another spin precession and thus resulting in a total precession angle of:

$$\phi_{\text{total}} = \phi_1 - \phi_2 = -\gamma_L \left(\frac{\mathbf{B_1}\, l_1}{v_1} - \frac{\mathbf{B_2}\, l_2}{v_2} \right) \tag{3.155}$$

  In the case of elastic scattering ($v_1 = v_2 = v$) and in the case of identical absolute magnetic fields ($l_1 = l_2 = l$ and $|\mathbf{B_1}| = |\mathbf{B_2}|$), $\phi = 0$ independently from the incoming energy. However, field inhomogeneities lead to a decay of the (elastic) scattering signal, resulting in observable

Fourier times up to several hundred nanoseconds. Since the energy transfers relevant for the investigation of diffusion processes as the ones described in this thesis are small compared to the average kinetic energy of the neutrons, we are in the limiting case of small energy transfers. The magnetic fields can be adjusted such that $\mathbf{B_1}\, l_1 = \mathbf{B_2}\, l_2$, so ϕ can be approximated at v_1 up to first order in $\hbar\omega$:

$$\phi \approx \gamma_L \, \frac{m^2 \lambda^3}{8\pi^3 \hbar^2} \, B_1 \, l_1 \, \omega \, . \tag{3.156}$$

By dividing by ω, we thereby obtain the *Fourier time*:

$$\tau = \gamma_L \, \frac{m^2 \lambda^3}{8\pi^3 \hbar^2} \, B_1 \, l_1 \, , \tag{3.157}$$

which scales with λ^3. After crossing the second spectrometer, the neutrons are $\pi/2$-flipped (orange flat plat), polarized (gray disk) and then hit a detector (blue cylinder) that measures the intensity of the x-component of the polarization vector of the neutron beam. By averaging all energy transfers, one obtains:

$$P_x = \langle \cos(\phi) \rangle = \frac{\int \, S(\mathbf{q}, \omega) \, \cos(\phi) \, \mathrm{d}\omega}{\int \, S(\mathbf{q}, \omega) \, \mathrm{d}\omega} = S(q, \tau) \, . \tag{3.158}$$

NSE thus measures directly the ISF depending on the Fourier time. If the neutron polarization changes during the scattering process, the given equation has to be modified [320] as it follows:

$$P_{\mathrm{NSE}} = P_S \langle \cos(\phi) \rangle = P_S \frac{\int \, S(\mathbf{q}, \omega) \, \cos(\phi) \, \mathrm{d}\omega}{\int \, S(\mathbf{q}, \omega) \, \mathrm{d}\omega} = S(q, \tau) \, . \tag{3.159}$$

Williams [321] demonstrated that for incoherently scattering samples, the scattering-induced change in polarization is $P_S = -\frac{1}{3} P_0$, where P_0 is the polarization of the incoming neutron beam. So, if $P_0 = 1$, the total scattering signal measured is thus [319]

$$S(q, \tau) = \frac{S_{\mathrm{coh}}(q, \tau) - \frac{1}{3} \, S_{inc}(q, \tau)}{S_{\mathrm{coh}}(q, \tau = 0) - \frac{1}{3} \, S_{inc}(q, \tau = 0)} \, . \tag{3.160}$$

To obtain the ISF as a function of the scattering vector q, the secondary spectrometer is rotated around the sample position, so that any changes in the scattering angle correspond to changes in q. On the other hand, to study the time-evolution, it is necessary to change the Fourier time τ by changing the wavelength of the incoming neutrons. For each wavelength, a τ-range can be accessed. In order to select specific τ values, one has to slightly change the symmetry of the first magnetic field. These small variations correspond to a few data points in the ISF and form an echo group (usually 3-4 measurements are performed).

IN15: a high-resolution spin-echo spectrometer

The high resolution spin-echo spectrometer (IN15) is a high energy and momentum resolution spin-echo spectrometer optimised for QENS. Benefiting from a last upgrade in 2014 [322], IN15 is the highest resolution NSE spectrometer in the world. The incident wavelength can span from 6 Å to 25 Å and is tuned by means of a velocity selector with a monochromatization (FWHM) $\Delta\lambda/\lambda_0 \approx 15\%$. The instrument can reach Fourier times up to 1000 ns. The selected wavelengths for the experiment in Chapter 6 – 6, 8 and 10 Å – allow to explore Fourier times up to 200 ns and a q-range from 0.028 to 0.19 Å^{-1}, which correspond to an accessible length scale of $3.34 - 22.4$ Å. Polarizers are Fe-Co-Si supermirrors on Si substrate, while the analyser is a Fe-Co supermirror. The angular range available

using the sample changer, as it was done for the experiment described in Chapter 6, spans from 2° to 30°, with an angular resolution of 2×10^{-3} rad. Detectors are placed at a distance of 4.6 m from the sample and are formed by array 32×32 pixels (1 cm^2 each) of 1 bar ^{3}He and 0.3 bar CF_4. Further details on IN15 spectrometer, Refs. [322–324] and the page IN15 @ILL can be consulted.

In this thesis, NSE measurements performed on the IN15 at ILL were used to access the temperature-dependence of the collective diffusion of the series of mAbs studied. In contrast with the previous instruments employed, for the measurements on IN15 the samples were sealed in quartz cells. This material gives in fact a lower incoherent background and allows for simultaneous sample monitoring via DLS, due to its optical transparency. Details about data collection, analysis and results of the experiment are described in Chapter 6.

3.4 Small-angle neutron scattering

The use of neutron scattering to study large-scale structures, i.e. supramolecular collections of atoms of sizes up to several thousand times interatomic distances, has experienced an impressive growth over the past decades. The origin of the discipline dates back to the '70s, when position-sensitive detector (PSD) became generally available for SANS experiments [325].

First, SANS is an elastic scattering technique, so the incident neutrons exchange no energy with the sample. The length scale accessible with this technique ideally go from fractions of nm to several μm (Figure 3.9). In ordinary Bragg diffraction in a lattice, intense coherent elastic scattering is observed whenever the following Bragg condition is satisfied:

$$\lambda_i = 2\, d\, \sin\theta\,, \tag{3.161}$$

where d is the distance between lattice planes and θ is the neutron incident angle . In the reciprocal space $d = (2\pi)/Q$, so 3.161 can be written as follows:

$$\lambda_i = \frac{4\pi}{Q}\, \sin\theta \;\Leftrightarrow\; Q = \frac{4\pi}{\lambda_i}\, \sin\theta \tag{3.162}$$

Q is thus the scattering vector at the Bragg peak. We also recall that the Bragg condition results from the constructive interference of neutron waves scattered from individual lattice planes. These planes define a periodically modulated neutron scattering length density (SLD). Practically speaking, a minimum scattering angle corresponding to the maximum plane spacing can always be derived from Equation 3.161. In principle, the SLD can vary with no physical restrictions, so even over several al interatomic distances. As implied by Equation 3.162, the scattering vector Q is inversely proportional to the characteristic distance over which the SLD fluctuates. Large objects thus give rise to scattering at small wave vectors and hence, in general, to scattering at small angles.

Let us consider the differential cross section for coherent neutron scattering from a group of N atoms introduced in Equation 3.70 in Section 3.1.2. The formula for individual atoms with potentially different scattering lengths will be:

$$\left(\frac{d\sigma}{d\Omega}\right)_{\text{coh}} = \frac{1}{N}\left|\sum_{\vec{R}} \overline{b_{\vec{R}}}\, e^{i\vec{Q}\cdot\vec{R}}\right|^2 . \tag{3.163}$$

For scattering at small wave vectors, $Q \ll \pi/d$, individual atoms cannot be resolved and the scattering process is effectively governed by the interference of neutron waves scattered from regions of linear

dimensions l such that $l \approx \pi/Q$. In this case, the summation over discrete atoms in Eq 3.163 can be written as a spatial integral as follows:

$$\left(\frac{d\sigma}{d\Omega}\right)_{\text{coh}} = \frac{1}{N}\left|\int_V \rho_b(\vec{R})\, e^{i\vec{Q}\cdot\vec{R}}\, \mathrm{d}\vec{R}\right|, \tag{3.164}$$

where $\rho_b(\vec{r})$ is the local SLD, that is a continuum approximation to the actual SLD at a particular point. The spatial integration is over the entire volume V of the sample. $\rho_b(\vec{r})$ can be de-composed in its average value plus fluctuations around the average:

$$\rho_b(\vec{r}) = \overline{\rho_b} + \delta\rho(\vec{r})\,. \tag{3.165}$$

The constant term $\overline{\rho_b}$ gives a contribution to $d\sigma/d\Omega$ at $Q = 0$ only. For $Q > 0$, the scattering results from the fluctuation term of the SLD:

$$\left(\frac{d\sigma}{d\Omega}\right)_{\text{coh}} = \frac{1}{N}\left|\int_V \delta\rho(\vec{R})\, e^{i\vec{Q}\cdot\vec{R}}\, \mathrm{d}\vec{R}\right|. \tag{3.166}$$

For the case of N particles of homogeneous SLD ρ_p embedded in a matrix of homogeneous SLD ρ_m, the scattering signal from Equation 3.166 reads

$$\left(\frac{d\sigma}{d\Omega}\right)_{\text{coh}} = (\rho_p - \rho_m)^2\left|\int_{V_p} \delta\rho(\vec{R})\, e^{i\vec{Q}\cdot\vec{R}}\, \mathrm{d}\vec{R}\right|. \tag{3.167}$$

The integral is calculated over the sample region occupied by the particles V_p, where $V_p < V$. If all N_p particles are identical, the differential cross section becomes:

$$\left(\frac{d\sigma}{d\Omega}\right)_{\text{coh}} = V_p^2 \frac{N_p}{N}\,(\rho_p - \rho_m)^2\,|F_p(\vec{Q})\,|^2\,, \tag{3.168}$$

where the last term $|F_p(\vec{Q})\,|^2$ is the single-particle *form factor* defined as [295]:

$$P(\vec{Q}) = F_p(\vec{Q})\,|^2 = \frac{1}{V_p}\left|\int_{V_p} e^{i\vec{Q}\cdot\vec{R}}\, \mathrm{d}\vec{R}\right|^2 \tag{3.169}$$

In the limit of $Q \to 0$, $P(\vec{Q}) = 1$, therefore

$$\left(\frac{d\sigma}{d\Omega}\right)_{\text{coh},\, Q\to 0} = V_p^2 \frac{N_p}{N}\,(\rho_p - \rho_m)^2\,. \tag{3.170}$$

The forms of the differential cross section for particles of different special shapes, such as spheres, ellipsoids, rods and many more can be found in refs. [295, 325, 326]. In the general case of a single particle with random shape and anisotropy, the scattering function cannot be expressed by a simple form. However, SANS data can analysed considering two limiting cases that can still provide useful information: the Guinier approximation [327] valid at low Q such that $Q \cdot l \ll 1$ and the Porod approximation [328], valid at sufficiently large Q values such that $Q \cdot l \gg 1$.

Up until now, we have explicitly assumed low particle concentrations so that inter-particle correlations could be safely neglected. However, in many cases the relative arrangement of large structural units within the sample is important, e.g. in colloidal solutions at high concentrations like the ones presented in this thesis. To obtain the differential cross section in the more general case, the system

can be subdivided into N_p cells such that each cell contains exactly one particle. The position of the centre of the j-th cell is given by $\vec{R_j}$ and the position of the k-th particle in the cell relative to the centre of the cell is denoted by $\vec{d_k}$. With these definitions and the form factor one, the macroscopic differential cross section becomes

$$\frac{d\Sigma}{d\Omega} = \frac{1}{V} \left\langle \sum_{j=1}^{N_p} \sum_{k=1}^{N_p} F_j(\vec{Q}) F_k(\vec{Q})\, e^{i\vec{Q}\cdot(\vec{R_j}-\vec{R_k})} \right\rangle \tag{3.171}$$

For a system of identical particles with the same orientation, or spherical particles, the form factors are the same for all particles and Equation 3.171 becomes:

$$\frac{d\Sigma}{d\Omega} = \frac{N_p}{V} |F(\vec{Q})|^2 S(\vec{Q}) = \frac{d\Sigma}{d\Omega} = \frac{N_p}{V} P(\vec{Q}) S(\vec{Q})\,, \tag{3.172}$$

where $S(\vec{Q})$ denotes the *inter-particle structure factor* defined as it follows: cross section becomes

$$S(\vec{Q}) = \frac{1}{N_p} \left\langle \sum_{j=1}^{N_p} \sum_{k=1}^{N_p} F_j(\vec{Q}) F_k(\vec{Q})\, e^{i\vec{Q}\cdot(\vec{R_j}-\vec{R_k})} \right\rangle \tag{3.173}$$

So, the SANS intensity from Equation 3.171 is basically proportional to the product of the form factor and the structure factor of the sample. For further reading, books by Feigin et al. [325], Baruchel et al. [329] and Kline et al. [330] can be consulted.

3.4.1 SANS instrumentation

Figure 3.8 displays the general layout of a SANS beam line. Thermal neutrons (coming from the left side of the image) reach the instrument via a curved guide that blocks fast neutrons and γ-radiation from the reactor core; afterwards, they pass through a chopper series or a velocity selector. The neutron beam is shaped by a collimation system and then guided onto the sample. After being scattered from the sample, the neutrons travel through an evacuated flight chamber before they hit the detector, where they are detected. By changing the sample-to-detector distance, the observed q range can be changed. Detector tanks are usually very long, precisely to achieve the small-angle condition. While classical SANS measurements are preformed with a relatively well defined energy of the incoming neutrons (via velocity selection), in some cases short pulses of a white neutron beam can be used to operate a SANS instrument in a so called TOF mode. In fact, the neutron energy can be determined in the secondary part of the instrument via the TOF; at each detector pixel, different q values are detected as a function of time. This mode offers access to larger q ranges without moving the detector.

The SANS instruments employed for collecting the data for this work are showcased below.

D11: a low momentum transfer and low background small-angle neutron scattering instrument

The lowest momentum transfer and lowest background small-angle neutron scattering instrument (D11) is the archetype of a long, pinhole geometry instrument for SANS, designed for the study of large scale structures in soft matter systems, chemistry, biology, solid state physics and materials science. D11 receives neutrons from the vertical cold source of the ILL reactor, which is situated about 100 m from the first part of the instrument and about 140 m from the sample position. The detector is hence in a very low background environment. The polychromatic beam from the cold source is monochromated by a helical slot velocity selector which selects neutrons of $\pm 9\%$ about a mean wavelength determined by the drum rotation speed. The neutrons are then collimated by a

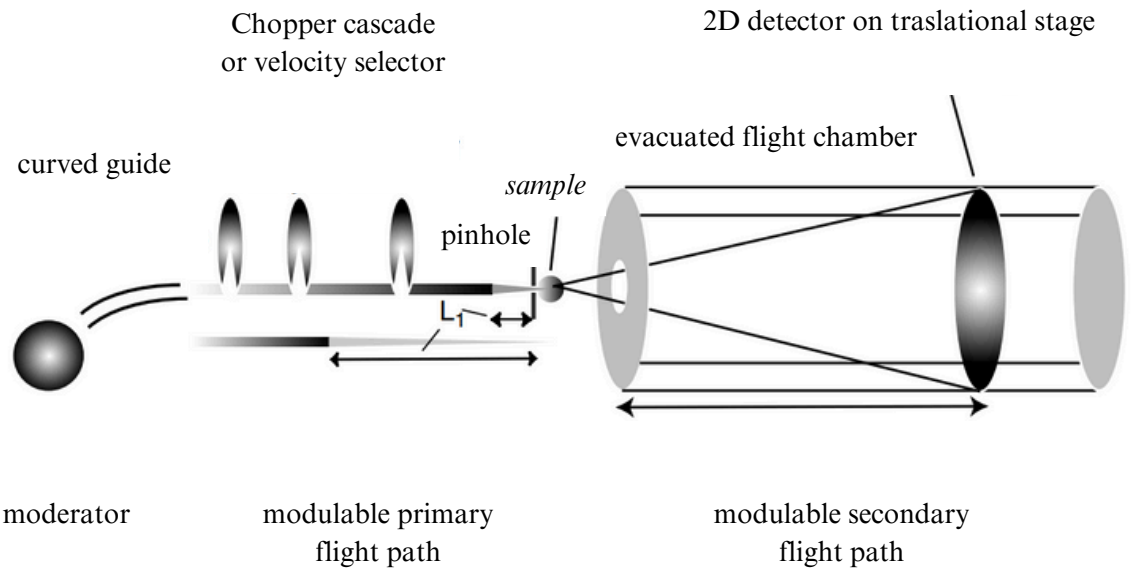

Fig. 3.8. Schematic setup of a SANS instrument. Figure adapted from Ref. [331] and rendered using Canva.

series of glass guides. The sample position is situated 40 m down-stream from the velocity selector and may be equipped with various sample environments. Neutrons scattered from the sample are detected on a 96×96 cm^2 ^{3}He multi-detector mounted on a moveable trolley within the evacuated detector tube. The detector may be placed at any distance between 1.2 and 39 m from the sample position, giving a quite wide accessible momentum transfer range of 3×10^{-4} to 1 Å^{-1}. Further details on the instrument can be found at the following page: D11 @ILL.

In this thesis, SANS measurements performed on the D11 at ILL were used in combination with NBS data from IN16B. Details about data collection, analysis and results of the experiment are described in Chapter 5.

D22: a large dynamic range small-angle diffractometer

Amongst all classical constant-wavelength pin-hole small-angle neutron scattering instruments, large dynamic range small-angle diffractometer (D22) is the one with the highest flux at the sample position in a wavelength range of $0.45 - 4$ nm. This is due to the brilliant horizontal cold source, the short rotor and high transmission of its velocity selector, and the relatively large beam cross-section (55×40 mm). The neutrons leaving the horizontal cold source pass through a velocity selector that selects a relatively narrow wavelength band (≈ 10 %). Other wavelength resolutions (from 8 to 20%) can be obtained by manually rotating the selector. The primary neutron guide system is prepared for a chopper system for potentially running D22 in TOF mode. The sample equipment consists of a remotely controlled table and a Eulerian cradle for mounting sample environment devices for working in air or in vacuum. D22 possesses a large-area multidetector (^{3}He), with a pixel size of 0.8×0.8 cm, corresponding to ~ 16000 resolution elements. The detector consists of 128 linear sensitive tubes arranged vertically with a spacing of 8 mm. Each tube has a dead time of 2 µs. The detector moves inside a 2.5 m wide and 20 m long vacuum tube providing sample-to-detector distances of 1.1 m to 17.6 m; the total q-range covered by D22 is thus $4 \times 10^{-4} - 0.85$ Å^{-1}. Further details on the instrument

can be found at the following page: D22 @ILL.

In this thesis, SANS measurements carried out on the D22 at ILL complemented NSE data from IN15 and all the information about the experiment and its results is reported in Chapter 6.

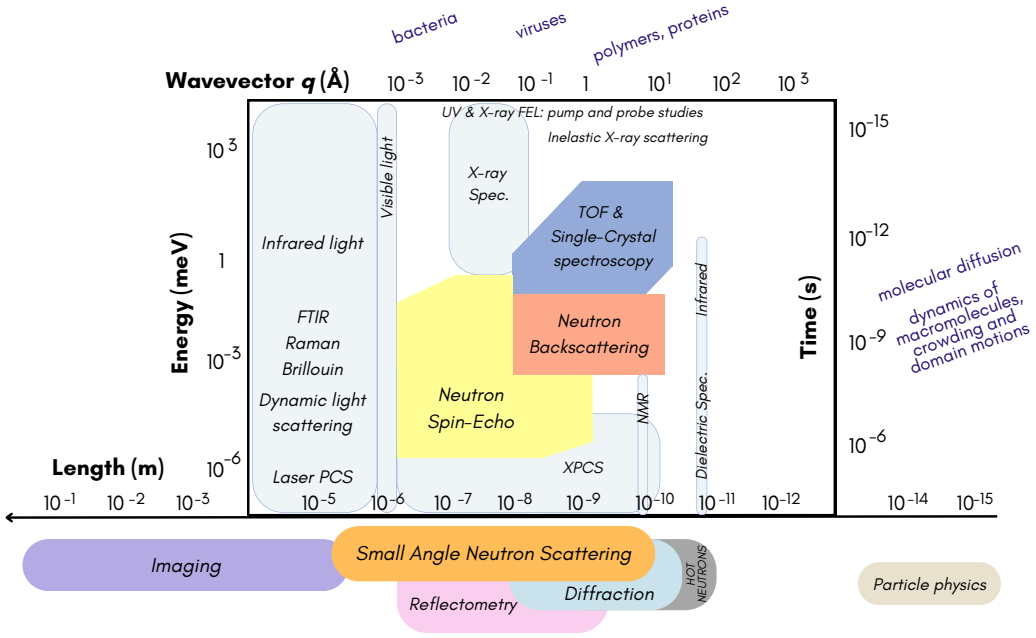

Fig. 3.9. Accessible length- (bottom axis) and time-scales (right axis) of typical scattering techniques depending on the energy (left axis) and wavevector q (top axis) probed by the instrumental setup. In the bottom area of the picture the static scattering techniques are reported. Some examples of biological and/or soft systems and phenomena accessible at specific length- and time-scales are also reported. Figure adapted from Ref. [1] and rendered using Canva.

Chapter 4

Materials and methods

In the present chapter, a detailed description of all the materials and methods employed in this work will be given. Since the neutron scattering techniques and details about the related instrumentation employed in this work are widely explained in Chapter 3, the present chapter only showcases the additional laboratory and computational methods complementing the neutron experiments. Section 4.1 reports comprehensive information on the proteins investigated in this work, namely the series of mAbs (Section 4.1.1) and BSA (Section 4.1.2), and on the solvents and chemical compounds used (Section 4.1.3). Sample preparation and laboratory techniques employed for a biophysical characterization of the samples are reported in section 4.2.2. *In silico* methods to align protein sequences, to extract useful sequence parameters and to predict their solution behaviour are presented in Section 4.2.1. Results of this computational analysis are also displayed in this chapter, in Section 4.3.2.

4.1 Materials

4.1.1 Lonza monoclonal antibodies

The mAbs employed in this work were manufactured in-house at Lonza AG/Ltd. The whole procedure was done in H_2O environment and more detailed information about protein production, purification and standard characterization is reported in Sec. 5.2.1 and in Mosca *et al*. [194]. The mAb H_2O solutions were buffer-exchanged into the formulation buffer (20 mM histidine-HCl buffer at pH 6.0) by tangential flow filtration, frozen in aliquots of 20, 40 or 150 mL, stored at $\leq$-65°C, afterwards sent to Grenoble and slowly thawed prior to use. The concentrations of the solutions were reported on their labels and were ranging from 10 to 17 mg/mL. All antibodies were manufactured in a human IgG1 isotype framework, except mAb4*, which is an IgG4 isotype. Moreover, most of them are formed by κ light chain isotype, while a subset – mAb12, mAb15 and mAb16 – contains λ light chains.

The main difference between κ and λ light chain isotypes is that the genes encoding for them are located on separate chromosomes; in fact, κ gene segments are encoded on chromosome 2 [332], whereas λ gene segments are encoded on chromosome 22 [333]. In human serum, there are more κ antibodies than λ ones, with the κ:λ ratio reported to be between approximately 1.5 and 2 [334–336]. Altered κ:λ ratios can be a signature of certain diseases [337]. Research has shown that κ and λ light chains have differences in their CDR physicochemical and structural properties, which can affect antibody specificity and function [338]. In the field of therapeutic antibody development, λ-antibodies are often considered less developable than κ-ones. However, tools to unbiasedly improve

the developability of both isotypes are now available [339]. More detailed information about the CDR of the mAbs investigated is reported in Sec. 4.3.2.

4.1.2 Bovine serum albumin

The protein BSA is the most abundant in bovine blood serum. Due to its high solubility, it serves as transport protein for molecules such as fatty acids, drugs and hormones but regulates also the osmotic pressure and the pH [340]. With a MW of 66.43 kDa, BSA has an isoelectric point ranging from 5.1 to 5.5; thus the protein has an overall negative charge (-18e) at pH 7. Due to its similarity to the human analogue human serum albumin (HSA) and due to its good availability and low cost, it is often used as standard test protein. This protein is highly interacting with metal ions and its behaviour in the presence of multivalent ions like YCl_3, $HoCl_3$, $LaCl_3$ has been extensively studied in our group. A literature overview on this topic is presented in Chapter 7 and for further reading we refer to Christian Beck's PhD dissertation [331].

For the research presented in this thesis, BSA (catalog no. A3039, batch no. SLCD4770, lyophilized powder $> 98\%$ purity, heat shock fraction, protease free, fatty acid free, essentially globulin free, pH 7) and $LaCl_3$ (Sigma-Aldrich catalog no. 449830, batch no. 0000088871, anhydrous, 99.9% purity) were obtained from Sigma-Aldrich of Merck KGaA and used without additional purification. Results of the study on the BSA-$LaCl_3$ system are presented in Chapter 7.

4.1.3 Solvents

Water H_2O and heavy water D_2O

Water clearly stands out as one of the most essential molecules in biology, possessing a variety of remarkable properties that are fundamental to the development of life. Its finite dipole moment, high dielectric constant, exceptional heat capacity, substantial surface tension, and unusual density anomaly upon freezing are particularly noteworthy. Most biological processes occur in an aqueous environment, where water's solubility facilitates critical functions such as membrane assembly and molecular mobility.

The current paragraph focuses on the properties of normal water H_2O and its heavy variant, deuterium oxide D_2O, which is of interest in a number of applications in physics and engineering. The isotopic difference in these two special substances leads to distinct physical and chemical properties: D_2O is denser than H_2O (1.1 g/cm^3 vs. 1.0 g/cm^3 at 25°C), is more viscous (1.25 mPa·s vs. 0.89 mPa·s at 25°C) has a higher boiling point (101.4°C vs. 100°C at standard atmospheric pressure), and a higher freezing point (3.8°C vs. 0°C) [341,342]. Although H_2O and D_2O are chemically the same compound, reactions involving D_2O often proceed at slower rates compared to those with H_2O due to the kinetic isotope effect. As far as biological processes are concerned, D_2O is non-toxic and tolerated in small quantities; nevertheless, it can be disruptive in large amounts due to its physical properties which may affect biochemical reactions and cellular activities.

As mentioned above, another important property of water as a solvent is its viscosity, which strongly depends on temperature in a solvent-specific manner. Understanding these temperature-induced changes is crucial for accurately interpreting diffusive motions within our samples. To address this, we apply a formula proposed by Cho *et al*. [342] to account for the temperature dependence of normal and heavy water viscosity:

$$\eta_0 = C(\Delta T + a\Delta T^2 + b\Delta T^3 + c\Delta T^4)^{-\gamma} \tag{4.1}$$

The reason why heavy water is particularly relevant to our work lays in the distinct neutron cross-sections of hydrogen and deuterium, both in absorption and scattering processes (Table 3.2, Sec. 3.1.4). Due to deuterium's lower neutron absorption cross-section, D_2O is more transparent to neutrons and less attenuating to the neutron beam. More relevantly, the difference in H and D scattering cross-sections provides the significant contrast enhancement necessary for discerning the protein (H-rich object) signal from the solvent one, which strongly motivates the use of heavy water as a solvent in our experiments.

Nevertheless, it must be pointed out that the isotopic composition of these two solvents may affect the behaviour of the solutes, especially in the case of biomolecules. Regarding protein in solutions, H_2O/D_2O substitution can modify their thermal and conformational stability [343, 344], structure, hydration, flexibility, compactness, solubility, self-assembly and aggregation pathways and can cause shift in their phase diagram [345]. For instance, Braun *et al.* studied through SAXS the effective interactions of proteins in the presence of multivalent ions and observed strong differences between the systems studied in H_2O and D_2O [346]. The effect was more pronounced upon entering the LCST-LLPS region, where entropic contributions dominate, indicating that isotopic composition cannot be neglected when dealing with entropy-driven phenomena.

For all the samples prepared for this thesis, the H_2O employed is milli-Q from Merck / Millipore-Sigma (Darmstadt, DE). Concerning D_2O, different batches from different companies were used time to time. Details on the sample preparation for each experiment are reported in the corresponding result chapter (5, 6, 7).

Buffer used

The primary reason for using a buffer system in a pharmaceutical product, especially for biologics, is to control the pH in order to optimize stability during storage and handling [347]. In fact, many active pharmaceutical ingredients are pH-sensitive and can degrade or lose efficacy if the pH deviates from their optimal range, leading to reduced drug potency and shelf life. Secondly, buffer usage also ensures that the drug effectiveness is not compromised and enhances its solubility, absorption, distribution, metabolism, and excretion within the organism. This optimization is crucial for achieving the desired pharmacokinetic and pharmacodynamic profiles.

Regarding the drug product delivery, one has to distinguish between the different routes of administration. For IV administration a drug volume representing a small percentage of the available blood volume is infused over a typically long time (15-30 minutes and longer); the added volume is therefore not significant and the body has good measures to react on the infusion and reestablish a balance. In addition, drug products for IV administration are often diluted in physiological saline (0.9%) or dextrose solution (5%), so the buffer component is diluted and the solution is iso-osmotic and well tolerated. The situation is different for SC or intravitreal injection. In this case, the drug is delivered in a smaller volume of drug as a quick bulk injection and without further dilution, so pH and buffer type can play a more significant role. Moreover, for formulations administered via injection, using a buffer and maintaining a pH close to physiological levels is important to avoid irritation and discomfort for the patient.

In this work, a 20 mM histidine-HCl buffer at pH 6.0 for the samples in H_2O and at pD 6.4 for the deuterated solutions was employed, as for most ($> 80\%$) formulations of highly concentrated approved mAb drug products [348]. There are several reasons supporting the choice of a histidine buffer in mAb formulations. Firstly, with a pKa of approximately 6.0 at the side chain, histidine showcases an effective buffering capacity in the pH range of 5.5-6.5, optimal for most mAb formulations

due to its proximity to physiological pH and its compatibility with both IV and SC delivery routes. This feature helps maintain stability during storage and administration. Furthermore, histidine has been shown to reduce antibody aggregation and improve overall stability through non-electrostatic, non-structural mechanisms, likely by shielding hydrophobic regions on the protein surface [147, 148] and rendering the mAb hinge stiffer [148]. Besides this, histidine is compatible with lyophilization processes that are crucial for many mAb formulations and it also allows for low ionic strength formulations, which further confirms its being one of the most versatile excipient in the protein-based biopharmaceutical formulations [146].

4.2 Methods

4.2.1 In silico methods: sequence analysis

The PDB files of the antibodies provided by Lonza were used to extract important information through sequence analysis and MD simulations. The setup, the analysis and the results of the latter are reported in Sec. 5.3.3 and in Mosca *et al.* [194]. The PDB file format is a textual file format providing the three-dimensional structure of a molecule and other information including atomic coordinates, secondary structure assignments, as well as atomic connectivity. The PDB files of the antibodies were processed with different bioinformatics tools, such as the Biopython package [349], using Bio.PDB and Bio.SeqUtils modules and ProtParam [350]. Although not directly related to the experimentally determined quantities, the information accessed has definitely improved the knowledge about the proteins.

Extraction of parameters In the following lines, the physico-chemical properties extracted from the PDB files will be listed along with a brief explanation. The computed parameters are: chemical formula, number of residues and their charge, amino acid content, MW, aromaticity, grand average of hydropathy (GRAVY), aliphatic index, pI, charge at pH 6, instability index, extinction coefficient, fraction of α-helices, β-strands and β-turns present in the secondary structure.

The *aromaticity* of a protein is the relative frequency of aromatic amino acids, namely Phenylalanine (Phe), Histidine (His), Tyrosine (Tyr), Tryptophan (Trp) [351], with the last two being the ones determining the absorbance peak at a wavelength of $\sim$280 nm for proteins.

GRAVY (grand average of hydropathy) is a bioinformatics term that is used to predict the hydrophobicity (or hydrophilicity) of a protein. Hydrophobicity refers to the non-polar nature of a molecule and its tendency to avoid contact with water. The GRAVY score is calculated as the average hydropathy index of all the amino acids in a protein sequence:

$$\frac{\sum_{a=1}^{N} h(a)}{\sum_{a=1}^{N} a} = \frac{\sum_{a=1}^{N} h(a)}{N} \tag{4.2}$$

which basically stands for the sum of hydropathy values over all the amino acids, divided by the total number of residues in the sequence N. The hydropathy index of each amino acid $h(a)$ is determined based on its physical and chemical properties. A high GRAVY score indicates a hydrophobic (non-polar) protein, while a low GRAVY score indicates a hydrophilic (polar) protein. Positive GRAVY values indicate hydrophobic; negative values mean hydrophilic, in fact water-soluble proteins commonly report a GRAVY value of -0.4 [352]. GRAVY is used to study the relationship between protein hydrophobicity and function and is relevant in protein analysis, prediction and design.

The *aliphatic index* is another measure of the hydrophobicity (or hydrophilicity) of a protein. It is defined as the relative volume occupied by aliphatic (non-polar/hydrophobic) residues – Alanine (Ala), Valine (Val), Isoleucine (Ile) and Leucine (Leu) – divided by the total number of residues in the protein. A high aliphatic index indicates a higher proportion of hydrophobic residues, which can influence the stability and folding of a protein. A low aliphatic index indicates a higher proportion of hydrophilic (water-soluble) residues, which can facilitate interactions with other molecules in aqueous environments.

The *pI* is the pH at which a protein has a net zero charge. At this pH, the number of positively charged amino acids is equal to the number of negatively charged amino acids in the protein, leading to neutral charge overall. The pI is important as it affects the solubility, stability, and interactions of a protein. In practice, a protein with an excess of basic amino acids will bear an isoelectric point roughly greater than 7 (basic), while a protein with an excess of acidic amino acids – Aspartic acid (Asp) and/or Glutamic acid (Glu) – will often have an isoelectric point lower than 7 (acidic). The further you get from pI by varying the pH of the buffer in which the protein is immersed, the more the protein gets charged and prone to electrostatic repulsion. Given that, a key quantity to be known is the monomer *charge at the solution pH*, in the present case 6. The higher the charge at a given pH, the higher the electrostatic repulsion between monomers. Conversely, the lower the protein charge at the same pH, the weaker the repulsion and higher their propensity to form aggregates. However, it must be emphasised that protein-protein interactions not only depends on the overall net charge, but also how charges are distributed locally, e.g. forming more or less extended negatively/positively charged patches. This aspect is crucial for in silico protein rational design.

A protein *instability index* can be calculated based on the occurrence of 400 distinct dipeptides in the protein sequence and averaged over it [353]. If this index is smaller than 40 the protein is predicted as stable, while a value above 40 indicates that the protein may be unstable.

The *extinction coefficient* of a molecule is a measurement of how strongly it absorbs, and thereby attenuates, light at a given wavelength. It is an intrinsic property of the molecule and it depends on the atomic species present in it. For proteins, one can calculate the molar extinction coefficient at 280 nm (where the main absorbance peak is observed) based on the amino acid sequence, with reduced cysteines or with disulphide bridges. This quantity is crucial for concentration determination via UV-Vis spectroscopy; in fact, it enters the Lambert-Beer law which is used for this purpose and presented in Sec. 4.2.2.

Sequence alignment and amino-acidic composition In order to explore the differences in the primary structure of the antibodies, sequence alignment was performed with UniProt 'Align' module [354] with ClustalOmega program and also with VMD (Visual Molecular Dynamics) [355] using the 'MultiSeq' module with ClustalW algorithm [356].

Fv modelling, CDR prediction and therapeutic developability ABodyBuilder-ML is a suite from SAbPred ('The Antibody Prediction Toolbox') [357] that employs machine-learning to model the variable domain (Fv) and predict the complementarity determining region (CDR) of antibodies. Heavy and light chains were extrapolated from the full sequences via Biopython and separately given as inputs for ABodyBuilder-ML. The tool returns a Fv model by checking sequence identities of variable domain of the heavy/light chain (VH/VL) with all the antibodies in the Structural Antibody Database (SAbDab) [358] and selecting as framework the one giving the highest score for the input chains. VH and VL are then oriented with respect to each other using ABangle tool [359]. CDRs are predicted

and the accuracy estimation is done by using the deep-learning tool ABlooper [360]. This estimation is entrusted to a parameter referred to as *CDR diversity score*, defined as the root mean square deviation (RMSD) of alignment to crystal structure and benchmarked on a test dataset of over 100 antibody VH/VL paired sequences. Please note that it only refers to the CDR-H3 loop prediction, due to the higher variability of this small region compared to the other loops intervening in the CDR formation. This parameter is reported in column 3 of Table 4.3, where values ≤ 1.25 Å indicate a quite good CDR prediction, while values ≥ 2 Å a less accurate one.

In order to push further the analysis, the tool TAP, the 'Therapeutic Antibody Profiler' [339, 361, 362] from Antibody Prediction Toolbox (SAbPred) was employed to determine some other mAb CDR properties in order to assess their developability as drugs compared to a huge dataset of existing therapeutics. All these parameters are reported in Table 4.3 and constitute the 5 developability guidelines introduced by Raybould *et al.* [362] are:

- CDR total length, which has a median value of 48 amino acids based on a dataset of 137 CST (clinical stage therapeutics) [362];
- Patches of Surface Hydrophobicity (PSH) score, namely the extent and therefore the magnitude of surface hydrophobicity based on Kyte and Doolittle hydrophobicity scale [352]; this calculation yields higher scores if hydrophobic residues tend to neighbor one another in the CDR.
- Patches of Positive Charge (PPC) score, meaning the positive charge distribution in the CDR.
- Patches of Negative Charge (PNC) score, meaning the negative charge distribution in the CDR.
- structural Fv charge symmetry parameter (SFvCSP), that is the asymmetry in the net heavy- and light-chain surface charges. For this evaluation, structural considerations are also taken into account, therefore only residues that are surface-exposed and not locked in salt bridges are included in the calculation of the net charge [362].

The colour assigned to the values in Table 4.3 is based on where each antibody sits within the 5 parameter distributions of the latest set of 754 post Phase-I therapeutic Fv domains.

4.2.2 Laboratory methods: buffer exchange, concentration determination, viscometry

Buffer exchange via dialysis and concentration via centrifugation

Since deuterium ^{2}H has a significantly lower neutron scattering cross-section than hydrogen ^{1}H, the ideal sample composition in order to perform meaningful neutron scattering experiments is having fully protonated proteins in a deuterated solvent, in order to measure them in their aqueous environment while minimizing the scattering signal from the latter. To this scope, concentration via centrifugation and dialysis were employed to buffer exchange the antibodies into 20 mM Histidine in pure D_2O at pD 6.4.

For the dialysis, 3 mL cassettes containing cellulose membranes with 30 kDa nominal molecular weight cutoff (MWCO) from ThermoFisher Scientific (Waltham, MA, USA) were used. Two baths of at least 2 hours were performed to obtain a dilution factor of at least 104 of residual H_2O in the samples. A graphical representation of this method is provided in Figure 4.1.

Concerning buffer exchange via centrifugation, 15 mL 30 kDa Amicon®-Ultra concentrators from Merck / MilliporeSigma (Darmstad, DE) were used. Protein stock solutions in H_2O were centrifuged

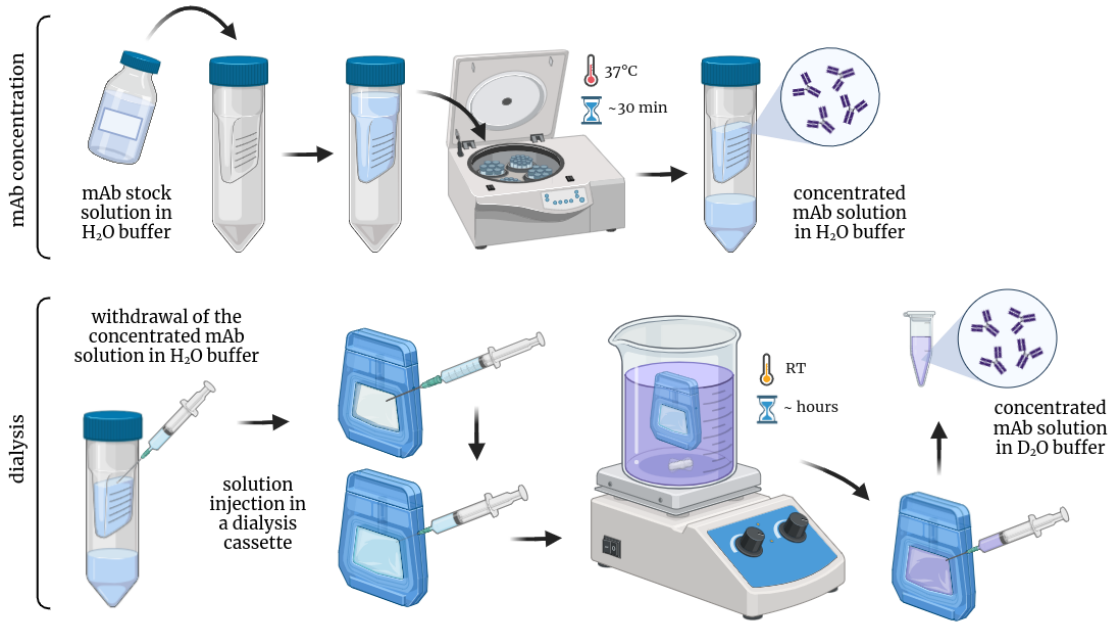

Fig. 4.1. Graphical representation of the *dialysis* method used for exchanging the H_2O buffer (coloured in cyan) of the mAbs into the analogous D_2O one (shown in lilac). The first step of the procedure (upper part of the figure) is to concentrate the mAb stock solutions in H_2O until ≤ 60 mg/mL using ultra-concentrators. Afterwards, the concentrated mAb solution is withdrawn with a syringe and injected in a previously hydrated 30 kDa MWCO dialysis cassette. The latter is then immersed in a bath containing the D_2O buffer and kept at ambient temperature for some hours to maximize the buffer exchange in the samples and under stirring all the time. After the long bath in D_2O, the protein solution is withdrawn from the cassette. The figure is created using Biorender and the colors used are just an aid for the reader and do not refer to any actual differences in the two solvents; objects are not depicted in real scale.

at 37°C to concentrate them until $\simeq 1$ mL and afterwards resuspended in the new D_2O buffer and concentrated again. This step was done 3 times in order to minimize the H_2O content in the samples. After testing both methods, centrifugation was preferred over dialysis because it usually requires less amount of D_2O. A graphical representation of this method is provided in Figure 4.2.

Concentration determination via Ultraviolet-Visible (UV-Vis) spectroscopy

The final concentrations of the samples were determined via UV-Vis spectroscopy by measuring dilution series of each protein using a Jasco V-630 Spectrophotometer (Tokyo, JP). For each dilution step, absorbance curves were collected and their peak values at 280 nm were plotted against the sample reciprocal dilution factor. The datasets obtained were fitted using the Lambert-Beer law, which links the absorbance A of the sample to its concentration c via the following relation:

$$A = \varepsilon_{280}\, c\, \ell\,, \tag{4.3}$$

with ℓ being the optical path-length, i.e., the thickness of the cuvette, and ε_{280} the sample extinction coefficient at 280 nm.

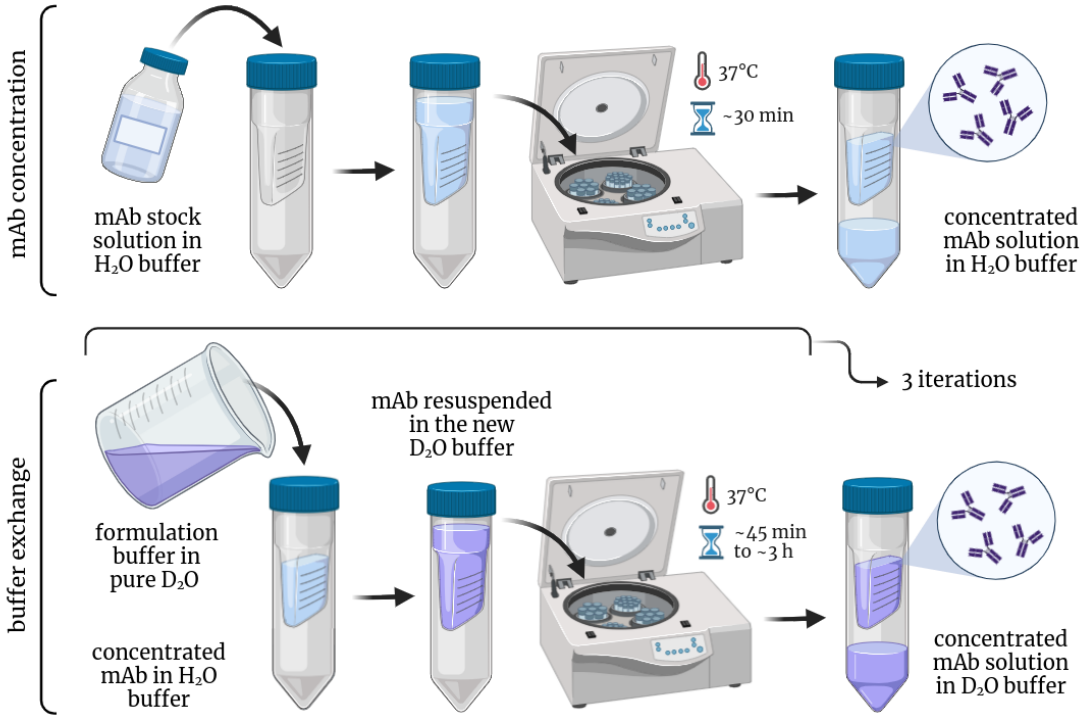

Fig. 4.2. Graphical representation of the *concentration via centrifugation* method used for exchanging the H_2O buffer (coloured in cyan) of the mAbs into the analogous D_2O one (shown in lilac). The first step of the procedure (upper part of the figure) is to concentrate the mAb stock solutions in H_2O until ~ 1 mL using ultra-concentrators. Afterwards, the concentrated mAb solution in H_2O is resuspended in the D_2O buffer and concentrated again until ~ 1 mL. This procedure is repeated for three times in order to maximize the buffer exchange in the samples. In the final step (bottom right) the proteins are concentrated in the new deuterated buffer. The wide time-span reported for the centrifugation step strongly depends on the antibody type; in fact, the least viscous ones took ~ 30 mins, while the ones exhibiting high viscosities could take some hours. The figure is created using Biorender.

In most experiments conducted for this thesis, polyclonal IgG solutions were measured as references and prepared with lyophilized powder of bovine γ-globulin ($\geq 95\%$ purity, essentially salt-free), purchased from Merck / Millipore-Sigma (Darmstadt, DE) and directly dissolved in the 20 mM Histidine-HCl D_2O buffer at pD 6.4.

Viscometry

All the antibodies mentioned in this work have been characterized with viscometry before being investigated with neutron scattering. Measurements were collected at 25°C in the antibody original formulation buffer, that is 150 mM sucrose 20 mM His-HCl aqueous buffer at pH 6. For each antibody solution, a concentration series from 30 to 180 mg/ml was measured.

In addition, a subset of the antibodies (mAb9, mAb12, mAb16 and bovine γ-globulin) in deuterated solutions was measured. The aim was to collect complementary information on macroscopic viscosity at the same conditions needed in neutron experiments which included two different buffers (20 mM His-HCl and 20 mM His-HCl 58 mM trehalose, both in D_2O) and three different temperatures, namely 7, 22 and 37°C (280, 295 and 310 K). The experiments were performed at Lonza AG/Ltd.

(Basel) in the labs of the Formulation Development division, by using a Rheosense VROC® Initium rheometer (San Ramon, CA, USA), whose schematic is reported in Figure 4.3. The instrument operates using a viscometer / rheometer-on-a-chip (VROC) technology [363, 364]. The viscosity is obtained by measuring the pressure drop as a test liquid flows through its rectangular slit microfluidic channel. The sample to be analyzed is drawn from its vial by a syringe, then injected and forced to flow into a micro-channel, where it encounters a chip with pressure sensors at different positions (Figure 4.4); here, the pressure drop ΔP as a function of position is measured. The wall shear stress σ_w is calculated as a ratio between the ΔP necessary to drive the flow a streamwise distance L and L itself:

$$\sigma_w = -\frac{\Delta P}{L}\frac{wh}{2\,(w+h)}\ . \tag{4.4}$$

Equation 4.4 is also known as Hagen-Poiseuille law [365, 366]. For incompressible 2D flow of a constant viscosity liquid in a rectangular channel, the wall shear rate $\dot{\gamma}_w$ is a linear function of the applied flow rate of the liquid through the channel Q:

$$\dot{\gamma}_w = \frac{6Q}{wh^2}\ , \tag{4.5}$$

where Q represents the volumetric flow rate, L stands for the flow path length, ΔP is the pressure drop within the distance L, w and h respectively indicate the flow channel width and height/depth. The shear stress σ_w and the shear rate $\dot{\gamma}_w$ are then used to calculate the dynamic viscosity η:

$$\eta = \frac{\sigma_w}{\dot{\gamma}_w} \tag{4.6}$$

This is no longer valid for flows of non-Newtonian fluids (with a rate-dependent viscosity), for which the calculation of $\dot{\gamma}_w$ needs to be corrected. This also applies to the highly concentrated mAb solutions under study. In this case, equation 4.5 gives an apparent shear rate $\dot{\gamma}_a$ and the true wall shear rate can be found using the Weissenberg–Rabinowitsch–Mooney equation [367, 368]:

$$\dot{\gamma}_w^{true} = \frac{\dot{\gamma}_a}{3}\left[2 + \frac{d(ln\dot{\gamma}_a)}{d(ln\sigma_w)}\right] \tag{4.7}$$

where σ_w is calculated from equation 4.4. The true viscosity is then computed as it follows:

$$\eta(\dot{\gamma}_w^{true}) = \frac{\sigma_w}{\dot{\gamma}_w^{true}} = -\frac{\Delta P}{L}\frac{wh}{2(w+h)}\frac{1}{\dot{\gamma}_w^{true}} \tag{4.8}$$

To ensure accuracy, the instrument software applies this correction automatically. The instrument can be loaded with a maximum of 40 samples for each measurement routine. A medical grade viscosity standard from Paragon Scientific (ISO 17025 & 17034), reporting a dynamic viscosity of 9.994 mPas and a density of 1.1567 g/mL at 25°C, is normally used to perform a system suitability test (SST).

All the measurements reported in the present work have been performed using the standard viscosity protocol typically used at Lonza, which is further explained in the following lines. An automatic shear rate is applied to the solution withdrawn from the vial and a viscosity value is recorded; the viscosity measurement is repeated for nine more times and the output viscosity value is the mean of the 10 repetitions, with an assigned uncertainty given by the standard deviation of the distribution. The "automatic measurement" protocol makes an estimation of the viscosity value without a predefined shear rate and then finds an appropriate shear rate to target the 50% of the full scale pressure of the chip.

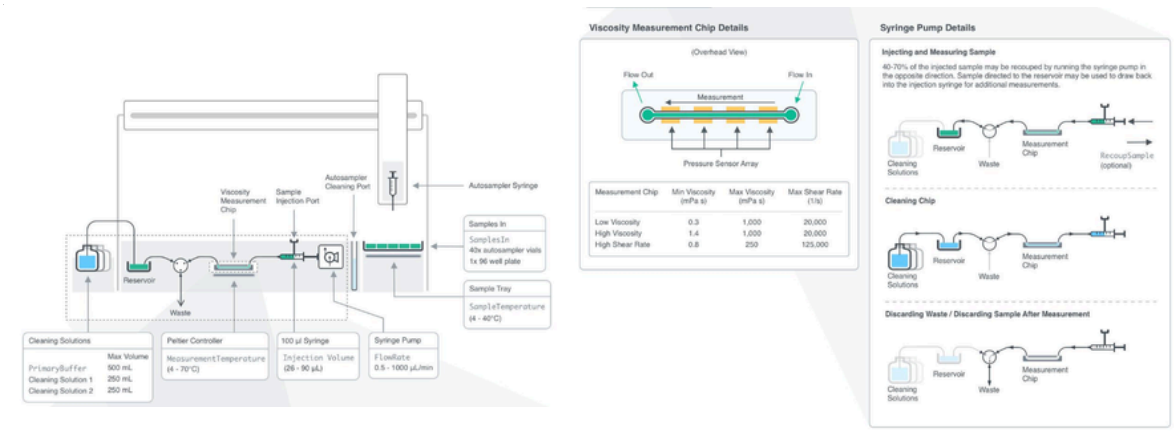

Fig. 4.3. Schematic of a RheoSense VROC® Initium rheometer with detailed explanation of the chip and the syringe pump. Image source: *rheosense.com*

After each sample acquisition, the instrument automatically executes a standard cleaning before the following one through three solvent suppliers ('Cleaning solutions' in Figure 4.3). The three bottles are respectively filled with milli-Q water (500 mL), 1% Aquet® liquid detergent (Merck/MilliporeSigma, Darmstadt, DE) in milli-Q water solution and 100% isopropanol (250 mL each). A deeper cleaning procedure is typically required when the samples injected in the setup reach high viscosities, such as in the case of highly concentrated protein solutions. To do so, 10% Terg-a-zyme® enzyme detergent (Merck/MilliporeSigma, Darmstadt, DE) dissolved in milli-Q water was employed. In our specific case, the deep cleaning with Terg-a-zyme® was done after measuring a series of one antibody with increasing protein concentration before switching to another protein.

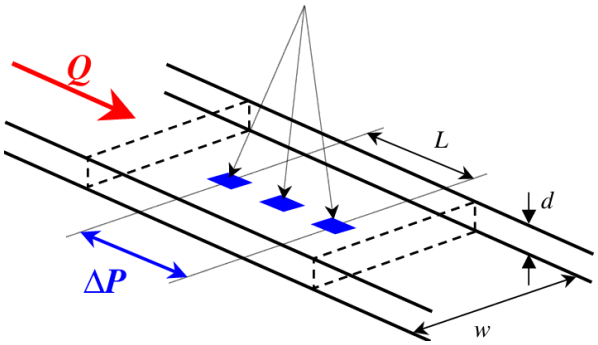

Fig. 4.4. Sketch of the rectangular slit, consisting on a glass micro-channel lying on a gold-coated silicon base with a pressure sensors array, of a RheoSense VROC® Initium rheometer [368]. Q represents the volumetric flow rate, L stands for the flow path length, ΔP is the pressure drop within the distance L, while w and h respectively indicate the flow channel width and height/depth. The image is adapted from Ref. [368] and rendered using Canva.

4.3 In silico protein sequence analysis results

4.3.1 Sequence alignment and amino-acidic composition

In the current paragraph, the results from full-chain and Fv sequence alignment are reported, along with the amino-acidic composition of the Fv domain of all the mAbs. As already mentioned, the alignment procedure was carried out using UniProt 'Align' module [354] with Clustal Omega [369,

370]. The results are depicted in the form of a sequence identity matrix and shown in Figure 4.6 for the antibody full chains and for their Fv domains. From the full chain analysis, mAb16-mAb4* and mAb12-mAb4* show the lowest sequence identity ($\sim$ 69%), followed by mAb16-mAb24 and mAb5-mAb16 ($\sim$ 71%). On the other hand, mAb3-mAb25 feature the highest similarity ($\sim$ 97%), followed by mAb3-mAb19 ($\sim$ 95%), and mAb19-mAb25 ($\sim$ 94%). Performing the Fv domain alignment basically means looking for discrepancies in the most variable part of the molecules. From the Fv domain analysis, mAb16-mAb24 and mAb5-mAb16 show the lowest sequence identity ($\sim$ 43%), followed by mAb16-mAb4* ($\sim$ 45%). On the other hand, mAb3-mAb25 feature the highest similarity ($\sim$ 90%), followed by mAb3-mAb19 ($\sim$ 84%), and mAb19-mAb25 ($\sim$ 83%).

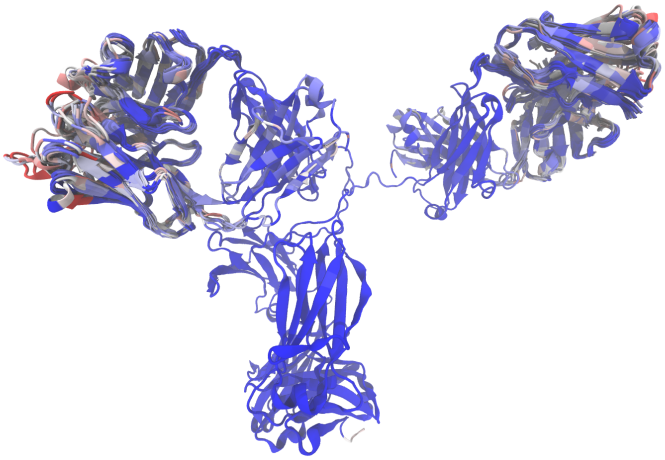

Fig. 4.5. Full chains of all IgG1 mAbs (left) and the IgG4 mAb4* (right) depicted using the 'NewCartoon' representation in VMD [355]. The colors used result from the full sequence alignment visualized based on sequence similarity calculated with BLOSUM100 method, and range from blue – 100% identity – to red – 0% identity. A significant part of the primary sequence of the mAbs can be de facto superimposable, with the Fc domain being almost identical in all variants. The discrepancies are instead in the Fv domains located in the final part of the two upper lobes, namely the CDR. The same depiction for mAb4*, the IgG4 variant studied in this work, is reported in Figure 6.1 in Chapter 6.

The same analysis was also realized with VMD (Visual Molecular Dynamics) [355] using the 'MultiSeq' module with ClustalW algorithm [356], in order to qualitatively visualize the alignment results directly onto the antibody structure. Figure 4.5 shows mAb1 structure as a template to visualize where the sequence discrepancies among all the IgG1 full chains are located. Blue regions correspond to 100% sequence identity, whereas the red ones indicate 0% identity. The mAbs obviously differ the most in their Fv domains, especially in the CDR. The alignment and representation using VMD of Fv domains are reported in Figure 4.7. Focusing on Fv domain, it becomes evident that the most significant variations are observed in the CDR loops. These differences extend beyond the amino acid composition, encompassing aspects such as loop length and spatial organization.

Concerning the amino-acidic composition of the Fv of the antibodies, Figure 4.8 reports the relative abundance of every amino acid on the total Fv sequence for each mAb sequence. The same information is shown in Figure 4.9, this time sorted by the individual amino acids. The amino acid with the highest abundance in the variable domain of the mAbs is definitely Ser (serine), with an average value of $\sim$ 12%, followed by Gly (glycine) and Thr (threonine), reaching $\sim$ 8%. The least

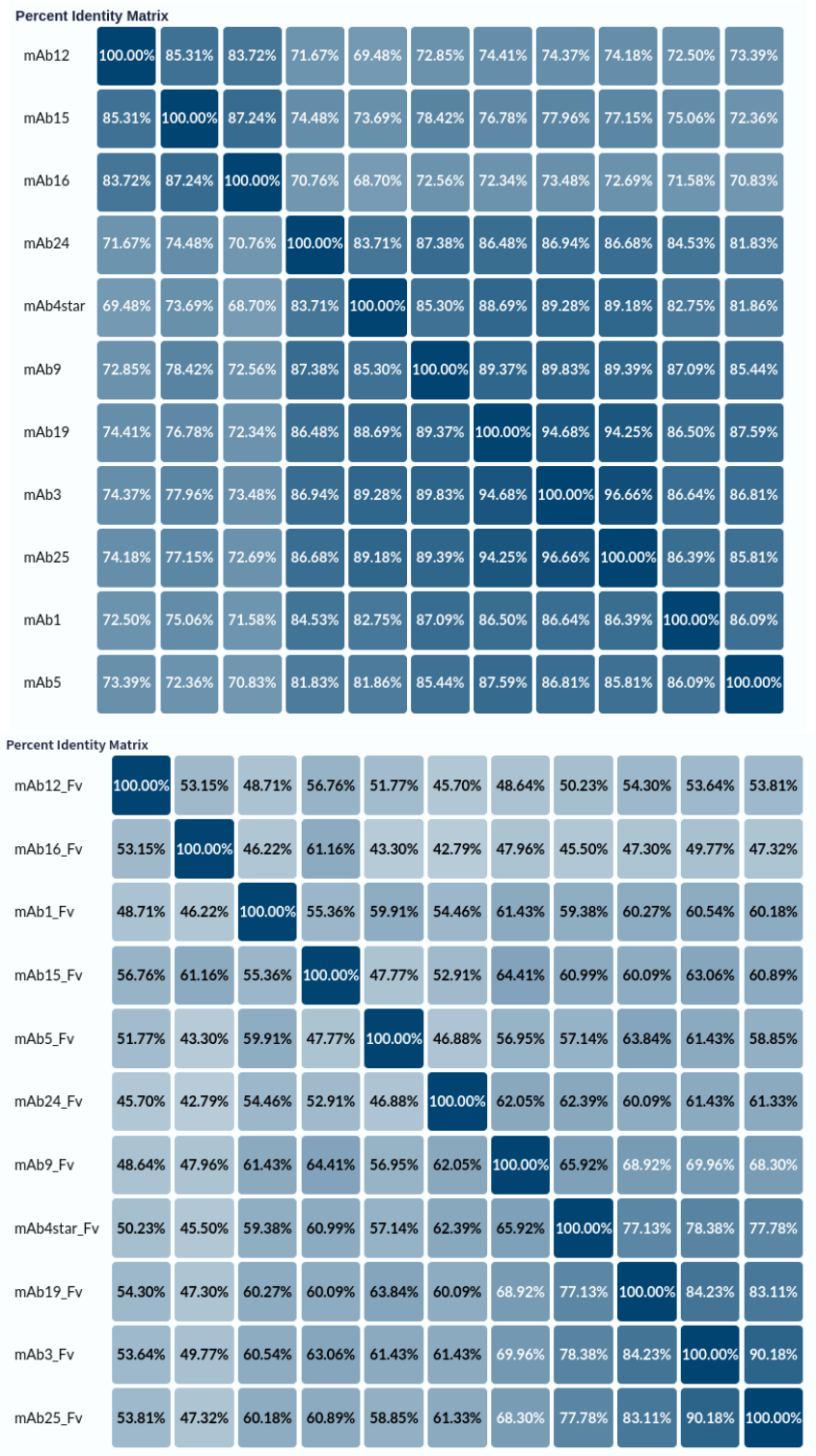

Fig. 4.6. Sequence identity matrices for the full chains (top) and the variable domains Fv (bottom) of the mAbs, with 100% being perfect identity. This value appears in the matrix diagonal because it contains the correlations of each mAb with itself. The matrices are by definition symmetric, because for each element it holds $a_{ij} = a_{ji}$, where i and j indicate two different mAbs.

present ones are instead histidine (His), cysteine (Cys), methionine (Met), all $\leq$ 2%. For instance, mAb19 Fv contains no His residue. Another observable difference is a higher % of asparagine (Asn) in the IgG4 antibody mAb4* Fv, compared to the other IgG1 proteins. Let us now focus on the subset of mAbs exhibiting higher viscosities compared to the others (mAb12, mAb15, mAb16, mAb24). For instance, mAb16 Fv stands out for the highest Cys and Val (valine) content. While Val is an hydrophobic residue, Cys is a special amino acid that can associate with hydrophobic residues, which may suggest a higher propensity to form hydrophobic interactions in solution and contribute to a viscosity increase. mAb12 and mAb15 show a slightly higher Asp (aspartic acid) content, while it is the case of Glu (glutamate) for mAb24; both Asp and Glu are negatively charged residues, which can possibly mediate electrostatic interactions. This is also the case of His (positively charged) in mAb24.

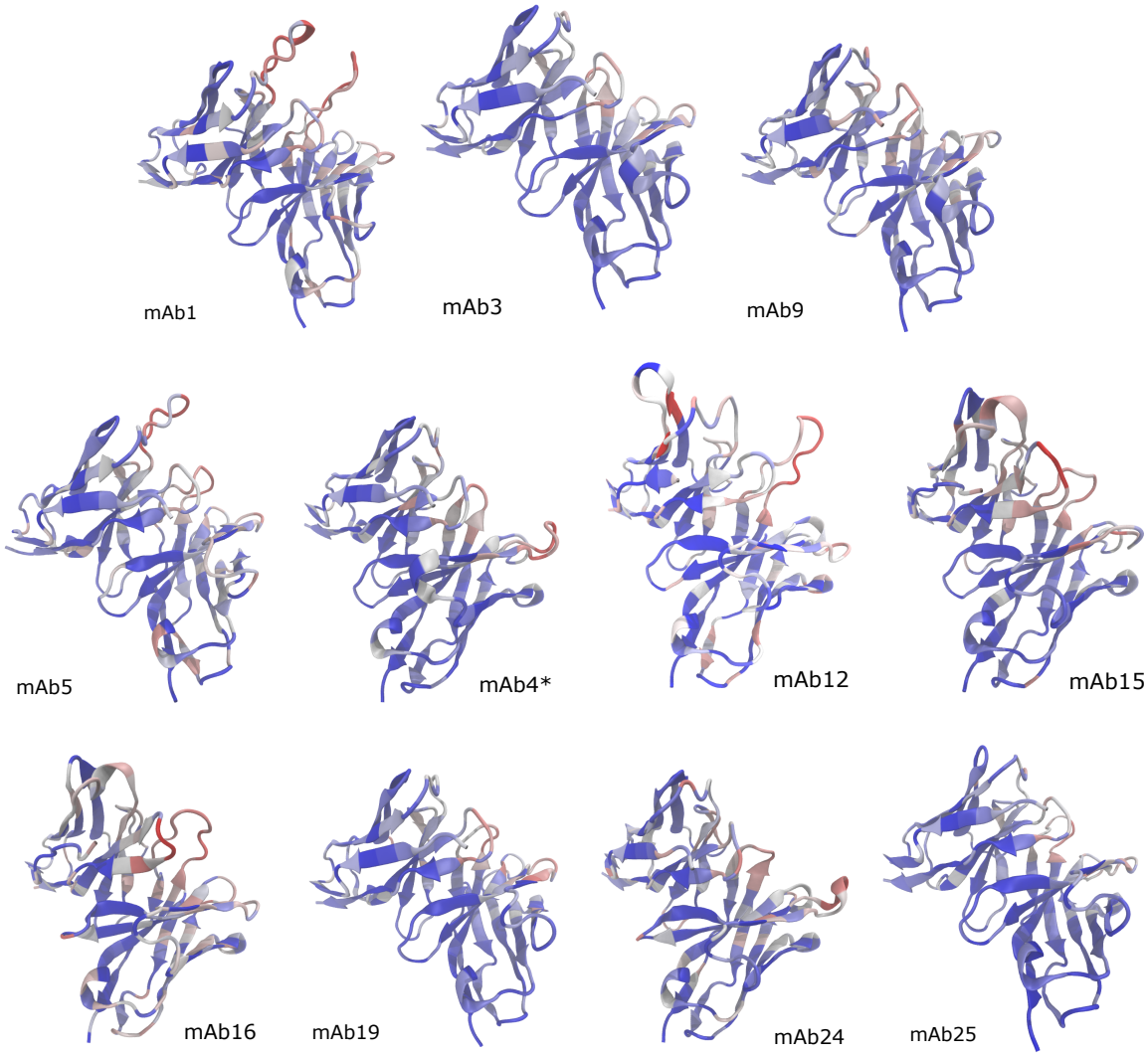

Fig. 4.7. Variable domains Fv of all the mAbs depicted using the 'NewCartoon' representation in VMD [355]. The colors used result from the Fv sequence alignment visualized based on sequence similarity calculated with BLOSUM100 method, and range from blue – 100% identity – to red – 0% identity. As already pointed out, more important differences are found in the CDR loops, not only in amino acid content, but also in their length and spatial arrangement.

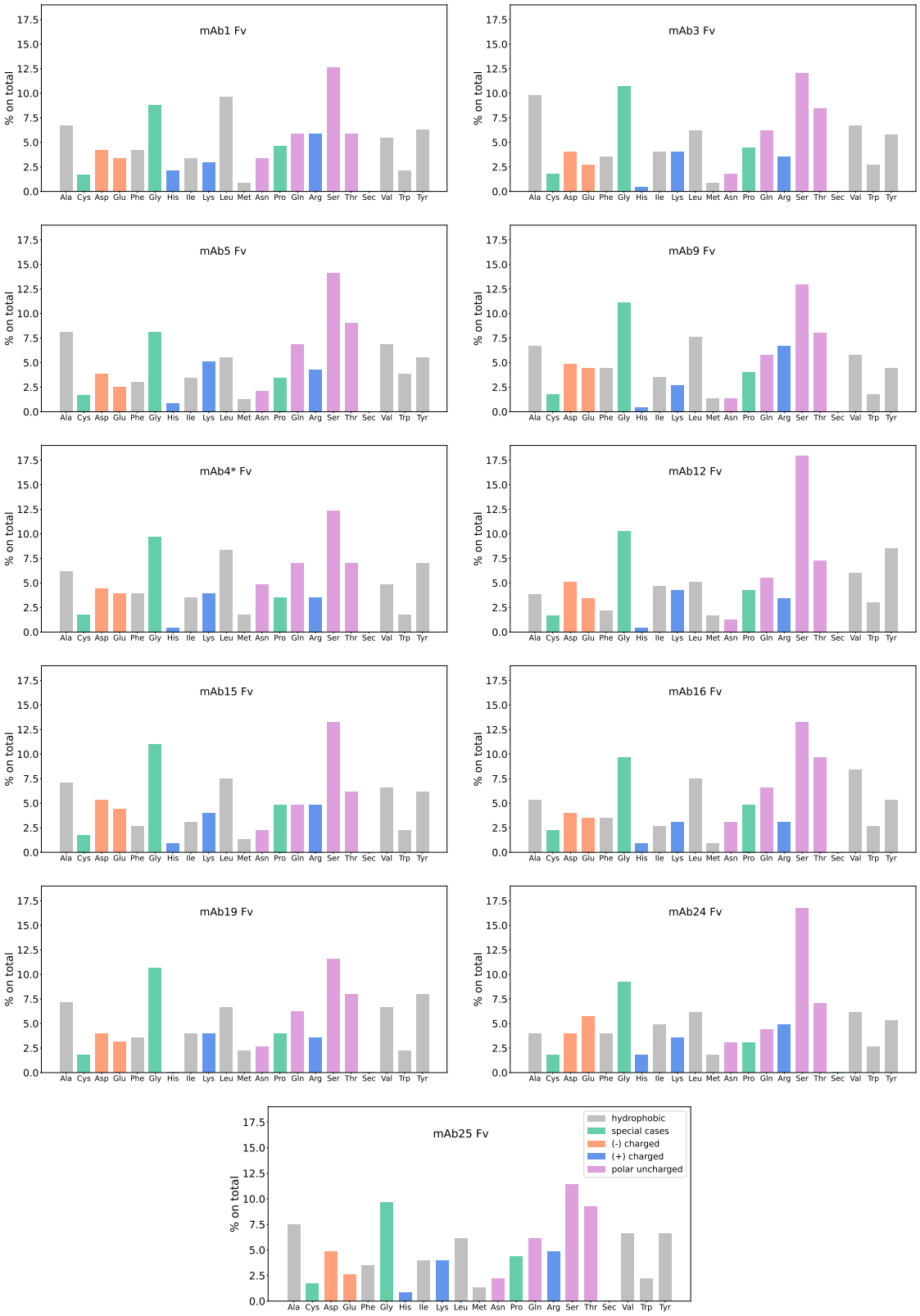

Fig. 4.8. Amino-acidic composition of the Fv of the antibodies. % value (y-axis) of all proteinogenic amino acids (x-axis) in each mAb Fv structure. Each plot refers to a single protein and the amino acids are colour-coded based on their side-chain type: grey - hydrophobic, green - special cases, orange - positively charged, blue - negatively charged, pink - polar uncharged.

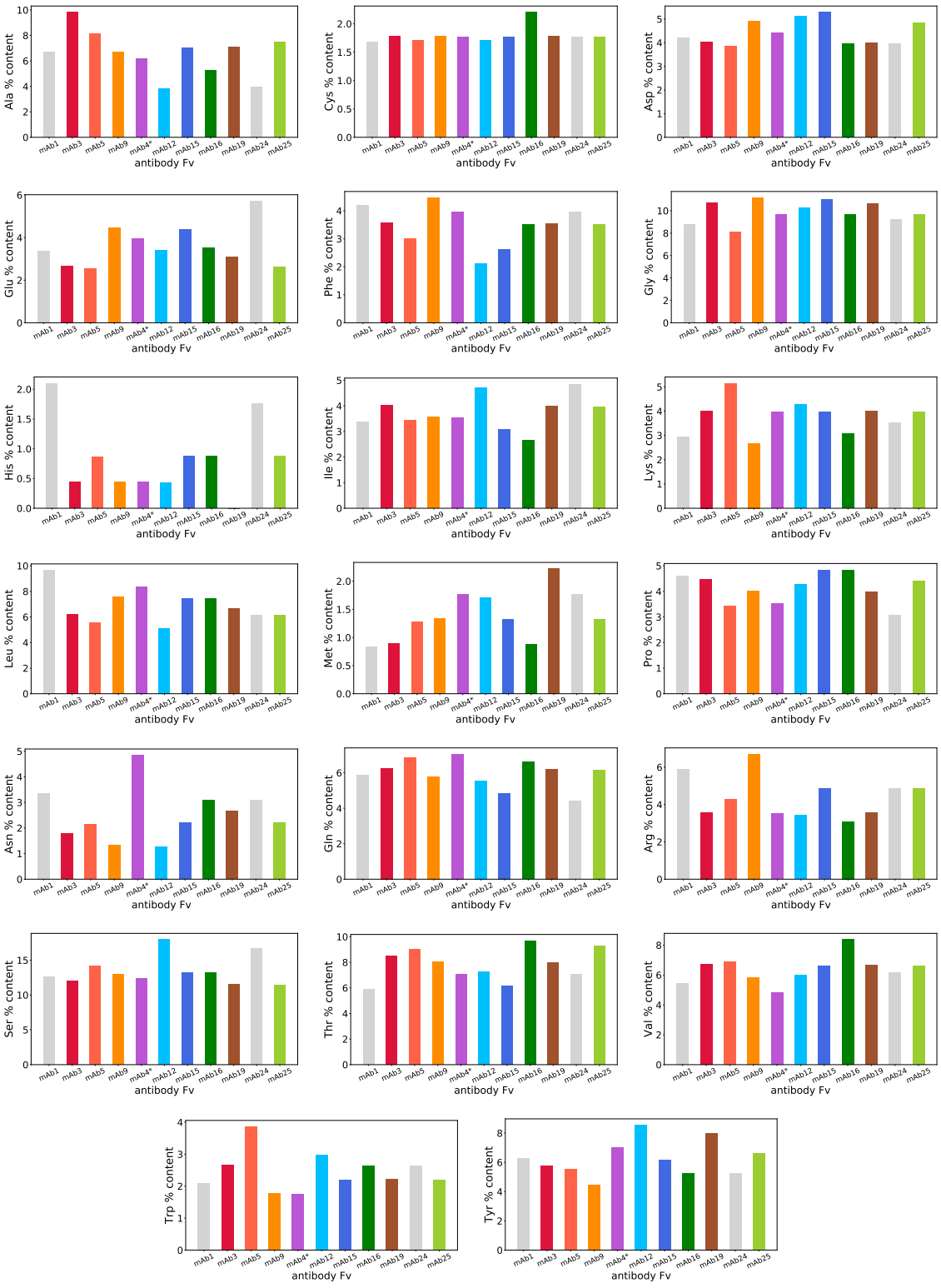

Fig. 4.9. Single-amino acid abundance in the Fv domains of the mAbs. Each plot shows the % abudance (y-axis) of a single amino acid - from alanine (Ala, top left plot) to tyrosine (Tyr, bottom right plot) - in the Fv of all antibodies (x-axis). The only amino acid not contained in any of the mAbs is selenocystein (Sec).

4.3.2 Sequence properties

In the present section, results from the antibody sequence analysis (see Sec. 4.2.1) are reported. Results arising from running Therapeutic Antibody Profiler (TAP) [339, 361] on the antibody sequences are instead shown in Table 4.3.

Table 4.1 and 4.2 report all the physico-chemical properties computed for the full chains and the variable domains, respectively. For better readability, results for the antibody full sequences and variable domains Fv are also represented in Figure 4.10 and Figure 6.17 in Chapter 6. It must be noted that full chain results are shown in the left column plots, while Fv domain ones are always in the right column. Figure 4.10 depicts the antibody molecular weights and the amount of positively/negatively charged residues on the total number. Figure 6.17 shows no significant differences among the mAbs in their aliphatic index, except for mAb12, featuring a much lower value than the others in both full sequence and Fv domain. Concerning GRAVY, all mAbs (full chains) basically report a typical value of ~ 0.4, as expected for water-soluble proteins [352]. Slight differences are found in values obtained for Fv, with mAb12, mAb24 and mAb4* exhibiting the least hydrophobic Fv in the set. It must be noted that the GRAVY values reported in Tables 4.1, 4.2 refer to the global hydrophobicity of the protein full chains or Fv domains, not accounting for the distribution of the hydrophobic residues along the sequence potentially leading to the formation of hydrophobic patches, which are particularly relevant for PPIs.

The isoelectric point pI of a biomolecule is an essential parameter to account of in biopharmaceutical developability. In the present case, the mAbs studied exhibit full chain pI ranging from ~ 6 to ~ 9 (Table 4.1), but their differences become more marked if we merely consider the Fv pI (Figure 6.17). Makowski et al. identified Fv pI as the most significant parameter to predict the viscosity behaviour of mAbs in solution, observing that all mAbs in a training set of 173 molecules exhibiting high viscosities were those featuring Fv pI ≤ 6.3 [183]. Among the mAbs studied in this work, the ones with high viscosities – mAb24 (starting from ~ 90 mg/mL), mAb12 (from ~ 120 mg/mL), mAb16 (from ~ 140 mg/mL), mAb4* and mAb15 (from ~ 170 mg/mL) – all feature Fv pI ≤ 6.3 (Table 4.2, third column), as expected [183].

Table 4.3 reports the results of the CDR prediction based on the heavy and light chains performed using SAbPred tools. The predicted CDR total length spans from 44 (mAb5, mAb9) to 59 residues (mAb1), with no evident correlation to the macroscopic viscosity of the mAbs . Overall, all the scores reported in Table 4.3 indicate good predictions for the mAbs studied in this work, meaning in the range of the values obtained for the Fv domains of the latest 754 post Phase-I therapeutic antibodies. The parameters predicted reveal remarkable differences among the CDR of the 11 mAbs, which could potentially influence their stability and propensity to self-association in solution. Starting with the CDR length, mAb1 stands out with the longest CDR at 59 residues, which may enhance its binding flexibility. In contrast, mAb3 and mAb9, with CDR lengths of 44 residues, may exhibit less conformational variability. In terms of CDR diversity, mAb12 exhibits the highest diversity score of 2.63 Å, suggesting a greater potential for structural variability of the CDR-H3 loop and, consequently, higher possibility of exposing hydrophobic patches. This property may contribute to its aggregation tendency, as confirmed by several experimental techniques employed. Conversely, mAb3 and mAb19 show lower diversity scores (0.86 Å and 0.74 Å, respectively), indicating a more stable conformation that may mitigate aggregation risks.

The scores for CDR vicinity metrics also highlight notable differences among the antibodies. For instance, mAb19 and mAb25 have the lowest CDR hydrophobicity scores, while mAb3 and mAb15 have the highest, which suggests the presence of a remarkable hydrophobic patch in their CDR. The

most viscous mAbs in solution – mAb12, mAb16, and mAb24 – all have PSH score around 130, like mAb4* and mAb9. In comparison, mAb3 and mAb5 exhibit more moderate PSH scores, suggesting a lower risk of self-association, again supported by experiments. Notably, mAb15 stands out with a PSH score of 159.5318 combined with a PPC score of 2.4303, indicating a potentially unstable charge distribution that may enhance its aggregation propensity. Further examining the PNC scores, mAb12 has a PNC score of 0.2424, while mAb4* has a lower score of 0.3316, suggesting differences in their charge distributions that may influence self-association behaviors. The structural Fv Charge Symmetry Parameter (SFvCSP) scores provide additional insight, with mAb15 showing a negative score of -0.09, indicating an imbalance in charge that could favor aggregation.

MAb24, with a CDR length of 47 residues and a diversity score of 0.62 Å, has a PSH score of 135.0241, a PPC score of 0.1978, and a PNC score of 0.0493. These characteristics suggest that while mAb24 may exhibit compactness and potentially lower charge interactions, it still possesses sufficient hydrophobic characteristics to contribute to aggregation risk.

In summary, the observed differences in CDR length, diversity, charge distribution, and hydrophobicity among the analysed mAbs significantly impact their overall stability and self-association behaviour in solution. The insights gained from this analysis underscore the importance of understanding these CDR characteristics, as they play a critical role in the development of antibody formulations for therapeutic applications. By addressing these properties, researchers can mitigate aggregation risks and enhance the solubility and efficacy of monoclonal antibodies in clinical settings.

While CDR properties can provide valuable insights into the potential for self-association, they are only part of a larger picture involving the entire antibody structure.

mAb (full chain)	**iso--type**	**light chain**	**MW [kDa]**	ε_{280} $[\mathbf{Lg^{-1}cm^{-1}}]$	**pI**	**aliph. idx**	**GRA--VY**	**arom--aticity**	**charge at pH 6**
mAb1	IgG1	κ	148.353	1.434	8.41	70.85	-0.416	0.098	28.97
mAb3	IgG1	κ	143.441	1.520	8.31	69.42	-0.362	0.095	22.94
mAb4*	IgG4	κ	144.790	1.555	6.27	67.48	-0.438	0.102	4.28
mAb5	IgG1	κ	147.001	1.299	8.71	67.20	-0.434	0.097	33.90
mAb9	IgG1	κ	144.122	1.299	8.03	68.66	-0.414	0.091	19.20
mAb12	IgG1	λ	146.460	1.781	7.79	51.89	-0.439	0.101	17.05
mAb15	IgG1	λ	143.887	1.522	7.81	67.77	-0.417	0.090	18.13
mAb16	IgG1	λ	143.751	1.555	7.47	68.44	-0.370	0.092	15.94
mAb19	IgG1	κ	144.731	1.519	8.17	68.99	-0.378	0.101	20.01
mAb24	IgG1	κ	145.610	1.476	7.19	67.88	-0.438	0.095	16.25
mAb25	IgG1	κ	145.175	1.467	8.41	69.54	-0.414	0.097	25.96

Table 4.1. Antibody full chains. Physico-chemical properties of the investigated antibodies (full chains): antibody isotype, light chain type (κ/λ), molecular weight MW, extinction coefficient at 280 nm ε_{280}, isoelectric point pI, aliphatic index, GRAVY (grand average of hydropathy), aromaticity, charge at pH 6. Calculations were performed using Biopython [371].

mAb (Fv)	MW [kDa]	pI	aliph. idx	GRAVY	aromaticity	charge at pH 6
mAb1	26.431	8.62	73.36	-0.342	0.126	5.74
mAb3	23.975	8.34	69.29	-0.179	0.120	2.73
mAb4*	25.023	5.44	66.61	-0.407	0.128	-1.18
mAb5	25.627	9.21	63.22	-0.380	0.124	8.20
mAb9	24.316	6.87	67.05	-0.333	0.107	0.863
mAb12	25.695	5.44	59.53	-0.453	0.137	-1.18
mAb15	24.583	5.74	67.44	-0.386	0.110	-0.64
mAb16	24.602	5.34	69.07	-0.25	0.114	-1.79
mAb19	24.621	7.83	68.04	-0.228	0.138	1.27
mAb24	25.103	5.83	64.8	-0.404	0.119	-0.61
mAb25	24.843	8.61	66.17	-0.335	0.123	4.24

Table 4.2. Antibody variable domains (Fvs). Physico-chemical properties of the investigated antibodies (Fv domain only): Fv molecular weight MW, isoelectric point pI, aliphatic index, GRAVY, aromaticity, charge at pH 6. Calculations were performed using Biopython [371].

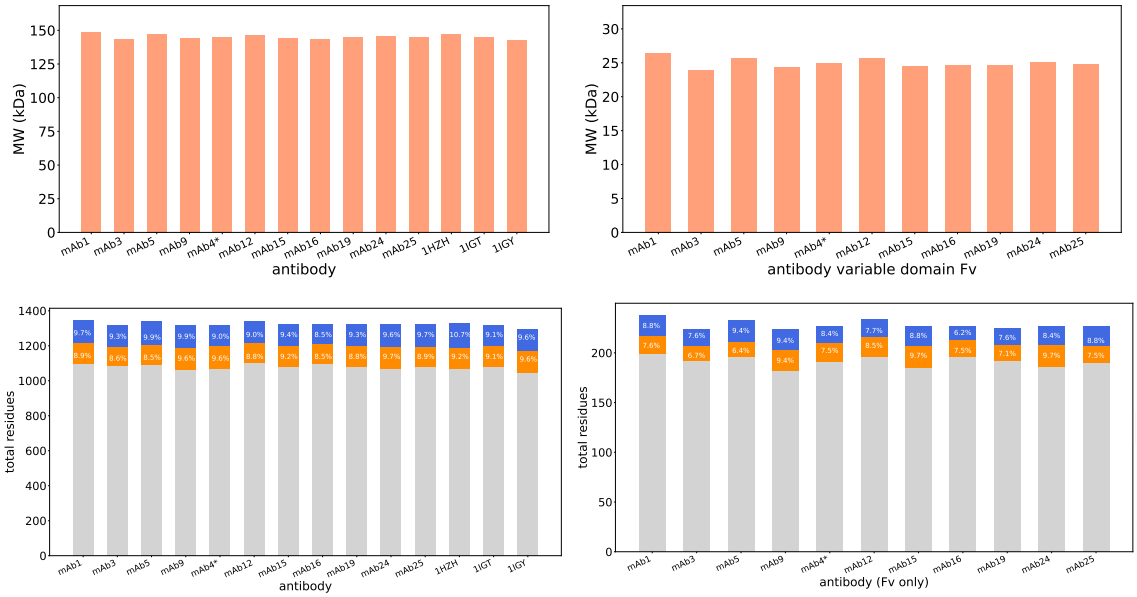

Fig. 4.10. Molecular weight MW (top line) and total number of residues of the antibodies (bottom line), also showing the number of positively charged, negatively charged and non-charged amino acids (in blue, orange and grey, respectively). For the charged residues, their percentages on the total are also reported. Plots on the left refer to the full chains of the molecules, while the right column depicts the same parameters for the antibody Fv.

mAb	CDR length	CDR diversity score [Å]	CDR vicinity PSH score	CDR vicinity PPC score	CDR vicinity PNC score	SFvCSP score
mAb1 (κ)	59	2.04	143.89	0.1185	0.1271	3.4
mAb3 (κ)	44	0.86	152.5569	0.0076	0.0464	6.3
mAb4* (κ)	47	0.82	132.511	0.103	0.3316	0.0
mAb5 (κ)	54	1.34	134.8611	0.0419	0.0	10.0
mAb9 (κ)	44	0.86	132.1588	0.2347	0.346	-11.6
mAb12 (λ)	53	2.63	138.8106	0.0385	0.2424	6.0
mAb15 (λ)	49	1.09	159.5318	2.4303	2.5495	-0.09
mAb16 (λ)	49	1.33	139.7167	1.2984	0.1034	0.0
mAb19 (κ)	45	0.74	117.9533	0.0	0.0521	0.0
mAb24 (κ)	47	0.62	135.0241	0.1978	0.0493	-0.18
mAb25 (κ)	47	0.75	113.3143	0.2412	0.0865	9.0

Table 4.3. Results of the CDR prediction based on the antibody heavy and light chains performed using SAbPred tools. The parameter shown in the third column is the CDR diversity score calculated from ABlooper [360], defined as the RMSD of alignment to crystal structure. This parameter has been benchmarked on a test dataset of over 100 antibody VH/VL paired sequences and it refers to the CDR-H3 loop prediction, due to its higher variability compared to the other CDR loops. Scores ≤ 1.25 Å indicate a quite good CDR prediction, while values ≥ 2 Å a less accurate one. The other columns report further CDR parameters computer using TAP, the 'Therapeutic Antibody Profiler' [339, 361]; in the second column there is the CDR length (in no. of amino acids), while in the others vicinity scores of the CDR region in different metrics can be found. The metrics taken into account are the following: PSH = Patches of Surface Hydrophobicity, PPC = Patches of Positive Charge, PNC = Patches of Negative Charge, SFvCSP = Structural Fv Charge Symmetry Parameter. The colour assigned to the values is based on where each antibody sits within the five TAP metric distributions of the latest set of 754 post Phase-I therapeutic Fv domains. For further details, see main text and Ref. [339].

Chapter 5

Biophysical determinants for the viscosity of monoclonal antibody solutions

Chapter 5 is based on the following publication:

Biophysical determinants for the viscosity of monoclonal antibody solutions

Molecular Pharmaceutics **2023**, 20 (9), 4698-4713, Ref. [194]

Authors: Ilaria Mosca[1,2], Kévin Pounot[1,2,**], Christian Beck[1,2], Louise Colin[1,2], Olga Matsarskaia[2], Christoph Grapentin[3], Tilo Seydel[2], and Frank Schreiber[1]

[1] *Institut für Angewandte Physik, Universität Tübingen*, Germany
[2] *Institut Max von Laue - Paul Langevin*, Grenoble, France
[3] *Lonza AG/Ltd.*, Basel, Switzerland
[**] current address: *European Synchrotron Radiation Facility*, Grenoble, France

Author contribution: All authors performed experiments, contributed to data analysis and in writing the manuscript. K. P. performed simulations, L. C., K. P., C. B. prepared the samples. F. S., T. S., O. M. and C. G. designed the research and are co-proposers and supervisors of the associated InnovaXN project (innovaxn.eu).

Experiments: Data presented in this chapter were collected during ILL experiments 8-04-908 and 8-04-923.

Abstract

Monoclonal antibodies (mAbs) are particularly relevant for therapeutics due to their high specificity and versatility and mAb-based drugs are hence used to treat numerous diseases. The increased patient compliance of self-administration motivates the formulation of products for subcutaneous (SC) administration. The challenge associated with is to formulate highly concentrated antibody solutions to achieve a significant therapeutic effect, while limiting their viscosity and preserving their physicochemical stability. Protein-protein interactions (PPIs) are in fact the root cause of several potential problems concerning the stability, manufacturability and delivery of a drug product. The understanding of macroscopic viscosity requires an in-depth knowledge on protein diffusion, PPIs and self-association/aggregation. Here, we study the self-diffusion of different mAbs of the IgG1 subtype in aqueous solution as a function of concentration and temperature by quasi-elastic neutron scattering (QENS). QENS allows to probe the short-time self-diffusion of the molecules and therefore to determine the hydrodynamic mAb cluster size and to gain information on the internal mAb dynamics. Small angle neutron scattering (SANS) is jointly employed to probe structural details and to understand the nature and the intensity of PPIs. Complementary information is provided by molecular dynamics (MD) simulations and viscometry measurements, thus obtaining a comprehensive picture of mAb diffusion.

5.1 Introduction

Since the development of the hybridoma technology by Köhler and Milstein [69], monoclonal antibodies (mAbs) made their way to therapeutic applications with 10 mAbs approved by the FDA in 2001 [372] to 100 mAbs in 2021 [373], and 153 in 2022 (among which 59 were approved for cancer therapy) [374]. The transition from mouse antibodies, to chimeric and eventually human antibodies [372] has led to a drastically reduced immune reaction, and has driven the recent increase in the number of mAbs in use or under development. The actual and potential clinical applications of mAbs cover a wide range of diseases [375], including cancers [74], infectious and autoimmune diseases (such as rheumatoid arthritis and Crohn's disease) [77,78] and multiple sclerosis [79]. The most employed type of mAb for therapeutic use is immunoglobulin G (IgG), which is a Y-shaped molecule of ≈ 150 kDa. The four main types of IgGs - IgG1, IgG2, IgG3 and IgG4 - show very similar structures and amino acid sequences (90% of identity). They differ in their relative abundance in the serum, their affinity with different types of antigens and receptors and their half-life [376]. IgGs consist of four polypeptide chains, two heavy chains of ≈ 50 kDa each and two light chains of ≈ 25 kDa each, cross-linked by disulphide bonds. Heavy chains contain a variable domain (VH) and three constant domains (CH1, CH2 and CH3), with a flexible hinge region between CH1 and CH2; light chains contain a variable domain (VL) and a constant domain (CL) [379], [380]. The segments CH1, VH, CL and VL form the "fragment antigen binding" (Fab) region, while the CH2 and CH3 domains form the "fragment crystallizable" (Fc) region (Figure 5.1). While polyclonal antibodies are usually produced by several different plasma cell lineages and bind to multiple epitopes, monoclonal antibodies result from the cloning of a unique cell and thus bind only a single epitope [66]. This feature gives mAbs high specificity and high affinity due to the complementarity determining region (CDR) within the Fab, whose shape complements the one of the corresponding antigen. The Fc region of mAbs instead allows to reduce side-effects and toxicity compared to polyclonal antibody solutions [375]. In addition, their half-life can extend to a month after injection thanks to the binding to the neonatal Fc receptor. How-

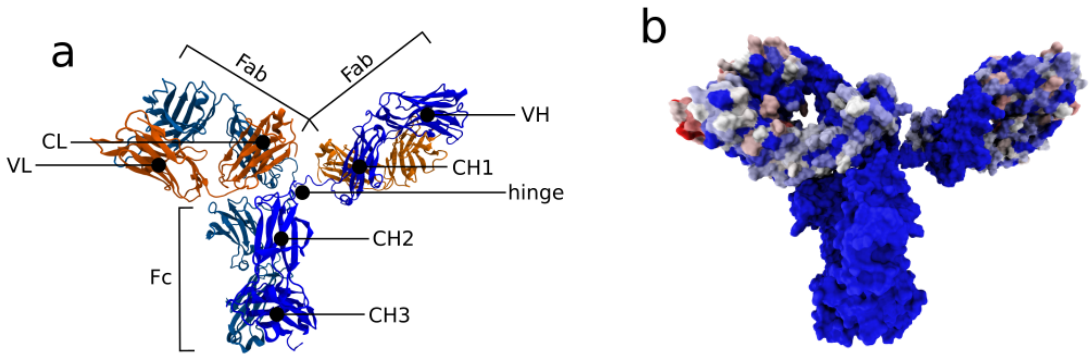

Fig. 5.1. Structure of the mAbs and sequence similarity between the mAbs . **(a)** The structure of mAb1 was used to represent the mAb using Visual Molecular Dynamics (VMD) [377]. The different regions of the mAb are annotated on the structure represented using the 'NewCartoon' style. The heavy chains are represented in shades of blue and the light chains in shades of orange. **(b)** The sequences of the mAb variants were aligned using the VMD 'MultiSeq' module [378] and the sequence similarity obtained with the BLOSUM100 matrix is represented with a colour range from blue for high similarity to red for low similarity. The different mAbs under study show almost identical structures in the Fc region, while they differ in the extremal parts of the Fab regions (CDR), namely the ones involved in the binding with the specific antigen.

ever, their size prevents them from entering cells and crossing the blood-brain barrier. In addition, oral administration results in rapid degradation of the mAbs and limited bioavailability [381], thus limiting their administration to parenteral routes, namely intravenous (IV), intramuscular (IM) or subcutaneous (SC) injections. Some diseases require life long treatment; if the drugs are administered via IV, patients need to see a doctor or go to a hospital to receive their medication, which can compromise patient compliance. For this reason, mAb delivery via SC injection has recently become a market interest in pharmaceutics, since no skilled personnel is required for drug administration, thus enabling patients to benefit from self-administration and more flexibility, and also ensuring lower healthcare costs [88].

The amount of mAb required to ensure a significant therapeutic effect (typically hundreds of mg) and the typically low injection volume in subcutaneous administration (0.5-2 mL) imply the use of highly concentrated mAb solutions of mAbs, which can exhibit high viscosities [94]. This potentially affects the stability, manufacturability, and delivery of these biopharmaceuticals [96,97]. The dynamic viscosity of highly concentrated mAb formulations can easily exceed the tolerance threshold for injectability ($\sim$ 15-20 mPa·s) [93] and render their administration difficult or impossible for patients and some injection devices due to the high forces required [88,95]. Extensive research aiming to minimize the viscosity of highly concentrated mAb solutions is ongoing [94], along with several studies on the optimization of physico-chemical solution stability and manufacturability [98,99].

The presence of reversible self-association was proposed as the main mechanism determining viscosity changes in the works by Kanai et al. [101] and Liu et al. [100]. Self-association and hence viscosity of highly concentrated mAb solutions can be influenced by multiple parameters, including concentration, pH, ionic strength [100], or specific interactions, like charge-dipole or dipole-dipole, between domains of monomers [102, 103]. Charged molecules such as NaCl or Arginine-HCl can shield protein charges, thus reducing protein-protein-interactions and thereby viscosity [382]. Although electrostatic interactions seem to dominate in driving reversible self-association, hydropho-

bic interactions also play a key role [104] and therefore have impact on the solution viscosity. Arginine can also shield antibody hydrophobic interactions [129], enhancing its viscosity-reducing function. Other excipients with analogous effects are caffeine [135], hydrophobic salts [134], or amino acid derivatives [136], but they are not yet employed in commercialized drug products. Addition of viscosity-reducing pharmaceutical excipients to mAb formulations is indeed a common practice and also the subject of continuous research [138–140].

More recent work involving experiments and coarse-grained simulations paved the way to viscosity predictors based on amino acid sequence and structural properties of the Fv region [383, 384]. Apgar and coworkers applied the same approach optimizing the charge distribution and hydrophobicity in the variable region (VH and VL) to successfully reduce the viscosity of a mAb solution while preserving its stability and its affinity for the antigen [385].

Schmitt et al. recently presented a predictive modeling approach for viscosity employing artificial neural networks and based on both experimental and simulation-derived parameters and viscosity data from 27 highly concentrated mAbs [184], showing that sequence-based optimization of mAb properties is a powerful method for rational mAb design. In addition, recent studies have successfully investigated the link between viscosity and cluster formation using small-angle X-ray scattering, microrheology and coarse-grained simulations and used cluster theory to predict structure factors of highly concentrated mAb solutions [171, 172]. The same systems have also been investigated using again SAXS, viscometry, static and dynamic light scattering, in combination with other analytical techniques [173] and also coarse-grained modeling [174]. In general, computational approaches, such as coarse-grained and atomistic modeling, hydrodynamic calculations and ML based methods, seem to successfully predict viscosity, inter-molecular interactions, aggregation and physical instabilities in highly concentrated mAb solutions [386–390].

Polyclonal antibody solutions have also been widely investigated with SAXS [391], XPCS [392], QENS and NSE [273], establishing a quite robust framework for the research on monoclonal antibody solutions. In this area, neutron scattering techniques have already been successfully used [236] to fully understand the link between macroscopic and microscopic phenomena. For example, neutron reflectometry has been widely employed to study adsorption of mAbs on hydrophobic surfaces, which typically leads to protein aggregation and degradation [216,393]. Neutron spin-echo and small-angle neutron scattering experiments have identified the formation of dynamic clusters of proteins (including antibodies) in concentrated solutions [229, 234].

In this context, the self-association or cluster formation of mAbs in aqueous solution can be reliably obtained via the self-diffusion of these clusters measured by high-resolution quasi-elastic neutron spectroscopy (QENS) probing the spatially incoherent scattering and, thus, ensemble-averaged single-particle self-correlation of the mAb hydrogen ^{1}H atoms. This self-diffusion unambiguously informs on the hydrodynamic size of the clusters via the Stokes-Einstein relation. In concentrated solutions of protonated (^{1}H) proteins in D_2O (^{2}H), the signal from the proteins dominates over the solvent signal in the neutron scattering experiment.

Here, we comprehensively study a set of 5 different mAbs in terms of this cluster size which is accessed via their self-diffusion at different temperatures and concentrations in solution, the associated macroscopic viscosity of these solutions, and, for selected samples, their solution structure and protein-protein interactions by small-angle neutron scattering (SANS). Moreover, we perform fully atomistic molecular dynamics (MD) simulations to identify possible determinants for the experimentally observed behaviour in the sequence of the mAbs . Simultaneously, we also obtain information on the internal diffusive dynamics of these mAbs on the level of protein backbone and side-chain

fluctuations from both simulations and QENS spectra. Thus, we associate the macroscopic properties with several microscopic properties in the pursuit to enhance the understanding required for rational design of high-concentration, low-viscosity mAb formulations. Resulting from the energy resolution of the QENS experiment, the diffusion of the proteins is observed during the coherence time of a few nanoseconds. On this time scale, protein-protein collisions can be neglected, and the observed center-of-mass diffusion corresponds to the so-called short-time diffusion, which is governed by hydrodynamic and electrostatic interactions [34].

5.2 Materials and methods

5.2.1 Sample preparation

We employed 5 different monoclonal antibodies of IgG1 isotype with κ and λ light chains, with molecular weight (MW) ranging from approximately 145 to 148 kDa and different isoelectric points (pI) ranging from 7.2 to 8.4 (see Table 5.2 in section 5.5). In this work, we denote these antibodies mAb1, mAb9, mAb12, mAb16 and mAb24, consistent with previous work on the same proteins [184]. All mAbs were manufactured in-house at Lonza AG/Ltd. double gene vectors (DGV) containing the heavy and light chains were transfected into chinese hamster ovary (CHO) K1SV glutamine synthetase knockout (GS-KO) cells [394] from Lonza Biologics (Slough, UK) and cultured under selection conditions as stable pooled cultures. Clarified supernatant was obtained by centrifugation followed by filter sterilization using 0.22 µm filters Stericup® Quick Release from Merck/MilliporeSigma (Darmstadt, DE) and Protein A chromatography was used for mAb purification. Size exclusion-high-performance liquid chromatography (SE-HPLC) showed that all mAbs were $> 96\%$ monomers, with small amounts of aggregates and fragments. All proteins were concentrated to final concentration of 10 mg/mL (nominal) and buffer exchanged into the formulation buffer by tangential flow filtration. A 20 mM histidine-HCl buffer at pH 6.0 was employed as for most ($> 80\%$) formulations of highly concentrated approved mAb drug products [348]. All mAb solutions were then frozen in aliquots, stored at $-80°$C and slowly thawed prior to use.

For QENS and SANS samples, molecules were buffer-exchanged into 20 mM Histidine in pure D_2O at pD 6.0, using 3 mL dialysis cassettes containing cellulose membranes with 30 kDa nominal molecular weight cutoff from ThermoFisher Scientific (Waltham, MA, USA). Two baths of at least 2 hours were performed to obtain a dilution factor of at least 10^4 of residual H_2O in the samples. We remark that exchanging the buffer from H_2O to D_2O is an essential step in neutron experimental techniques, because it enables to measure proteins in their aqueous environment while minimizing the scattering signal from the surrounding solvent. Subsequently, the samples were concentrated using 15 mL 30 kDa MWCO Amicon®-Ultra concentrators from Merck/MilliporeSigma until the volume needed for the QENS experiment ($\sim$ 800 µL) was reached. Final concentrations of the samples were determined via UV-Vis spectroscopy on dilution series of each mAb using a Jasco V-630 Spectrophotometer. For each dilution step, absorbance curves were collected and their peak values at 280 nm were plotted against the sample reciprocal dilution factor. The data obtained were therefore fitted using the Lambert-Beer law, which links the absorbance A of the sample to its concentration c via $A = \varepsilon\, c\, \ell$, with ℓ being the optical path-length, i.e., the thickness of the cuvette, and ε the sample extinction coefficient. The determined concentrations were (76.53 ± 2.59) mg/mL for mAb1, (54.44 ± 1.82), (64.34 ± 4.60) and (80.12 ± 3.65) mg/mL for mAb9, (76.12 ± 3.15) mg/mL for mAb12, (80.44 ± 4.79) mg/mL for mAb16 and (45.38 ± 1.52) mg/mL for mAb24.

For reference, samples of polyclonal IgG solutions were prepared employing lyophilized powder of γ-globulin from bovine serum ($\geq 95\%$ purity, essentially salt-free), purchased from Merck/MilliporeSigma (Darmstadt, DE) and directly dissolved in a 20mM Histidine-HCl D_2O buffer at pD 6.0. The desired concentrations for these samples were reached and verified via UV-Vis using a Nanodrop One© Spectrophotometer from ThermoScientific, obtaining three samples at c_p = 60, 140, 180 mg/mL, respectively.

5.2.2 Quasi-elastic neutron backscattering spectroscopy

Quasi-elastic neutron scattering (QENS) accesses molecular dynamics on time and length scales commensurate with the motions of individual proteins and their domains and side chains.

The experiments were performed at the spectrometer IN16B at the Institut Max von Laue - Paul Langevin (ILL), Grenoble, France. This instrument provides an energy resolution of 0.8 μeV and an energy transfer range of $\pm$30 μeV, allowing the investigation of motions on a timescale of approximately 100 ps to 10 ns [315]. IN16B was used with Si(111) monochromator and analyser crystals, corresponding to an elastic wavelength of 6.27 Å. A linear motor Doppler drive carrying the monochromator was used to define the energy transfer. The samples were put into double-walled cylindrical aluminum cans with a 0.15 mm gap and an outer diameter of 23 mm, sealed with indium wire, and mounted in a standard cryofurnace for temperature control during the data acquisition. The QENS signal was integrated for 4 hours for each sample at each temperature. The QENS data are curated under DOI 10.5291/ILL-DATA.8-04-908 [395]. The data were processed with Mantid [396] applying standard reduction including monitor normalization and empty can subtraction, and subsequently fitted using python employing *scipy.optimize.curve_fit* [397]. The observable in neutron spectroscopy is the dynamic structure factor $S(q,\omega)$ depending on the energy transfer $\hbar\omega$ and momentum transfer $\hbar q$. IN16B spans a q-range from 0.2 to 1.9 Å^{-1}, corresponding to lengths from 3 to 30 Å. S is the sum of the scattering contributions from the aqueous (D_2O) solution and the antibodies. The latter consists of the contributions from the global and internal diffusion of the proteins. The superposition of these contributions is convoluted with the spectrometer resolution function $R(q,\omega)$ obtained from a Vanadium calibration measurement. The experimental data were fitted by [306]

$$S(q,\omega) = R(q,\omega) \otimes \left\{ \beta(q) \left[A_0(q)\, \mathcal{L}(\gamma(q),\omega) + (1 - A_0(q))\, \mathcal{L}(\gamma(q) + \Gamma(q),\omega) \right] + \beta_{D_2O}(q)\, \mathcal{L}(\gamma_{D_2O}(q),\omega) \right\}, \tag{5.1}$$

where $R(q,\omega)$ is the resolution function, $\beta(q)$ and $A_0(q)$ are q-dependent scalars, where the latter is identified with the elastic incoherent structure factor (EISF). The parameters $\beta_{D_2O}(q)$ and $\gamma_{D_2O}(q)$ were fixed based on measurements of the pure solvent, accounting for the solvent volume excluded by the proteins in $\beta_{D_2O}(q)$. Each contribution to $S(q,\omega)$ accounts for a diffusive motion and, thus, is a Lorentzian function $\mathcal{L}(\Gamma,\omega) = \Gamma/(\omega^2 + \Gamma^2)$, whose width provides the associated relaxation rate. $\mathcal{L}(\gamma(q),\omega)$ is the Lorentzian connected to the self-diffusion of the protein center of mass, $\mathcal{L}(\gamma(q) + \Gamma(q),\omega)$ describes the internal diffusive motions and $\mathcal{L}(\gamma_{D_2O}(q),\omega)$ is the signal from the deuterated buffer solution. Samples at $c_p \leq 50$ mg/mL were fitted accounting for just two Lorentzian functions (center of mass and solvent diffusion), due to their lower signal potentially causing overfitting if using equation 5.1. All samples were prepared in D_2O solutions to reduce the signal from the solvent relative to the protein signal, due to the large difference of the incoherent neutron scattering cross sections of hydrogen ^{1}H and deuterium ^{2}H.

A two-step approach was used for fitting. First, by q-wise fits, scalar fit parameters were fitted

independently for each q. From this procedure we observe that the center-of-mass dynamics follows a Fickian-type diffusion as expected and found previously [306], meaning that the width γ of the center of mass Lorentzian is

$$\gamma(q) = D\,q^2 \tag{5.2}$$

where D is the apparent global diffusion coefficient. From a physical point of view, this means that the center of mass exhibits continuous diffusion. Second, global fits were performed by imposing the q-dependence of some parameters to render the fit more robust and include knowledge on the systems from the q-wise fits, as established in previous works [34, 306, 307, 398]. One approach was to impose a Fickian center of mass diffusion (equation 5.2) without imposing any q-dependence of the internal diffusion. A q-dependence on the initial guess for the internal dynamics parameters was, however, included, by following the so-called jump-diffusion model [253]

$$\Gamma(q) = \frac{D_{\mathrm{int}}\,q^2}{1 + D_{\mathrm{int}}\,\tau\,q^2}\ , \tag{5.3}$$

where D_{int} and τ respectively represent the diffusion coefficient related to the internal dynamics and the average residence time in the state of oscillatory motions. A prior knowledge from the q-wise fit was also exploited in the EISF $A_0(q)$, which was parameterised in the global fits as [307, 308, 399]

$$A_0(q) = p_0 + (1 - p_0)\,[p_1\,A_{\mathrm{3jump}}(q) + (1 - p_1)\,A_{\mathrm{sphere}}(q)]\,, \tag{5.4}$$

i.e., by a superposition of a component accounting for orientational jumps among three sites equally distributed on a circle and placed at distance a one from another,

$$A_{\mathrm{3jump}}(q) = \frac{1}{3[1 + 2\,j_0(qa)]}, \tag{5.5}$$

and a contribution from diffusion confined in a spherical volume with radius R,

$$A_{\mathrm{sphere}}(q) = \left|\frac{3j_1(qR)}{qR}\right|^2, \tag{5.6}$$

where $j_0 = \sin(x)/x$ and $j_1(x) = \sin(x)/x^2 - \cos(x)/x$ denote the spherical Bessel functions of the zeroth and first order, respectively. p_0 (equation 5.4) is the fraction of hydrogen atoms that appear immobile on the timescale explored by the instrument (elastic contribution), while $(1 - p_0)$ is the fraction of mobile H atoms. In this picture, the coefficients p_1 and $(1 - p_1)$ respectively represent the fraction of H atoms undergoing jump-diffusion among three sites and diffusion confined in a sphere. The first class of H atoms accounts for methyl groups, the reorientations of which are described by equation 5.5 with the fixed jump distance a = 1.715 Å. In this interpretation, H atoms jump between three sites at an angular distance of $120°$. The second class of H atoms, namely those undergoing diffusion inside a sphere (equation 5.6), accounts for the protein backbone, with R being a free fit parameter. The q-dependent scalar $\beta(q)$ in equation 5.1 accounts for the thermal Debye-Waller factor due to vibrational motions of hydrogen atoms:

$$\beta(q) \propto \exp\left(-\frac{1}{3}\left\langle r^2\right\rangle q^2\right), \tag{5.7}$$

with $\left\langle r^2\right\rangle$ being the corresponding MSD.

5.2.3 Small-angle neutron scattering (SANS)

Small-angle neutron scattering (SANS) was performed on a subset of the antibodies, namely mAb9, mAb12 and mAb24, in order to determine their time-averaged structural and thermodynamical properties as a function of temperature and protein type. The SANS experiments were carried out on D11 [400] at the ILL. MAb samples at 80 mg/mL each were filled into 1 mm round quartz cuvettes (Hellma, Mülheim, Germany) and placed onto a copper sample holder. A q range from 0.006 - 0.7 Å^{-1} was covered by two sample-to-detector distances (16 and 1.7 m) with respective collimation lengths of 16.5 and 2.5 m. A wavelength of 4.6 Å with a FWHM wavelength spread of 9 $\%$ was used. Scattered neutrons were detected using a multitube ^{3}He gas detector with a pixel size of 4 × 8 mm^2. Raw data were saved in the .nxs (NeXuS) format [401, 402]. Data reduction was performed using Mantid [396]. All data were corrected for empty cell scattering, transmission (by measurements performed using beam attenuators) and electronic noise (by measuring a $^{10}B_4C$ absorber). Calibration to absolute scale was performed using attenuated direct beam measurements. Scattering of the solvent (20 mM His-HCl deuterated buffer at pD 6.0) was subtracted from sample scattering. The SANS data are curated under DOI 10.5291/ILL-DATA.8-04-923 [403].

5.2.4 Viscometry

All mAb samples were characterised by viscometry as reported in Schmitt et al. [184]. They were measured at $T = 25°\text{C}$ (~ 298 K) in their original 20 mM His-HCl aqueous buffer at pH 6.0. In addition, a subset of the antibodies (mAb9, mAb12, mAb16 and polyclonal IgG) was measured in the corresponding deuterated buffer at the same nominal concentrations at 7, 22 and 37°C (280, 295 and 310 K), to collect complementary information on viscosity for the conditions studied in neutron experiments. The procedure used for preparation is the same as the one described for QENS and SANS samples in 5.2.1, with dilutions from 180 to 30 mg/mL. The employed apparatus was a Rheosense VROC® Initium rheometer (San Ramon, CA, USA) equipped with a B05 chip and operating using VROC® (Viscometer/Rheometer-on-a-Chip) technology [363]. A medical grade viscosity standard from Paragon Scientific (ISO 17025 & 17034), reporting a dynamic viscosity of 9.994 mPas and a density of 1.1567 g/mL at 25°C, was used for the SST. The protocol consisted in measuring the dynamic viscosity of each sample ten times at 25°C whilst applying an automatic shear rate, which is determined by the instrument software in order to induce a pressure inside the chip targeting the 50% of the full instrumental range [184].

5.2.5 Sample characterization by DLS, SLS, and HIC

Dynamic light scattering (DLS), SLS and hydrophobic interaction column (HIC) measurements were carried out by Schmitt et al. [184] and these data were used as inputs for the simulations.

5.2.6 MD simulations

Single-molecule simulations and analysis

The PDB files for the different mAbs available internally at Lonza were employed to run single-molecule simulations using NAMD [404] with the CHARMM36 force field [405], [406]. For each antibody, the starting condition was to place a single monomer in a box with explicit water (TIP3 model [407]) using the solvate plugin of VMD [377] with a padding distance of 25 Å. The system

was neutralized (every charge having a counter-charge) using Na^+ and Cl^- ions to avoid electrostatic artifacts during the simulation using the autoionize plugin of VMD [377]. The pressure was maintained at 1 atm using the Nosé-Hoover Langevin piston algorithm [408], [409] and the temperature controlled using Langevin dynamics. All bonds were constrained with the SHAKE algorithm [409]. The integration of the equation of motions was performed using the Verlet-I/r-RESPA algorithm [410], [411] with integration time of 2, 2 and 4 fs for the short-range bonded and non-bonded forces and long-range forces, respectively. The electrostatic interactions were computed using the Ewald summation method [412], [413] with a smooth switching function between 12 and 14 Å. The 5 systems, mAb1, mAb9, mAb12, mAb16 and mAb24, were equilibrated at 300 K in the NVT (N = number of atoms, V = volume, T = temperature) ensemble for 2 ns to remove any bad contacts that may occur during model building. The NPT (P = pressure) ensemble was then used for 60 ns equilibration at 300 K. The production runs were performed for 120 ns in the NVT ensemble to match the experimental conditions where V and T are fixed.

The features (MSD, angles between the lobes) were computed using the block average method [414]. Briefly, the simulation trajectory is divided into blocks of increasing size. For each block at a given size, the observable and its standard deviation between the blocks are computed. The standard deviation is expected to reach a plateau value when the sampling is sufficient for the computed observable [414] (Figure S4). The minimum block size is defined when the standard deviation reaches the plateau and that block size is used for calculating the variable average and standard deviation. Using this block average method, the large scale motions of the lobes are computed by taking the scalar product of the normalized position vectors shown in Figure S4 to extract the angles. Subsequently, for different time origins, the deviation of the angle from the initial value is computed. The result is averaged over the blocks and the standard deviation between the blocks is extracted. The MSD is obtained as

$$MSD = \langle u^2 \rangle = \frac{1}{N} \sum_{i}^{N} \langle ||\vec{r_i}(t_0 + \Delta t) - \vec{r_i}(t_0)||^2 \rangle, \tag{5.8}$$

where $\vec{r_i}(t)$ is the position vector of atom i at time t and the angular brackets denote the average over multiple time origins.

Feature extraction from the structure and the sequence.

To obtain the charge at pH 6, a protein structure file in the .pqr format was generated using $pdb2pqr$ [415] along with $propKa$ [416] to assign the expected protonation states. The charge of the different protein domains is then extracted by summing the charge of the atoms pertaining to a given domain. The other features, namely pI, GRAVY index and aromaticity were obtained using the BioPython [371] package.

Simulations at high concentration, computed SANS profiles.

The system was constructed by randomly placing 6 monomers into a simulation box using the VMD [377] tcl script. The preparation of the system and the simulations were performed using a modified GROMACS [417,418] package (GROMACS-SWAXS [419]) designed for interfacing with experimental small-angle scattering data. As above, the CHARMM36 force field was used, the proteins were solvated using TIP3P water and the system was neutralized with NaCl using GROMACS command-line tools. The 10 ns equilibration and the 200 ns simulation runs were performed using the same algorithms cited above. The computed SANS curves were obtained by averaging 100 frames on the last 20

ns of simulation for mAb9, mAb12 and mAb24. An envelope at a distance of 0.7 nm from the protein surface was used. Further analysis of protein contacts network and hydrogen bonds was conducted using the MDAnalysis package [420,421]. Protein network graphs were generated by finding the minimum distance between each pair of monomers for each frame in the simulation. Subsequently, all pairs for which the minimum distance was lower or equal to 5 Åwere registered as interacting for the frame concerned. Among these interacting pairs, only the ones whose interactions were lasting for more than 1 ns were kept and used to produce the protein network graphs 5.10. The number of times a given pair is involved in an interaction throughout the simulation was used as a weighing factor to draw the graphs, where a higher number of times is represented by a thicker black line. Graphs were generated and clustering coefficients obtained using the NetworkX Python package [422].

5.3 Results and discussion

5.3.1 Viscometry

The viscosity was analysed depending on antibody concentration c_p and volume fraction φ (Figure 5.2). φ is calculated from the protein concentration c_p as $\varphi = c_p V_s$, assuming the specific volume $V_s = 0.739$ mL/g [307]. An increase in the viscosity of the solutions at increasing antibody concentra-

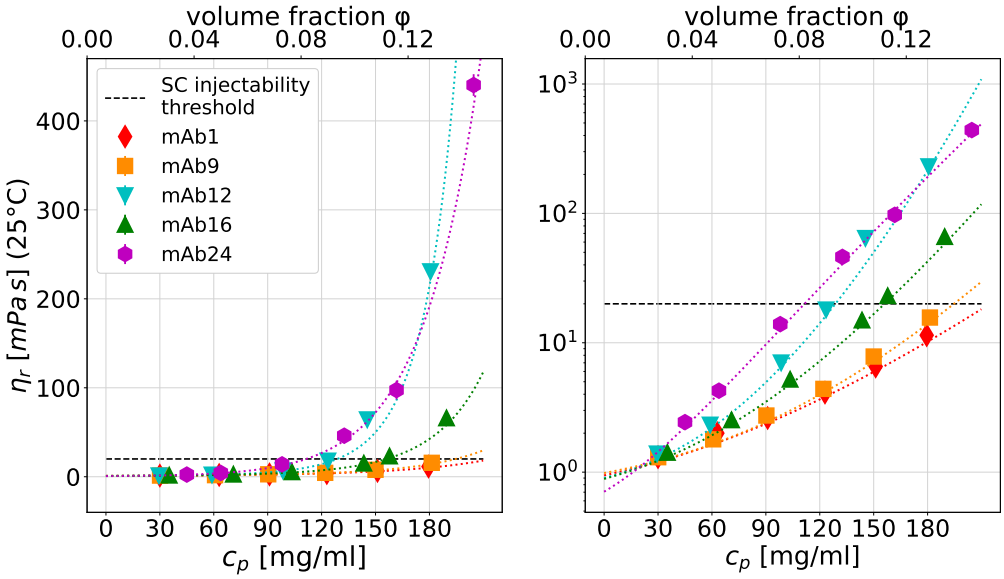

Fig. 5.2. Linear (left) and logarithmic (right) plots showing the relative viscosity $\eta_r = \eta/\eta_0$ (symbols) of aqueous (H_2O) solutions of different mAbs of the IgG1 subtype produced and characterised at Lonza, in 20 mM Histidine-HCl buffer at pH 6.0, at $T = 25°C$ ($\approx$ 298 K), versus mAb concentration c_p (lower x-axis) and volume fraction φ (upper x-axis), from dynamic viscosity measurements using a Rheosense VROC® Initium rheometer. Dotted lines are fits to the data using equation (5.9). The black dashed line represents the typically defined viscosity threshold for syringeability ($\sim$ 15-20 mPa·s used in this work as guidance value, but in practical terms depending on volume, syringe, needle, acceptable injection force). The strong dependence of the viscosity on the mAbs , in spite of them only differing in the CDR (Figure 5.1), underlines the need of understanding its microscopic origins.

tion is observed. This increase follows an exponential trend and shows large differences between the mAbs . In addition, some of them exceed 15-20 mPa·s already at relatively low protein concentration. Data obtained were fitted using the heuristic model

$$\eta_r(\varphi) = \frac{\eta}{\eta_0} = 1 + \exp\left(a\,\varphi + b\,\varphi^2\right) , \tag{5.9}$$

with η_0 representing the solvent viscosity, and a and b being scalar fit parameters. Data collected from the mAbs in their original H_2O buffer are shown in Figure 5.2; the viscosity of the solvent alone was $\eta_0\,(\mathrm{H_2O}) = 0.92$ mPas. Results for the deuterated solutions are reported in Figure 5.14 in section 5.5.

The data show a strong dependence of the viscosity η on the type of mAb, although their structures only differ in the Fab and CDR regions. This observation suggests the microscopic origins of this phenomenon and underlines the importance of investigating the interactions between mAb molecules.

5.3.2 Dynamic and static light scattering

Parameters obtained via light scattering measurements can give indications on the interactions between mAbs in solution. In particular, the second virial coefficient $\mathrm{A_2}$ can be obtained from SLS and diffusion-interaction parameter $\mathrm{k_D}$ from DLS. In Table 5.1, we report the values determined previously by Schmitt et al. [184]. mAb1 and mAb9 are characterized by larger positive values of $\mathrm{A_2}$, which are pointing towards electrostatic repulsion and might explain the relatively low viscosity. In contrast to mAb1 and mAb9, mAb12 shows a still positive but slightly smaller $\mathrm{A_2}$, indicating the presence of weaker repulsive forces between its monomers. However, mAb12 undergoes a significant increase in the viscosity at high concentrations compared to mAb1 and mAb9. On the other hand, mAb16 and mAb24 feature negative $\mathrm{A_2}$ values, suggesting the presence of attractive interactions between monomers and justifying their viscosity increase at increasing mAb volume fraction.

Concerning the diffusion-interaction parameter $\mathrm{k_D}$, $\mathrm{k_D} > 0$ indicates net repulsive interactions, whereas $\mathrm{k_D} < 0$ is a signature of net attractive interactions between mAb monomers [102]. Again, while mAb1 and mAb9 show almost equal and largely positive $\mathrm{k_D}$ values, mAb12 has a weakly positive $\mathrm{k_D}$, meaning that mAb1 and mAb9 feature way more repulsive PPIs and lower viscosities than mAb12. An opposite behaviour is observed for mAb16 and mAb24, which are characterized by negative $\mathrm{k_D}$ and therefore experience attractive PPIs and higher viscosities. Moreover, the trend of increasing viscosity at increasing mAb concentration is more pronounced for mAb24, having $\mathrm{A_2} = -0.72$ and a largely negative $\mathrm{k_D}$ (Table 5.1).

MAb	$\mathbf{A_2 \times 10^{-4}\ [mol\,mL\,g^{-2}]}$	$\mathbf{k_D}$ **[mL /g]**
mAb1	1.96	18.40
mAb9	1.10	18.50
mAb12	0.44	1.37
mAb16	-0.11	-6.17
mAb24	-0.72	-21.10

Table 5.1. Second virial coefficients $\mathrm{A_2}$ determined by SLS and diffusion-interaction parameters $\mathrm{k_D}$ from DLS obtained for the 5 mAbs by Schmitt et al. [184].

5.3.3 Quasi-elastic neutron spectroscopy and MD simulations

QENS spectra from different mAb solutions at comparable protein concentration c_p at the same temperature and same momentum transfer q show significant differences (Figure 5.3) already visible without modelling.

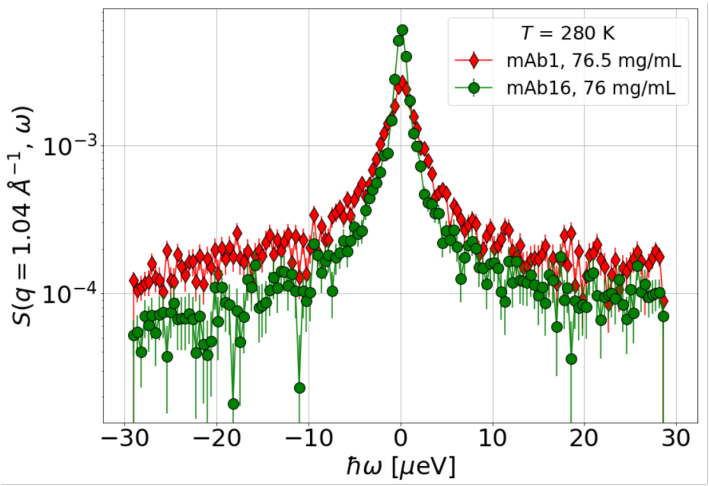

Fig. 5.3. Model-free comparison of QENS spectra at q = 1.04 Å^{-1} for $T = 280$ K from two mAbs (mAb1 and mAb16) in D_2O solutions with 20 mM His-HCl, at nearly the same protein concentration ($\sim$ 76 mg/mL). Despite the identical conditions, the two spectra show significant differences in intensity and width.

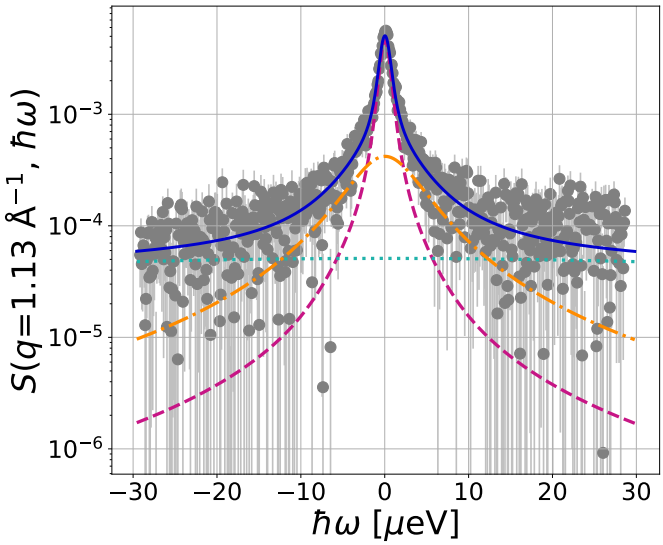

Fig. 5.4. QENS spectrum (symbols) obtained from mAb16 at $c_p = (80.44 \pm 4.79)$ mg/mL at $T = 280$ K with different dynamic contributions (lines) at q = 1.13 Å^{-1}. The blue solid line represents the fit consisting of the different dynamical contributions in equation 5.1: global (magenta dashed), internal (orange dash-dotted) and solvent diffusion (cyan dotted line).

Global self-diffusion varies substantially among the mAbs

Due to the dominant nuclear incoherent scattering from the proteins, the obtained dynamic structure factor represents the ensemble-averaged single-particle self-dynamics. From the narrowest Lorentzian contribution in the QENS spectra the observable apparent global self-diffusion coefficients $D = D(D_r, D_t)$ were obtained, which contain the contributions from both rotational D_r and translational D_t diffusion. $D = D(\varphi)$ is sensitive to the crowding effects mediated by hydrodynamic and electrostatic interactions, but also to the presence of clusters, which can be transient [398]. The comparison with existing models from colloid theory gives hints on the factors affecting short-time diffusion and ultimately, viscosity.

Diffusion of antibody solutions as soft colloid suspensions

As stated above, proteins in solution experience both translational center-of-mass diffusion and rotational diffusion. The measured dynamic structure factor contains both contributions which together account for the global dynamics and result in the observable D. The width $\gamma(q)$ of the first Lorentzian contribution in equation 5.2 is associated with this apparent diffusion coefficient D. To interpret the experimental D in terms of colloid physics, a theoretical $D^{\mathrm{theo}}(\varphi_t) = D^{\mathrm{theo}}(D_r^{\mathrm{theo}}(\varphi_t), D_t^{\mathrm{theo}}(\varphi_t))$ was calculated as established in Ref. [306], based on an analytical expression for this implicit function and on the protein hydrogen radial density distribution $\rho(r)$ calculated from their PDB structures (see Figure 5.16 in section 5.5). An interpretation of the φ-dependence of D in terms of colloid physics is only possible by simplifying the protein shape [4,161,423]. Due to the observation time of our backscattering experiment of a few nanoseconds, resulting from its energy resolution, we access the diffusion in the so-called short-time limit, where protein-protein collisions can be neglected and hydrodynamic as well as electrostatic interactions prevail.

In a strongly simplified picture, the mAbs may be approximated as colloidal hard spheres to obtain an analytical expression of the crowding dependence of the translational diffusion D_t^{theo},

$$D_t^{\mathrm{theo}}(\varphi_t) = D_t(\varphi_t = 0)\, f(\varphi_t) = D_t(0)\, f(\varphi_t), \tag{5.10}$$

in which the theoretical reduced translational diffusion $f(\varphi_t)$ depending on the hydrodynamic volume fraction φ_t can be described by a polynomial expression [161], and $D_t(0)$ denotes the dilute limit translational diffusion coefficient [161]. The rotational diffusion can be approximated by the charged-sphere model [4]

$$D_r^{\mathrm{theo}}(\varphi_t) = D_r(\varphi_t = 0)(1 - 1.3\,\varphi_t^2)\,, \tag{5.11}$$

where $D_r(0)$ denotes the dilute limit rotational diffusion coefficient [4], and which holds for low volume fractions. Due to the protein hydration shell moving along with the proteins an effective hydrodynamic volume fraction φ_t was assumed [306]. φ_t is connected to the protein volume fraction φ given by the sample preparation employing a dry protein powder by

$$\varphi_t = \varphi \left(\frac{R_h}{R_{dry}} \right)^3, \tag{5.12}$$

such that the volume fraction is rescaled by the ratio between the hydrodynamic radius obtained from the Stokes-Einstein relation,

$$R_h = (K_b T)/(6\pi\eta_{\mathrm{D2O}}(T) D_t(0)), \tag{5.13}$$

and the bare effective antibody radius

$$R_{\mathrm{dry}} = \sqrt[3]{3\,V_{\mathrm{dry}}/4\pi}. \tag{5.14}$$

All parameters entering these calculations, namely $D_t(0)$, $D_r(0)$ and the bare antibody volume V_{dry} to calculate R_{dry}, were derived via HYDROPRO10 [160] employing the PDB structure for each mAb, and for the reference polyclonal IgG using the structures of murine and human immunoglobulin G [380, 424]. For consistency with the neutron data, HYDROPRO10 calculations were performed using the viscosity and solution density of D_2O [342]. Values calculated for 7, 22 and 37°C (280, 295, 310 K) can be found in Table S2. Figure 5.5 depicts the summary (at T= 280, 295, 310 K) comparing the experimental D (symbols) for the different mAbs and an average of $D^{\mathrm{theo}} = D^{\mathrm{theo}}(D_t^{\mathrm{theo}}, D_r^{\mathrm{theo}})$ for monomeric solutions of all mAbs (lines). Grey shaded areas can be uncertainties associated to the solid lines and represent the regions delimited by D^{theo} for 1IGT (lower) and mAb12 (upper limit). Dashed brown lines are the approximated dimer curves obtained by rescaling the monomer ones by the dilute limit $D^{\mathrm{theo}}(0)$ of the dimeric immunoglobulin IgA solution structure 2QTJ [425]. Note that $D^{\mathrm{theo}}(0)$ was again a function of its translational and rotational components at the dilute limit $D_t(0)$ and $D_r(0)$, calculated via HYDROPRO10 [160]. Figure 5.5 shows that D varies significantly among the 5 mAbs and the reference IgG. The trend in D (Figure 5.5) follows the trend in η (Figure 5.2). Highly viscous mAb solutions, e.g. mAb12, display a lower D compared to less viscous ones, e.g. mAb1 and mAb9.

The interpretation of the observable apparent diffusion of mAb solutions by colloid physics allows to estimate the level of aggregation in these systems. Diffusion coefficients (symbols) similar to the monomer hard-sphere prediction (solid line) suggest an overall monomeric solution, whereas smaller diffusion coefficients corroborate the presence of antibody aggregates which are mainly dimers or constituted by few monomers, since the symbols are not far from the theoretical prediction of dimer diffusion (dashed lines, Figure 5.5). As stressed earlier, the hard-sphere model constitutes a very simplistic approximation for the non-spherical antibodies, and the assumption on the ratio R_h/R_{dry} enters sensitively by the third power (equation 5.12). The global diffusion also varies with temperature as expected. Diffusion coefficients increase from 280 to 310 K, meaning that attraction between proteins and self-aggregation is not favoured at high temperatures, consistently with SANS results (see section 5.3.4); mAb clusters overall undergo dissociation when exposed from storage to body temperature ($\sim$ 7 to 37°C).

Moreover, by evaluating equation 5.7, we find that vibrational MSDs $\langle u^2 \rangle$ of hydrogen atoms in the mAbs studied are in the range 0.2 to 1.2 Å^2 with the expected temperature dependence, consistent with values found for other proteins [34].

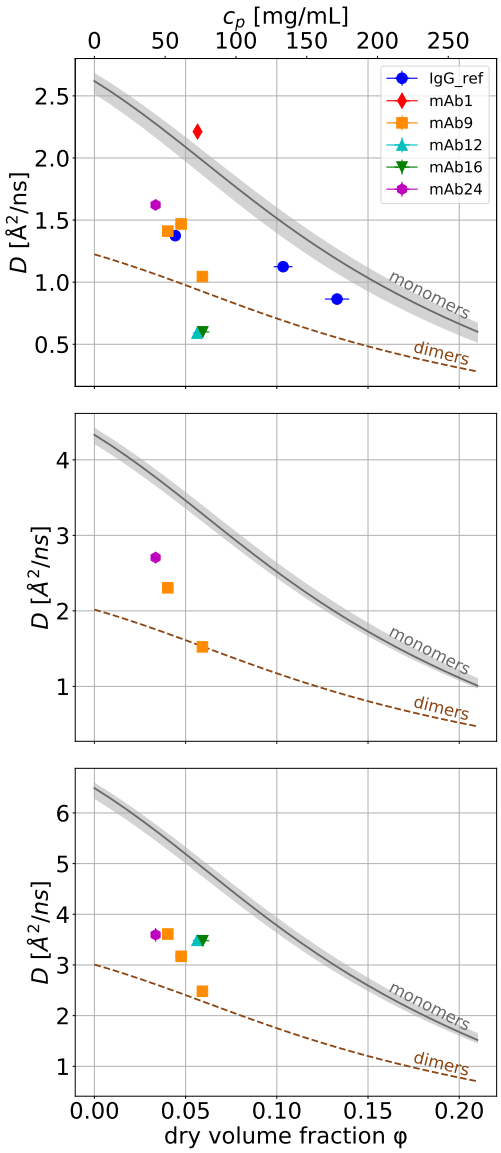

Fig. 5.5. Observable apparent diffusion coefficients D (symbols, obtained from global fits of QENS data) of the mAbs and polyclonal IgG vs protein dry volume fraction φ (lower) and concentration c_p (upper x-axis) in solution at $T = 280$ K (top), $T = 295$ K (center), $T = 310$ K (bottom). Grey solid lines denote the average value of D^{theo} for monomers of all mAbs , murine and human IgG [424], obtained using a colloid physics hard-sphere model as explained in section 5.5.4. Grey shaded areas are delimited by D^{theo} for 1IGT (lower) and mAb12 (upper limit). Dashed brown lines are the approximated dimer curves obtained by rescaling the monomer ones by the dilute limit $D^{\text{theo}}(0)$ of the dimeric immunoglobulin structure 2QTJ [425]. Symbols below the monomer lines corroborate the presence of clusters due to their larger hydrodynamic size. However, these clusters are mainly dimers or formed by few monomers and they dissociate at increasing temperature (from approximately storage to body temperature).

Internal dynamics and viscosity shows lower correlation on short time scales

Generally, protein internal dynamics on ps to several ns timescales can relate to the capacity of the protein to swiftly change conformation and possibly adopt conformers prone to self-association [34]. Such behaviour would be in favour of high viscosities. Hence, the internal dynamics of the mAbs was investigated experimentally through the QENS spectra and computationally through the MD simulations. The diffusion coefficient associated with internal motions D_i, as obtained from QENS fits, is similar within the confidence bounds for each mAb except for mAb9, for which D_i is 2 times lower. The residence time τ is similar for all mAbs , except mAb1 and mAb9, showing slightly higher values. These ensemble-averaged values for internal dynamics obtained from QENS do not present any clear correlation with the viscosity data in section 5.3.1.

The large scale domain motions - that is, the angle between the main lobes, Fc and Fab regions of the mAbs - were computed as described in Section 5.2, averaging over time blocks of 20 ns (Fig. 5.6). There are no significant differences between the different antibodies within the errors, as the angles between the three main lobes of the antibody fluctuate slowly around an equilibrium value. However, the viscosity could depend on weak transient interactions that can be facilitated by fast internal dynamics in the sub-ns time domain.

To investigate fast motions, the diffusive MSD $\langle u^2 \rangle$ was computed as explained in Section 5.2 for each amino acid of the different mAbs . The MSDs were obtained for a time delay of 50 ps, 200 ps and 1 ns. Globally, the MSDs appear similar for all mAbs without an obvious correlation with increasing viscosity (Fig. 5.7 (top)). Slightly more relevant differences in the MSD among the mAbs can be found in the light chains (Fig. 5.7 (bottom)), but without a visually clear trend with increasing viscosity. To better correlate with the viscosity, the dimension of the MSD vector was reduced by averaging over the main domains (VH, CH1, CH2, CH3, hinge, VL, CL) for all time delays. The resulting correlations

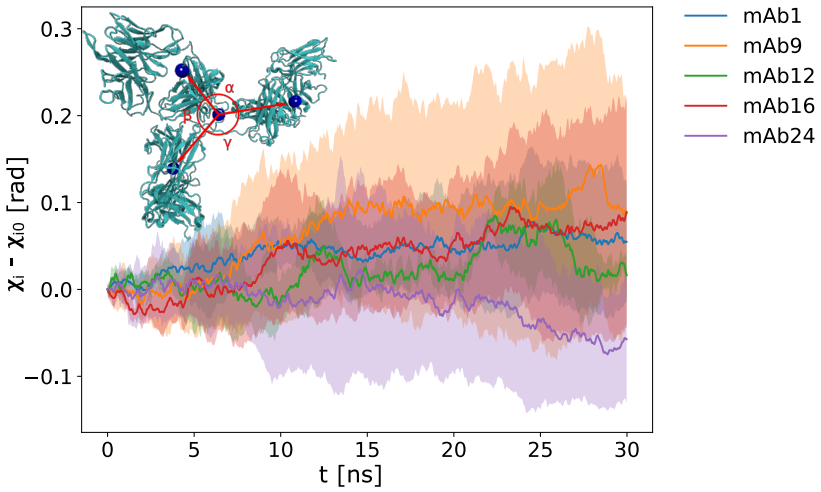

Fig. 5.6. Large scale domain motions observed during MD simulations of the mAbs . For each angle indicated on the cartoon structure in inset, the deviation of the angle χ_i = {α, β, γ} from the initial value χ_{i0} was computed as indicated in Section 5.2 using the block average method with a block size of 20 ns. The average of the blocks is plotted using coloured solid lines and the standard deviation of the blocks using coloured shaded areas for each mAb.

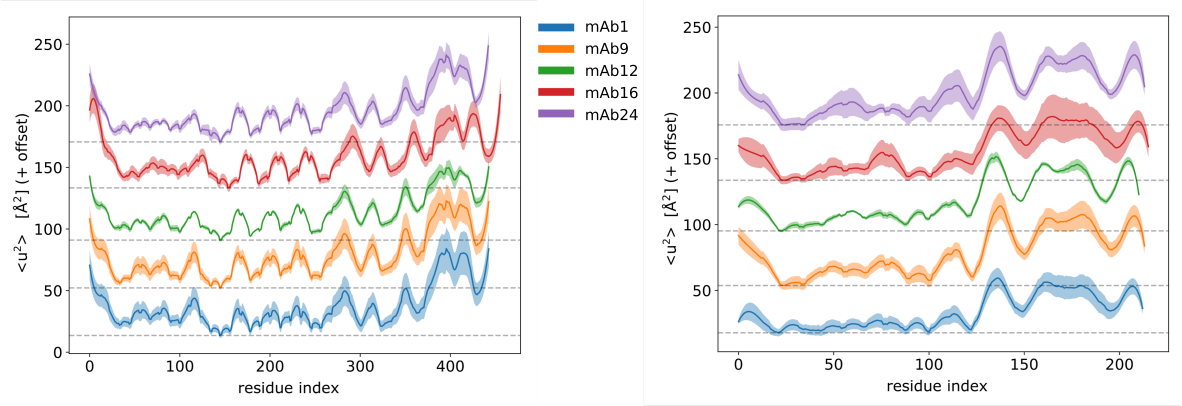

Fig. 5.7. Diffusive MSD $\langle u^2 \rangle$ derived from MD simulations of the 5 mAbs computed from the simulated trajectories as described in Section 5.2. The resulting average over the blocks of 20 ns size is plotted for each mAb using solid coloured lines and corresponding shaded areas for the standard deviations. MSDs for the heavy chains (left) and for the light chains (right plot) with an offset on y-axis for better visualization and for increasing viscosity from bottom to top.

with the viscosity are presented in Fig. 5.8. It appears that the viscosity is significantly correlated ($\rho_{\text{viscosity},\theta_i} > 0.5$) with the features related to protein-protein interaction strength (virial coefficient A_2 and diffusion-interaction parameter k_D). Moreover, the charge on VH/VL regions appears to correlate with viscosity as well, suggesting that electrostatic interactions are dominant. The internal dynamics represented by the MSD presents some correlation with viscosity, but the correlation coefficients are systematically lower than 0.5 indicating that such dynamics plays a subordinate role.

To assess whether the features used to compute the correlation can provide a good predictor of viscosities, the viscosity was removed from the dataset, resulting in a reduced dataset. A principal component analysis (PCA) was performed on the covariance matrix of this reduced dataset using routines from the *scikit-learn* package [426]. The observable values from Figure 5.8 were then projected on the first 3 principal components to visualize how the different mAbs are separated in PCA space (Fig. 5.9). It appears that the use of either the full feature dataset or a reduced one where MSD are removed allows for a good separation of the mAbs according to the viscosity. However, the MSDs alone do not provide a good separation of the mAbs , and hence do not constitute a reliable predictor for the viscosity.

Viscosity strongly depends on VH/VL domain charges and hydrophobicity

To further explore the determinants of the viscosity, additional features, obtained directly from the amino-acid sequence, were computed (see Section 5.2). The obtained features were used to compute the statistical covariance with the viscosity. The input values used for the viscosity were collected from concentration series (30, 60, 90, 120, 150, 180 mg/mL) of the 5 mAbs in solution at 25°C (data in Section 5.3.1). The hydrophobicity and the charge, especially on the VH/VL domains, are correlated with the viscosity (Figure 5.8). The second virial coefficient A_2, the diffusion-interaction parameter k_D and the isoelectric point pI present a pronounced correlation with viscosity. **Protein network dynamics differs between mAb9, mAb12 and mAb24.** Next, we investigate the protein-protein interactions by putting 6 monomers in a simulation box. The simulations were run for 200 ns and analysed using a protein network graph computation of the hydrogen bond dynamics between individual monomers.

Building a protein interaction network allows to identify protein clusters, their size and their dynamics by tracking the interaction lifetime for each pair of monomers in the simulation. The network graphs were constructed as described in Section 5.2 and the result is shown in Figure 5.10. The graph for mAb9 shows two clusters of 4 and 2 monomers that are present for most of the trajectory and can

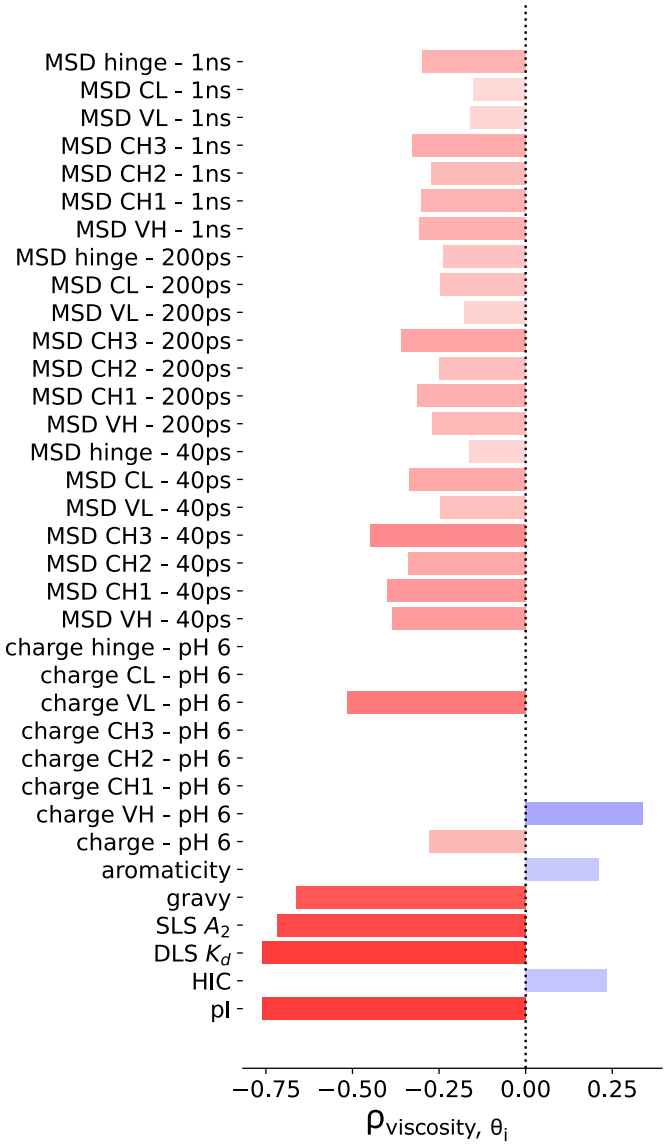

Fig. 5.8. Correlation of the viscosity with parameters derived from protein sequence and MD simulations. The MSD as well as the features extracted from the sequence (see section 5.2) were used to compute the statistical correlation with the viscosity $\rho_{\text{viscosity},\theta_i}$ given by $\rho_{x,y} = \frac{\text{covariance}(x,y)}{\sqrt{\sigma(x)}\sqrt{\sigma(y)}}$, where σ is the variance and θ_i the value of the observable i. The result is shown as a vertical bar plot with the features arranged on the y-axis and the bars ranging from deep red for a correlation of -1 to deep blue for a correlation of 1. The charges are computed at pH 6 and the labels include the concerned protein domain except for 'charge pH 6', which is the total charge of the protein. The labels for MSD values include the concerned protein domain followed by the time delay used to compute it. Image by Dr. Kévin Pounot, co-author of Ref. [194].

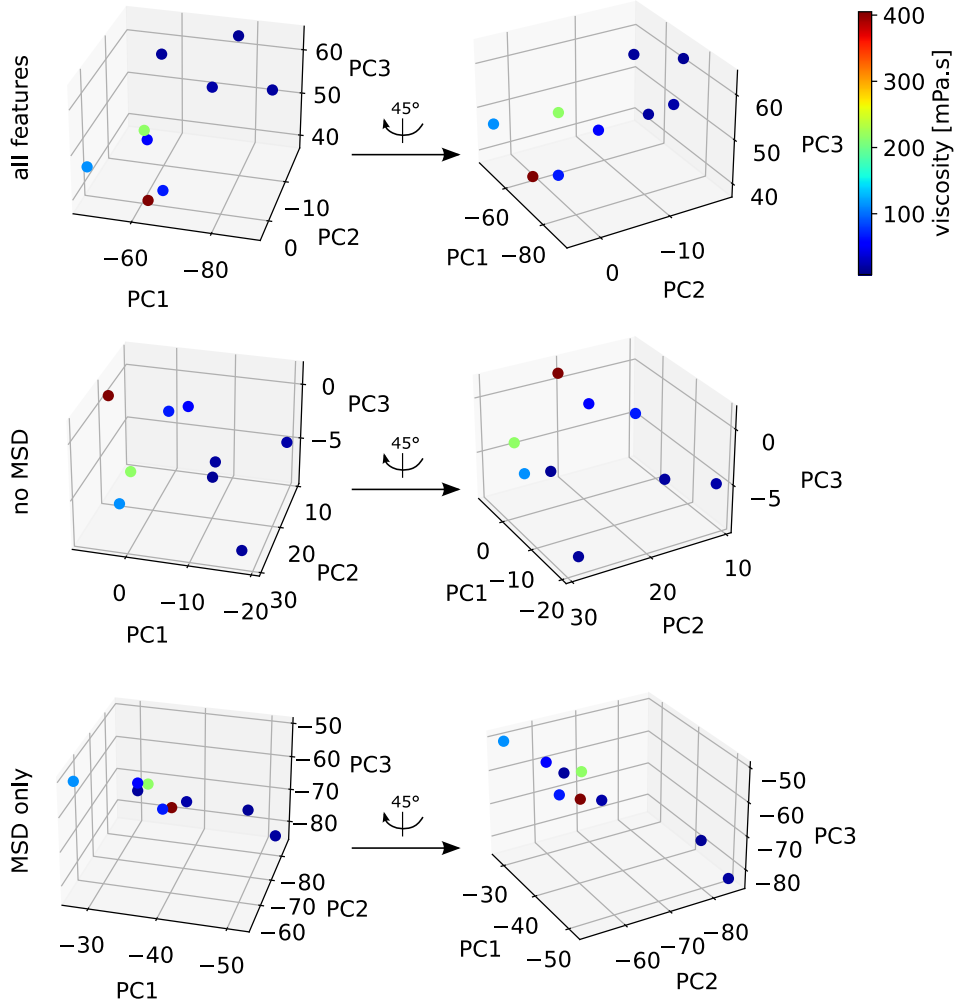

Fig. 5.9. Separation of mAbs using computed features. A principal components analysis (PCA) was performed on the features computed for Figure 5.8 using routines from the *scikit-learn* Python package [426]. The initial observable vectors were projected on the first 3 principal components (PC) and plotted with dots whose colour corresponds to viscosity (ranging from deep blue for low η to brown for high η). Top plots: projections for a PCA using all features; middle plots: projections for a PCA on a dataset where the MSD was removed; bottom plots: projections for a PCA performed on a dataset containing MSD only. Image by Dr. Kévin Pounot, co-author of Ref. [194].

sometimes interact with an interaction lifetime of 1.1 ns, which crosses the backscattering observation time window. The graphs for mAb12 and mAb24 present a higher connectivity quantified by the clustering coefficient (CC) of the graphs, being 0.73 for mAb12 and 0.47 for mAb24, against a value of 0.36 for mAb9. This result is in agreement with the slow diffusion and the marked trend to cluster of mAb12 revealed by QENS (Figure 5.5), as well as with its stronger protein-protein interactions probed by SANS (Figure 5.13 in the next paragraph), compared to the ones present in mAb9 and mAb24 solutions. Moreover, the average relaxation rate (obtained by computing the inverse average lifetime of graph vertices) is lowest for mAb9 and highest for mAb24, thereby demonstrating a more dynamic protein interaction network for mAbs with higher viscosities.

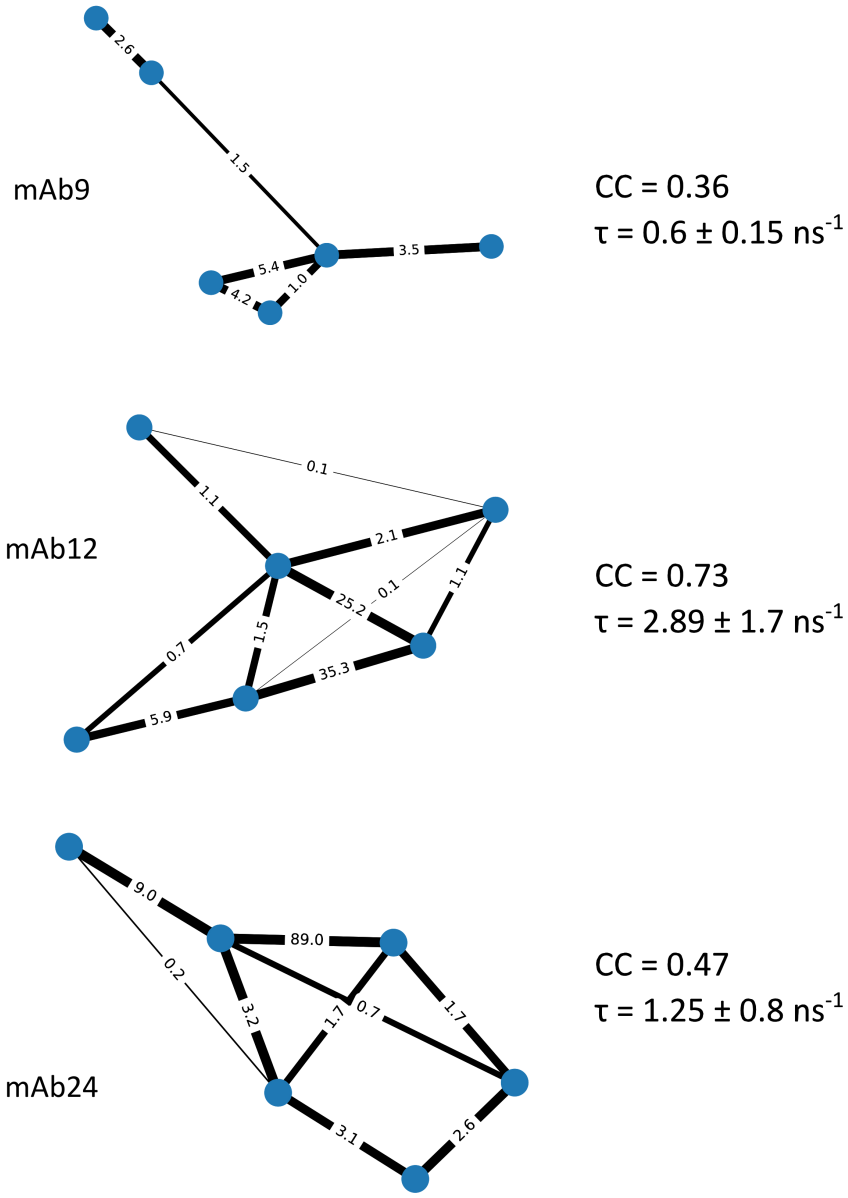

Fig. 5.10. Protein network graphs for mAb9, mAb12 and mAb24, produced from the simulations at high concentration. Each blue node represents a single mAb monomer and two nodes are connected by an edge when their atoms are at a minimum distance of 5 Å. The width of the edge line is proportional to the number of times a given pair of monomers are in interaction during the simulation and the number labels indicated on the edges are the average lifetime of the interaction given in ns. The clustering coefficient (CC) and the average relaxation rate (inverse lifetime) τ are shown for each protein graph. Protein network dynamics at high concentration strongly depends on the mAb. Image by Dr. Kévin Pounot, co-author of Ref. [194].

5.3.4 Small-angle neutron scattering

Small-angle neutron scattering (SANS) provides thermodynamic and structural information on the nanometer-micrometer scale. The intensity of scattered neutrons is expressed as [326, 427]

$$I(q) = \frac{d\sigma}{d\Omega}(q) = n(\Delta\rho)^2 V_{part}^2 P(q) S(q), \tag{5.15}$$

where n is the particle number density, $\Delta\rho$ is the difference in scattering length density between the solvent and the particles (also known as the scattering contrast), and V_{part} is the volume of a single particle [326, 427]. The term $P(q)$ is referred to as the particle form factor, determined by the protein shape [427,428]. The structure factor $S(q)$ (details in, e.g., Refs. [325,327,429]) characterises the interactions between particles in solution. $S(q \to 0)$ can be expanded into a series of virial coefficients A_n [430–432]

$$S(q \to 0) = \frac{RT}{M_W}\Big(\frac{\partial \Pi}{\partial c}\Big)^{-1} = \frac{1}{1 + 2M_W A_2 c + ...} \tag{5.16}$$

with M_W (g/mol), the molecular weight of the particles. The second virial coefficient B_2 [433]

$$B_2 = 2\pi \int_0^\infty dr\ r^2 [1 - e^{\frac{-u(r)}{k_B T}}] \tag{5.17}$$

is related to A_2, which can be determined by SLS (see above) [184] via [434]

$$B_2 = A_2 \cdot \frac{M_W^2}{N_A}. \tag{5.18}$$

We employ the reduced second virial coefficient B_2^*, defined as the ratio B_2/B_2^{HS} (B_2^{HS}: second virial coefficient for hard spheres) and linked to the stickiness parameter τ by

$$B_2^* = B_2/B_2^{HS} = 1 - \frac{1}{4\tau}\,, \tag{5.19}$$

where $B_2^{HS} = 2\pi\sigma^3/3$, with σ being the diameter of the hard spheres [433]. In the case of the mAb samples studied here, we employ the approach by Da Vela et al. [391] for bovine γ-globulin). The SANS data were fitted using the NIST software package for SANS analysis Igor Pro [330] by WaveMetrics, Inc. (Lake Oswego, OR, USA). The model used is a combination of an ellipsoid form factor $P(q)$ (oblate ellipsoid with axes of 7-8 Å and 58-60 Å) and a sticky hard sphere (SHS) structure factor $S(q)$ for mAb12 and mAb24. For mAb9, the SHS structure factor was not properly fitting the data at low q, so we opted for simple hard-sphere (hard-sphere (HS)) potential, also due to the repulsive feature of its $I(q)$ at low q. We note that in spite of the anisotropic shape of mAbs , an isotropic interaction potential is used here. This approach has been justified by Yearley et al. [227] and Castellanos et al. [223]. Background-corrected SANS data for mAb9, mAb12 and mAb24 with the corresponding fits are shown in Figs. 5.11,5.12, in order to better visualize antibody-type and temperature dependence of the data, respectively.

Overall, a decrease of the intensity $I(q)$ in the low-q region is observed when the samples are heated up from 21°C to human-body temperature, suggesting a weaker inter-protein attraction at high temperatures and likely dissociation of microscopic aggregates formed at lower temperatures (Figure 5.11). High-q features of $I(q)$ (around 0.2 $\mathrm{Å}^{-1}$) are due to the molecular shape of the mAbs , which is preserved across the temperature range studied. However, differences in the low-q region are also variant-dependent (Figure 5.12), meaning that the three mAb solutions feature different PPIs. In fact, mAb9 shows less attractive PPIs than mAb12 and mAb24, which may result in a lower level of clustering and a higher diffusion coefficient, as observed through QENS (Figure 5.5), along with a

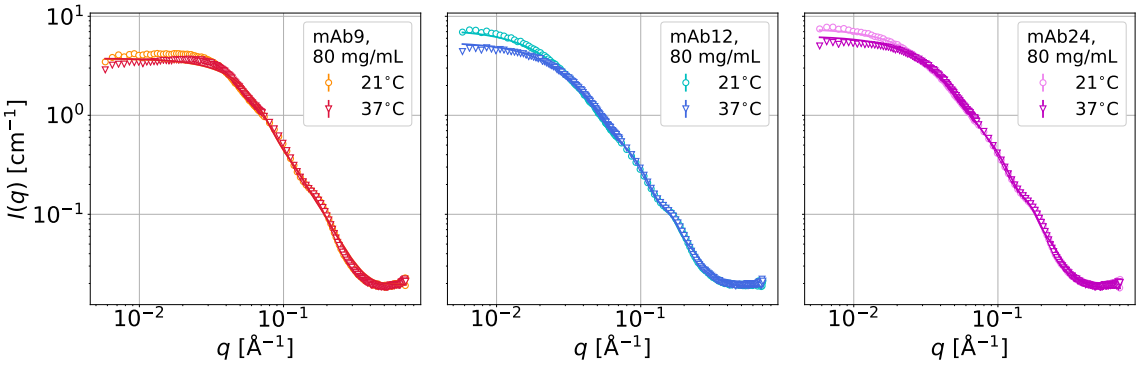

Fig. 5.11. Temperature dependence of mAb-mAb interactions probed using SANS. Experimental curves (empty symbols) and their corresponding fits obtained from a subset of mAbs: mAb9 (top), mAb12 (center), mAb24 (bottom) at $c_p = 80$ mg/mL in 20 mM His-HCl buffer at pH 6.0 in D_2O. A decrease of $I(q)$ at low q with increasing temperature T reveals weaker PPIs and a potential dissociation of aggregates.

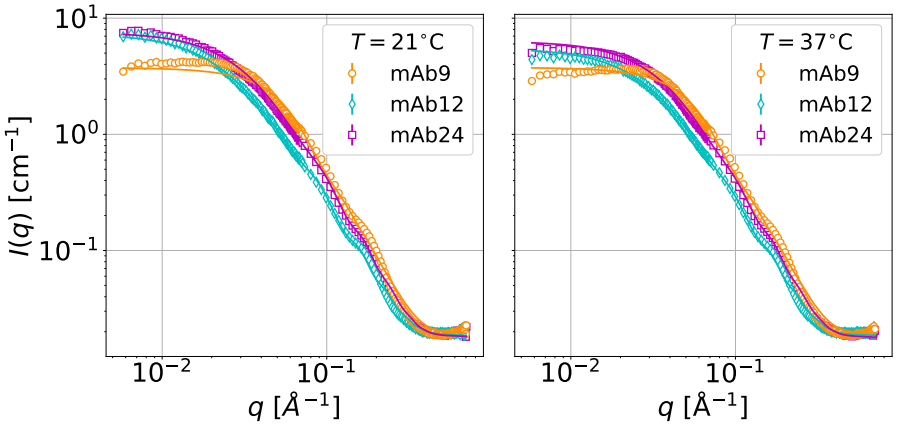

Fig. 5.12. Antibody dependence of protein-protein interactions probed through SANS. Comparison among SANS curves (empty symbols) and their corresponding fits of mAb9, mAb12 and mAb24 at 21°C (left) and 37°C (right). Protein concentration in all samples is 80 mg/mL in 20mM His-HCl buffer in D_2O. $I(q)$ does not show significant changes at high-q, while differences in the low-q region are visible at both 21 and 37°C and suggest the presence of different PPIs in the three mAb solutions; mAb9 shows much less attractive PPIs than mAb12 and mAb24.

lower CC determined from protein network analysis (Figure 5.10). For mAb12 and mAb24, based on the SHS $S(q)$ fit, the normalised second virial coefficient B_2/B_2^{HS} was determined. $B_2/B_2^{HS} < 0$ indicate overall attractive interactions between the mAb molecules, whereas $B_2/B_2^{HS} > 0$ point towards overall repulsive interactions. The resulting B_2/B_2^{HS} are shown in Figure 5.13. Lower B_2/B_2^{HS} are observed at lower temperature, which means that mAb-mAb attraction is stronger and aggregation is favoured; this result is in agreement with conclusions from QENS data (section 5.3.3). For mAb12, the A_2 value mentioned above indicated a slight repulsion while the B_2/B_2^{HS} values indicate an attraction. This might be due to the usage of the sticky hard sphere model, which is incapable to cap-

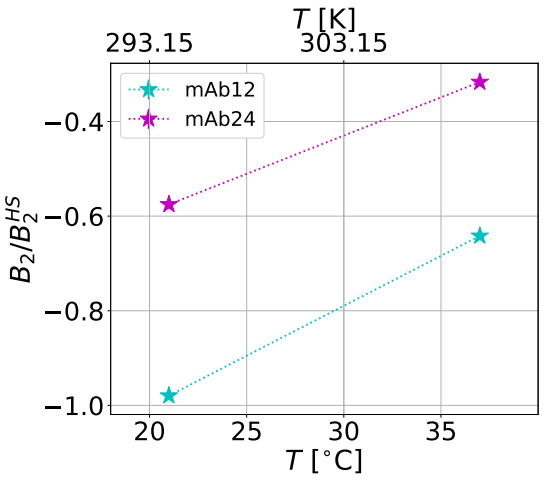

Fig. 5.13. Reduced second virial coefficient B_2/B_2^{HS} (symbols) determined from the SANS fits plotted against temperature T in °C (lower x-axis) and Kelvin (upper x-axis). Data from the two mAbs presented here (mAb12 and mAb24) show an increase in B_2/B_2^{HS} with increasing temperature from 21 to 37°C, meaning that attraction among antibodies decreases when the solutions experience higher temperatures. Dashed lines are guides to the eye.

ture reversible self-association or anisotropic or directional interactions. A reversible self-association would also explain the significantly reduced diffusion coefficient observed above.

5.4 Conclusions

The present work provides a deeper understanding of the link between microscopic dynamic properties and macroscopic viscosity of the solutions of 5 different monoclonal antibodies of the IgG1 subtype. By a multi-technique approach employing neutron backscattering spectroscopy, small angle neutron scattering, molecular dynamics simulations and viscometry, we find biophysical determinants for the variation in the viscosity of mAb solutions. Consistent with previous work [205,234,435], we identify the formation of clusters of self-associating antibody molecules as the main mechanism responsible for the increase in viscosity at high antibody concentrations.

In particular, QENS experiments access the different dynamical contributions of the systems studied. Global and internal dynamics can be decoupled and analysed separately. The global dynamics refers to the protein center-of-mass motion, accessing the observable apparent diffusion coefficient D, which can be interpreted in terms of the physics of dense colloidal suspensions of hard spheres, within the approximations of short-time diffusion and an effective spherical shape. By approximating mAb molecules as hard spheres, D obtained from QENS are compared to the theoretical estimation $D_{\mathrm{theo}}(\varphi)$ obtained employing the hard-sphere model. Importantly, due to the prevailing nuclear incoherent scattering from the protein hydrogen atoms, our QENS experiment probes the self-diffusion (synonymously: tracer diffusion) of the mAbs . For this reason it unambiguously provides the hydrodynamic size of the mAb assemblies unobstructed by structural features seen by coherent scattering. For most mAbs , $D < D_{theo}(\varphi)$ in agreement with a cluster picture. Moreover, most diffusion coefficients are larger than those estimated for mAb dimers, such that the QENS results support a picture

of very small clusters with less than two members on average. The clusters may be transient in time, and the QENS spectra are recorded with an observation time of a few nanoseconds resulting from the $< 1\mu$eV energy resolution, thus, not ruling out dissociation on longer times. This short observation time comes with the advantage that protein-protein collisions can be neglected, and the observed diffusion is governed by hydrodynamic and electrostatic interactions. From the QENS analysis we can infer that all mAbs undergo self-association and cluster formation at the lowest temperature measured, 280 K ($\approx 7°$C), which is a storage temperature, while short-time diffusion is enhanced at 310 K ($\approx 37°$C), which is the physiological temperature. Moreover, different mAbs result in significantly different diffusion, with smaller diffusion, i.e., larger average cluster size for higher viscosity.

In addition, all mAbs measured show higher D with increasing temperature, consistent with enhanced diffusion with higher T as expected. We point out that the mAb concentrations measured by QENS in the present work are low compared to those used in previous studies on model protein solutions [34]. For this reason, the scattering signal is weak, and the accuracy of the information on the internal diffusive dynamics is limited. Nevertheless, this internal dynamics information is consistent with earlier work on γ-globulin [307] within the uncertainties. The low signal required that global fits of the spectra for all momentum transfers at once had to be used. These global fits might result in a systematic error for the global diffusion due to a possible cross-talk of the global and internal dynamics Lorentzians at large momentum transfers.

SANS was used to probe structural and thermodynamic features of mAb solutions on a subset of the mAbs studied by QENS, and the second virial coefficient was extracted to estimate the interaction among mAb molecules, revealing that protein-protein attraction decreases with decreasing viscosity and increasing temperature. This trend is consistent with the cluster formation seen in QENS. Our data set indicates that the clusters tend to dissociate with increasing temperature, the weak electrostatic interactions being outweighed at higher temperatures. As the data set is currently limited, this trend should be substantiated with further measurements in the future.

The single-molecule MD simulations provide an atomistic view of the internal dynamics, complementary to the QENS data. The result shows that the internal dynamics is not a good predictor of the viscosity. The internal dynamics was found to be similar for all mAbs , as expected based on the fact that the molecules are basically identical apart from small differences in the CDR regions of their sequences. The presence of strong correlation of viscosity with hydrophobicity and second virial coefficient indicates that protein-protein interactions and possibly protein-solvent interactions mainly drive the viscosity. The MD simulations with 6 molecules per simulation box provide some insight on the protein cluster dynamics for mAb9, mAb12 and mAb24. It appears that high viscosity mAbs tend to form clusters with more monomers, but with shorter interaction lifetimes and less frequent pairs of monomers such that the protein network reorganizes faster. As a result of strong cluster dynamics, a shear stress results in inefficient momentum transfer between molecules because of short-lived interactions, in high friction between clusters, and hence in high viscosity. We note that the conclusions from the simulations are limited by the achievable sampling time. Yet, the results are convincing and appeal for further work fully dedicated to simulations of mAbs at high concentration.

We have presented an extended study of an unprecedentedly large number of different mAbs with neutron and complementary techniques, and have established incoherent high-resolution neutron backscattering spectroscopy as a new technique to study mAb solutions and to unambiguously access their average hydrodynamic cluster size. A key finding from this work is that the clusters seen on the nanosecond observation time of our neutron spectroscopy experiment consist on average of less than two members per cluster at physiological temperature (Figure 5.5 bottom). This average size can be

assumed to reflect a highly dynamic picture of the self-association and resulting viscosity of the mAb solutions and depends sensitively on the type of mAb. The sensitivity on the mAb type cannot be understood by internal motion, as revealed by the simulations, but rather by differences of the mAbs in specific regions near the protein surface. The simulations are consistent with this picture of highly dynamic transient protein association.

Acknowledgements

This research has been supported by InnovaXN, a EU Horizon 2020 MSCA COFUND programme (innovaxn.eu, grant agreement No 847439). I.M. acknowledges an ILL PhD studentship funded by this programme. Moreover, we are grateful for support by the DFG and ANR (ANR-16-CE92-0009, ImmunoglobulinCrowding), notably in the initial phase of this project, and by the BMBF (ErUM-pro 05K19VTB and 05K22VTA). The authors acknowledge the support of the European Synchrotron Radiation Facility (ESRF) and ILL for using the platforms of the Partnership for Soft Condensed Matter (PSCM). The authors are also thankful to Trevor Forsyth, Michael Haertlein and Juliette Devos (ILL, Grenoble) for advice and for providing access to the Life Science lab facilities. We thank Jonathan Schmitt (Lonza Basel) for support with rheometry.

Associated content

Supplementary material: Supplementary material available in section 5.5 with the following contents: biophysical properties of mAbs, viscometry on deuterated antibody solutions, additional example neutron spectra, HYDROPRO10 calculations and hydrogen density distributions from PDB structures, additional QENS and SANS fit parameters and simulation results.
Data availability: Neutron data are permanently curated under DOI and available at Refs. [395, 403], in agreement with ILL data policy.

5.5 Supplementary Information

5.5.1 Biophysical properties of mAbs

MAb	Light chain	MW [kDa]	ε_{280} $[\mathbf{Lg^{-1}cm^{-1}}]$	pI	Aliphatic index	GRAVY
mAb1	κ	148.35	1.434	8.96	70.85	-0.416
mAb9	κ	144.12	1.299	8.61	68.66	-0.414
mAb12	λ	146.46	1.781	8.24	51.89	-0.439
mAb16	λ	143.75	1.555	8.20	68.44	-0.37
mAb24	κ	145.69	1.476	7.54	67.88	-0.438

Table 5.2. Biophysical properties and specific parameters of the mAbs. Type of light chain contained in the structure, molecular weight MW, extinction coefficient at a wavelength of 280 nm ε_{280}, pI, aliphatic index and GRAVY for all the mAbs studied. Note that the extinction coefficient ε_{280} was measured, while MW, aliphatic index and GRAVY were obtained from the mAb PDB structures via Expasy, using the ProtParam tool [350] from the Swiss Institute of Bioinformatics. pI values were obtained from the amino acid sequence using the Prot pi Protein Tool, as in Schmitt et al. [184].

5.5.2 Viscometry on deuterated antibody solutions

Viscometry measurements were performed on a subset of the antibodies (mAb9, mAb16 an polyclonal Ig). It was not possible to complete the whole dataset due to low protein availability. In fact, the preparation of the deuterated antibody solutions requires a long dialysis process (section 5.2.1) during which a discrete amount of proteins can be lost, especially if their viscosity are high. Figure 5.14 shows that the trend of increasing η at increasing protein volume fraction is also preserved in D_2O environment; same applies to the more viscous behaviour of mAb16 compared to mAb9 that we encounter in H_2O solutions and we also see in Figure 5.14 (upper row) at all temperatures measured. In addition, we observe an expected increase of η at decreasing T, which seems less pronounced in mAb9 with respect to mAb16. The difference between η in D_2O buffer at 22°C and η in H_2O buffer at 25°C is not so marked (cf. bottom row in Figure 5.14).

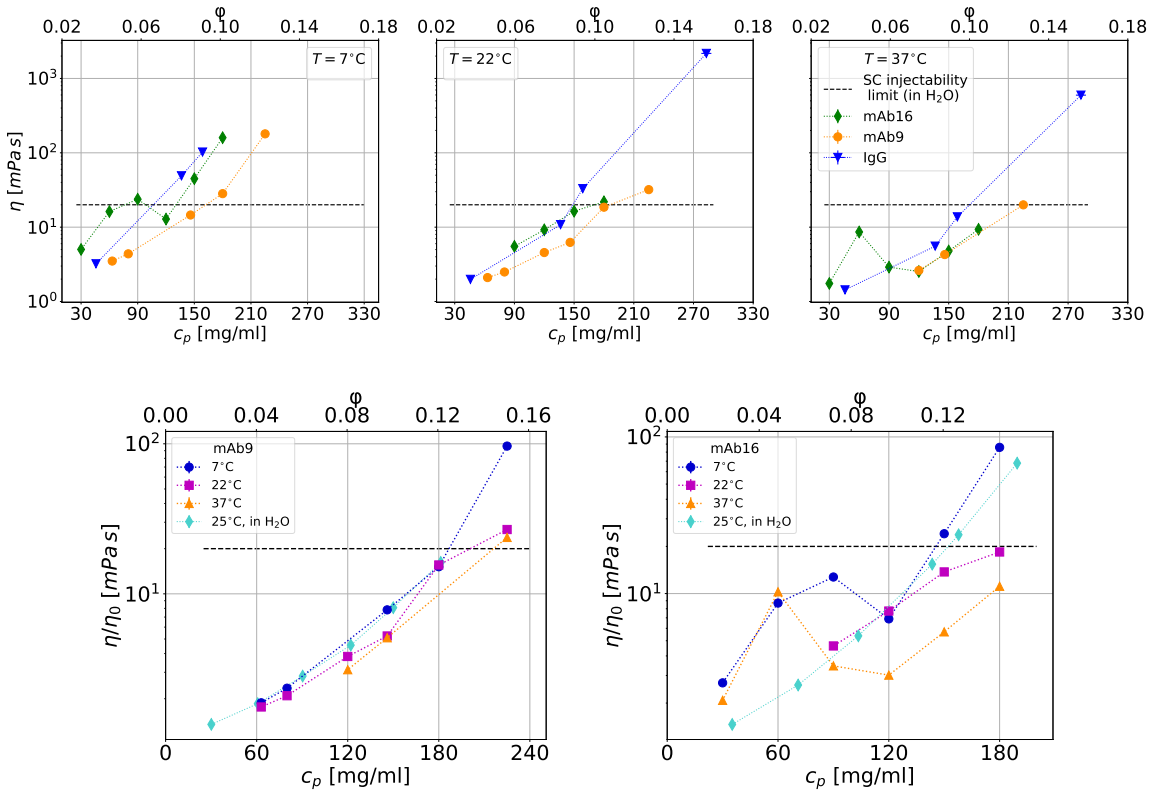

Fig. 5.14. Viscosity of a subset of antibodies in deuterated formulation buffer. In the upper row, we report the dynamic viscosity η at 7°C (left), 22°C (center) and 37°C (right) for mAb9 (orange), mAb16 (green) and polyclonal Ig (blue symbols) in 20 mM His-HCl D_2O buffer. In all plots, the dashed black line corresponds to the viscosity threshold for SC injectability of aqueous solutions ($\sim$ 15-20 mPa·s), while dotted lines are always a guide to the eye. In the lower row, we report the same data sorted depending on antibody type (mAb9 on the left, mAb16 on the right plot) and compared with viscosity values in the normal H_2O buffer at 25°C. Note that the viscosity in the lower plots is the relative η/η_0, where η_0 is the viscosity of D_2O or H_2O at the corresponding temperature. It should also be noted that the concentrations of the measured samples were nominal and not further verified, a fact that introduces a level of uncertainty on the x-axis.

5.5.3 Quasi-elastic neutron backscattering spectroscopy

Temperature dependence of QENS spectra

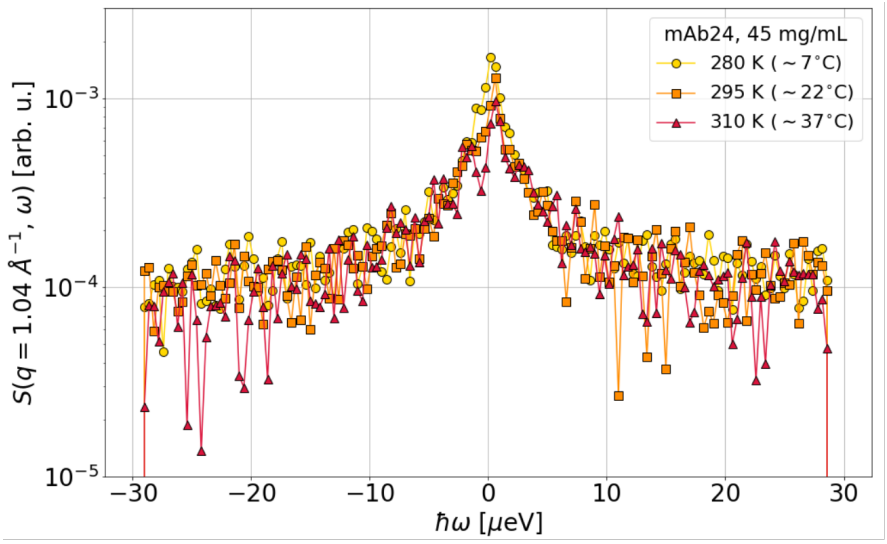

Fig. 5.15. Temperature dependence of QENS spectra without modelling. QENS spectra at q = 1.04 Å^{-1} measured at 280, 295 and 310 K from mAb24 in deuterated 20 mM His-HCl buffer at pD 6.0, at $c_p = (45.38 \pm 1.52)$ mg/mL. Despite c_p being quite low, the signal at the three temperatures shows visible differences especially in the intensity at the elastic peak (at zero energy transfer).

5.5.4 Antibodies as soft colloid suspensions

To interpret the experimental D in a colloid physics framework, a theoretical

$$D^{\text{theo}}(\varphi_t) = D^{\text{theo}}(D_r^{\text{theo}}(\varphi_t), D_t^{\text{theo}}(\varphi_t))$$

was calculated as established in Ref. [306], based on an analytical expression for this implicit function and on the protein hydrogen radial density distribution $\rho(r)$ calculated from the antibody PDB structures using Matlab and shown in Figure 5.16). All parameters entering the calculations for $D_r^{\text{theo}}(\varphi_t)$ and $D_t^{\text{theo}}(\varphi_t)$), namely their dilute-limit values $D_t(0)$, $D_r(0)$ and the bare antibody volume V_{dry} to calculate R_{dry}, were derived via HYDROPRO10 [160] employing again the PDB structure of the antibodies, and for the reference (for polyclonal IgG, using the structures of murine and human immunoglobulin IgG [380, 424]). Also the theoretical radius of gyrations R_g for all the molecules were calculated. The obtained parameters are in Table 5.3.

Antibody	T [K]	$D_t(0)$ [Å^2/ns]	$D_r(0)$ [Å^2/ns]	V_{dry} [nm^3]	R_{dry} [nm]	R_g [nm]
mAb1	280	1.985	0.00044	269	4.00	6.70
	295	3.271	0.00072	″	″	″
	310	4.877	0.00108	″	″	″
mAb9	280	2.017	0.00046	258	3.95	6.57
	295	3.322	0.00076	″	″	″
	310	4.953	0.00113	″	″	″
mAb12	280	1.998	0.00045	273	4.02	6.71
	295	3.292	0.00074	″	″	″
	310	4.909	0.00110	″	″	″
mAb16	280	1.977	0.00045	267	3.99	6.65
	295	3.257	0.00073	″	″	″
	310	4.856	0.00109	″	″	″
mAb24	280	1.996	0.00045	265	3.99	6.66
	295	3.289	0.00075	″	″	″
	310	4.905	0.00112	″	″	″
1IGT	280	1.984	0.00043	258	3.95	6.93
(Ig2 subtype)	295	1.984	0.00071	″	″	″
	310	4.875	0.00106	″	″	″
1IGY	280	1.984	0.00043	258	3.95	5.96
(Ig1 subtype)	295	1.984	0.00071	″	″	″
	310	4.875	0.00106	″	″	″
1HZH	280	1.984	0.00043	258	3.95	6.66
(Ig1 subtype)	295	1.984	0.00071	″	″	″
	310	4.875	0.00106	″	″	″

Table 5.3. Structural and diffusion parameters for all mAbs calculated from their structures. Translational and rotational components of the short-time self-diffusion coefficient at the dilute limit $D_t(0)$ and $D_r(0)$, dry antibody volume V_{dry}, dry radius R_{dry} and radius of gyration R_g at 7, 22 and 37°C (280, 295, 310 K), calculated via HYDROPRO10 [160] for all the antibody types, by employing their PDB structures. For the polyclonal IgG, we report the results obtained from three registered Ig structures: murine immunoglobulins 1IGT (an anti-canine lymphoma monoclonal antibody, IgG2 subtype) [424] and 1IGY (a monoclonal antibody for phenobarbital, IgG1 subtype) [436] and the human antibody 1HZH (neutralizing IGg against HIV-1 b12, IgG1 subtype) [380].

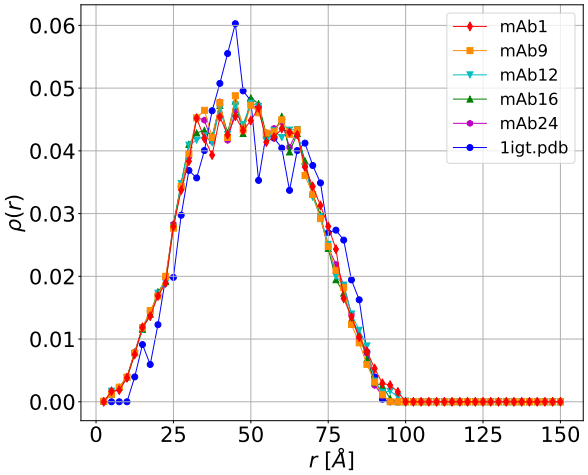

Fig. 5.16. Hydrogen radial distributions from PDB structures. Hydrogen radial distribution $\rho(r)$ of monomeric structures of the proprietary Lonza mAbs and murine antibody (1IGT from Protein Data Bank [424]), obtained from the corresponding PDB files as described in the text. It is remarkable that $\rho(r)$ from the different variants almost perfectly agree, while they differ a lot from the 1IGT structure.

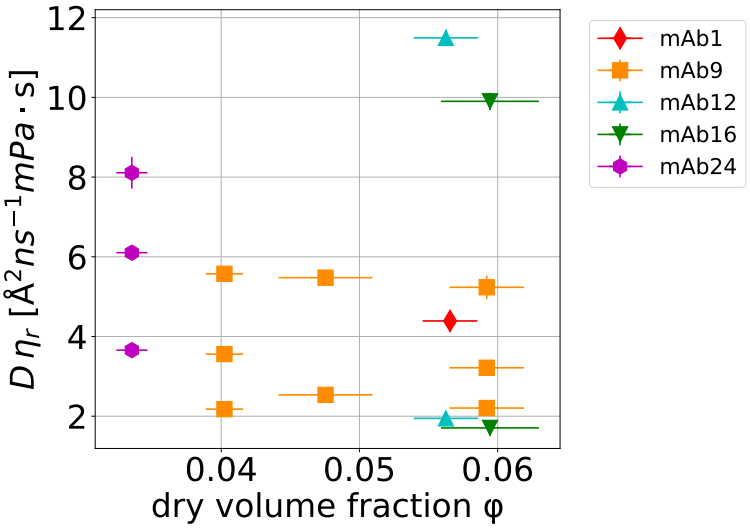

Fig. 5.17. Product of D and η_r *versus* crowding. The product $D \cdot \eta_r$ at 295 K ($\approx 22°$C) is plotted for all mAbs against the protein dry volume fraction φ. The crowding dependence of this quantity is as expected, since D is decreasing at increasing φ (Figure 5.5) and η_r is increasing at increasing φ.

Protein vibrational motions from the Debye-Waller factor

The q-dependent scalar $\beta(q)$ appearing in the $S(q,\omega)$ fit model (equation 5.1) takes into account the vibrational motions of hydrogen atoms in the antibodies. By plotting $ln\beta(q)$ against q^2 and fitting it using a linear function according to equation 5.7, the vibrational mean square displacements $\langle r^2 \rangle$ of

the protein hydrogen atoms can be obtained from the fit slope. An example of this analysis done on one of the samples in shown in Figure 5.18. The influence of temperature increase of these vibrational motions has also been studied (Figure 5.19), revealing an expected increasing of the MSD values when samples are gradually heated.

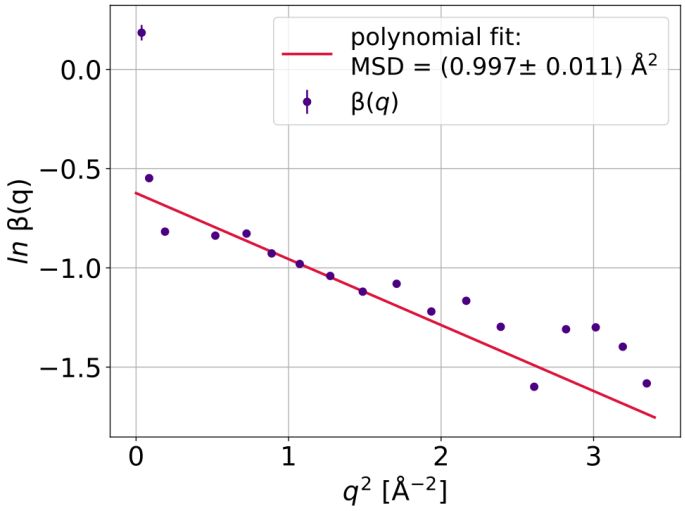

Fig. 5.18. Example of $\beta(\mathbf{q})$ obtained from QENS fits. $\ln(\beta(q))$ *versus* squared momentum transfer q^2 for mAb1 in 20 mM His-HCl buffer in D_2O at 76.53 mg/mL and $T = 280$ K. The slope of the linear fit gives the vibrational MSD of the H atoms in the mAb molecules.

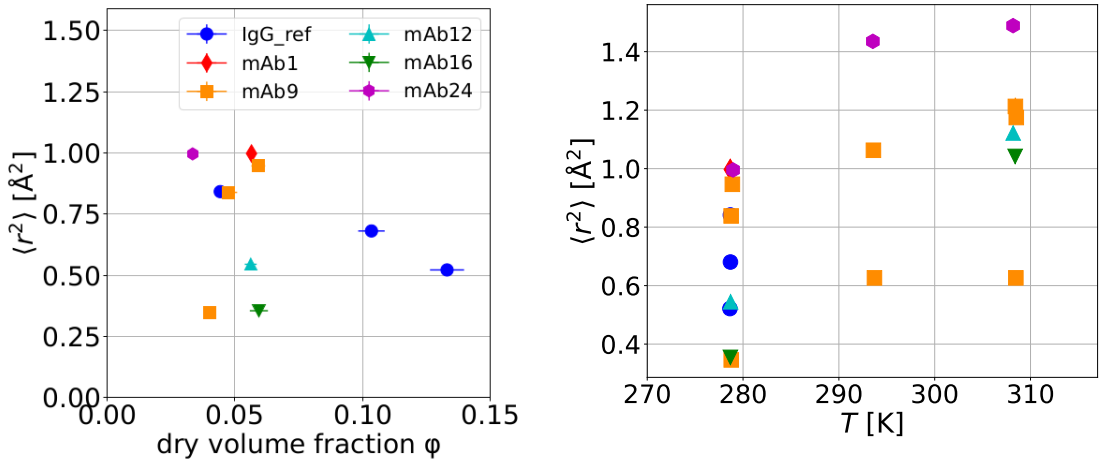

Fig. 5.19. Crowding and temperature dependence of vibrational MSDs in mAb solutions. Vibrational mean square displacements $\langle r^2 \rangle$ of protein hydrogens *versus* dry protein volume fraction φ, obtained from linear fits of $\ln(\beta)$ *versus* q^2 for the mAb studied solutions at $T = 280$ K (left plot). Vibrational mean square displacements $\langle r^2 \rangle$ of protein hydrogens vs temperature T for the mAb solutions (right plot).

5.5.5 Simulations

Block average method

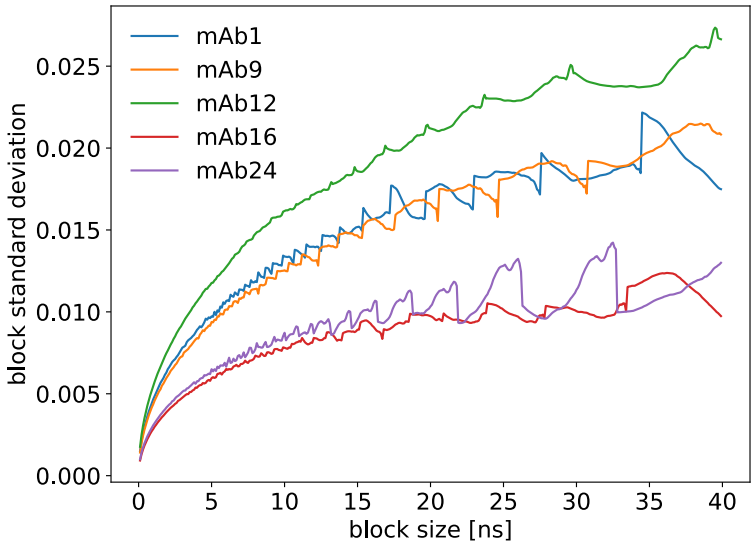

Fig. 5.20. Block average method to determine sampling time threshold. The block average method [414] was used as described in Methods to determine the size of the time blocks to be used to compute the observable used for Figures 5.6, 5.7, 5.8 and 5.9. Image by Dr. Kévin Pounot, co-author of Ref. [194].

Hydrogen bonds dynamics between monomers

To understand what kind of interaction is involved in the protein network dynamics observed on Figure 5.10, the time auto-correlation of hydrogen bonds formed between individual monomers was computed (Fig. 5.21). It appears that hydrogen bond autocorrelation decays similarly for mAb9, mAb12 and mAb24. Hence compared to the graph dynamics observed on Figure 5.10, the hydrogen bonds do not seem to have a significant effect on the cluster dynamics difference between the mAbs tested here. This indicates that hydrogen bonds have little effect on viscosity, which is thus determined mainly by other forces such as electrostatic interactions mediated by the charges on the variable regions as observed on Figure 5.9.

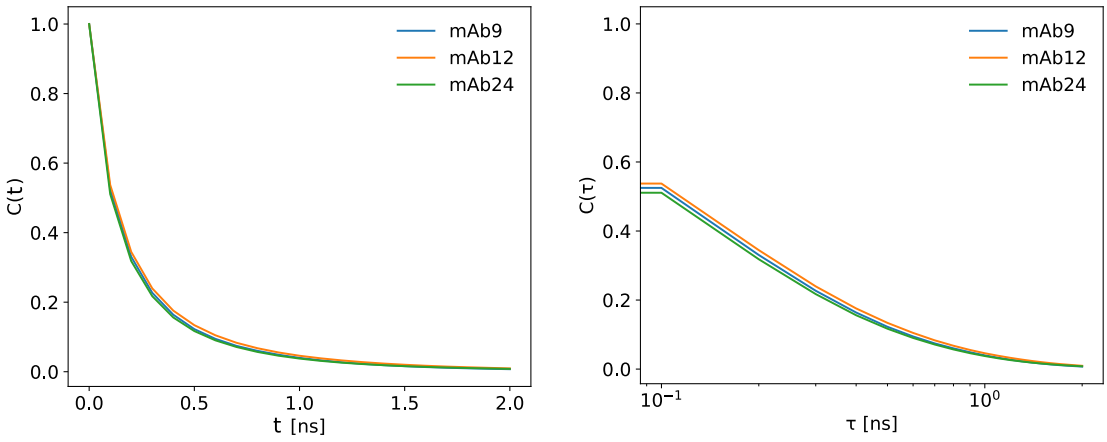

Fig. 5.21. Hydrogen bond network relaxation of mAbs in solution from simulations. The hydrogen bonds were identified and their lifetime computed using the MDanalysis Python package [420, 421]. The hydrogen bonds lifetime were computed for each pair of monomers in the simulation trajectory and averaged over trajectory frames and pair of monomers. The resulting autocorrelations $C(t)$ depending on time t, reported in both linear (left) and logarithmic scale (right), are represented in blue for mAb9, orange for mAb12 and green for mAb24. Images by Dr. Kévin Pounot, co-author of Ref. [194].

5.5.6 Small angle scattering

Fit parameters

Antibody	T [°C]	R_a[Å]	R_b[Å]	background [cm^{-1}]	stickiness τ
mAb9	21	7.46181	50	0.019	-
	37	7.52797	50	0.019	-
mAb12	21	7.7412	60.7799	0.0183958	0.126221
	37	7.8458	58.3276	0.0183924	0.15227
mAb24	21	7.92158	57.4777	0.025864	0.158688
	37	7.94632	56.3973	0.025599	0.189863

Table 5.4. SANS fit parameters. Parameters obtained from the fit of SANS data with a combination of an ellipsoid form factor $P(q)$ and a sticky hard sphere (mAb12, mAb24) or normal hard sphere (mAb9) structure factor $S(q)$. For all samples, the dry volume fraction of the antibodies is $\varphi = 0.05912$, while the perturbation parameter for mAb12 and mAb24 was fixed at a value of 0.01. As mentioned above, neither stickiness nor perturbation parameters are entering the fit for mAb9.

Structure factor from SANS fits and antibody flexibility revealed by SANS

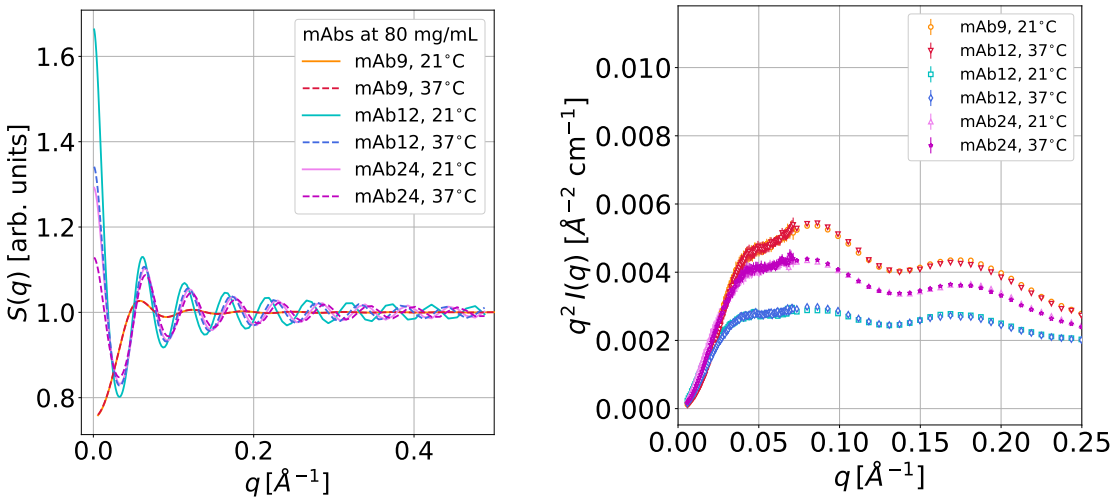

Fig. 5.22. Structure factor from SANS fits and Kratky plot of SANS data for a subset of mAbs. Left: Structure factor $S(q)$ vs q for mAb9, mAb12 and mAb24 at 21 (solid lines) and 37°C (dashed lines) obtained from fits of background-corrected SANS data. The q-range used for the determination of $S(q)$ is (0.001, 0.488008) Å^{-1}. Note that the fit for mAb9 was performed using a hard-sphere structure factor, while a sticky hard-sphere potential was used for the two other mAbs. Curves for mAb9 at 21 and 37°C show a perfect overlap. **Right:** SANS intensity $I(q)$ multiplied by q^2 plotted against the momentum transfer q for mAb9 (orange and red symbols), mAb12 (cyan and blue symbols) and mAb24 (pink and purple symbols), at 21 and 37°C, all at the same $c_p = 80$ mg/mL. Despite their different intensities, the two bumps are a persisting feature in all curves, confirming the multi-domain structure of the proteins studied. The trend of the curves at high q denotes a pronounced molecular flexibility of the mAbs.

Chapter 6

Multi-scale diffusion, dynamic cluster formation and inter-molecular interactions in pharmaceutically relevant monoclonal antibody formulations

Chapter 6 is the basis for the following publication:

Multi-scale diffusion, dynamic cluster formation and inter-molecular interactions in pharmaceutically relevant monoclonal antibody formulations (in preparation)

Authors: Ilaria Mosca[1,2], Christian Beck[1,2], Laura Mateo-Miñarro[1,2,4], Roody Nasro[1], Anna Grundel[2,6], Ingo Hoffmann[2], Kévin Pounot[5], Olga Matsarskaia[2], Christoph Grapentin[3], Tilo Seydel[2], Frank Schreiber[1,2]

[1]*Institut für Angewandte Physik, Universität Tübingen*, Germany [2]*Institut Max von Laue-Paul Langevin*, Grenoble, France [3]*Lonza AG/Ltd.*, Basel, Switzerland [4]*Université Grenoble-Alpes*, Saint-Martin d'Hères, France [5]*European Synchrotron Radiation Facility*, Grenoble, France [6]*Fakultät für Physik und Astronomie, Universität Heidelberg*, Germany

Author contribution: All authors performed experiments, contributed to data analysis and in writing the manuscript. I. M. wrote the manuscript first draft. I. M., C. B., L. M. M., R. N., A. G. prepared the samples. F. S., T. S., O. M. and C. G. designed the research and are co-proposers and supervisors of the associated InnovaXN project (innovaxn.eu).
Experiments: Data presented in this chapter were collected during ILL experiment 8-04-932.

Abstract

Due to their specificity and versatility, monoclonal antibodies (mAbs) are the most popular class of biopharmaceuticals, spanning a wide range of therapeutic applications and typically administered via intravenous injection. One of the current pharmaceutical challenges concerns mAb formulations for subcutaneous (SC) injection, which is becoming of increasing importance as an alternative administration route offering convenience to patients by allowing self-administration compared to other parenteral delivery methods. With volumes lower than 1-2 mL being better tolerated in the subcutaneous space, highly concentrated mAb formulations are needed to achieve significant therapeutic effects, potentially increasing solution viscosity and altering drug injectability. The main challenge is maintaining solution viscosity below the SC injectability threshold (15-20 mPa·s) while preserving solution stability. Since the understanding of macroscopic viscosity requires an in-depth knowledge on protein multi-scale diffusion, mutual interactions and aggregation, we employ two complementary neutron scattering techniques to investigate 9 different mAbs of IgG1/IgG4 subtypes in aqueous solution as a function of protein concentration and temperature. The synergy between neutron spin-echo (NSE), a spectroscopy technique providing dynamic information, and small angle neutron scattering (SANS), a time-averaged static technique, enables us to probe the short-time collective diffusion of the different mAbs, explore their self-association into small transient clusters, their inter-molecular interactions and ultimately access their internal dynamics. This study builds on previous neutron backscattering (NBS) findings, bridging a critical gap between the timescales probed by NBS and viscometry. It also confirms that the formation of short-lived clusters comprising more than two monomers is a key factor driving high solution viscosity, phase separation, and opalescence.

6.1 Introduction

Scientific relevance When Köhler and Milstein developed the Nobel-prize winning hybridoma technology in the '70s [69], it was not immediately obvious at that time that monoclonal antibodies (mAbs) would become the most popular class of biopharmaceuticals. This technology was employed to develop Orthoclone OKT3® (muromonab-CD3), which became the first monoclonal antibody approved by the U.S. Food and Drug Administration (FDA) [70]. Since that time, antibody therapeutics research and development have experienced a remarkable growth, especially in the last two decades. Until the end of 2023, nearly 200 mAbs in total have received approval in the U.S. or other countries, with 13 new ones in 2023 [71], 21 in 2024 [72,73], and more were forecast to be either approved or to enter regulatory reviews by the end of 2025 [73]. The already broad spectrum of clinical applications of these biopharmaceuticals is currently expanding and includes the treatment of several types of cancers [74–76], infectious and autoimmune diseases [77,78], multiple sclerosis [79], kidney diseases [80], migraine [81,82] and the prevention of malaria [437]. In the last two decades, the development of mAbs for the treatment of neurodegenerative pathologies such as Alzheimer's disease has been the subject of an extensive research [83–85,438], but still a lot of work has to be done for substantial steps forward [86,87].

Motivation Due to the extremely acidic environment of the gastrointestinal tract and mostly to the challenges related to absorption and bio-distribution via this route, monoclonals cannot be administered orally without suitable delivery vehicles [106]. Therefore, the more suitable route is parenteral administration via intravenous (IV) or subcutaneous (SC) injections. Whereas IV refers to inject-

ing the drugs directly in the blood vessels, with SC the substance is injected into the subcutaneous space. IV administration is normally performed in hospitals by specialised personnel, which is not always practical and a limiting factor for patients suffering from chronic diseases and requiring life long treatment. In recent years, pharmaceutical research has been working to engineer and produce antibody formulations specific for SC injection [88,89] in order to enable patients to benefit from self-administration and more flexibility [90–92]. Moreover, SC administration allows a sustained systemic availability of the drug due to slower transfer from subcutaneous tissue (into blood) and reduced side effects due to avoidance of concentration peaks.

Since the amount of antibody needed to achieve a significant therapeutic effect is around hundreds of mg and the injectable volume in the subcutaneous space is in the range of 0.5-2 mL, this administration route requires high concentrations (in the 100-200 mg/mL range), potentially leading to viscosities exceeding a tolerance threshold of ∼15-20 mPa·s (or cP) [93, 94]. High viscosity translates into high injection forces or long injection times [88, 95]. Besides rendering the drug administration painful or difficult (and sometimes impossible), high viscosity may also compromise the physicochemical stability of these pharmaceuticals before, during and after the injection [96, 97]. Since the procedure of SC injection alone overall reduces the physicochemical stability of mAbs [439], controlling their solution viscosity is of great interest. To this end, several studies on the microscopic origin of macroscopic viscosity of highly concentrated mAb solutions have been conducted to optimize their design and manufacturability [98,99] by attempting to reach a fundamental understanding of this phenomenon and, ultimately, to design strategies for viscosity reduction.

State of the art Proteins in solution may undergo reversible self-association (RSA) and potential irreversible aggregation, two dissimilar processes in terms of physicochemical properties [440–442], but equally concerning issues for manufacturability. RSA has been identified as one of the main reasons for high viscosity in mAb solutions [100, 101] and can be influenced by multiple parameters including concentration, pH, temperature, ionic strength [100], or specific interactions between protein domains [102, 103]. On a macroscopic level, RSA strongly impacts the visual appearance of antibody solutions, causing opalescence, increased turbidity and even phase-separation [196, 443–447]. Both electrostatic and hydrophobic protein-protein interactions (PPIs) seem to play a role in driving RSA [104] and thus in increasing solution viscosity. As a result, minimizing protein self-interactions is the key for viscosity reduction and it can be achieved through two complementary approaches: protein engineering and formulation optimization.

Protein engineering is usually the first explored route for viscosity reduction based on applying small modifications in the antibody primary sequence and predicting how viscosity is affected by those. Kastelic et al. found that different viscosity trends depend on how the different mAb binding sites – Fab and Fc – contribute to aggregation, proving that inter-molecular interactions and, hence, viscosity are controllable through modifying specific sites of the antibody [181]. Some works involving experiments and simulations established predictors for viscosity, aggregation and inter-molecular interactions based on amino acid sequences, structural properties, charge distribution and hydrophobicity of the full sequences and the Fv region of the antibodies [383–386, 389, 390, 448]. By predicting viscosity using artificial neural networks based on experimental and simulation-derived parameters, Schmitt et al. confirmed that sequence-based optimization of mAb properties is a crucial tool for rational drug design [184]. More recently, Armstrong et al. observed that antibody sequence mutations aiming to reduce hydrophobic patches significantly reduced mAb solution viscosity, suggesting the effectiveness of hydrophobic based predictors; conversely, mutations altering only electrostatic

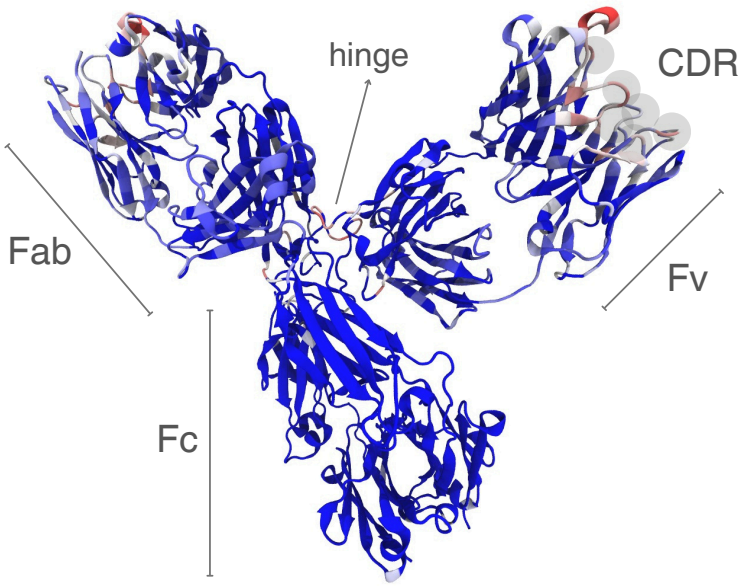

Fig. 6.1. Stucture of an IgG4 mAb and sequence similarity with IgG1 mAbs. The sequences of the mAbs were aligned using VMD [377] 'MultiSeq' module [378] with ClustalW algorithm [356] and their results shown by sequence similarity using BLOSUM100. Sequence similarity is shown directly in the structure of mAb4* (IgG4) and represented with a colour ranging from blue for high similarity to red for low similarity. The graphic was rendered with 'NewCartoon' style. The different mAbs under study show almost identical structures in the Fc region, while they differ in their variable domain Fv, especially in the six CDR loops (or hypervariable regions, highlighted in grey) responsible for the binding with the antigen.

patches were insufficient to influence viscosity [185]. Variable domain mutational analysis identifies Fab-Fab hydrophobic interactions – rather than electrostatic ones – as the major contributors to the high viscosity of an anti-GCGR IgG1 [180]. In line with this approach, Li et al. developed a promising tool for controlling mAb aggregation based on systematic pairwise replacement of hydrophobic residues L (leucine), V (valine)/I (isoleucine), and F (phenylalanine) with Q (glutamine), T (threonine) and Y (tyrosine) [449]. Machine learning was also extensively employed to reduce mAb viscosity, always emphasizing the relevance of the Fv domain in the underlying molecular mechanism [182,183].

Concerning formulation optimization, a widely employed strategy is to improve the formulation by adding molecules able to shield and/or tune those interactions and to reduce the solution viscosity. So far, some successful excipients have been found among salts (NaCl, Na_2SO_4, NaAc) [125] and amino acids in their pure or salt forms (arginine, glycine, proline and ornithine, arginine-HCl, histidine-HCl, lysine-HCl) [125, 127–130]. Other molecules with analogous effects are hydrophobic salts [134], caffeine [135], amino acid derivatives [136] and even amino acid polymers [137]. Moreover, the combination of some viscosity-reducing agents, e.g. amino acids and anionic excipients, has also been observed to enhance the performance of one excipient alone [131].

Framework of the present study Despite the progress made in the field, the correlation between viscosity, RSA and cluster formation is still being studied using several techniques including small-angle X-ray and neutron scattering, microrheology, viscometry, atomistic and coarse-grained simula-

tions and colloid theory [172–174,203,232,448,450]. In the present work, we systematically investigate a set of 9 humanized mAbs produced, characterized and provided by Lonza AG/Ltd. These mAbs in solution feature big changes in macroscopic viscosity for a given concentration; some of them – mAb12, mAb16, mAb24 – exceed the SC injectability limit of 15-20 mPa·s before high concentrations (see Figure 6.2 and Refs. [184, 194]). However, the most significant differences in their amino acid sequences are in the hypervariable regions of their Fv domains (Figure 6.1), which confirms that the Fc domain plays a minor role in inter-protein interactions [451] compared to Fv domain.

In order to systematically explore the link between macroscopic viscosity and microscopic cluster formation, we combined neutron spin-echo (NSE) spectroscopy and small angle neutron scattering (SANS) experiments, expanding on previous work where we employed neutron backscattering (NBS), SANS and MD simulations [194]. Several mAbs already investigated in that work show an apparent self-diffusion coefficient D below the value expected for monomers suggesting the formation of small transient clusters formed by few monomers. NSE was already confirmed as an effective technique to study concentrated mAb solutions [229, 234, 235, 452], revealing the formation of small "reversible clusters with extended open structures" [234] or dimers which can "reversibly associate into loosely connected clusters" [229], likely resulting in higher viscosities [100,229]. NSE allows to investigate several mesoscopic diffusive modes of the proteins at once [229,234,235,452,453], e.g. translational and rotational components [273, 453], and domain motions. Importantly, due to the longer time scales (up to $200\,$ns) compared to the previously collected NBS data ($\approx 4\,$ns), these NSE data close a critical gap in the observation times between the results from viscometry and NBS.

IgG1 and IgG4 antibodies IgG is the most abundant class of immunoglobulins in human blood and the most used in therapeutics. IgG is a Y-shaped ∼150 kDa protein formed by two identical heavy chains (HC) of ∼50 kDa each and two identical light chains (LC) of ∼25 kDa each, cross-linked through interchain disulphide bonds. Both heavy and light chains contain a variable domain (VH/VL) and a constant one (CH, CL); two CH sub-domains (CH_1, CH_2) are linked by a flexible hinge [379, 380] which gives IgG a pronounced mobility. In addition, CH_2 and CH_3 sub-domains of the heavy chains form the trunk of the Y-structure, which is called Fc (crystallisable fragment), whereas the two arms of the molecule are formed by CH_1, CL, VH and VL and are called Fab (antigen-binding fragments). At their extremities, the subdomains VH and VL constitute the variable domain Fv that acts as the actual antigen-binding site. The binding occurs in specific Fv segments, referred as complementarity determining regions (CDRs) or hyper-variable regions, typically exhibiting loop structures (Figure 5.1).

IgGs exist in four different isotypes – IgG1, IgG2, IgG3, and IgG4 – which differ in multiple structural and functional details. The present study focuses on IgG1 and IgG4 antibody isotypes. The length of the hinge is of 15 amino acids in IgG1 and 12 in IgG4, leading to the formation of four interchain disulphide bonds in IgG1 and two in IgG4 and resulting in IgG1 being more flexible than IgG4 [454]. The hinge stabilization in IgG4 is believed to arise from the amino-acidic substitution Ser228Pro (proline to serine at position 228) from IgG1 [455]. The two isotypes also differ in the angles between the Fab regions [456], in their immune response [457], viscosity behaviour at high concentrations [458] and self-interactions [448].

6.2 Materials and Methods

6.2.1 Sample Preparation

In the present work we investigate 8 different humanized monoclonal antibodies of IgG1 isotype with κ light chains – referred as mAb3, mAb5, mAb9, mAb19 and mAb25 – and λ light chains – mAb12, mAb15, mAb16 – and one mAb of IgG4 isotype with κ light chains – mAb4*. Further physicochemical properties of these mAbs are reported in Section 6.5 for both full chains and Fv domains.

All mAbs were manufactured in-house from Lonza AG/Ltd. Double gene vectors (DGV) containing the heavy and light chains were transfected into CHOK1SV GS-KO$^{\mathrm{TM}}$ cells [394] from Lonza Biologics (Slough, UK) and cultured under selection conditions as stable pooled cultures. Clarified supernatant was obtained by centrifugation followed by filter sterilization using 0.22 µm Stericup® Quick Release filters from Merck/MilliporeSigma (Darmstadt, DE). Protein A chromatography was used for mAb purification. All proteins were concentrated to final concentrations of 10-20 mg/mL (nominal) and buffer exchanged into the formulation buffer by tangential flow filtration. A 20 mM Histidine-HCl buffer at pH 6.0 was employed as it is done for more than 80% of formulations of approved highly concentrated mAb drug products [348]. All mAb solutions were then frozen in aliquots, stored at -80°C and slowly thawed prior to use.

From these solutions, samples for the neutron experiments were prepared by first exchanging the buffer to 20 mM Histidine-HCl in pure D_2O at pD 6.4 (pD = pH + 0.4, so pH = 6.0 [459]). To this scope, 15 mL Amicon® centrifugal filters with 30 kDa nominal molecular weight cutoff from Merck/MilliporeSigma were employed to obtain a dilution factor of at least 10000x of the H_2O in the samples. With the same filters, mAb solutions were then concentrated until around 2 mL, in order to reach a concentration of at least 60 mg/mL. The aforementioned deuterated buffer was prepared by dissolving L-Histidine monohydrochloride monohydrate ($\geq$ 98% purity) from Merck/MilliporeSigma in deuterium oxide from Innovachem (Angervilliers, FR) to get a molarity of 20 mM; the desired pH was reached by adjusting with NaOD and the obtained solution was filtered using a 0.22 µm Stericup® QuickRelease from Merck/MilliporeSigma. Concentrations of the antibody solutions after buffer exchange were determined by UV-Vis via a V-630 Spectrophotometer from Jasco (Tokyo, JP), diluting them 50, 100, 200, 400 and 500x. Samples for neutron experiments were subsequently prepared by diluting concentrated stock solutions until 50 mg/mL. As reference, a polyclonal IgG stock solution was prepared employing lyophilized powder of γ-globulin from bovine serum ($\geq$ 95% purity, essentially salt-free), purchased from Merck/MilliporeSigma and directly dissolved in a 20 mM Histidine-HCl deuterated buffer at pD 6.4. Concentration of the stock solution was measured via UV-Vis and the actual sample was prepared diluting the stock solution to 50 mg/mL (nominal, not further measured). It should be noted that solutions of protonated (^{1}H) proteins in D_2O (^{2}H) are required in neutron scattering experiments, in order to distinguish the signal arising from the macromolecules from the solvent one.

The selected concentration of 50 mg/mL has been targeted to safely avoid overlapping among the proteins in solution in the neutron spin-echo measurements, based on the following considerations. Since the distances between the extremal residues of the antibodies are on average shorter than $d_{\max} \approx 16$ nm (slightly overestimated, see Section 6.5), each protein occupies a cubic volume of side-length $d_{\max}$ and therefore can move in a maximum volume $V_{\max} \approx 4096$ nm^3 in the solution. Since a sample volume $V_{\mathrm{sample}} \sim 2$ mL is needed for the neutron experiments, the maximum number of mAbs in the sample would then be $N_{\max} = V_{\mathrm{sample}}/V_{\max} =$ (2 mL) / (4096 nm^3) $\sim 4.88 \times 10^{17}$,. The

overlap protein concentration can be therefore determined as follows:

$$c_p^{\text{overlap}} = [\text{mAb}]^{\text{overlap}} \cdot \text{MW} = \frac{N_{\max}}{N_{\text{A}} \cdot V_{\text{sample}}} \cdot \text{MW}\,, \tag{6.1}$$

with N_{A} being the Avogadro number (6.022×10^{23} mol^{-1}) and MW the antibody molecular weight ($\sim$150 kDa). $[\text{mAb}]^{\text{overlap}}$ indicates the overlap mAb molarity calculated as $N_{\max}/(N_{\text{A}} \cdot V_{\text{sample}})$ – number of mAb moles in the sample divided by the sample volume – giving a value of 0.406 mM. The overlap protein concentration c_p^{overlap} is thus $\sim$ 61 mg/mL, higher than the selected 50 mg/mL.

6.2.2 Viscometry and light scattering

All the mAbs were characterised by viscometry, static and dynamic light scattering (SLS and DLS) as reported in Schmitt et al. [184] and Mosca et al. [194]. The measurements were performed at $T = 25$°C ($\sim$298 K), with concentrations ranging from 180 to 30 mg/mL, in the antibody original formulation buffer (20 mM His-HCl in H_2O, pH 6.0). The instruments used and the measurement protocols are described in Refs. [184, 194].

6.2.3 Neutron Spin Echo (NSE) Spectroscopy

Neutron spin echo (NSE) experiments were conducted at the IN15 spectrometer at the Institut Laue-Langevin (ILL) in Grenoble, France. NSE is a high-resolution inelastic scattering technique that leverages neutron spin precession to measure velocity changes experienced by neutrons as they interact with matter. This method offers exceptional resolution, allowing to investigate multi-scale short-time collective dynamics. Samples were measured at four different instrument configurations, each with a specific incident neutron wavelength and detector angular position (measuring the scattered neutrons): 10 Å - 3.5°, 8 Å - 5.5°, 6 Å - 9.5° and 6 Å - 6.5°. The accessible q range spans from 0.028 to 0.19 Å^{-1}, for a total of 12 values of the momentum transfer q, resulting from slicing the detector in 3 areas for each configuration. This instrumental setup allows to explore Fourier times up to 200 ns for the 10 Å - 3.5° configuration, up to 100 ns for the 8 Å - 5.5° one and up to 50 ns for the two configurations at 6 Å.

All samples were loaded in flat transparent quartz containers purchased from Aireka Scientific Co., Ltd. (Hong Kong) with the size of 40 x 30 mm and internal thickness of 1 and 2 mm (depending on protein availability), closed with plastic caps and carefully sealed with Parafilm® (Merck / MilliporeSigma) to avoid evaporation of the solutions along the measurements. A graphite sample and the antibody formulation buffer (20 mM His-HCl in D_2O at pD 6.4) were measured as references for resolution and background, respectively. The sample environment employed was a sample changer with temperature control. All samples were first measured at $T = 37$°C ($\simeq$ 310 K), temperature of the human body, and afterwards at $T = 7$°C ($\simeq$ 280 K), which is closer to the usual storage temperature of biopharmaceuticals just before administration to patients. A complete acquisition run – accounting for the four aforementioned configurations – was about 4 hours for one sample at one temperature. Two samples, selected for their high viscosity, slightly milky appearance and higher clustering propensity [194] – mAb12 and mAb16 –, were additionally measured while cooling down at just one instrument configuration (6 Å - 6.5°) in order to further explore any temperature-driven changes. In this case, echoes were acquired at 4 different temperatures and the whole measurement time was $\sim$1 hour. Raw data were resolution-corrected and background-subtracted applying standard data reduction routines in Igor [460]. Further analysis was performed using Python.

6.2.4 *In situ* fixed-angle dynamic light scattering (DLS) during NSE measurements

Dynamic light scattering (DLS) measurements at a fixed angle of $\theta = 90°$ were concurrently obtained using an in-situ DLS system integrated into the NSE machine. The employed setup is a He-Ne laser with a wavelength of 632.8 nm. Detection was carried out by two Excelitas SPCM AQRH-13 APD detectors, and the correlation function was computed using a Flex02-01 digital correlator in pseudo-cross correlation mode to mitigate artifacts at short correlation times caused by detector after pulsing. Unlike standard DLS experiments, in this setup the autocorrelation functions were averaged over the duration of an NSE scan, which is on average one hour for each wavelength-angle combination. As in the NSE experiment, DLS profiles for mAb12 and mAb16 were collected also while cooling down.

6.2.5 Small Angle Neutron Scattering (SANS)

Small-angle neutron scattering (SANS) was performed on the same mAb solutions measured with NSE, in order to determine their time-averaged structural and thermodynamical properties as a function of temperature and protein type. The SANS experiments were carried out on D22 [400] at the ILL. Antibody solutions at 50, 20, 10, 5, 2, 1 mg/mL were prepared, filled into 1 mm plate quartz cuvettes (Hellma, Müllheim, DE), sealed with Parafilm® and placed onto a copper sample holder. A q range from 0.006 - 0.7 Å^{-1} was covered by two sample-to-detector distances (16 and 1.7 m) with respective collimation lengths of 16.5 and 2.5 m. A wavelength of 4.6 Å with a full width-half maximum (FWHM) wavelength spread of 9% was used. Scattered neutrons were detected using a multitube ^{3}He gas detector with a pixel size of 4 × 8 mm^2. SANS profiles were obtained at a set-point temperatures T_{set} of 37 and 22°C, corresponding to $\sim$ 310 and $\sim$ 295 K, respectively. For a reduced dataset, SANS curves were also measured at 7°C, corresponding to $\sim$ 280 K. The actual temperature of the sample changer rack was monitored throughout the experiment to check how it differed from that of the set-point. For the three temperatures selected ($T_{\mathrm{rack}} \pm \Delta T_{\mathrm{rack}}$) was calculated, with T_{rack} and ΔT_{rack} being the mean and the standard deviation of the values, respectively (Table 6.1). The largest temperature fluctuations were observed at $\sim$ 37°C, as reported in Table 6.1.

Raw data were saved in NeXuS format [401,402] and data reduction was performed using Graphical Reduction and Analysis SANS Program (GRASP), an ILL Matlab™ based software [461]. Data were corrected for empty cell scattering, transmission (by measurements performed using beam attenuators) and electronic noise (by measuring a $^{10}B_4C$ absorber). Calibration to absolute scale was performed using attenuated direct beam measurements. The signal of the solvent (20 mM His-HCl deuterated buffer at pD 6.4) at 7°C was chosen as reference – due to its lower incoherent baseline at high q compared to the buffer profiles at 21 and 37°C – and subtracted from sample scattering accounting for the volume occupied by the solvent:

$$I(q)^{\mathrm{sub}}_{\mathrm{sample}} = I(q)_{\mathrm{sample}} - \varphi_{\mathrm{solvent}} \cdot I(q)_{\mathrm{solvent}} \tag{6.2}$$

With $\varphi_{\mathrm{protein}}$ being the protein volume fraction, the volume occupied by the solvent in the samples is given by:

$$\varphi_{\mathrm{solvent}} = (1 - \varphi_{\mathrm{protein}}) = (1 - c_p \vartheta) \tag{6.3}$$

where c_p and ϑ are the protein concentration and specific volume, respectively. ϑ was calculated with MDAnalysis [421] using the PDB of the mAbs and obtaining 0.739 mL/g for mAb3, 0.729 mL/g for mAb5, mAb9, mAb12, mAb15, mAb16, mAb19, mAb25 and 0.727 mL/g for mAb4*.

$\mathbf{T_{set}}$ [°C]	$\mathbf{T_{rack} \pm \Delta T_{rack}}$ [°C]
37	34.59 ± 1.63
22	21.83 ± 0.21
7	7.21 ± 0.77

Table 6.1. Differences in the set-point and measured temperatures of the sample changer rack throughout the SANS experiment. The values reported T_{rack} and ΔT_{rack} are respectively the mean and the standard deviation of the temperatures probed by the rack thermometer during the measurements.

6.3 Results and Discussion

6.3.1 Viscometry and light scattering

As described in Refs. [184, 194], the relative viscosity $\eta_r = \eta/\eta_0$ (with $\eta_0 = \eta_{\mathrm{solvent}} = 0.92$ mPa·s) was analysed at varying antibody concentration c_p (Figure 6.2). Some data on viscosity and light scattering, e.g. A_2 and $\mathrm{k_D}$ results, are taken from Refs. [194] and included here for clarity. The data already shown in Ref. [194] correspond to mAb1, mAb9, mAb12, mAb16, mAb24, while the additional ones reported here refer to mAb3, mAb5, mAb4*, mAb15, mAb19, mAb25. The viscosity increase at increasing antibody concentration is strongly mAb-dependent and is well-described by the model used in our previous work [194]. From the fit model used, the viscosity values for the protein solutions at 50 mg/mL – which is the concentration employed in the neutron experiments – were extrapolated (Table 6.2). From Figure 6.2, one can observe that all mAbs eventually reach the viscosity limit for syringeability; however, while mAb9, mAb15, mAb25 and mAb4* exhibit high viscosity at $\simeq 180$ mg/mL, for some others this is observed already at 140 (mAb16), 120 (mAb12) and 90 mg/mL (mAb24).

MAb	$\eta_{\mathbf{r}}$ **(50 mg/mL)**
mAb1	1.46 ± 0.14
mAb3	1.56 ± 0.14
mAb5	1.47 ± 0.19
mAb9	1.47 ± 0.18
mAb4*	1.55 ± 0.37
mAb12	1.78 ± 0.46
mAb15	1.41 ± 0.06
mAb16	1.63 ± 0.14
mAb19	1.39 ± 0.26
mAb24	2.60 ± 0.24
mAb25	1.55 ± 0.11

Table 6.2. Relative viscosities $\eta_r = \eta/\eta_0$ ($T = 25$°C) at mAb concentration $c_p = 50$ mg/mL calculated from the model used to fit the data in Figure 6.2. Uncertainties associated with the values are calculated by error propagation using the errors on the parameters derived from the fit. The samples characterised by high η_r at high c_p show higher values compared to the others already at 50 mg/mL.

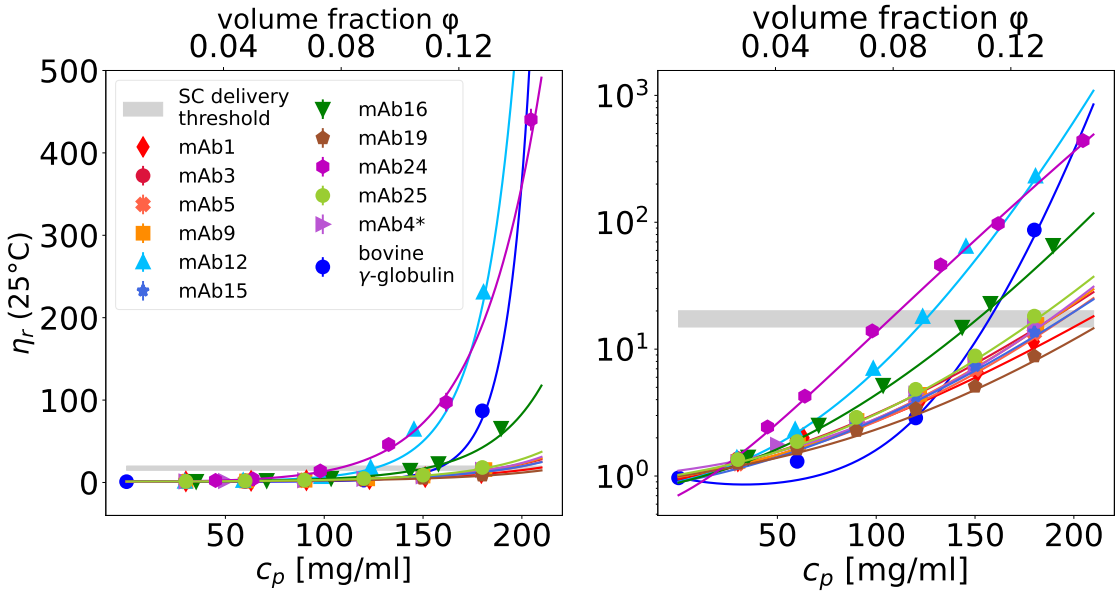

Fig. 6.2. Linear (left) and logarithmic (right) plots showing the relative viscosity $\eta_r = \eta/\eta_0$ (symbols) of aqueous (H_2O) solutions of 10 mAbs of IgG1 subclass and one IgG4 mAb (mAb4*) in 20 mM His-HCl buffer (pH 6.0) at $T = 25°C$, versus mAb concentration c_p (lower x-axis) and dry volume fraction φ (upper x-axis). Errorbars are mostly hidden behind the symbols. Solid lines are fits to the data using a heuristic model [194]. The grey shaded area stands for the subcutaneous (SC) injectability threshold ($\sim$ 15-20).

Primary sequence analysis (available in Sections 6.5 and 4.3.2) reveals that the pI of Fv domain of mAb4*, mAb12, mAb15, mAb16 and mAb24 is < 6.3, identified for mAbs analysed in the work by Makowski et al. as threshold value below which lay all the mAbs with high solution viscosity [183]. Fv pI values are in fact 5.44 for mAb4* and mAb12, 5.74 for mAb15, 5.34 for mAb16, and 5.83 for mAb24. Moreover, the Fv net charge for these mAbs with high viscosities is closer to 0 compared to that of the other variants and always slightly negative (see Figure 6.17). One could hypothesize that for these mAbs the charges on VH/VL regions are essentially equal and opposite, with a slight imbalance on the negative side, in agreement with their opposite correlations with viscosity [194]. These observation underline again the importance of Fv domain sequence and confirm its central role in driving inter-molecular interactions in the mAbs [180, 451]. The differences in viscosity depend on which protein subdomains drive the aggregation and how the oligomers are formed and organised [181, 451]. Highest viscosities are apparently determined by a strong presence of Fab-Fc association [181, 446] or Fab-Fab interactions [101, 173, 180]. Both association mechanisms could contribute to high viscosities in mAb24, mAb16 and mAb12 solutions. Fc-Fc association is also likely to be present and possibly mediated by a small hydrophobic patch at the bottom of the Fc domain (see Section 6.5). However, since the Fc domain is highly similar in all the mAbs studied (Figure 6.1), Fc-Fc cannot explain the increase in viscosity observed in only a few variants (see also Section 6.5.4). With regards to light scattering methods, the second virial coefficient A_2 from static light scattering (SLS) and the diffusion-interaction parameter k_D from dynamic light scattering (DLS) can provide insights into the solution behaviour of the mAbs by understanding their PPIs, which directly im-

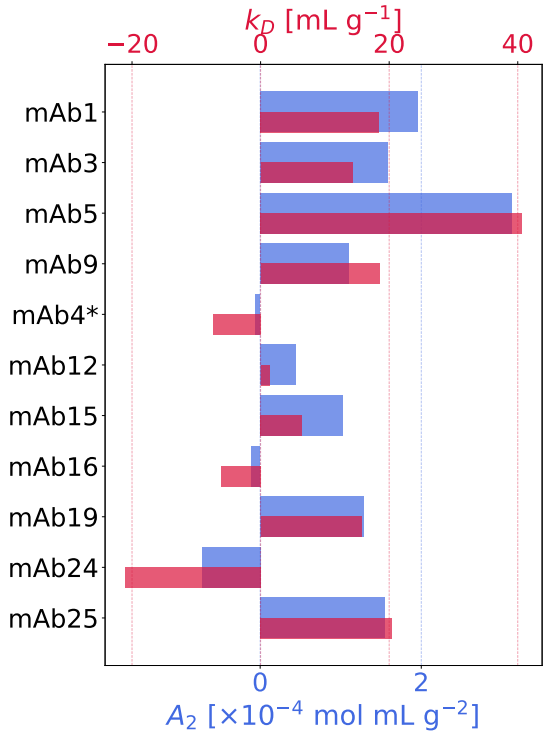

Fig. 6.3. Second virial coefficient A_2 from SLS (lower x-axis) and diffusion-interaction parameter k_D from DLS (upper x-axis) for the mAbs investigated in their original formulation buffer (20 mM His-HCl in H_2O, pH 6.0) at $T = 25°C$.

pact their physicochemical stability. These two key parameters obtained by Schmitt et al. [184] are represented here in Figure 6.3 and their exact values are reported in Section 6.5. A_2 and k_D are generally correlated, with positive values indicating repulsive interactions between mAb molecules, while negative values suggest attractive interactions. Repulsive interactions typically lead to better solution stability, whereas attractive interactions may promote aggregation. Among the mAbs studied, a wide range of behaviours in the selected buffer is observed (Figure 6.3). MAb5 stands out with the highest positive values for both A_2 and k_D, indicating strong repulsive interactions. This suggests that mAb5 is likely to exhibit excellent solution stability and to be less prone to aggregation in the chosen buffer. Similarly, mAb1, mAb3, and mAb25 show moderately positive values, implying good stability characteristics and making them ideal candidates for therapeutic development. Conversely, mAb24 displays the lowest values for both parameters, suggesting strong attractive PPIs, as previously observed [194]. The same trend is observed for mAb4* and mAb16, with slightly weaker mAb-mAb attractions but still pointing towards aggregation and instability. The formulation of these antibodies could be adjusted to improve their stability, e.g. by adding stabilizers or modifying the solution ionic strength. The remaining mAbs exhibit more nuanced behaviors. MAb12 shows a weak positive A_2 but an almost neutral k_D; mAb9, mAb15 and mAb19 show comparable positive A_2, but different positive k_D, higher for mAb9 and lower for mAb15. This suggests that PPIs are less attractive in mAb9 and mAb19 compared to mAb12 and mAb15, but other factors, e.g. microscopic diffusion, should be influencing their behaviour and their solution visual appearance. In fact, all mAbs whose parameters indicate aggregation are not transparent in solution at 50 mg/mL (see Section 6.5). More

specifically, their k_D values are below the threshold of 20 mL/g set by Kingsbury et al., above which lie all "well behaved" mAbs in a 10 mM His-HCl buffer at pH 6.0 [462], namely the ones featuring viscosities < 30 mPa·s and opalescences < 12 nephelometric turbidity units (NTU). This additional constraint on k_D further supports that mAb5, with $k_D \approx 40$ mL/g, exhibits the most favourable behaviour among the studied mAbs in a 20 mM His-HCl buffer at pH 6.0. We stress again the fact that these results are completely buffer-dependent, meaning that some "well behaved" mAbs in 20 mM His-HCl at pH 6.0 may behave poorly in another formulation.

6.3.2 Neutron Spin-Echo Spectroscopy

If, as an approximation, internal degrees of freedom are neglected, antibody solutions can be treated as suspensions of charged colloids. For such systems, different time scales are typically associated with different types of dynamics. Denoting τ_B as the characteristic time of particle momentum autocorrelations and $\tau_I = R_h^2/D_0$ as the characteristic time for diffusion across a distance equal to the particle hydrodynamic radius, the time scale of short-time dynamics is within the range $\tau_B \leq t_{\text{short}} \leq \tau_I$ [4]. Based on the average size of these proteins, quantified by an average hydrodynamic radius 4 nm $\leq R_h \leq$ 6 nm and a self-diffusion coefficient at the infinitely dilute limit $D_0 \simeq 3.7$ Å^2/ns at 25°C, the correlation times accessed by the conducted NSE experiment probe the short-time diffusion of the studied mAbs. Specifically, "short" length scales refer to roughly 10 nm, or the size of the protein, and "short" time scales extend up to about 50 ns, which is much smaller than τ_I.

The ISF arising from the measured neutron echo was fitted using a cumulant expansion until the second order of an exponential function, as already done for multi-domain proteins: [269]

$$ISF = \frac{I(q,t)}{I(q,0)} = A \cdot \exp\left(k_1 t + \frac{1}{2}k_2 t^2\right), \tag{6.4}$$

with A, q and t being a weighing prefactor, the neutron momentum transfer and the NSE Fourier time, respectively. Echoes measured were fitted independently for each q; an example of ISF fit (with residuals) is reported in Figure 6.4. The coefficients k_1 and k_2 in Equation 6.4 represent the first- and second-order cumulants of the exponential expansion. The same fit procedure was applied on all the samples and the fit range employed was the whole Fourier time range allowed by the instrument in the specific configurations used. The first-order cumulant k_1 contains insightful information on the diffusion processes in the samples, as it is defined as:

$$k_1 = \lim_{t\to 0} \frac{\partial}{\partial t} \frac{I(q,t)}{I(q,0)} = -\Gamma = -q^2 D_{\text{eff}}(q) \tag{6.5}$$

k_1 is negative by definition and its inverse Γ can be interpreted as the diffusion decay rate with its reciprocal value being the relaxation time τ:

$$\tau = \frac{1}{\Gamma} = \frac{1}{q^2 D_{\text{eff}}} \tag{6.6}$$

$D_{\text{eff}}(q)$ is the effective short-time diffusion function given by the coherent scattering of the incoming neutrons with the sample, therefore containing information on its collective dynamics. Figure 6.5 reports $D_{\text{eff}}(q)$ obtained from NSE data for the mAbs in solution at $c_p = 50$ mg/mL (coloured symbols connected by solid lines), at human body and storage temperatures (top and bottom plot, respectively). Dashed coloured lines represent the rigid-body diffusion functions of mAb monomers calculated with the PDB files of the proteins using Jscatter [463]. The dashed black line is the diffusion

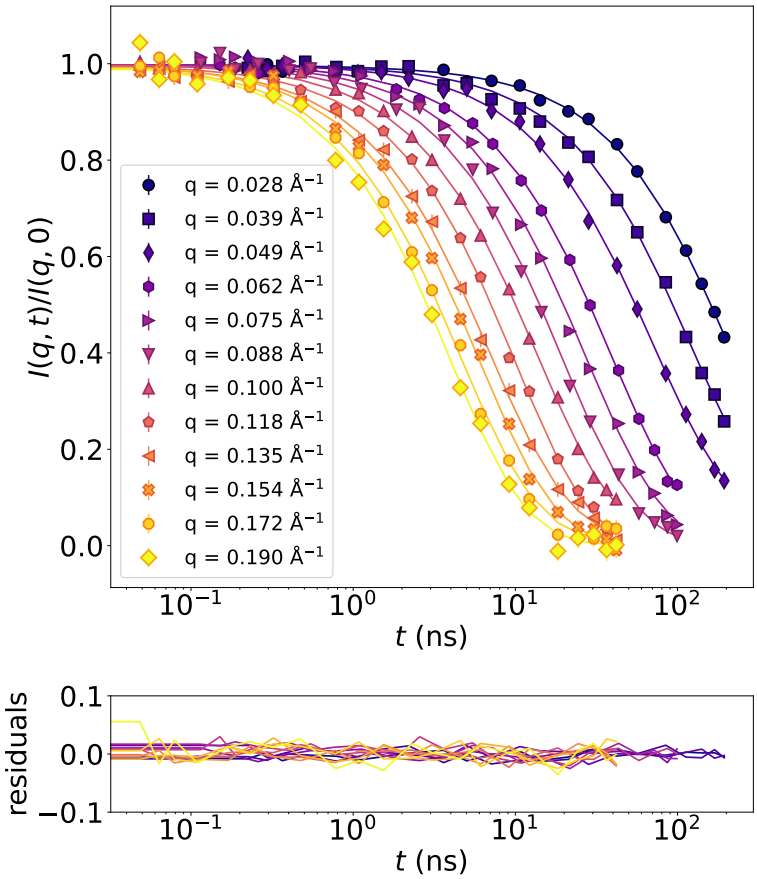

Fig. 6.4. Intermediate scattering function $I(q,t)/I(q,0)$ (neutron echoes vs Fourier time t) of mAb5 at $c_p = 50$ mg/mL and $T = 37$°C, in solution with 20 mM His-HCl buffer at pD 6.4, measured with IN15 spectrometer. The experimental points obtained are the combination of the four different instrument configurations used (wavelength of incident neutron and detector angle). Each data series, denoted by a specific symbol and colour, corresponds to the neutron echo at a specific value of the momentum transfer q, ranging from 0.028 (dark purple dots) to 0.19 Å^{-1} (yellow diamonds). Solid lines in corresponding colours are fits to the data with a cumulant expansion of the exponential (Equation 6.4) using all Fourier times. Data are presented in lin-log scale (top) with the corresponding fit residuals at each q depicted with the same color code (bottom).

of an example Fab-Fab dimer built by merging two mAb5 structures and calculated with the aforementioned software. The choice of mAb5 for this comparison is justified by its remarkably "good behaviour" in solution with the employed buffer with respect to the others, as discussed in § 6.3.1. Since dashed curves are calculated at 20 °C, they were rescaled for temperature and viscosity using the Stokes-Einstein relation and by a factor accounting for the crowding effect at the selected concentration [3]. A non-trivial q-dependence of the experimental $D_{\text{eff}}(q)$ is observed in all samples, also in qualitative agreement with the diffusion curves obtained from the simulations. The mAbs investigated at the same conditions display diverse diffusive dynamics (Figure 6.5). For instance, mAb5 shows a faster diffusion compared to mAb12 and mAb16 (Figure 6.5, top), which are the ones exhibiting higher viscosities already at 50 mg/mL, as reported in Table 6.2. The shape of their $D_{\text{eff}}(q)$

at at 7 °C (Figure 6.5, bottom, cyan and green symbols) is instead peculiar and to be interpreted with the aid of DLS data simultaneously collected on these two mAbs, which reveal abrupt changes in the correlation functions while cooling down to 7°C; in addition, after the measurements the two samples showed signs of opalescence and phase-separation. These observations indicate that the solutions underwent changes during the experiment, resulting in NSE data points collected at different instrument configurations representing varying sample conditions rather than a consistent state. The peculiar behavior of the diffusion curve is therefore signature of phase separation [445]. Further details are in in Section 6.5. In Figure 6.5, the experimentally derived $D_{\text{eff}}(q)$ is compared to the one calculated via MD simulations using the PDB structures of the mAbs and considering them as rigid bodies. These calculated diffusion functions are shown as coloured dashed lines in Figure 6.5 for monomeric structures, while an example of a dimer diffusion is depicted as black dashed line. In this case, the dimer structure was built by manually combining two mAb5 monomers via their Fab arms. The comparison between the experimental and computed diffusion of the mAbs provides insights on their clustering behaviour. Figure 6.5 shows that all the experimental diffusion functions lie under the prediction for their corresponding monomeric structure, indicating oligomerization already at 50 mg/mL at 37°C, which becomes more marked at 7°C. For most of the mAbs, $D_{\text{eff}}(q)$ lies between the monomeric and dimeric diffusion predictions, consistent with NBS results from our previous work [194]. The mAbs exhibiting higher viscositites lie instead under the dimer line as already observed [194], suggesting the presence of attractive intermolecular interactions [443, 464] leading to the formation of short-lived clusters of more than two mAb monomers in these samples, e.g. trimers or small network-like assemblies, which have been previously identified as the cause of opalescence and high viscosity in mAb solutions [446, 447, 465]. Since the clusters do not reach sizes larger than dimers for "well behaved mAbs" and small oligomers for the stickiest ones, the aggregation mechanism might be nucleation dominated (ND) [451].

Figure 6.5 also shows how cooling down to 7°C slows down all the dynamic components, from the translations to the internal relaxations at higher q, by smoothing the $D_{\text{eff}}(q)$. The drop in temperature also strengthens the PPIs, binding, for example, Fab from one mAb and Fc from another, thus altering the internal dynamics of individual proteins [466]. Also note that the purple curve representing mAb4* (the only IgG4 in the set) appears to be smoother than the others depicting the rest of the mAbs investigated (all IgG1), consistent with the already-known reduced flexibility of the IgG4 variant compared to IgG1 [454].

Since at finite concentrations inter-molecular interactions cannot be neglected, $D_{\text{eff}}(q)$ contains information about the sample solution structure and its hydrodynamic interactions and can be expressed as [3]

$$D_{\text{eff}}(q) = D_0 \frac{H(q)}{S(q)} \tag{6.7}$$

with $S(q)$ and $H(q)$ being the structure factor obtained from SANS and the hydrodynamic function, respectively. At infinite dilution there are no hydrodynamic interactions, therefore $H(q) = 1$. At non-zero particle concentration, the hydrodynamic interactions give rise to undulations in $H(q)$ [4].

Furthermore, the coefficient of the second order term in the fit function used (Equation 6.4), that is k_2, can be linked to the polydispersity of the samples via the following relation borrowed from light scattering theory [467]:

$$\text{PDI} = \frac{2k_2}{k_1^2} \tag{6.8}$$

The polydispersity index (PDI) trend *vs* the momentum transfer q obtained from NSE fits is reported in Figure S2 in Section 6.5.

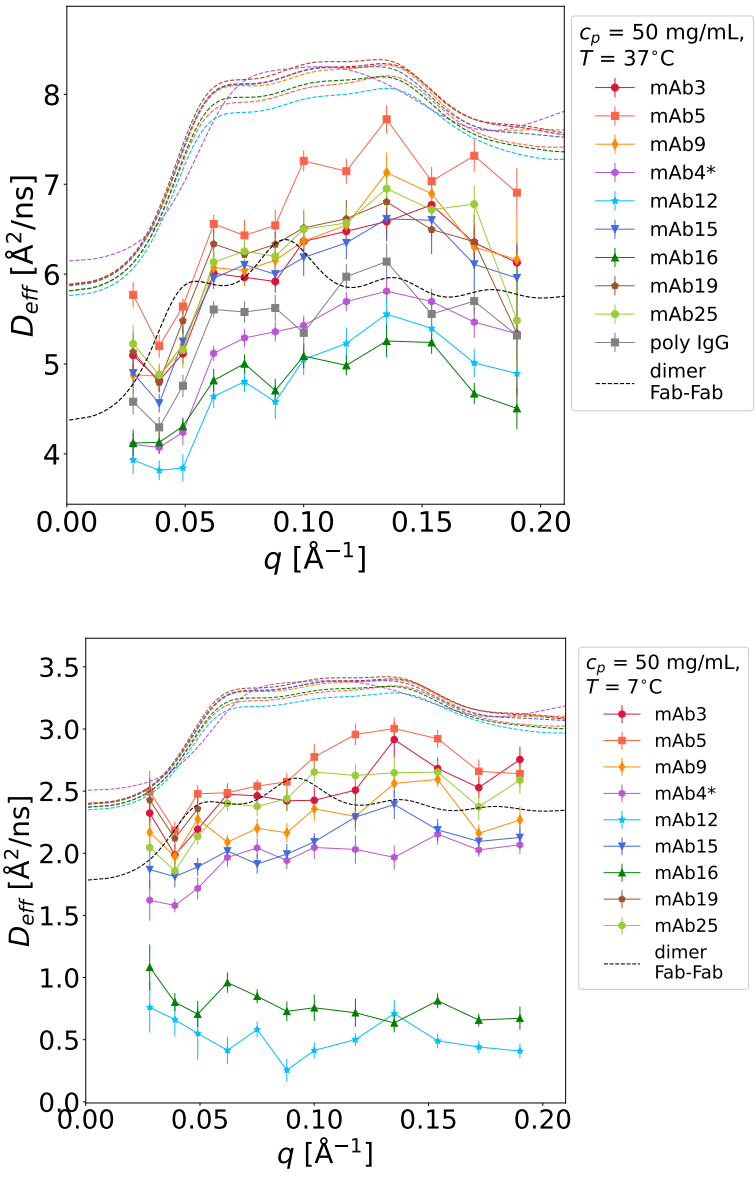

Fig. 6.5. Collective diffusion function of the mAbs. D_{eff} (symbols) for all the mAbs investigated at $c_p = 50$ mg/mL, at body temperature $T = 37$°C (top) and storage conditions $T = 7$°C (bottom), as a function of the momentum transfer q. Solid lines connecting the symbols are guide to the eye, while dashed lines represent the rigid-body diffusion functions of mAb monomers (coloured) and dimers (black) calculated with the PDB of the proteins using Jscatter [463]. The dimer diffusion was evaluated using an example Fab-Fab dimer built by merging two mAb5 structures. For further details, see text.

Fixed-angle dynamic light scattering DLS data were collected in order to monitor sample stability over time while conducting the NSE experiment. For the samples showing a basically constant decay over time, namely all the solutions at 37°C, the correlation functions $g_2(t)$ obtained were fitted with a single exponential indicating just one relaxation process:

$$g_2(t) = \mathrm{A}\,(\,1 + \mathrm{B}e^{-2\Gamma t}\,)\,, \tag{6.9}$$

with A and B being the baseline and the intercept of the correlation function, respectively, and:

$$\Gamma = \frac{1}{\tau} = D_c^{\text{long}} q^2 \,, \tag{6.10}$$

where D_c^{long} is the long-time collective diffusion coefficient, as opposed to the short-time one obtained from NSE. The momentum transfer q probed reads as:

$$q = \frac{4\pi n}{\lambda_0} \sin\frac{\theta}{2} \,, \tag{6.11}$$

where $\lambda_0 = 632.8$ nm is the laser wavelength, $\theta = 90°$ is the fixed angle where the scattered light is detected and $n = n(\lambda_0, T)$ is the refractive index of D_2O calculated at the temperatures of interest via interpolation from existing data fitted with the Cauchy formula as in Ref. [468]. The values obtained are 1.33 and 1.32 at 7 and 37°C, respectively. The momentum transfer probed by the DLS measurements performed is therefore 0.0186 $Å^{-1}$, as calculated from Equation 6.11, corresponding to a real-space distance of 33.8 nm, much larger than the hydrodynamic radius of an antibody monomer. This approach was also applied to the samples at 7°C, along with a double-exponential fit for the ones exhibiting an additional shoulder and a more turbid visual appearance, e.g. the stickiest and most viscous ones (mAb12 and mAb16). From the single-exponential fits, the long-time collective diffusion coefficient D_c^l and the hydrodynamic radius R_h of the samples were extracted, the latter calculated based on the Stokes-Einstein relation. All correlation functions obtained from DLS, some additional information on this analysis, some pictures of the samples taken after the experiment and a more detailed discussion about them are reported in in Section 6.5.

Normal modes of the antibodies The effective diffusion function $D_{\text{eff}}(q)$ of the different mAbs was calculated via Jscatter [463] using the protein PDB structures as inputs. The mAbs are treated as rigid bodies with their shape and anisotropy. Their diffusion is first evaluated taking into account the first 6 trivial eigenmodes (3 translational + 3 rotational degrees of freedom) and then progressively adding the contributions of higher-order modes.

Figure 6.6 reports $D_{\text{eff}}(q)$ for the mAb monomeric structures and for an example dimeric one solely taking into account translations and rotations (top plot), and also accounting for additional normal modes (other plots, normal mode (NM) 7, 8, 9, 10, 11, 12). From previous NSE studies, it is known that the antibody flexible hinge region acts as an entropic spring, around which the three fragments (Fc and 2 Fabs) move with Brownian motion in a harmonic potential [235]. The observable diffusive motion of the antibodies should thus be seen as a combination of these harmonic NM. The NM effective diffusion curves in Figure 6.6 do not show remarkable differences among all IgG1 monomeric structures of the mAbs (Figure 6.6). However, mAb12, mAb15 and mAb16 reach higher peak values in the diffusion calculation that includes NM 7, 8, 9, 11, suggesting more flexible structures able to explore more extended modes which may enhance self-association. Major discrepancies are instead observed between IgG1 and IgG4 proteins, with the latter systematically displaying a different as well as a smoother shape of the diffusion function and significantly lower values, especially when additional NM are considered, with respect to the IgG1 isotype. This again points towards a higher rigidity and thus lower propensity to wide movements of IgG4 with respect to IgG1 molecules [454], as already observed in the D_{eff} obtained from NSE data.

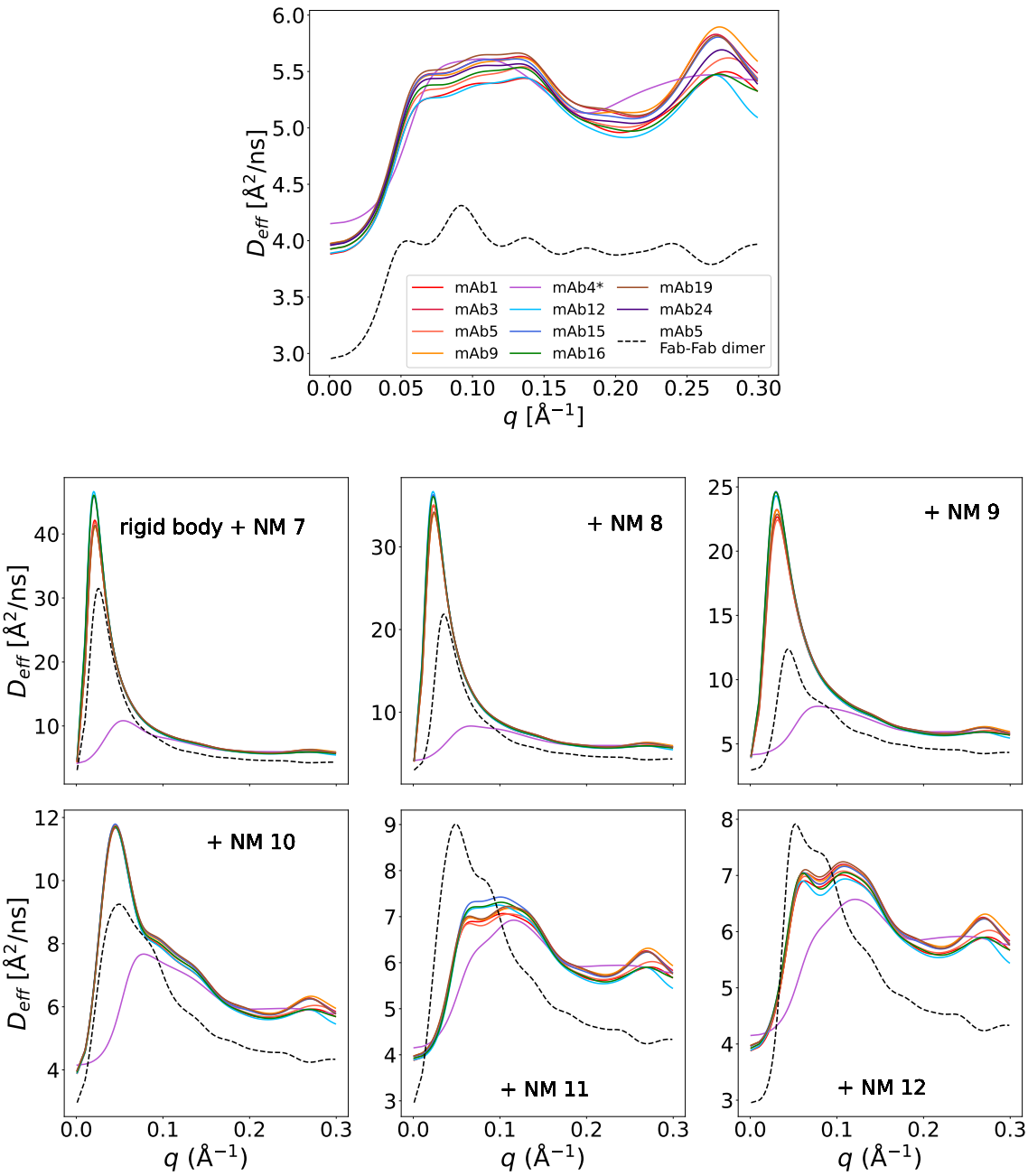

Fig. 6.6. Effective diffusion D_{eff} of the different mAb monomeric structures (coloured solid lines) and one example Fab-Fab dimeric structure built using mAb5 monomers (black dashed line) calculated via Jscatter [463], by considering the proteins as rigid bodies, therefore only taking into account 3 translational + 3 rotational degrees of freedom (top plot), and by evaluating relaxations arising from additional normal modes (other plots, normal modes (NM) 7, 8, 9, 10, 11, 12).

6.3.3 Small Angle Neutron Scattering

Besides providing structural information on the nm-µm scale of mAb solutions, SANS also sheds light on their inter-molecular interactions. The intensity of scattered neutrons measured with SANS is expressed as [326,427]

$$I(q) = n(\Delta\rho_{SL})^2 V_{\text{part}}^2 P(q) S(q)\,, \tag{6.12}$$

with n being the particle number density, $\Delta\rho_{SL}$ the difference in scattering length density between the solvent and the sample particles (also known as the scattering contrast), and V_{part} being the volume of a single particle [326,427]. $P(q)$ is the particle form factor, determined by the protein shape [427,428], which equals unity in the $q \to 0$ limit. $S(q)$ is the structure factor [325,327,429], which contains the information on the mutual interactions between mAbs and their organization in solution and $S(q)$ for $c_p \to 0$, when PPIs are negligible.

Given a minimum accessible q of 0.006 Å^{-1} in the SANS experiment conducted, the largest length scale that can be resolved corresponds to $R_{\text{max}} = 104.7$ nm ($= 2\pi/q_{\text{min}}$) in real space. Considering an average antibody radius R being in the range $4 \leq R \leq 6$ nm, the q-region satisfying the criteria $qR < 1.3$ required for the Guinier approximation is $0.10 \leq R \leq 0.16$ Å^{-1}. Mathematically, the Guinier approximation for the scattering intensity reads as:

$$\ln I(q) = \ln I(0) - \frac{R_g^2}{3} q^2\,, \tag{6.13}$$

where $I(0)$ is the intensity at zero scattering angle and R_g is the radius of gyration of the particles. In Figure 6.7 we report the collected curves for different mAbs at the same concentration of 20 mg/mL at $T = 37$°C (top) and $T = 21$°C (bottom). An example of a concentration series measured for mAb4* (Figure 6.8) shows a nicely decreasing intensity at low q at decreasing protein concentration, which is indeed expected for these systems.

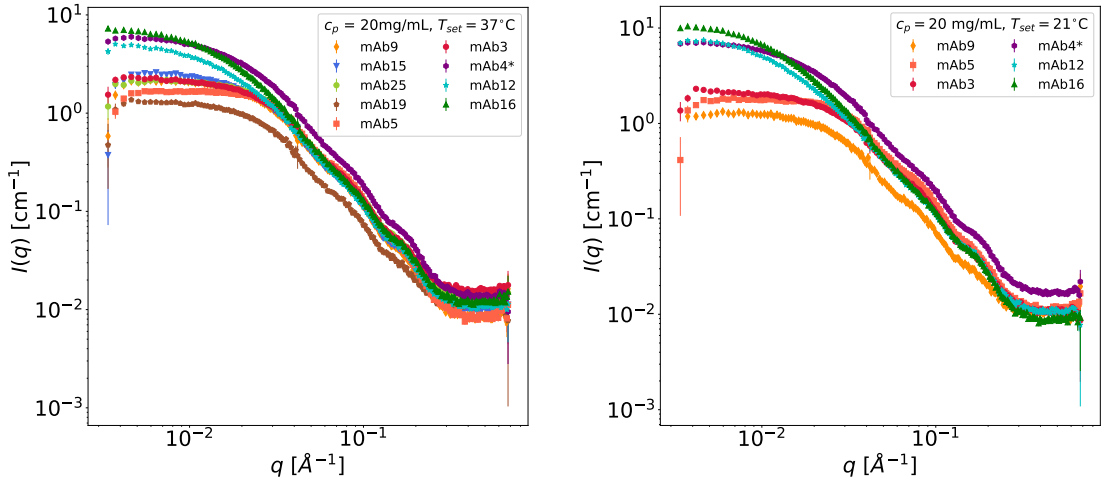

Fig. 6.7. SANS profiles of all mAbs at c_p = 20 mg/mL at $T = 37$ °C (top) and $T = 21$ °C (bottom), background-subtracted taking into account the volume fraction occupied by the solvent.

At first glance one can already hypothesize about the nature and the intensity of PPIs. In particular, mAb16 and mAb12 (cyan and green curves in Figure 6.7) display high values of $I(q \to 0)$, clearly suggesting the presence of more attractive PPIs already at 20 mg/mL. MAb5 (coral squares

curve) shows, on the other hand, lower intensity at low q, indicating the presence of more repulsive interactions. These qualitative considerations are also confirmed by a quantitative Guinier analysis performed on the samples. Guinier plots with fit results for all the samples are reported in Section 6.5, along with Kratky plots that give an idea of the molecular flexibility of mAb monomers and oligomers.

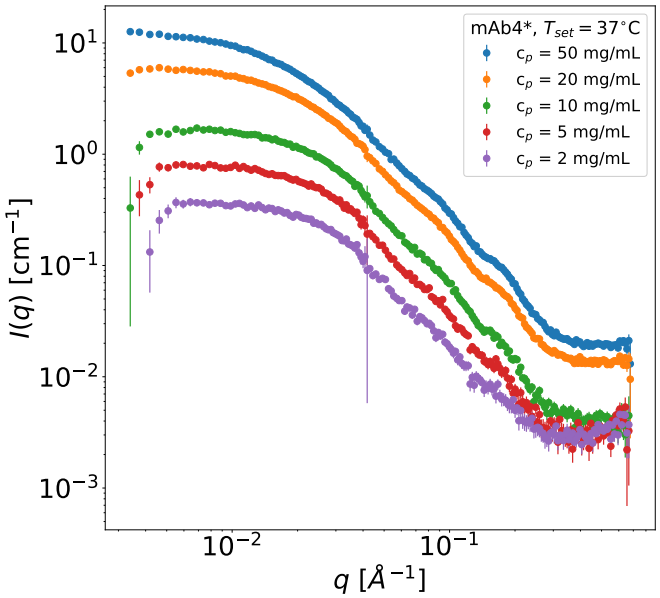

Fig. 6.8. SANS profiles of mAb4* (IgG4) at $T = 37$°C at different protein concentrations c_p ranging from 50 to 2 mg/mL, background-subtracted taking into account the volume fraction occupied by the solvent.

6.4 Conclusions

In this work, we present a systematic comparison of an unprecedented series of monoclonal antibodies (mAbs) – 8 IgG1 and 1 IgG4, evaluating various physicochemical properties, such as macroscopic viscosity, multi-scale diffusion, protein-protein interactions (PPIs), and molecular flexibility. This study builds on previous findings that observed the formation of transient, small clusters in mAb solutions, which dissociate at physiological temperatures [194]. Via NSE we investigate the collective diffusion of the mAbs in the q-region from 0.06-0.19 Å^{-1}, corresponding to a longer length scale than the one previously probed by NBS [194], and to longer coherence times. We observe that all the mAbs undergo self-association in this window explore. These transient clusters contribute to dimers, trimers and network-like assemblies, highlighting differences between antibody isotypes, particularly in terms of molecular flexibility. Notably, we observe the formation of transient clusters at concentrations of 50 mg/mL, which is below the concentrations typically used for pharmaceutical formulations to be administered via subcutaneous injection. As observed in previous works, studying protein solutions at semi-dilute conditions could still help in the understanding of their behaviour at high concentrations [181,196,197,469]. This raises important considerations for formulation design, as clustering at lower concentrations can impact solution stability and viscosity.

Additionally, we compare our experimental results with computational modeling based on the protein structures obtained from PDB files. Using normal mode analysis, we find that the computational results are qualitatively consistent with experimental data, further validating the models. Key factors influencing the behavior of these mAbs include surface charge and hydrophobicity, which play crucial roles in determining both molecular interactions and aggregation tendencies. These insights provide a deeper understanding of the physical properties of mAb solutions, offering valuable guidance for optimizing therapeutic antibody formulations.

Acknowledgements

This research has been supported by InnovaXN, a EU Horizon 2020 MSCA COFUND programme (innovaxn.eu, grant agreement No 847439). I.M. acknowledges an ILL Ph.D. studentship funded by this programme. The authors are grateful for support by the DFG and ANR (ANR-21-CE06-0047 IDPXN, ANR-16-CE92-0009, ImmunoglobulinCrowding), in the initial phase of this project, and by the BMBF (ErUM-pro 05K19VTB and 05K22VTA). The authors acknowledge the support of the ESRF and ILL Partnership for Soft Condensed Matter (PSCM) for providing access to equipment and lab facilities. The authors are also thankful to Juliette Devos (Life Science group at ILL, Grenoble) for support, Jonathan Schmitt (Lonza Basel) for advice and help with viscometry, Laura Stingaciu (ORNL) for stimulating discussions and Ralf Biehl (JCNS) for advice on the Jscatter software.

Associated content

Supplementary material: In Section 6.5 the following information is reported: additional information on NSE data analysis, NSE measurements while cooling down, visual appearance of the samples after the experiment, DLS results, Guinier and Kratky plots of SANS data, physicochemical properties of the antibodies (full sequence and Fv domains), distribution of charged and hydrophobic residues.
Data availability: Neutron data are permanently curated under DOI and available at Ref. [470], in agreement with ILL data policy.

6.5 Supplementary Information

6.5.1 Neutron spin-echo spectroscopy (NSE)

Additional parameters from the fits

Figure 6.9 reports the parameter τ obtained from the fit of NSE data *vs* the momentum transfer q. The $\tau(q)$ trend is very similar in all the mAbs at the two different temperatures studied. However, for mAb12 and mAb16 values are higher than those of the other mAbs, indicating a slower diffusion maybe due to phase-separation, as stated in the main document.

Figure 6.10 reports instead the q-trend of the polydispersity index (PDI) obtained from the fit of NSE data, specifically from parameters k_1 and k_2 as stated in equation 8 in the main document. The most viscous mAbs in solutions – mAb12 and mAb4*, but mostly mAb16 – feature a higher polydispersity compared to the others at 37°C. The data of PDI at 7°C for these two mAbs are not shown because the samples were phase-separated after the measurements. Also, the shape of the curves

overall become less smooth at decreasing temperature, where the self-association plays a higher role and leads to a higher solution viscosity.

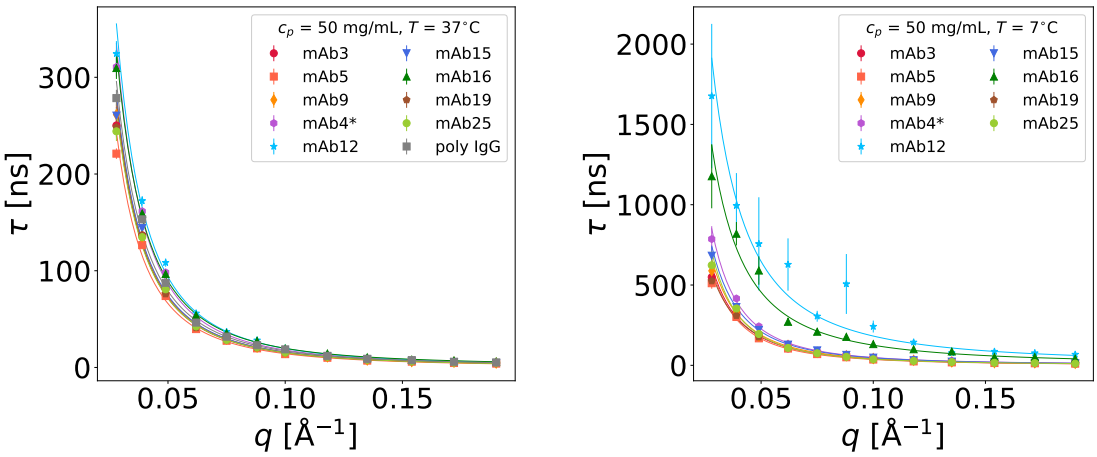

Fig. 6.9. Collective relaxation time. $\tau(q)$ (coloured symbols, from Equation 6.10 in the main document) of all the antibodies investigated at $c_p = 50$ mg/mL, at $T = 37$°C (left) and $T = 7$°C (right), as a function of the momentum transfer q. Solid lines are guides for the eye obtained by fitting the data using $\tau(q) = a/q^n + \mathrm{bkg}$, with a, n and bkg as free parameters.

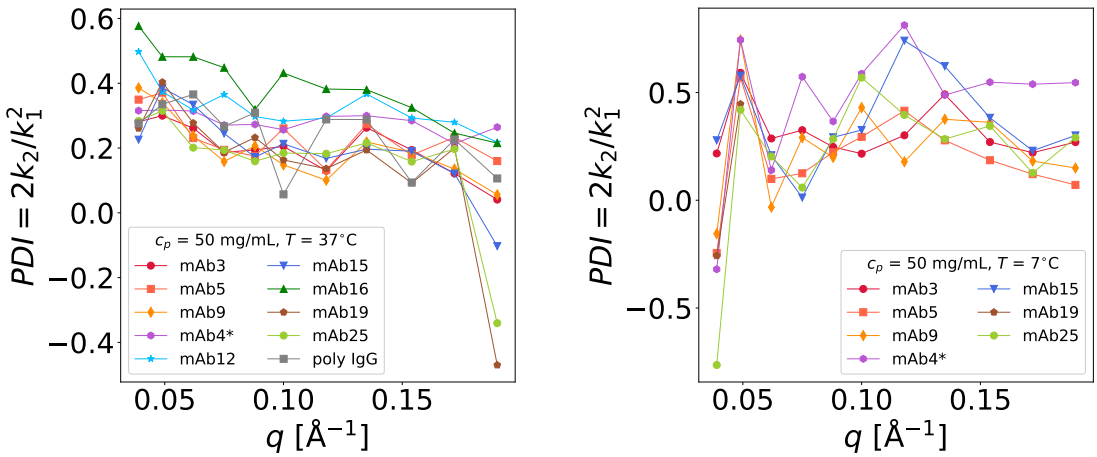

Fig. 6.10. PDI. Polydispersity index PDI $= 2k_2/k_1^2$ (coloured symbols) of all the antibodies investigated at $c_p = 50$ mg/mL, at $T = 37$ °C (left) and $T = 7$°C (right), as a function of the momentum transfer q.

Visual appearance of the samples after cooling down

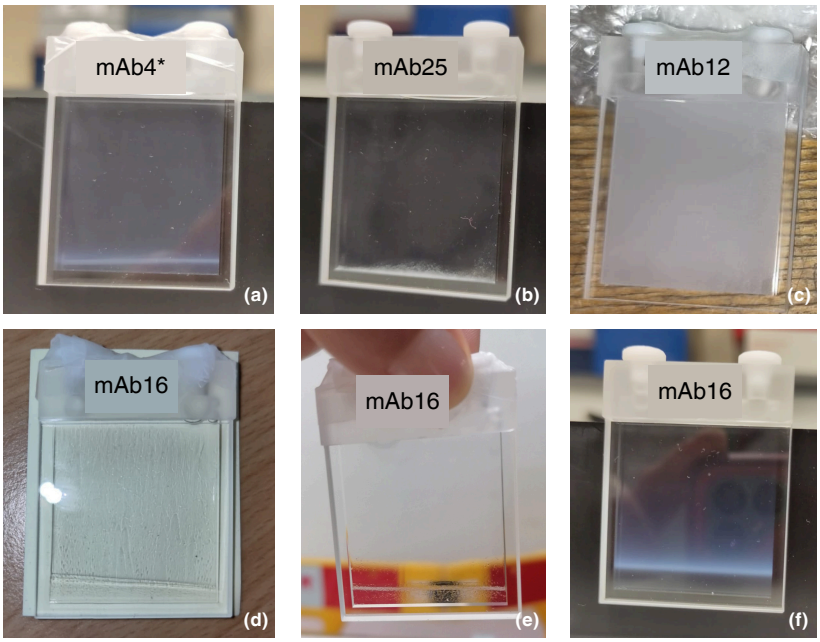

Fig. 6.11. Quartz cuvettes containing mAb4* **(a)**, mAb25 **(b)**, mAb12 **(c)** and mAb16 **(d, e, f)** solutions at $c_p = 50$ mg/mL after cooling them down until 7°C and collecting neutron echoes for all the configurations and simultaneous DLS, resulting in a total time of some hours. In contrast with the other samples not reported here, which were clear and transparent, these solutions show mild precipitation (mAb4*, mAb25), opalescence (mAb4*, mAb12), increase of turbidity (mAb12) and clear phase-separation (mAb16). For mAb16, pictures with three different backgrounds are reported for better visualization of the phase-separation. It should me remarked that mAb4*, mAb12 and mAb16 are the stickiest and the most viscous antibodies among the ones investigated in this work.

Temperature-dependent echoes

Among the antibodies measured with NSE, two proteins featuring a higher viscosity and a more pronounced aggregation propensity compared to the others – mAb12 and mAb16 – were selected to collect echoes during cooling them down to 7°C. In order to follow the process on the scale of some minutes, just one instrument configuration was employed; therefore, only data until Fourier times of $\sim$ 30 ns and $q = 0.062$, 0.075, 0.088 Å^{-1}, which correspond to $\sim$ 10.1, 8.4, 7.1 nm in real space. The collected data are reported in Figure 6.12 and fitted with the following expression:

$$\frac{I(q, \tau = 30\,\text{ns})}{I(q, 0)}(T) = (1 - a) + a \exp^{-\lambda T}, \tag{6.14}$$

where the prefactor a and the decay λ are free parameters. The choice of the model is simply justified by the good agreement found between the collected data points and the single-exponential decay in T. The parameters obtained from the fits are reported in the legend of Figure 6.12. From dimensional analysis, λ should be the reciprocal of a "characteristic" temperature T_c. Calculating then $T_c = 1/\lambda$, we obtain (i) at $q = 0.062$ Å^{-1}: $T_c = 22.2$ °C for mAb12 and 28.6 °C for mAb16; (ii) at $q = 0.075$ Å^{-1}: $T_c = 35.7$ °C for mAb12 and 34.5 °C for mAb16; (iii) at $q = 0.088$ Å^{-1}: $T_c = 62.5$ °C for mAb12 and

43.5 °C for mAb16. In the meanwhile, DLS data at a fixed angle were also collected for these two selected samples (see Section 6.5.2 and Figure 6.13).

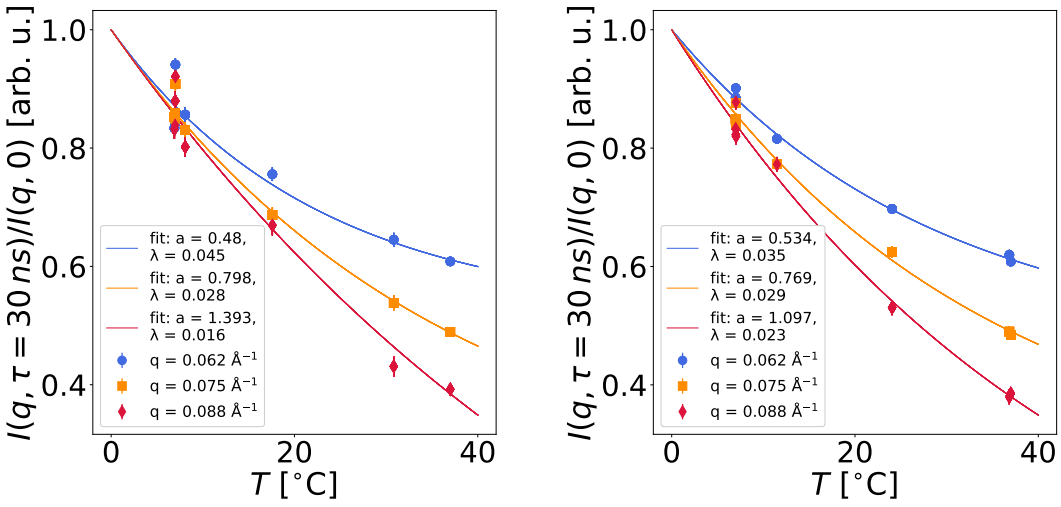

Fig. 6.12. Slowing down of the diffusion while cooling down. Normalized intermediate scattering functions vs temperature for mAb12 and mAb16. The echoes were collected while cooling down the samples from 37 to 7°C, employing just one instrument configuration: therefore, only data until Fourier times of $\sim$ 30 ns and at q = 0.062, 0.075, 0.088 Å^{-1} were collected. The symbols are the ISF values at $\sim$ 30 ns and different colours in the plots represent different q-values. For both antibodies, we observe ISF values approaching to 1 as long as low temperatures are reached (reading the x-axis from right to left), which suggests that decay rates become slower and correlations times longer. Solid lines are fits to the data using Equation 6.14.

6.5.2 *In situ* fixed-angle DLS

The DLS setup mounted in line with the NSE machine was used to collect measurements at a fixed angle of 90° and check the stability of the samples during the relatively long neutron measurements. The complete DLS measurement consists in four acquisitions, one for each NSE instrumental configuration; the time lag from one run to another depends on the duration of the NSE scan at that specific configuration, so it is not constant. However, we took track of it in order to monitor how the solutions behaved over time and at varying temperature. Figure 6.13 shows all the correlation functions obtain from DLS for all the antibodies at both 37 (red dots) and 7°C (blue dots).

All antibodies seem to preserve quite well their stability over time at body temperature, e.g. mAb9 (second row from top, first column from left) and mAb19 (third row, third column) show the same decay in their $g_2(t)$ even after $\sim$ 15 and $\sim$ 13 hours, respectively. Nevertheless, mAb3 and mAb25 show a weak shoulder after the first decay, hence a tentative fit with a two-exponential function was done.

The scenario is slightly different when the samples are cooled down to 7°C. While the DLS curves for mAb3, mAb5, mAb9, mAb15, mAb19 are basically superimposed and only show a smooth single decay, the ones collected for mAb4*, mAb16 and mAb25 are characterised by another additional contribution, indicating some sort of aggregation and loss of solution stability. Also, it should be

noted that for mAb4* and mAb16 the last DLS acquisition was done after more than 12 hours, which means that they were kept for more time at low temperature compared to the previous subset. These results can be justified by simply looking at the visual appearance of the samples after the end of the experiment (Figure 6.11. In fact, macroscopic precipitation, opalescence and phase-separation can reasonably explain less smooth DLS correlation functions. Focusing now on mAb16 (Figure 6.11 d, e, f) and its DLS profile changing over time and temperature, it is observed that the $g_2(t)$ features one smooth single decay until $\sim$ 24°C, while an additional shoulder appears 7 mins after at 11.5°C. Mab12, on the other hand, constitutes a special case: although its correlation function is constant over time and regular at 37°C – signature of a stable, monomeric solution –, it gives rise to a "bad" signal at 7°C, suggesting a suspected turbidity of the solution and the presence of aggregates too large to be resolved by DLS. This is confirmed by the visual appearance of this sample after removing it from the beam, very turbid and "milky", as reported in Figure 6.11 (c). Moreover, by looking at the DLS profile changing over time and temperature, one can notice that the $g_2(t)$ looks regular until $\sim$ 18°C and "spoiled" after 7 mins reaching 8°C. One can hypothesize that both mAb12 and mAb16 undergo liquid-liquid phase separation (LLPS) below their UCST laying in the range 8–10°C. All reported studies of antibody solutions undergoing LLPS at low ionic strength show a UCST phase behavior [196, 445, 464, 471], with a pH-dependent critical temperature [472] and a critical concentration of $\sim$ 90 mg/mL [472–474]. However, the antibodies just described show UCST-LLPS already at 50 mg/mL and the transition seems quite fast upon reaching 8–10°C. The significant macroscopic difference between the two mAbs (Figure 6.11) might be explained by different droplet growth rates. One can speculate that as soon as the solutions are cooled down the critical temperature, they become immediately turbid as protein-rich droplets form within seconds [475]. After that, droplet grow at different rates and in the case of mAb16 they might also irreversibly associate into larger condensates (droplet coalescence [475]) leading to flocculation and formation of two visible distinct phases.

The results overall suggest that the more intense temperature-driven changes are observed in antibodies exhibiting higher viscosities already at 50 mg/mL (see Figure 2 in the main article). At this concentration, the difference in viscosity among the mAbs is not extremely pronounced (at least at 25°C). Nevertheless, the different subsets of mAbs behave completely different both microscopically and macroscopically, with LLPS already setting at 50 mg/mL. This observations suggest that studying semi-dilute conditions of protein solutions may help to shed light on their behavior at high concentrations. This was already observed in previous works addressing the prediction of viscosity and protein-protein interactions at high concentrations based on data on dilute solutions [181, 197, 469].

It can be reasonably stated that the solution stability of the majority of the mAbs studied in this work is compromised when cooling them down from 37°C (body temperature) to 7°C (typical storage temperature). Inter-molecular interactions leading to aggregation, self-association and/or network formation on the microscopic level, give rise to opalescence, increased turbidity, precipitation and phase separation on the macroscopic scale.

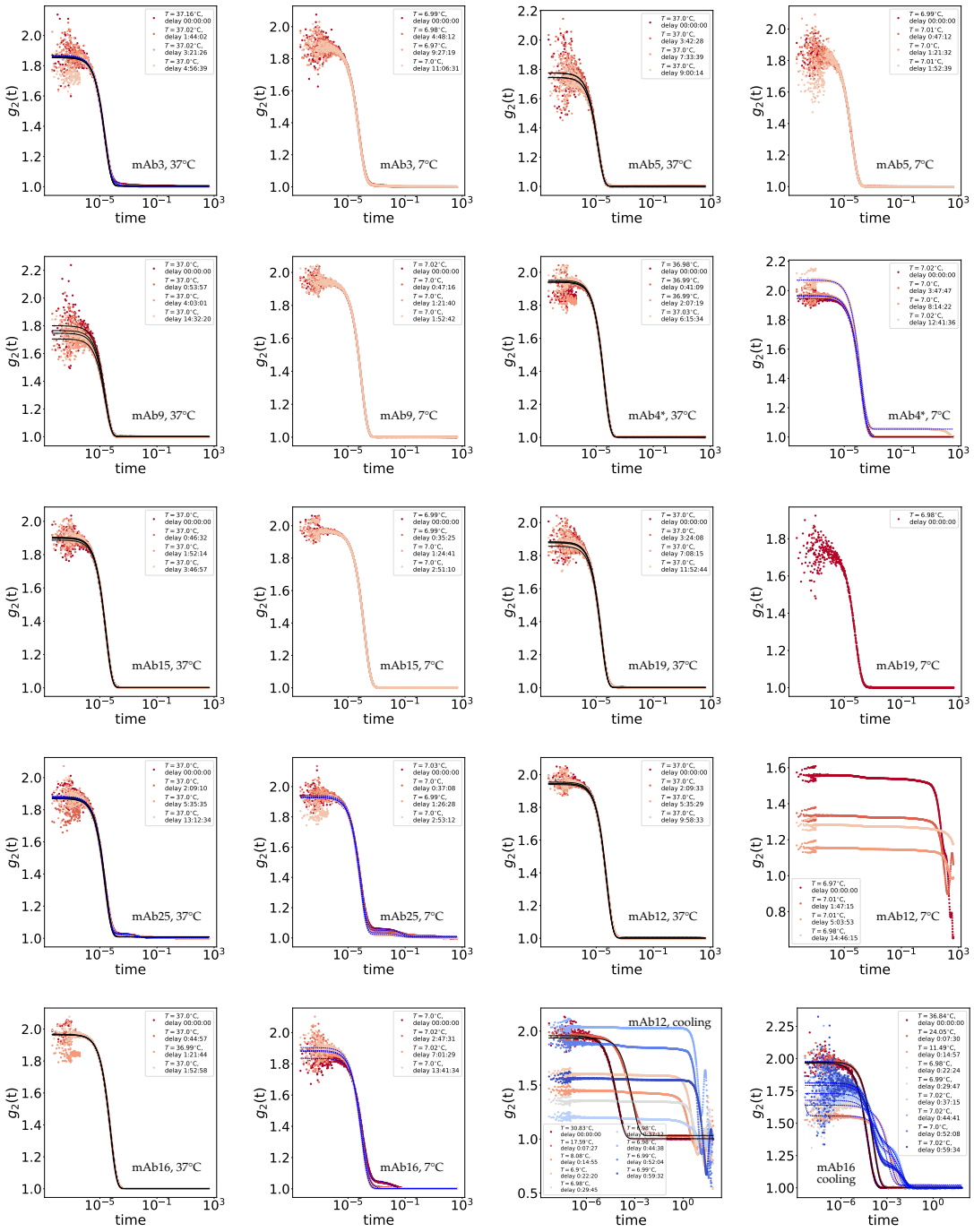

Fig. 6.13. Correlation functions $g_2(t)$ obtained by DLS measurements at 90° (dots) performed on all samples. For each antibody, $g_2(t)$ at 37 and 7°C are represented using red and blue, respectively. Each curve corresponds to the DLS signal collected at one NSE configuration and the corresponding time delay after the first acquisition is also indicated. All the antibodies are at a concentration of 50 mg/mL. For the antibodies measured during the cooling – mAb12 and mAb16 –, the correlation functions at intermediate temperatures are also shown (two bottom right plots). Black solid lines are fits to the data using a single exponential, while dashed blue ones stand for a two-exponential fit.

6.5.3 Small angle neutron scattering

Guinier plots

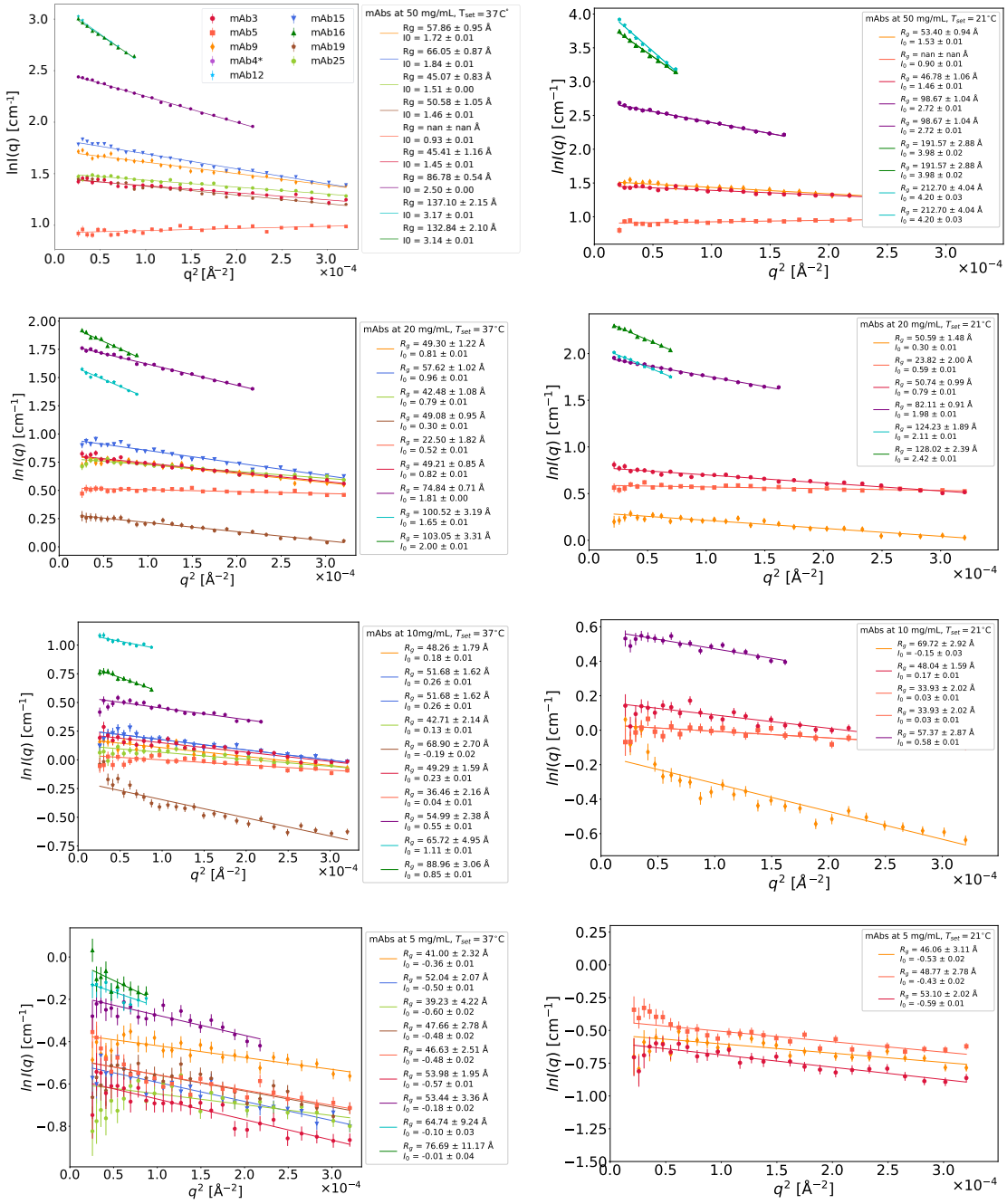

Fig. 6.14. Guinier representation, $ln(I)$ vs q^2, of the SANS data (symbols) of the mAbs at different c_p (50, 20, 10, 5 mg/mL from top to bottom) and temperatures (left: 37°C; right: 21°C). Solid lines are Guinier fits to the data, from which the radius of gyration R_g and the intensity I_0 with their uncertainties were calculated (see legends). The range of the fits, or "Guinier region", is $[q_{\min}, q_{\max}]$, where $q_{\min}$ is the least value accessible by the instrument and $q_{\max}$ is defined by $q_{\max} \cdot R_g \leq 1.3$.

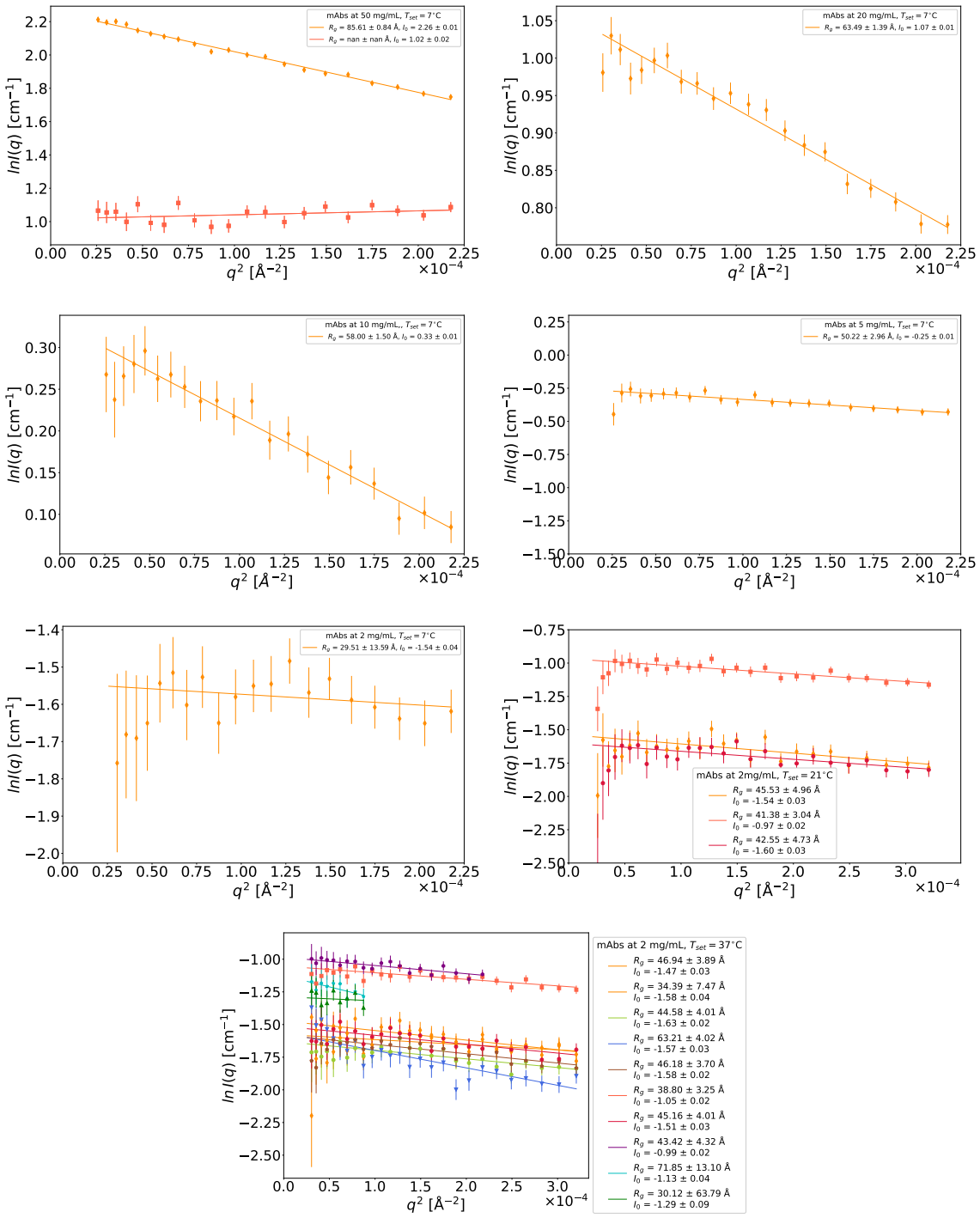

Fig. 6.15. Guinier representation of the SANS data (symbols) of the mAbs measured at 7°C, namely mAb12 (orange diamonds) at 50, 20, 10, 5 mg/mL and mAb3 (coral squares) only at 50 mg/mL. The last three bottom plots are the mAbs measured at 2 mg/mL at 7, 21 and 37°C. Solid lines are Guinier fits to the data, from which the radius of gyration R_g and the intensity I_0 with their uncertainties reported were calculated (see legends). The range of the fits is the so called "Guinier region" $[q_{\min}, q_{\max}]$, where $q_{\min}$ is the least value accessible by the instrument and $q_{\max}$ is defined by $q_{\max} \cdot R_g \leq 1.3$.

Kratky plots

As far as SANS data analysis is concerned, it may be remarkably useful to plot the data in Kratky mode, which can provide valuable insights into the structural and conformational properties of macromolecules, particularly proteins.

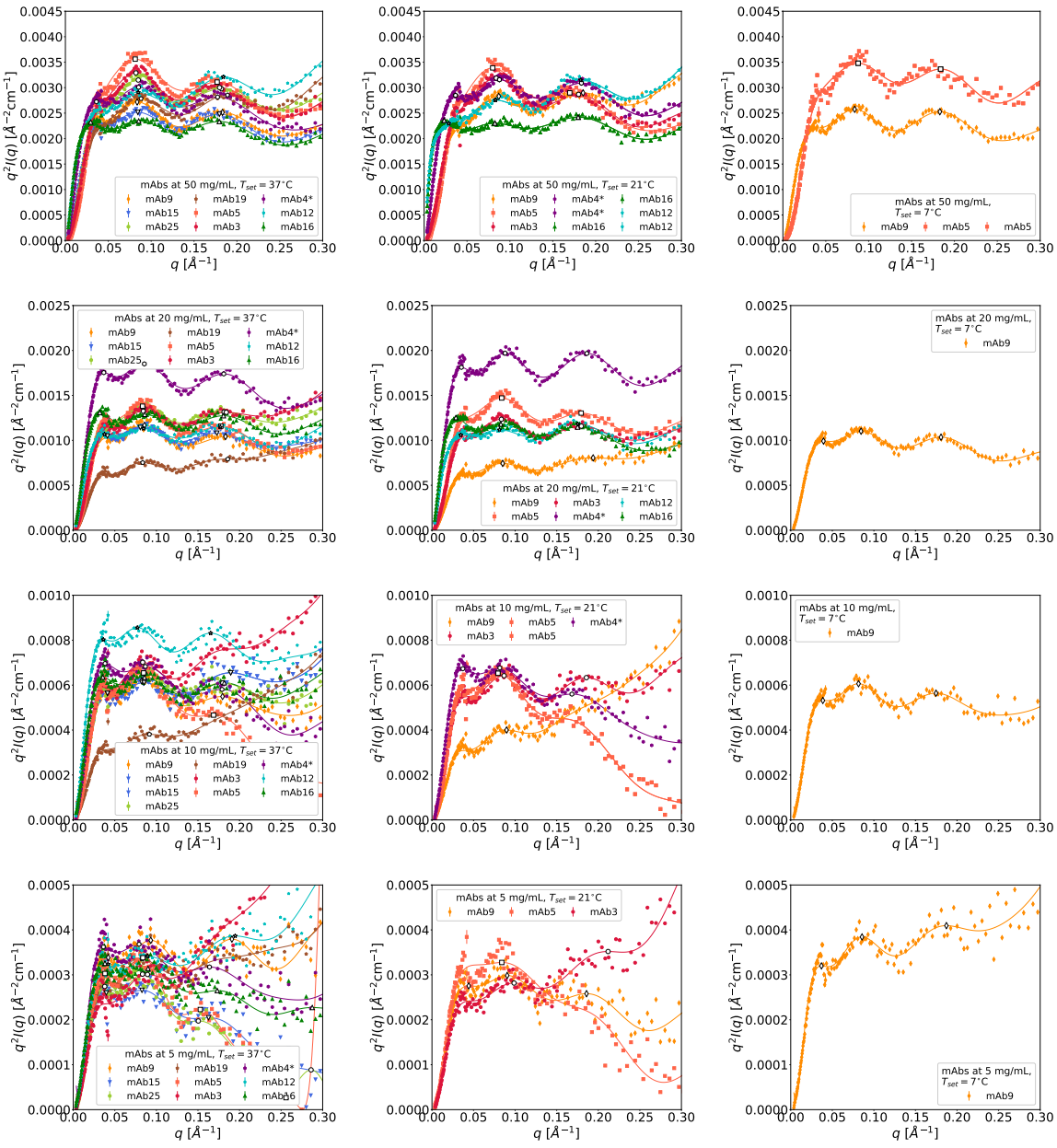

Fig. 6.16. Kratky representation, that is (Iq^2) vs q (symbols), of the buffer-subtracted SANS data of the mAbs collected at different concentrations (rows: 50, 20, 10, 5 mg/mL from top to bottom) and temperatures (columns: 37, 21 and 7°C from left to right). Solid lines are fits to the data using polynomial functions of varying degrees and black empty symbols are the local maxima of the curves, identifying the the three typical features of an antibody protein as revealed by SANS and which correspond to its three-lobed structure.

A Kratky plot shows the scattering intensity $I(Q)$ multiplied by the squared momentum transfer q^2 plotted against q^2. In the case of mAb solutions, it reveals the characteristic shape of the proteins, their degree of flexibility and their aggregation in solution. Figure 6.16 reports Kratky plots of all samples sorted by antibody concentration (row-wise) and set-point temperature (column-wise). As expected, plots of the more dilute samples (bottom rows in Figure 6.16) look noisier than the ones at higher concentrations (top rows in Figure 6.16) and a decrease of the peak intensities at decreasing concentration is observed. Effects of temperature variation are not easily detectable in this representation.

Nevertheless, this data visualization nicely emphasizes the peculiar shape of the antibodies with the three peaks always showing up in the curves. This unique curve shape confirms that the mAbs studied are multi-domain proteins with flexible linkers, characterized by different degrees of compactness and flexibility, which visually translate into smoother or sharper peaks in their Kratky plots. For almost all antibodies – except for the lower concentrations that show noisier curves – the x position of the peaks oscillates around the same values. For instance, the third peak q_3 is always around 0.16-0.17 $Å^{-1}$, which corresponds to a distance of 3.5-3.9 nm, in agreement with the computed distances between CH_1 and CH_2 Fc subdomains [214]. A deeper analysis of the subpeaks could reveal more on the inter- and intra-domain correlations in the different mAbs [214, 215]. However, this would be out of the scope of this work.

6.5.4 Physico-chemical properties of the mAbs and solution stability

Parameters from sequence analysis

In the following section, we report the results obtained processing the PDB files of the antibodies with different bioinformatics tools, such as Biopython, using Bio.PDB and Bio.SeqUtils modules [349] and ProtParam [350]. Although not directly related to the experimental results, the information accessed has definitely improved the knowledge about the proteins investigated. All relevant properties of the antibody full chains and Fv domains are reported in Tables 4.1, 4.2 in Chapter 4. Some parameters are also graphically shown in Figure 6.17 and they include: aromaticity, aliphatic index (AI), GRAVY, isoelectric point pI and protein net charge at pH 6.0, for both mAbs full chain and Fv domain.

The *aromaticity* of a protein is the relative frequency of aromatic amino acids, namely histidine (His), phenilalanine (Phe), tyrosine (Tyr), tryptophan (Trp) [351]. One can notice that mAb12, mAb19 (IgG1 isotype) and mAb4* (IgG4 isotype) show a slightly higher aromaticity, indicating that the content of aromatic amino acids in these proteins is higher than in the others.

The *aliphatic index (AI)* of a protein is defined as the relative volume occupied by aliphatic residues, namely alanine (Ala), valine (Val), isoleucine (Ile) and leucine (Leu). This value is directly proportional to the structural stability of a protein. A general observation is that proteins with AI > 65 possess a good thermal stability [476]. In the present case, mAb12 shows a value of ~ 50 against the ~ 70 reported for the other molecules, indicating that it is the most thermally unstable amongst them, feature also supported by visual inspection of the sample (Figure 6.11 **(c)**) and by the experimental results of this work.

The *GRAVY* (grand average of hydropathy) is defined by the sum of hydropathy values of all amino acids divided by the protein length. Typically, GRAVY values range between -2 and 2, where a negative or positive value indicates that the protein possesses low or high or hydrophobicity, respectively. As all water-soluble proteins, our mAbs expectedly report a GRAVY value of -0.4 [352], with mAb3, mAb16 and mAb19 featuring a slightly higher value.

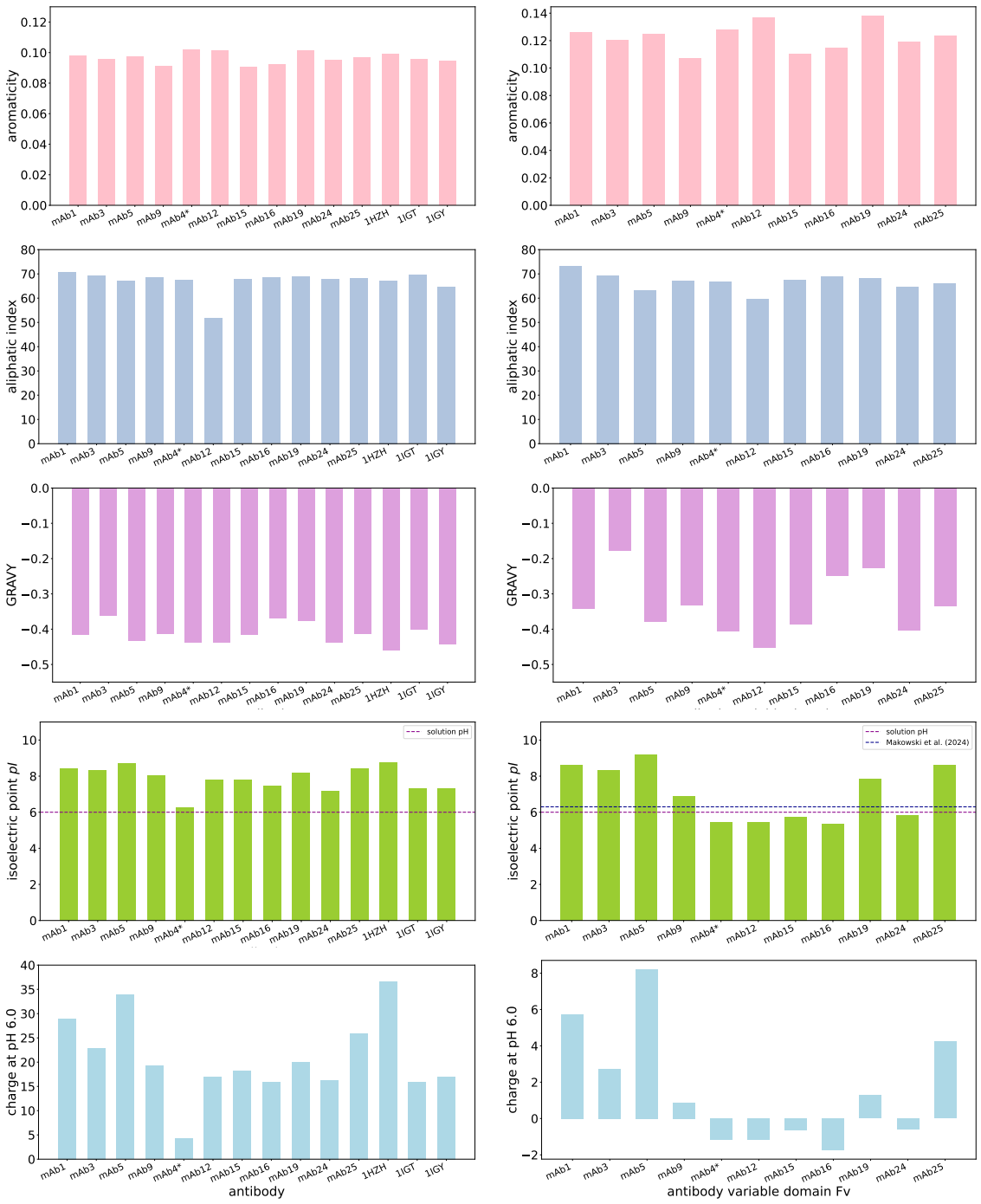

Fig. 6.17. Aromaticity (top row, pink), aliphatic index (second row, mid-blue), GRAVY (center row, lilac), isoelectric point pI (fourth row, lime) and charge at pH 6 (bottom row, light-blue) of the antibodies studied. Plots on the left side refer to the full chains of the molecules, while the right column depicts the same parameters for the antibody variable domain Fv. For the isoelectric point plots, the purple dashed line stands for the pH of the formulation used (= 6.0), while the blue one in the Fv right plot is the value of 6.3 indicated by Makowski et al. [183] as the upper Fv pI limit for mAbs exhibiting high viscosities. Further details are reported in Chapter 4.

The parameters presented in the bottom line plots in Figure 6.17 are connected. The isoelectric point pI of the full-chain proteins (bottom left plot) is in fact the pH at which the protein has zero net electric charge. The bigger the difference between the solution pH and the protein pI, the higher – in modulus – the protein net charge. All the antibodies employed here have pIs $>$ pH $= 6.0$, so their net charge at pH 6.0 is overall positive but differs quite a lot amongst the mAbs. If only electrostatic interactions are considered and each protein carries a positive charge, repulsion should dominate. However, this repulsion is less pronounced for mAbs with a lower net charge, e.g. mAb4* and – to some extent – mAb12, mAb16, mAb24. More interesting information concerns instead the pI and net charge of local regions of the mAbs, e.g. the Fv domain (lime and light blue right plots in Figure 6.17). The Fv domain of the most viscous mAbs feature a slightly negative charge, closer to 0 compared to well behaved variants like mAb5. Thinking in terms of the pI, the Fv pI of the antibodies featuring high viscosities is way more different from the pI of the whole protein, compared to the other mAb variants. The Fc of the viscous mAbs must thus have higher pI and charge, suggesting the presence of intra-molecular dipoles that enhance inter-molecular Fab-Fc aggregation and high solution viscosity.

Protein-protein interaction parameters from light scattering

MAb	$\mathbf{A_2}$ **[**$\times 10^{-4}$ **mol mL g**$^{-2}$**]**	$\mathbf{k_D}$ **[mL/g]**
mAb1	1.96	18.40
mAb3	1.58	14.30
mAb5	3.12	40.70
mAb9	1.10	18.50
mAb4*	-0.06	-7.34
mAb12	0.44	1.37
mAb15	1.03	6.50
mAb16	-0.11	-6.17
mAb19	1.29	15.68
mAb24	-0.72	-21.10
mAb25	1.55	20.50

Table 6.3. Values of the second virial coefficient A_2 and the diffusion-interaction parameter k_D obtained for the 11 mAbs by Schmitt et al. [184] plotted together in Figure 6.3.

Charged and hydrophobic residues

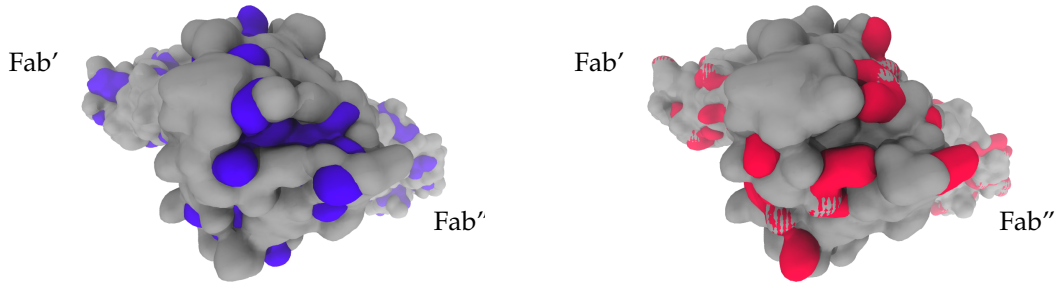

Fig. 6.18. Hydrophobic and charged residues in Fc domain. Structure of mAb1 seen from the bottom of the Fc domain, which is essentially identical in all the variants. Fab' and Fab" regions in the background are just indicated for clarity. On the left side, hydrophobic (Ala, Leu, Val, Ile, Pro, Phe, Met, Trp) and non-hydrophobic residues are represented in purple and silver, respectively. On the right side, charged (Arg, His, Lys, Hsp, Asp, Glu) and non-charged amino acids are depicted in magenta and silver, respectively. Fc-Fc association, common in mAb solutions, could be in this case mediated by the hydrophobic sites in purple. Figures rendered using VMD [377].

Estimation of mAb intra-molecular distances

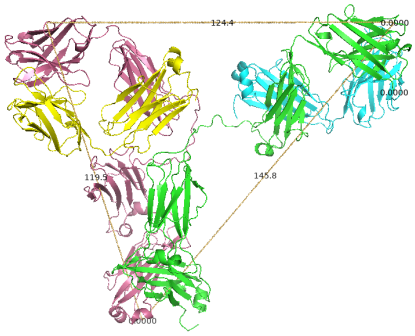

Fig. 6.19. Example of an antibody structure. The PDB structure of mAb9 is rendered with PyMol [477] using a 'Cartoon' representation, revealing the features of its secondary structure mainly composed of β-strands. Different colours refer to the different chains forming the molecule; the two heavy chains (~ 50 kDa each) are displayed in pink and green, while the light chains (~ 25 kDa each) are shown in yellow and cyan. Yellow solid lines with labels are the computed distances (in Å) between three residues placed at the vertexes of the protein subdomains. In the specific case of mAb9, all these distances are smaller than 15 nm, indicating that the value of $d_{max} = 16$ nm (in Section 6.2.1 of the main document) used to calculate the overlap concentration of the samples is a safe overestimation.

Chapter 7

Continuity of short-time dynamics crossing the liquid-liquid phase separation in charge-tuned protein solutions

Chapter 7 is based on the following publication:

Continuity of short-time dynamics crossing the liquid-liquid phase separation in charge-tuned protein solutions
Journal of Physical Chemistry Letters **2024**, 15, 12051-12059, Ref. [288]

Authors: Ilaria Mosca[1,2], Christian Beck[1,2], Niina H. Jalarvo[3], Olga Matsarskaia[2], Felix Roosen-Runge[4], Frank Schreiber[1], and Tilo Seydel[2]

[1]*Institut für Angewandte Physik, Universität Tübingen*, Germany
[2]*Institut Max von Laue - Paul Langevin*, Grenoble, France
[3]*Neutron Scattering Division, Oak Ridge National Laboratory*, Oak Ridge, Tennessee, USA
[4]*Department of Physical Chemistry*, Lund University, Sweden

Author contribution: T. S., O. M., C. B., F. R.-R., and F. S. designed the research. I. M., N. H. J., and T. S. performed the neutron scattering experiment on site at the SNS. I. M. and T. S. prepared the samples at the SNS. C. B., I. M. and T. S. analysed data. C. B. carried out complementary sample characterizations in the PSCM in Grenoble. All authors contributed to interpreting the data and writing the manuscript.

Experiments: Data presented in this chapter were collected during SNS experiment IPTS-23886.

Abstract

Liquid-liquid phase separation (LLPS) constitutes a crucial phenomenon in biological self-organization, not only intervening in the formation of membraneless organelles, but also triggering pathological protein aggregation, which is a hallmark in neurodegenerative diseases. Employing incoherent quasi-elastic neutron spectroscopy (QENS), we examine the short-time self-diffusion of a model protein undergoing LLPS as a function of phase splitting and temperature, to access information on the nanosecond hydrodynamic response to the cluster formation both within and outside the LLPS regime. We investigate the samples as they dissociate into microdroplets of a dense protein phase dispersed in a dilute phase, as well as the separated dense and dilute phases obtained from centrifugation. By interpreting the QENS results in terms of the local concentrations in the two phases determined by UV-Vis spectroscopy, we hypothesize that the short-time transient protein cluster size distribution is conserved at the transition point, while the local volume fractions separate.

Graphical abstract

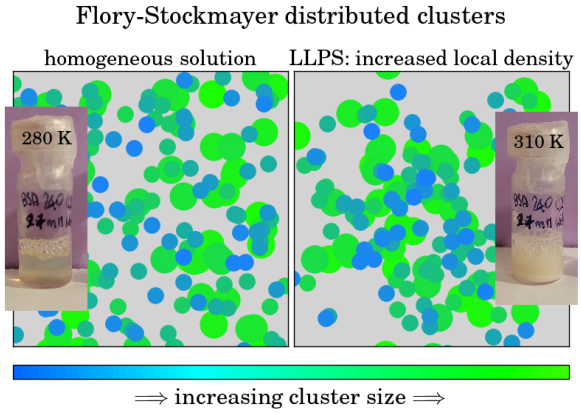

Fig. 7.1. Graphical abstract. Cluster distribution calculated according the Flory-Stockmayer theory in a generic group of particles before (left) and after (right) the LLPS sets. The two inset pictures show the protein sample at 280 K, still appearing clear before the LLPS sets (left), and at 310 K, when becoming milky and turbid and entering the LLPS regime (right).

7.1 Introduction

Metastable liquid-liquid phase separation (LLPS) of protein solutions plays crucial roles in protein crystallisation [478], cellular signalling [479] as well as pathologies such as eye cataract [480], metab--olic [481, 482] and neurodegenerative diseases [483, 484]. LLPS is increasingly being understood as a fundamental mechanism of biological self-organisation, self-assembly [485–492] and functional regulation [493–495]. Moreover, the naturally occurring LLPS inspires an interest in synthetically employing this phenomenon [496]. The understanding of protein-protein interactions and the underlying phase behaviour is, thus, of outstanding importance in, e.g., healthcare and pharmaceutical applications, as well as in bio-engineering and nanotechnology. LLPS is a thermodynamically driven process in which a homogeneous protein solution splits into micro- or nanodroplets of a protein-rich

phase immersed in a dilute phase. The two coexisting phases are maintained through balanced chemical potentials of solutes and osmotic potentials of solvents, arising from the minimization of the total free energy [497, 498]. This separation has been described by random phase approximation theories enhanced by Flory-Huggins interaction models [499, 500], for the case of intrinsically disordered proteins (IDPs) that constitute the majority of proteins for which LLPS has been found [500, 501]. LLPS has also been described as dynamic outcome of the interplay between a diffusion-limited protein-protein encounter and the exhaustion of available valencies within smaller clusters [502], and been discussed in terms of a phase transition [503–505].

Thermodynamically, the demixing of an initially homogenous protein solution is associated with a dramatic increase in correlation length visible by small-angle scattering [506] as well as by photon correlation spectroscopy [507], possibly preceded by a bimodal cluster size distribution [508]. Other models for LLPS in globular proteins include adhesive hard-sphere models to describe dynamical arrest, involving percolating clusters [509–511]. Moreover, patchy-particle models [512, 513], as well as simulations [514] were employed to predict phase diagrams. Picosecond time-resolved fluorescence anisotropy showed that nanosecond transient nanoclusters underlie the long-range correlations in protein LLPS [515]. Using static and dynamic light scattering (SLS/DLS), a universal osmotic equation of state and dynamical behavior was previously observed for lysozyme protein solutions undergoing LLPS [516]. It was discussed in terms of the theory of corresponding states [516–520] that close to LLPS, the osmotic compressibility and the collective diffusion of protein solutions are only determined by the volume fraction and the temperature relative to the critical temperature or, equivalently, by the second virial coefficient [516], and that the sensitivity of thermodynamic properties to the details of the underlying interactions vanishes [516].

In terms of colloid theory [479], metastable LLPS is driven by a short-range attraction between the colloid particles. This concept can also be applied to proteins, for instance by employing trivalent metal cations, e.g. Y^{3+}, Ho^{3+} and La^{3+}, to create this short-range attraction for proteins such as bovine serum albumin (BSA) [521]. The multivalent metal ions provide an efficient and ion-specific way to tune interactions in protein solutions [522–524], where binding and bridging of the metal ions lead to a rich phase behaviour that includes crystallisation, re-entrant condensation and metastable LLPS with a lower critical solution temperature (LCST-LLPS) [521, 525] (figure 7.2). Protein cluster formation has been shown and characterized for aqueous solutions of BSA and multivalent salts [524, 526], including microscopy [346, 524, 527] and light scattering [528]. These solutions constitute a well-investigated model system for LLPS at suitable salt concentrations [524, 526, 529] and its kinetics was studied for instance by (ultra)-small-angle scattering [530] and by NMR with trifluoroethanol as a probe of the local densities in the two phases [531]. Theoretically, the phase behaviour of BSA solutions can be understood in terms of the above-mentioned patchy colloid models [512, 526, 532, 533]. BSA solutions with YCl_3 were also explored by DLS in the low-turbidity and low-concentration range accessible by this method, observing two diffusive time scales in the long-time limit of collective diffusion [528]. Both diffusion coefficients decreased monotonously with increasing salt concentration approaching the precipitation regime that precedes LLPS [528]. Due to the above-quoted substantial amount of previous work on BSA solutions, the BSA-$LaCl_3$-system constitutes our model of choice to experimentally access the unique dynamic regime of short-time self-diffusion during LLPS by high-resolution spin-incoherent quasi-elastic neutron spectroscopy (QENS), motivated in the following paragraph. The observation or coherence time of our experiment is on the order of one nanosecond, resulting from its high energy resolution of a few μeV.

Molecular dynamics (MD) simulations show that relaxation in suspensions of associative proteins

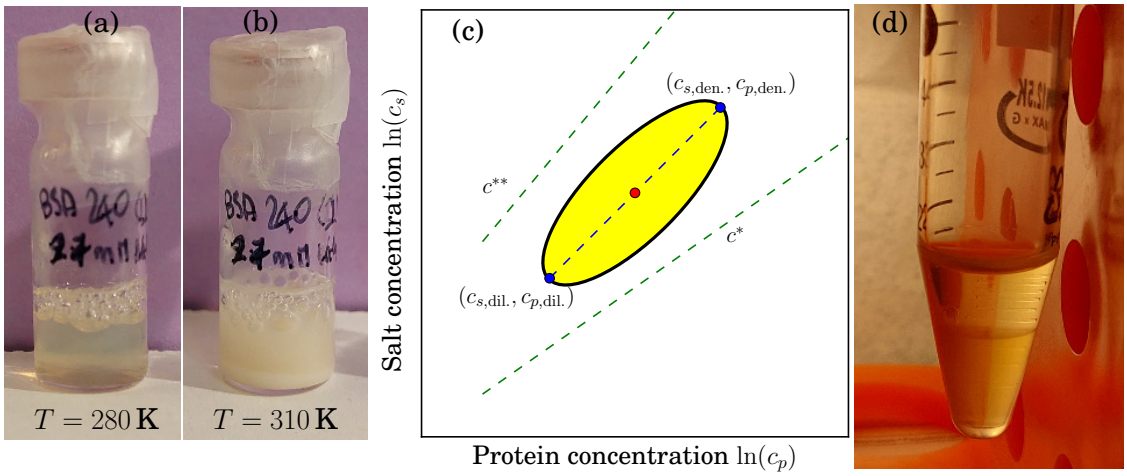

Fig. 7.2. **(a)** BSA at $c_p = 240$ mg/ml with 27 mM $LaCl_3$ ($c_s/c_p = 7.5$) in D_2O displays signatures of LLPS, being transparent at $T \approx 280$ K and **(b)** milky/turbid at $T \approx 310$ K.We note that the optical transparency alone is not a suitable criterion for LLPS, cf. main text. **(c)** Schematic of a cut at constant T through a generic protein-salt phase diagram, illustrating the splitting of a mixture prepared at the (c_s, c_p) point (red circle symbol) in the center of the LLPS region (shaded area). Due to LLPS, the two phases after the separation are located at the two points marked by blue circle symbols on opposite sides of the shaded LLPS region. The dashed lines labelled c^* and c^{**}, respectively, denote the salt concentration boundaries of the optically turbid regime $c^* < c_s < c^{**}$. **(d)** BSA at $c_p = 240\,\mathrm{mg/ml}$, $c_s = 27$ mM $LaCl_3$ ($c_s/c_p = 7.5$) after centrifugation for more than 12 h at 40°C. The splitting into two well-separated phases becomes visible, the dense protein-rich phase at the bottom of the Falcon tube and the dilute protein-poor phase above. The two phases were extracted and measured separately.

slows dramatically when the stoichiometry is balanced [534], revealing the substantial reduction of the long-time diffusion with increasing protein-protein bond relaxation time [534]. Since long-time diffusion is the result of both short-time hydrodynamic and longer-time direct interactions, accurate knowledge of the short-time diffusion is required to quantify the long time diffusion. Moreover, it is essential to understand bond fluctuations and resulting scaling behavior of diffusion described by mean-field theory [535], predicting a rather loose fluctuating network liquid as opposed to dynamically slowed clusters in the dense phase of LLPS [535]. Large-scale MD simulations also reveal a highly dynamic picture of LLPS even in the dense phase [536], finding time scales of less than 1 µs for protein-protein partner exchange and a nanosecond contact dynamics in a model of IDPs [536]. The simulations give rise to the hypothesis that fast nanosecond diffusion even in the dense phase allows for transport and signal transduction, which are considered crucial for biological function. On this nanometer length scale associated with nanosecond diffusion, hydrodynamic and electrostatic interactions dominate over negligible direct interactions and constitute part of the picture describing possibly transient cluster formation in short-range attraction long-range repulsion (SALR) systems [513, 537]. Notably, by measuring self-diffusion, our QENS experiment unambiguously accesses the hydrodynamic size of protein clusters unaffected by a superimposed static structure factor, and by measuring on the nanosecond time scale, detects even short-lived clusters. The nanosecond coherence time along with the access to self-diffusion by our experiment as opposed to long-time col-

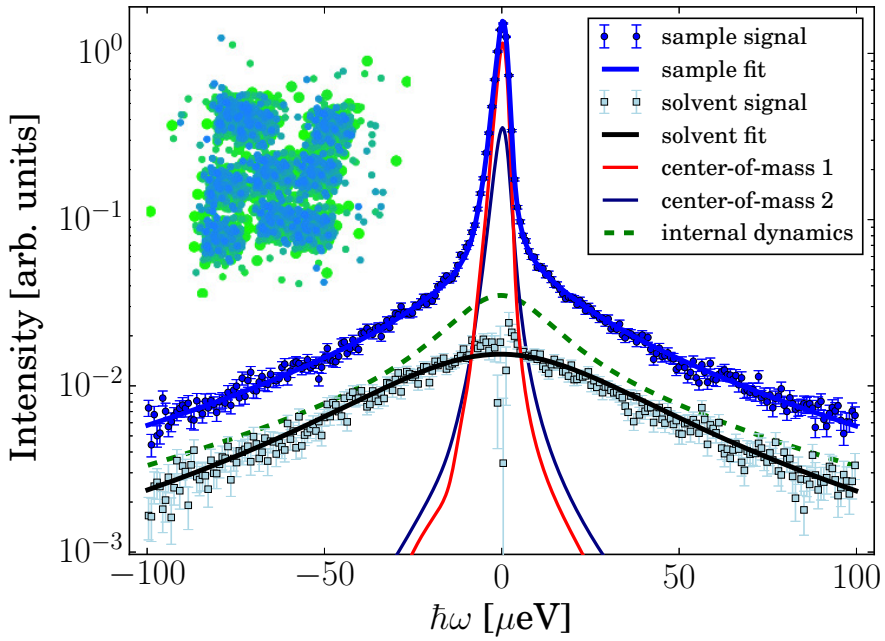

Fig. 7.3. Example spectrum recorded on BSA at $c_p = 240$ mg/ml in D_2O with $c_s = 27$ mM $LaCl_3$, at $T = 310$ K and $q = 0.55$ Å^{-1} (upper circle symbols). The lower square symbols denote the corresponding pure D_2O solvent spectrum scaled by $(1-\varphi)$. In both spectra the container contribution was subtracted. The thick solid lines superimposed on the spectra are fits to the data. The narrow solid lines represent the Lorentzians accounting for the two separate global center-of-mass diffusion coefficients attributed to the dense and dilute phase, respectively, subsequent to the convolution with the resolution function, explaining the peculiar shape of the narrowest Lorentzian. The dashed line represents the sum of the internal diffusion of the two phases, Equation 7.3. The inset artistic schematic illustrates the cluster distributions in the LLPS regime with local dense and dilute regions described by the Flory-Stockmayer model (cf. main text).

lective diffusion accessed, e.g., by DLS or long-time self-diffusion accessed, e.g., by NMR are crucial to interpret our results.

7.2 BSA-LaCl$_3$ as a model system

The protein solution samples were prepared following previously established protocols [306,538,539], at the nominal protein concentration $c_p := m_p/V_{D_2O} = 240$ mg/ml BSA in D_2O, with the protein mass m_p and D_2O volume V_{D_2O}, corresponding to the dry protein volume fraction $\varphi = m_p\nu_p/(V_{D_2O} + m_p\nu_p) = 0.15$ with the protein specific volume $\nu_p = 0.735$ mL/g [540], at different $LaCl_3$ salt concentrations $c_s = 0$, 20, 23, 25, 26, 27, 29, 30, 35 mM, corresponding to the number of salt ions per protein $c_s/c_p = 0.0$, 5.5, 6.4, 6.9, 7.5 and 8.0, respectively. Importantly, we measured on these samples in the mixed state and, at suitable salt concentrations, on samples that were separated into the dense and dilute phases by centrifuging, and we determined concentrations by UV-Vis (cf. Section 7.4).

The observable in QENS is the dynamic structure factor $S(q,\omega)$, as a function of the energy trans-

fer $\hbar\omega$ and the momentum transfer $\hbar q$. For our samples, $S(q,\omega)$ arises from the protein and aqueous (D_2O) solvent contributions. For globular proteins, the protein signal can be separated into the contributions from the apparent global center-of-mass (COM) diffusion of the protein or protein cluster $S_{\mathrm{global}}(q,\omega)$, and from the internal diffusion $S_{\mathrm{internal}}(q,\omega)$. The superposition of these contributions is convoluted with the spectrometer resolution function $R(q,\omega)$ obtained from a Vanadium spectrum and represented analytically by a sum of non-centred Gaussian functions [290] (figure 7.15). The measured $S(q,\omega)$ is therefore described by

$$S(q,\omega) = R(q,\omega) \otimes \left\{ S_{\mathrm{global}}(q,\omega) \otimes \left[A_0\, \delta(\omega) + (1 - A_0)\, S_{\mathrm{internal}}(q,\omega) \right] + \beta_{\mathrm{D_2O}} \mathcal{L}_{\gamma_{\mathrm{D_2O}}} \right\} , \tag{7.1}$$

where $A_0(q)$ is a scalar identified with the EISF characterizing dynamic confinement effects [308], and $\delta(\omega)$ the Dirac function. The scalar $\beta_{\mathrm{D_2O}}(q)$ is fixed in the fits based on a separate pure solvent measurement, accounting for the volume excluded by BSA, and the D_2O-signal is modeled by one Lorentzian $\mathcal{L}_{\gamma_{\mathrm{D_2O}}}$ with the width $\gamma_{\mathrm{D_2O}}(q)$ fixed from existing neutron TOF data [163,541]. For BSA in solution, it has been shown that the internal diffusive processes of the backbone and the side chains accounted for by S_{internal} can be separated and described by two coupled Lorentzians on the accessible $\hbar\omega$-range of BASIS [539,542,543] (cf. Section 7.4, eqs. 7.6, 7.7), and clusters can be represented by a single Lorentzian $\mathcal{L}_\gamma(\omega)$ with width $\gamma(q)$ accounting for the effective COM diffusion [538,542],

$$S(q,\omega) = R(q,\omega) \otimes \beta \left\{ A_0 \mathcal{L}_\gamma(\omega) + (1 - A_0) S_{\mathrm{internal}}(q,\omega) \right\} + \beta_{\mathrm{D_2O}} \mathcal{L}_{\gamma_{\mathrm{D_2O}}}. \tag{7.2}$$

Therein, we impose Fickian diffusion $\gamma = Dq^2$ in a global fit, i.e., simultaneous fit along q and ω as in previous studies [539,542], where D represents the average COM diffusion. $\beta(q)$ is an amplitude scaling factor accounting for the Debye-Waller factor.

For solutions containing two different types of proteins with different sizes and, thus, diffusion coefficients, it has been shown that the scattering signal can be described by either one Lorentzian accounting for an average COM diffusion or by two Lorentzians accounting for two COM diffusion coefficients [544]. Inspired by the latter approach, we allow for separate COM coefficients in the dilute and dense phase, denoted as D_{dil}, D_{dense}, in our fits. These two values are constrained by $D_{\mathrm{dense}} < D_{\mathrm{dil}}$ and connected by the intensity ratio $0 \leq r \leq 1$. Therefore, adding only two fit parameters, we generalize Equation 7.2 to

$$\begin{aligned} S(q,\omega) = \quad & R(q,\omega) \otimes \beta \cdot \{ A_0 \left[r \cdot \mathcal{L}_{\gamma_{\mathrm{dil}}}(\omega) + (1 - r) \cdot \mathcal{L}_{\gamma_{\mathrm{dense}}}(\omega) \right] \\ & + (1 - A_0) S_{\mathrm{internal}}(q,\omega,\gamma_{\mathrm{dil,dense}},r) \} + \beta_{\mathrm{D_2O}} \mathcal{L}_{\gamma_{\mathrm{D_2}O}} \end{aligned} \tag{7.3}$$

with $\gamma_{\mathrm{dil}} = D_{\mathrm{dil}}\, q^2$ and $\gamma_{\mathrm{dense}} = D_{\mathrm{dense}}\, q^2$. Therein, the additional dependence of S_{internal} on r and $\gamma_{\mathrm{dil,dense}}$ accounts for the separate convolution of the internal dynamics with each associated COM diffusion, at the correct ratio r. Figure 7.3 depicts an example spectrum with fit of Equation 7.3. We emphasize that D_{dil} and D_{dense} may each account for distributions of cluster sizes represented by one effective diffusion coefficient [542], assuming that the two coexisting phases both show some degree of polydispersity.

Depending on the best reduced χ^2, we employ Equation 7.2 or 7.3 for all samples that were not centrifuged, obtaining one or two COM diffusion coefficients D, depending on the sample (figure 7.16). For all centrifuged samples, where the protein-rich and protein-poor phases were physically separated, we solely employ Equation 7.2. Figure 7.4 represents these COM diffusion coefficients normalized to the corresponding diffusion coefficients of the BSA solution without salt at the same

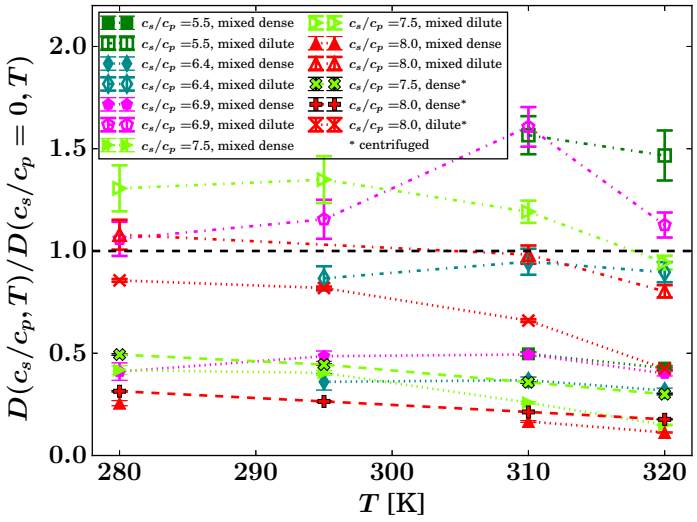

Fig. 7.4. Summary of the reduced apparent center-of-mass diffusion coefficients. Depending on salt concentration c_s, temperature T, and centrifuging, one or two diffusion coefficients D were fitted. In the plot, the fit results are displayed after normalization to the diffusion coefficient in the absence of salt at the respective temperature $D(c_s/c_p = 0,\, T)$. The legend denotes the calculated number of salt ions per protein c_s/c_p and whether the samples where centrifuged, resulting in "dense" and "dilute" phases, or "mixed". For all samples, the protein concentration as prepared was $c_p = 240\,\mathrm{mg/ml}$, prior to centrifuging where applicable.

temperature, referred to as $D(c_s/c_p, T)/D(c_s/c_p = 0, T)$, illustrating the relative speeding-up of the diffusion in the dilute phase and slowing-down in the dense phase upon LLPS. The diffusion coefficients of the centrifuge-separated dense phases are very similar to those obtained for the dense phases of the corresponding mixed samples (Figure 7.4). This observation confirms the validity of modelling the two phases in mixed, i.e. non-centrifuged, samples by two diffusion coefficients. Furthermore, the reduced diffusion coefficients $D(c_s/c_p, T)/D(c_s/c_p = 0, T)$ for the dense phases decrease approximately linearly with T, indicating an increasing cluster size with increasing T.

Figure 7.5 displays the ratio of the apparent diffusion coefficients in the dense and dilute phase from the QENS data (left column of the legend, area-enclosing symbols connected by solid and dashed lines), for those samples where two phases were fitted. The centrifuged sample (dashed line) is probably not separated as neatly as the *in situ* separated samples. In addition, figure 7.5 displays the ratio of the theoretical monomer hard-sphere apparent diffusion coefficients calculated from the concentrations determined by UV-Vis (figure S9), measured on the same BSA batch (right column of the legend, tripod symbols connected by dotted lines). This calculation using the UV-Vis determined volume fractions was carried out based on the theoretical apparent short-time diffusion coefficients of colloidal hard spheres described by scalar functions $D_t(\varphi, T) = D_{0,t}(T) f_t(\varphi)$ and $D_r(\varphi, T) = D_{0,r}(T) f_r(\varphi)$ [3,4] for translational and rotational diffusion coefficients, respectively, from which the apparent diffusion $D = D(D_r, D_t) = D_0 f(\varphi)$ is determined numerically involving series expansion and root finding [163], where $D_0(T)$ is the dilute-limit diffusion coefficient. The UV-Vis results are plotted for values where this root finding converges [163]. The inset of figure 7.5 displays the UV-Vis versus the QENS the results at $T = 303\,\mathrm{K}$. The resulting symbols coincide with the bisector

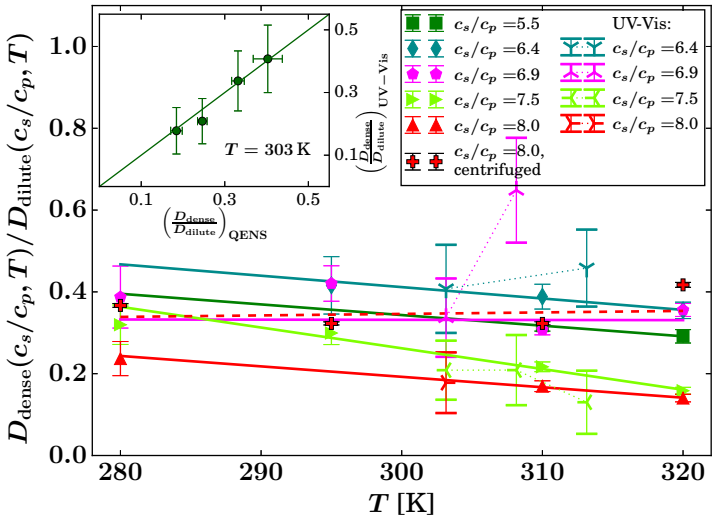

Fig. 7.5. Ratio of the reduced apparent center-of-mass diffusion coefficients in the dense and dilute phase of the samples at identical c_s, c_p, T (filled symbols), and calculated ratio for the apparent diffusion of hard sphere monomers $D = D_0 f(\varphi)$ at the same concentrations (cf. Equation 7.4), assuming the concentrations c_p and resulting protein volume fractions φ measured by UV-Vis in the centrifuged dense and dilute phases, respectively, on the identical same protein batch at identical c_s, c_p, T (tripod symbols). The solid and dashed lines are error-weighted linear fits to the QENS results (dashed for the centrifuged sample). The dotted lines are guides to the eye for the UV-Vis results. The inset reports the values at $T = 303\,\mathrm{K}$ from UV-Vis versus the fitted values at this temperature from QENS, from the main plot (symbols). The line marks the bisector.

(line) within the error, corroborating the agreement of the QENS and UV-Vis results in this picture, within the limits of the centrifugation efficiency affecting the UV-Vis samples.

We interpret the results depicted in Figs. 7.4 and 7.5 as follows. Both the salt and protein concentrations in both dense and dilute phases upon LLPS change relative to the homogeneous mixture, i.e. both c_s and c_p split up in some form into local concentrations. A graphical representation of a constant-T-cut through the LLPS phase diagram is reported in figure 7.2c. Both the dense and dilute phase should be on the phase boundary (at opposing sides), cf. dashed line in figure 7.2c.

Based on previous work [306, 538, 542] the dependencies on D_0 and on the crowding and salt master curves factorize. We assume that both the Stokes-Einstein scaling $D_0(T)$ and percolation-limit scaling cancel out in the ratio of COM diffusion coefficients. These assumptions define the central hypothesis that at a given constant temperature

$$\frac{D_{\mathrm{dense}}}{D_{\mathrm{dilute}}} = \frac{D_0\, g(c_s/c_p) f(\varphi_{\mathrm{dense}})}{D_0\, g(c_s/c_p) f(\varphi_{\mathrm{dilute}})} = \frac{f(\varphi_{\mathrm{dense}})}{f(\varphi_{\mathrm{dilute}})}, \tag{7.4}$$

where $f(\varphi)$ is the scalar function describing the relative slowing-down of the COM short-time self-diffusion of monomeric colloidal hard spheres depending on the colloidal volume fraction φ, i.e., due to the crowding [3,4], and $g(c_s/c_p)$ is the salt-induced master curve found earlier [538,542] describing the monotonous slowing-down of the self-diffusion with increasing salt concentration, depending only on the number of salt ions per protein c_s/c_p. This hypothesis implies that the slowing-down due

to the salt-induced cluster formation cancels out. Since this slowing-down [538]

$$D(\varphi, c_s, c_p, T) = D(\varphi, c_s = 0, T)\, g(c_s/c_p, T) \tag{7.5}$$

has been found to depend only on the ratio c_s/c_p at given volume fraction and temperature, to be a constant factor of 0.4 in the percolation limit [542], and to be independent from protein concentration after normalization to $D(c_s/c_p = 0)$ [542], the simple assumption appears reasonable.

7.3 Hypothesis and discussion

The central message combining measured LLPS COM and calculated diffusion ratios from concentrations measured by UV-Vis, thus, is: The results are consistent with the simple picture that in the LLPS regime, the cluster characteristics expressed by $g(c_s/c_p, T)$ and described by the Flory-Stockmayer model [542, 545–547] (cf. inset of figure 7.3) is the same in both the dense and dilute phase, and only the local concentration changes in the two phases. In other words, this picture implies a continuity of the cluster statistics at the phase boundary. Using only the factorization of the numerator and denominator in Equation 7.4 as input from previous work, our experiment agrees with this continuity.

There is no obvious direct association of the transition from optical transparency to turbidity (figure 7.2) with any strong change of the diffusion coefficients (figure 7.4). This finding indicates that although the correlation lengths in the system diverge to reach the lengths required to achieve optical turbidity, i.e., several hundred nanometers, the short-time diffusion remains consistent with small clusters independent from whether or not the sample is macroscopically separated into droplets.

The diffusion coefficients in the dense phase of the mixed samples agree very well with the diffusion coefficients in the dense phase after centrifuging (figure 7.4).

From earlier work [542] it is known that at sufficiently large c_s/c_p, the system can be presumed to be in the percolation limit, i.e., all bonding sites that can be involved in clustering are saturated, and the binding probability does not increase further with increasing c_s/c_p. Correspondingly, the distribution ρ_n of n-clusters converges to a stable $\rho_n/\rho(n, c_s/c_p)$, with ρ being the total number density of particles, that does not increase further with increasing c_s/c_p [542]. The minimum D/D_0 in figure 7.4 is similar to the minimum found for $c_s/c_p \approx 9$ in Ref. [542]. Per volume and mass conservation, confirmed by microfluidic experiments [548], the concentrations c in the two phases split up according to $c_{\mathrm{total}} = (c_{\mathrm{dense}} - c_{\mathrm{dilute}})\, V^*_{\mathrm{dense}} + c_{\mathrm{dilute}}$, where the normalized dense phase volume $V^*_{\mathrm{dense}} = V_{\mathrm{dense}}/V_{\mathrm{total}}$ is the fraction of the dense phase in the total volume. However, the volume splitting cannot be directly inferred from the QENS spectra and the fit parameter r of the mixed samples, since this step would require knowledge of the cluster size distribution function g, as opposed to the sole assumption of g being the same function in the two phases required for Equation 7.4 and, thus, the comparison made in figure 7.5 (cf. Figs. 7.23, 7.24).

From our QENS data we infer that short-time diffusion is present even in the fully percolated system, i.e., the effective hydrodynamic size of the presumably transient and not necessarily compact [542] clusters in the short-time limit does not seem to diverge, in contrast to the long-time correlation lengths observable by ultra-small angle neutron scattering (USANS) and XPCS. This QENS observation is consistent with the finding from simulations [532] that the system remains highly dynamic at the spinodal line. Moreover, we observe the absence of discontinuity in the temperature-dependence of the diffusion when entering the optically turbid regime, suggesting that there is no (first order) phase transition in the short-time diffusion. From the possibility to fit two apparent

global diffusion coefficients to the mixtures, we infer that micro-heterogeneity may set on much earlier than optical turbidity. This statement is corroborated by the consistent fit of distinct dense and dilute populations in the QENS spectra from the mixed phases at conditions below the associated critical temperature determined from UV-Vis absorption measurements (figure S7), which becomes obvious for instance for the sample depicted in figure 7.2a, that splits microscopically already at $T = 280\,\mathrm{K}$ according to the fit, Figs. 7.16 and 7.4, but macroscopically only at higher T (figure 7.2b).

We speculate that when small clusters, that may be rigid or transient on a time scale $> 1\,\mathrm{ns}$, cannot percolate further, the heterogeneity starts. In figure 7.4 we observe that the short-time diffusion coefficient is never reduced by more than a factor of about 10 compared to the corresponding salt-free system. From numerical evaluations of the model cluster scattering function we expect a maximum reduction of the salt-free diffusion coefficient by a factor of about 0.4 in the percolation limit [542]. If the reduction of the diffusion is larger, we speculate that a deviation of the cluster size distribution from the Flory-Stockmayer model occurs [545–547]. Such deviation from the Flory-Stockmayer distribution could imply that all surface charge patches on the proteins become fully "saturated" or "screened" by salt-induced charges, defining the onset of long-range correlations, possible breaking of small clusters and dynamic exchange of proteins between clusters on a time scale beyond the coherence time of this experiment of $\approx 1\,\mathrm{ns}$. A central question arises as to whether the system "rescales" itself such that the dense and dilute phases each keep following the corresponding master curve. In this context we find that when we fit only one average COM diffusion coefficient, we reproduce the previous results on the master curves [542] (figure 7.20). The ratio $D_{\mathrm{dilute}}/D_{\mathrm{dense}}(T)$ at constant c_s within LLPS seems to be a weakly decaying, nearly constant relation (figure 7.5). In this ratio, the Stokes-Einstein dependence cancels. Thus, at constant cluster size distribution, this ratio of diffusion coefficients represents the ratio of protein concentrations, as per the crowding effect. The trend qualitatively follows the binodal separation. Our results on the short-time self-diffusion are consistent with previous findings on the different system of γ-crystallin, where LLPS was induced by crowding as the main control parameter (as opposed to charge), and where the collective diffusion was accessed, finding the absence of a discontinuity in the collective diffusion upon entering LLPS [549,550].

We have employed spin-incoherent high-resolution QENS to access the self-dynamics of BSA in aqueous solution in the presence of a tri-valent salt inducing LLPS. We stress the possible sources of ambiguity in the best choice of the model to describe these data, in particular given the complexity of this model. Notably, the possibility to fit two distinct apparent global diffusion coefficients, which each represent a distribution of clusters, does not prove that this choice of model is correct. Risks regarding the interpretation may further arise from the limited energy resolution, from an inaccurate assumption of the excluded volume in the centrifuged samples, and from other sources of uncertainty such as background scattering. Nevertheless, our results provide a simple and convincing picture of the nanosecond dynamics upon entering LLPS which, in the limiting cases explored before, is consistent with results from earlier work. We find that the short-time self-diffusion of BSA is slowed down, but does not vanish at the LLPS, in agreement with the previously existing picture that protein clusters remain highly dynamic and interchanging at LLPS, even in the dense phase. We present a simple hypothesis concerning the short-time self-dynamics of the transient clusters present at the LLPS, namely that while the local concentrations split in the dense and dilute phases, the short-time cluster size distribution of the presumably transient clusters in these two phases remains unchanged at the separation. Our work provides experimental evidence for this novel hypothesis, by unambiguously accessing, for the first time in protein LLPS, the ensemble-averaged short-time self-dynamics informing on cluster characteristics, including systematic controls by comparing mixed and

centrifuge-separated phases. It associates the results with UV-Vis concentration measurements and theoretical colloid models. The new and systematic findings, employing a perfectly tunable model system, will contribute to the very active debate on the nature of LLPS.

7.4 Experimental Methods

BSA (catalog no. A3039, batch no. SLCD4770, lyophilized powder $> 98\%$ purity, heat shock fraction, protease free, fatty acid free, essentially globulin free, pH 7) and $LaCl_3$ (Sigma-Aldrich catalog no. 449830, batch no. 0000088871, anhydrous, 99.9% purity) were obtained from Sigma-Aldrich of Merck KGaA and used without additional purification. D_2O ($> 99.8\%$ purity, cat. no. 014764-30, batch no. 0438446) was obtained from ThermoFisher Scientific (Waltham, MA, USA). Further details on the sample preparation, testing conditions and choice of the samples for the neutron experiment are reported in the SI.

The QENS experiment was carried out on the cold neutron backscattering spectrometer (BASIS) [312] at the SNS, Oak Ridge, Tennessee, with a pulse repetition rate of 60 Hz, employing Si(111) analyzers corresponding to an elastic wavelength of 6.27 Å, energy resolution of $\sim 3.5\,\mu$eV FWHM and energy transfer range $-100\,\mu\text{eV} \leq \hbar\omega \leq +100\,\mu\text{eV}$, translating to the accessible time range $41\text{ ps} \leq \tau = h/(\hbar\omega) \leq 1.2\text{ ns}$. With the range in momentum transfer $\hbar q$, $0.4\text{ Å}^{-1} \leq q \leq 1.9\text{ Å}^{-1}$, BASIS allows to study motions at a length scale of $3.22\text{ Å} \leq \ell \leq 25\text{ Å}$. The samples were filled into double-walled cylindrical aluminum cells (23 mm outer diameter, 0.15 mm gap between inner and outer radius), sealed against vacuum with indium wire and inserted into a closed-cycle cryostat for the measurements. The acquisition time amounted to ~ 4 hours per sample per temperature.

The data were first processed using Mantid [396], including normalization to the incident flux and to a Vanadium standard for detector calibration, and subsequently analyzed using *python*, employing notably *scipy.curve_fit* [163, 290]. Prior to the fits, the sample container signal was subtracted, accounting for self-shielding by Paalman-Pings factors [551]. To account for possible container batch variation, an elastic peak describing residual container scattering was nevertheless allowed in the fits. We write the internal dynamics in the model scattering functions, eqs. 7.2, 7.3, convoluted with the COM diffusion characterised by the linewidth γ as

$$S_{\text{internal}}(q,\omega,\gamma) = \alpha\mathcal{L}_{\gamma+\lambda_1} + (1-\alpha)\mathcal{L}_{\gamma+\lambda_2}, \tag{7.6}$$

where the sum $\gamma + \lambda_{1,2}$ of the Lorentzian widths arises from the convolution of the internal with the COM diffusion, and where the widths $\lambda_{1,2}$ are coupled

$$\begin{aligned}
\lambda_{1,2} &= \frac{(\Gamma_1+\tau_1^{-1})(\Gamma_2+\tau_2^{-1}) \pm \Lambda}{2} \\
\Lambda &= \sqrt{\left((\Gamma_1+\tau_1^{-1}) - (\Gamma_2+\tau_2^{-1})\right)^2 + \frac{4}{\tau_1\tau_2}} \\
\alpha &= \frac{\tau_1\Gamma_2 + \tau_2\Gamma_1 + (\tau_1+\tau_2)(\tau_1^{-1}+\tau_2^{-1}-\lambda_1)}{(\lambda_2-\lambda_1)(\tau_1+\tau_2)} \\
\text{with} \quad & \Gamma_{1,2} = D_{1,2}\,q^2\,.
\end{aligned} \tag{7.7}$$

Therein, the only free fit parameters for the internal diffusion, $D_{1,2}$ and $\tau_{1,2}$, account for the internal diffusion separated into backbone and side chain motions, respectively, and are reported in Section 7.5.

Centrifuging was performed at constant speed of 3900 rpm (3.214 $\times$ g, maximum value for the selected rotor) and maintained at a temperature of 40°C for at least six hours until successful phase separation, using an Eppendorf$^{\mathrm{TM}}$ (Hamburg, DE) 5804-R centrifuge with a with a rotor radius of 18.9 cm.

Temperature dependent UV-Vis measurements were performed with a Jasco V-630UV-Vis Spectrophotometer at the PSCM in Grenoble, employing the identical same BSA protein batch as for the neutron experiments, starting at a set-point temperature of $T = 5$°C with temperature steps of 2.5 K and equilibration times of 15 minutes to observe the temperature dependent turbidity (figure 7.2). The sample temperature was recorded in the reference cell. The absorption values were normalized to the salt-free protein solution at $T_{\mathrm{set}} = 5$°C and averaged subsequently for the wavelength range $500\,\mathrm{nm} < \lambda < 700\,\mathrm{nm}$.

Acknowledgements

This research used resources at the SNS, a Department of Energy (DOE) Office of Science User Facility operated by the ORNL, Oak Ridge, Tennessee, USA. This work is based on experiments performed at the BASIS spectrometer supported by Jülich Center for Neutron Science (JCNS) at the SNS/ORNL, which the authors thank for beamtime allocation. I.M. and T.S. gratefully acknowledge the financial support provided by JCNS to perform the neutron scattering measurements at the SNS and thank R. Moody for excellent support in the SNS chemistry laboratory. Since the fragile samples had to be prepared on site, the experiment benefited from the laboratory infrastructure on site. Moreover, we acknowledge funding by DFG-ANR German-French collaborative grants (ANR-16-CE92-0009, ANR-21-CE06-0047 / DFG SCHR700/28-1, DFG SCHR700/42-1) and by the BMBF (ErUM-pro 05K19VTB and 05K22VTA). I.M. acknowledges an ILL PhD studentship in the spectroscopy group funded by InnovaXN, a EU Horizon 2020 MSCA COFUND programme (innovaxn.eu, grant agreement No 847439). This work also used tools and laboratories of the PSCM with support from ESRF and ILL in Grenoble.

Associated Content

Supporting Information: Section 7.5 reports details of the LLPS testing conditions and samples (Figs. 7.6-7.10, table 7.1). It also includes photographs of samples, UV-Vis results (Figs. 7.11-7.14), additional neutron data fit parameters (Figs. 7.15-7.23) and estimation of phase volume ratio (figure 7.24 and table 7.2). All code used to reduce and analyse the data, as well as the UV-Vis and reduced neutron data, are available in the ILL Gitlab code repository under *https://code.ill.fr/seydel/ipts-23886*.

Data availability: All raw neutron data are permanently curated by the SNS under experiment number IPTS-23886.

7.5 Supplementary Information

7.5.1 Sample preparation, testing conditions for LLPS and selected samples

All preparation and testing reported in this section was carried out on site at the SNS/ORNL immediately prior to and during the neutron experiment on one single protein batch. The most challenging steps of the described experiment are sample preparation and identifying conditions for LLPS, which are described in details in the following paragraphs.

Sample preparation. BSA – bovine serum albumin – (catalog no. A3039, batch no. SLCD4770, lyophilized powder >98% purity, heat shock fraction, protease free, fatty acid free, essentially globulin free, pH 7) and $LaCl_3$ (Sigma-Aldrich catalog no. 449830, batch no. 0000088871, anhydrous, 99.9% purity) were obtained from Sigma-Aldrich of Merck KGaA and used without additional purification. D_2O ($\leq$ 99.8% purity, batch no. 0438446) was obtained from ThermoFisher Scientific (Waltham, MA, USA). A volumetric flask (VWR cat.no. 10/24-136) was used to define the liquid volumes, notably of the $LaCl_3$-D_2O stock solution. It must be noted that the location of LLPS for BSA in the (c_s, c_p, T)-space is somehow subject to batch-to-batch variability, presumably due to residual salts after the purification process [552], such that attention was paid to carry out all neutron and complementary experiments reported in this work on the identical same batch.

The samples were prepared following the protocols established in previous works [306, 538, 539]. For all samples, given amounts of BSA powder were added to D_2O and after several hours on a roller mixer at room temperature, they were all completely dissolved and the solutions appeared clear. For a chosen nominal protein concentration c_p = 240 mg/mL (corresponding to 3.613 mM), a series of samples with increasing salt concentration c_s was prepared using a 100 mM $LaCl_3$ stock solution kept in a glass volumetric flask in the fridge. As long as the salt stock solution was added to the pure BSA solutions in D_2O, they soon became milky and likely to stick on the vial walls. After 1-2 hours on the roller mixer, samples were kept for some minutes in the fridge and then left setting at lab temperature (19 ± 1)°C, ready to be tested on their behaviour against temperature variation. This step was quite easy to accomplish for the samples with low content of salt, while it was more challenging for samples with higher c_s, which needed more time to reach a sufficiently homogeneous appearance. The 240 mg/ml BSA solutions in D_2O were prepared with the following $LaCl_3$ concentrations: $c_s = 20,\ 23,\ 25,\ 26,\ 27,\ 29,\ 30,\ 35$ mM.

Testing conditions for LLPS by visual inspection. Based on tests and previous works, we knew that for BSA at $c_p = 240$ mg/mL the range from 20 to 30 mM $LaCl_3$ salt concentration could be promising and started by preparing three samples at 20, 25 and 30 mM $LaCl_3$. The BSA powder was weighed and then dissolved in D_2O by keeping the tubes on a roller mixer until all visible aggregates completely disappeared. After the pure BSA solutions being ready and set, the respective amount of 100 mM $LaCl_3$ stock solution was added; this step typically causes an immediate increase of turbidity in the samples, which need some time to completely stabilize. They were therefore kept on a roller mixer for a time ranging from some hours to an entire night and later kept in the fridge for some hours until they appeared completely clear (figure 7.6).

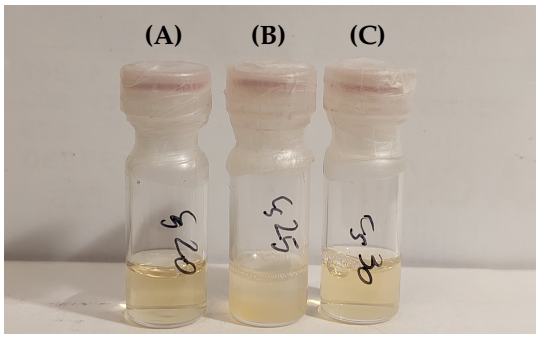

Fig. 7.6. BSA solutions with increasing $LaCl_3$ concentration at room temperature. A subset of the BSA solutions prepared at 240 mg/mL, with increasing concentration of the trivalent salt $LaCl_3$, namely $c_s = 20$ mM (sample **(A)**), 25 mM (sample **(B)**), 30 mM (sample **(C)**) from left to right. The picture was taken after preparing the samples and letting them set and stabilize at room temperature (18°C was the temperature reported on the thermometer of the chemistry laboratory). Just by visual inspection, one can notice that the 25 mM sample seems slightly less transparent than the two others.

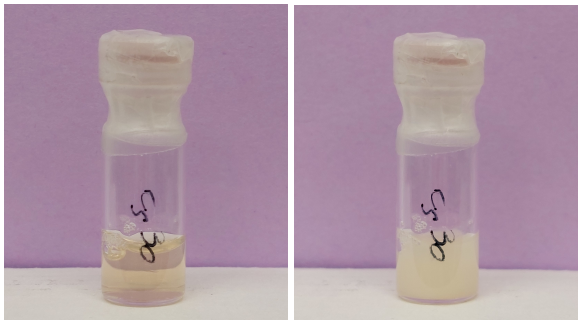

Fig. 7.7. BSA solution at 30 mM $LaCl_3$ after cold and hot baths. BSA solution at 240 mg/mL with 30 mM $LaCl_3$ after being for 1-2 mins in the cold bath at $0°$C (left) and after 1-2 mins in the hot bath at 39-40°C (right). The sample becomes clear at $0°$C, while it turns white and turbid if kept at its lower critical solution temperature (LCST). The procedure can be iterated without altering the samples, which means that the process is completely reversible.

In order to test the presence of LLPS, three water baths were prepared and kept at ~ 0, ~ 32 and ∼37-40°C, respectively. Each sample was immersed in the cold bath for 1-2 mins and afterwards in the hot ones. The 20 mM salt sample (figure 7.6-**(A)**) did not seem to change its appearance due to temperature variation, even if it was kept in the baths for some minutes. The other two samples (figure 7.6-**(B)**, **-(C)**) were instead more thermoresponsive, especially the one at 30 mM. After being at $0°$C it became clearer than it was at lab temperature (figure 7.7, left) and then it was tested in the two hot baths: at 32°C the solution turned milky after 7-8 mins, while at 39-40°C the transition to a turbid solution only took 2 mins (figure 7.7, right). Snapshots of this transition are also reported in figure 7.8. Due to its behaviour, the 30 mM salt sample was selected as a good candidate for extracting both dense and dilute phases separately and was therefore centrifuged at $40°$C overnight. In spite of showing a nice splitting between dense and dilute phases, the ratio obtained was approximately 20% dilute / 80% dense, which was not enough for the neutron experiment.
Two other sample conditions were also tested in order to look for other good candidates showing LLPS. We reached $c_s = 35$ mM and also prepared two equivalent samples at $c_s = 27$ mM, to explore

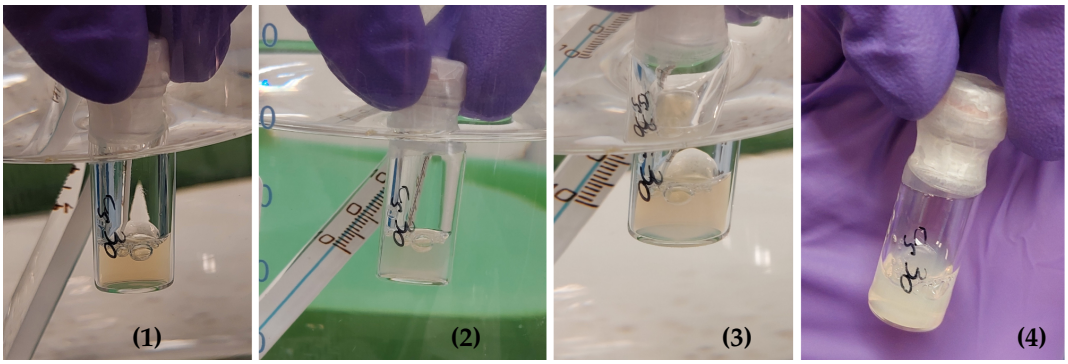

Fig. 7.8. Snapshots of temperature-driven changes in appearance of BSA solution with 30 mM $LaCl_3$. BSA solution at 240 mg/mL with 30 mM $LaCl_3$ **(1)** just immersed in the 39-40°C bath after being kept at 0°C, **(2)** few seconds later, **(3)** after $\sim$ 1 min and **(4)** after staying some minutes in and being removed. A transition of the sample appearance from clear/transparent to turbid/milky is observed from left to right (going from 0°C to 40°C).

the interval 25-30 mM. The 35 mM one was not very responsive to temperature variation, while the 27 mM ones showed a fast increase of solution turbidity after being immersed into the hot bath (figure 7.9). Since it exhibits strong signatures of LLPS, the 27 mM salt samples and the 25 mM one (very close in terms of c_s) were selected to extract the dense and dilute phases and were therefore centrifuged at 40°C for some hours. At the end of that step, the two 27 mM samples both showed a splitting ratio of approximately 70-65% dilute / 30-35% dense, whereas the 25 mM sample split in 85-90% dilute / 15-10% dense (figure 7.10).

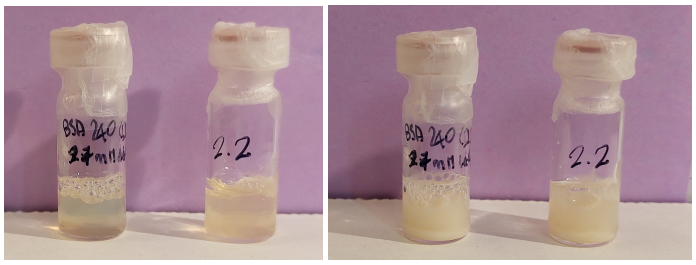

Fig. 7.9. BSA solutions at 27 mM $LaCl_3$ after cold and hot baths. Two equivalent samples of BSA solutions at 240 mg/mL with 27 mM $LaCl_3$ after being for around one minute in the cold bath at 0°C (left) and after one minute in the hot bath at 39-40°C (right). In the first step, the samples look clear, while after reaching the LCST and entering the phase separation regime they become milky and turbid. As above, the mechanism is reversible.

Systematic search of promising samples. To test LCST-LLPS behavior on all samples prepared, two water baths kept respectively at 0°C and 37-40°C were used; temperatures were constantly monitored using immersed mercury thermometers. Each sample, contained in a glass vial or a Falcon tube, depending on the volume prepared, was immersed in the cold bath, subsequently in the hot one and then back in the cold one. By visual inspection, most samples were quite clear at the lab temperature of (19 ± 1)°C and seemed to become even clearer when placed in the cold bath ($\sim$ 0°C). When immersed in the hot bath, they turned milky and turbid after some time and became clear again

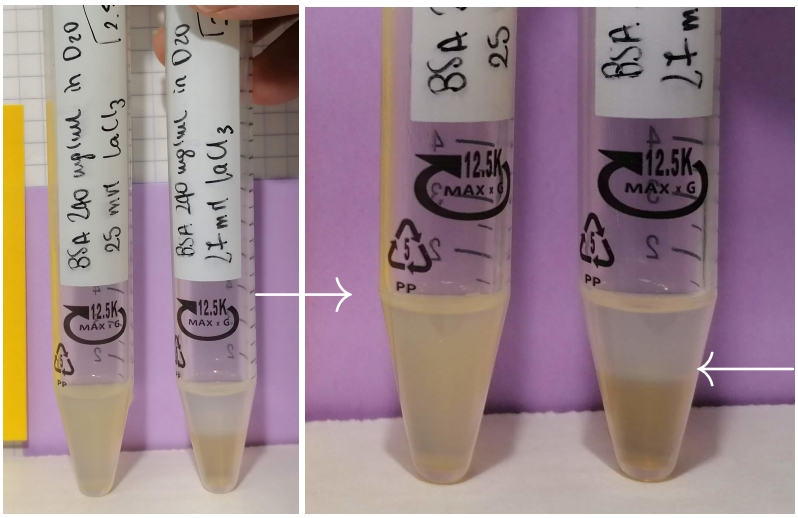

Fig. 7.10. BSA solutions with 27 mM $LaCl_3$ after centrifugation at 40°C. BSA solutions at 240 mg/mL with 25 and 27 mM $LaCl_3$ (respectively on the left and on the right in both images) after being centrifuged at 40°C for some hours. The figure on the right is a zoom on the sample for better visualization. White arrows indicate the meniscus/splitting interface between the dilute phase on top and the dense phase on the bottom.

when placed back in the cold bath. As mentioned before, the most promising of the prepared samples was undoubtedly the one with 27 mM $LaCl_3$ (figure 7.2), due to its almost immediate temperature-driven change of appearance. As a consequence, the fastest changes of transparency on temperature occurred closest to $c_s = 27$ mM, corresponding to $c_s/c_p \approx 7.5$ salt ions per protein, as reported in Table 7.1. We emphasize again that the conditions found depend on the protein batch.

Mechanical separation of the phases. BSA solutions with $c_s = 25$, 27 and 29 mM $LaCl_3$ were centrifuged at 20000 rpm at 40°C, i.e., above LCST, during 2 to 6 hours. After centrifugation, the selected samples nicely showed a clear LLPS with different ratios of dilute and dense phase depending on their salt concentrations (figure 7.2). All dilute phases were easily pipettable, while the dense ones were in some cases sticky, highly viscous and hard to pipette. The most promising samples in showing LLPS among the salt concentration series prepared, namely the BSA solution at c_p = 240 mg/mL with c_s = 25, 27 mM $LaCl_3$, were the ones selected to extract both dilute and dense phases arising from LLPS.

Samples measured with QENS. BSA solutions at c_p = 240 mg/mL in D_2O with $LaCl_3$ at $c_s = 20$, 23, 25, 27, 29 mM were measured with neutron backscattering. BSA samples with 20, 25 and 27 mM $LaCl_3$ were measured at 280, 295, 310 and 320 K in a sequence of heating steps on the same samples, and again at 280 K after cooling down for one sample to check reversibility. Dense and dilute phases extracted from the sample with $c_s = 27$ mM $LaCl_3$ and the dense phase from the sample with $c_s = 25$ mM were also measured separately, at the same temperatures and using the same heating rates. BSA c_p = 240 mg/mL + $LaCl_3$ mixtures with 23 and 29 mM $LaCl_3$ were measured at 280 K only. An empty aluminum can was measured at 295 K, along with pure D_2O at all temperatures studied, 280, 295, 310, 320 and 330 K.

$\mathbf{c_s}$ **[mM]**	0	20	23	25	27	29
$\mathbf{c_s/c_p}$	0.0	5.5	6.4	6.9	7.5	8.0

Table 7.1. From the salt concentration c_s, the number of salt counterions per protein c_s/c_p is calculated by assuming the nominal concentration of BSA in all samples $c_p = 240$ mg/mL and the molar mass of BSA $m_{\mathrm{BSA}} = 66.430$ kDa. The BSA concentration given in [M] = mol/L is thus: $c_p[\mathrm{M}] = c_p[\mathrm{mg/mL}]/m_{\mathrm{BSA}} = 3.613$ mM.

7.5.2 Phase diagrams determined by UV-Vis spectroscopy

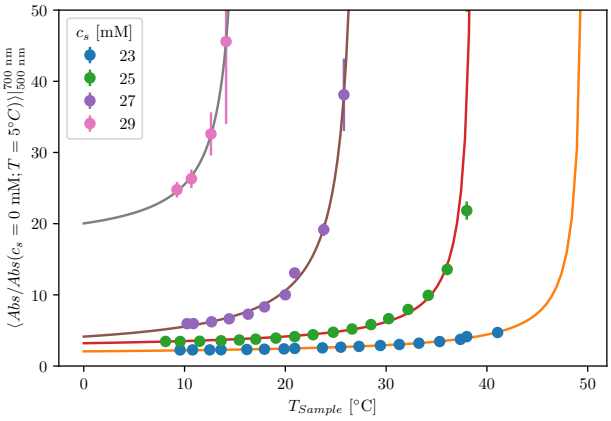

Fig. 7.11. Normalized averaged absorption measured with UV-Vis at different temperatures for different salt concentrations as indicated in the legend. Solid lines represent the fits of the temperature dependence as explained in the main text, equation 7.8.

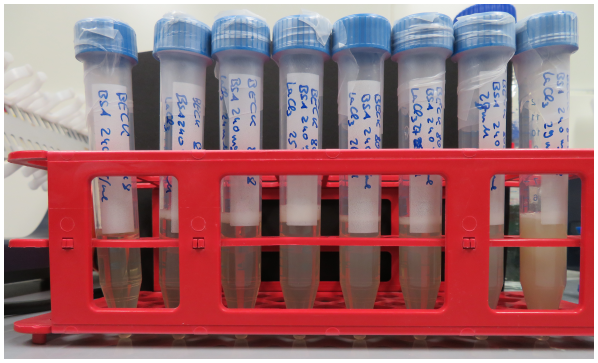

Fig. 7.13. Macroscopic turbidity of the samples is increasing with increasing salt concentration. Falcons shown contain $c_s = 0$ mM, 23 mM, 24 mM, 25 mM, 26 mM, 27 mM, 28 mM, 29 mM from left to right. Samples were stored at ≈ 6 °C before image acquisition.

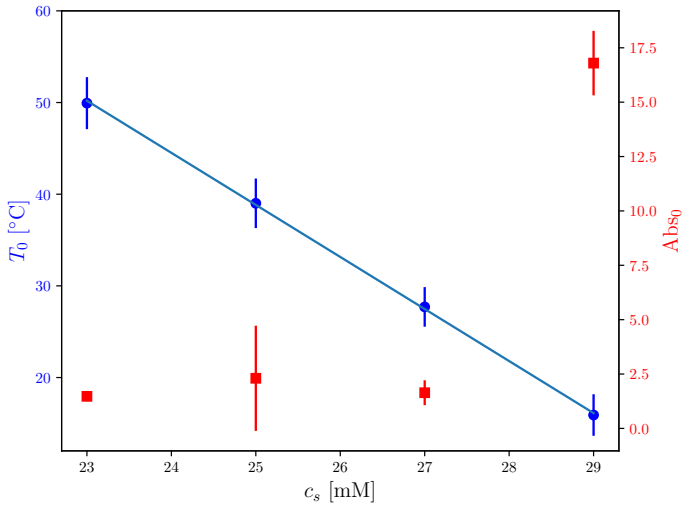

Fig. 7.12. Critical temperature T_0 from fits of equation 7.8 (figures 7.11) and absorption at low temperature Abs_0 as a function of c_s (symbols referring to the left and right y-axis, respectively). A linear decay can be observed in the critical temperature (blue line, slope: (-5.68 ± 0.57)°C/mM, offset 180.80 ± 15.07 °C), while an increase in the initial absorption is observed only for the highest salt concentration.

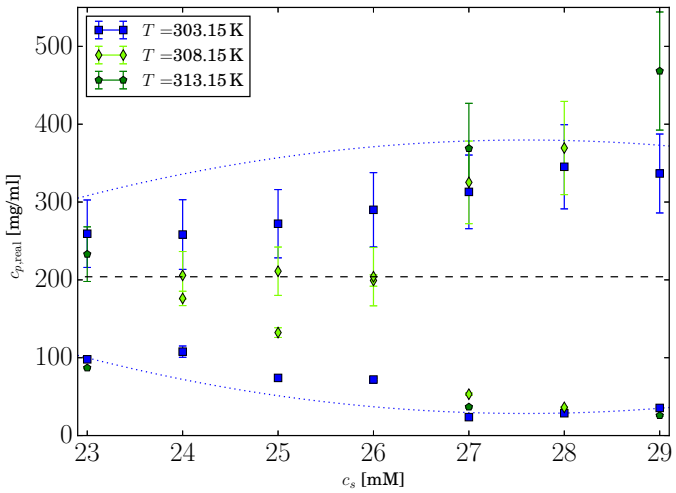

Fig. 7.14. Summary of UV-Vis data on the protein concentration c_p in the dense and dilute phase, respectively, versus the salt concentration c_s (symbols). The data were taken by centrifuging at 3 different temperatures, as indicated in the legend. The dashed line denotes the protein concentration at which all samples were prepared, namely at the nominal concentration $c_p = 240$ mg/ml, resulting in the real protein concentration $c_{p,\mathrm{real}} = c_p/(1 + c_p\,\nu) = 204$ mg/ml, where $\nu = 0.735$ ml/g is the specific volume of BSA. The dotted lines are guides to the eye; the lower one was obtained by a polynomial fit to the dilute concentrations measured at $T = 303.15$ K and then mirrored on the $c_p = 240$ mg/ml line to obtain the upper one.

Temperature dependent UV-Vis measurements have been performed with a Jasco V-630 UV-Vis Spectrophotometer at the Partnership for Soft Condensed Matter (PSCM) in Grenoble, employing the identical same BSA protein batch as for the neutron experiments, starting at a setpoint temperature of $T = 5°\mathrm{C}$ with temperature steps of 2.5 K and equilibration times of 15 mins to observe the temperature dependent turbidity (figure 7.2). The sample temperature was recorded in the reference cell. The absorption values were normalized to the salt free protein solution at $T_{\mathrm{set}} = 5°\mathrm{C}$ and averaged afterwards for $500\ \mathrm{nm} < \lambda < 700\ \mathrm{nm}$. The temperature dependence of this average is diverging at a critical temperature T_0 which depends on c_s (Figure 7.11). The temperature dependence can be approximated by

$$\mathrm{Abs} = \frac{a}{T - T_0} + \mathrm{Abs}_0. \tag{7.8}$$

The critical temperature T_0 decays linearly with increasing salt while the absorption Abs_0 increases with salt (Figure 7.12). The increase of Abs_0 does correlate nicely with the observed microscopically observed turbidity (Figure 7.13). To determine the protein concentration in the dense and dilute phase, the samples were centrifuged at different temperatures to separate the dense and dilute phase (Figure). The volume ratio of the two phases $r = V_{\mathrm{dil}}/(V_{\mathrm{dil}} + V_{\mathrm{dense}})$ has been determined by eye. The concentration of the dilute phase has been determined by UV-Vis measurements on a dilution series performed at room temperature using the absorption at $\lambda = 280\ \mathrm{nm}$. The concentration of the dense phase has been determined using the concentration of the dilute phase, the volume ratio r as well as the mass conservation.

Based on these data, it may be attempted to describe the binodals of the phase-separation by [553]

$$T = T_0 \left(\frac{|c - c_0|}{A\, c_0} \right)^{1/\beta} + T_0 \tag{7.9}$$

with $\beta = 0.325$ corresponding to a 3D Ising system and T_0 from equation 7.8 (figure 7.11).

The concentrations in the dense and dilute phase after phase separation by centrifuging, measured by UV-Vis, are reported in figure 7.14 on samples prepared at the same aforementioned conditions and using the same protein batch as for the the neutron experiment.

The partitioning ratio should be connected to the magnitude of the second virial coefficient [513]. The densities of the phases are subject to equilibrium requirements, resulting in equal chemical potentials across the phase boundary [513, 554].

7.5.3 Additional QENS data analysis and additional fit parameters

This section contains complementary results on internal dynamics from the QENS data fitting, along with alternative approaches used, and tests of the robustness of the analysis.

Figure 7.15 displays the energy resolution function of BASIS, recorded on a Vanadium foil in the same cylinder geometry as the samples, for two example momentum transfers (symbols) and its description by a sum of Gaussians functions (lines). Figure 7.16 displays additional example spectra recorded on a BSA solution sample, and associated fits.

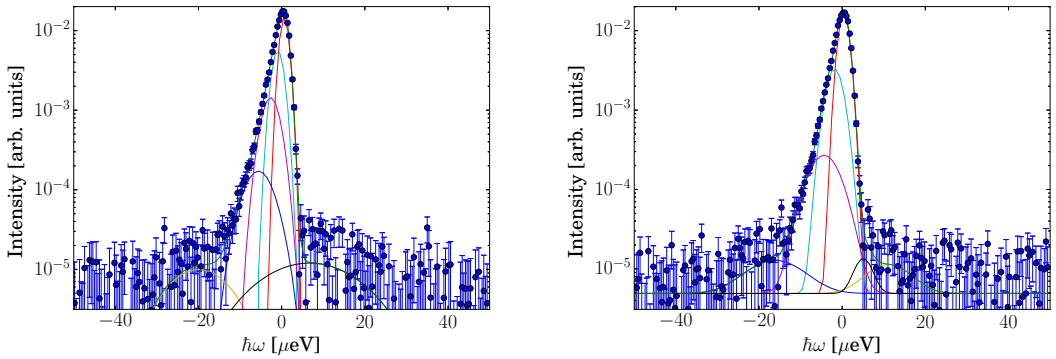

Fig. 7.15. BASIS spectrometer resolution function at $\mathbf{q = 0.75\ \text{Å}^{-1}}$ (left) and $\mathbf{q = 1.25\ \text{Å}^{-1}}$. Energy resolution function of BASIS measured using a Vanadium foil as sample at $q = 0.75$ Å^{-1} (left) and $q = 1.25$ Å^{-1} (right, symbols) and a description by a sum of 6 Gaussian functions (lines) and a constant background. The Gaussians are used for the analytical convolution of the model function in the fits. (Note the logarithmic intensity axis, showing more than 3 orders of magnitude in accessible range, and "zoom" into the energy axis, showing only the region near the elastic peak.)

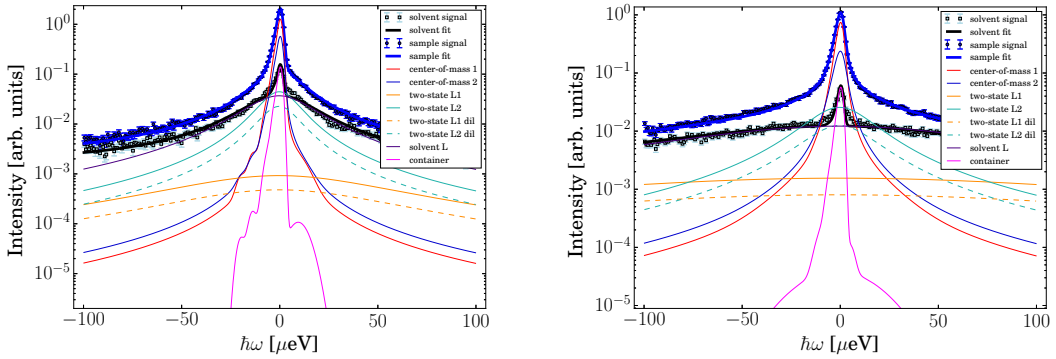

Fig. 7.16. Additional example spectra. QENS spectra recorded on BSA at 240 mg/ml in D_2O with 27 mM $LaCl_3$ at $T = 280$ K, at $q = 0.45$ Å^{-1} (left) and $q = 1.05$ Å^{-1} (right), respectively (upper dark circle symbols). The lower square symbols represent the D_2O solvent signal prior to the container subtraction, and the model employed here included a fit of the container signal (narrow magenta line). All fit components are shown subsequent to the convolution with the energy resolution (cf. figure 7.15), resulting in "skew" curves. The blue and red solid lines denote the two apparent global diffusion processes, the broader solid and dashed lines mark the coupled internal Lorentzians.

Figure 7.17 summarizes the apparent global center-of-mass diffusion coefficients for all measured spectra during the reported QENS experiment, employing the global fits explained in the main article. Figure 7.18 illustrates that the data can be fitted for each q individually if the model contains not more than three Lorentzians in total. For a larger number of Lorentzians, the fits are always carried out along the q and ω axis simultaneously in this work, consistent with previous work that has established this requirement to be able to account for more than one internal diffusive contribution [539].

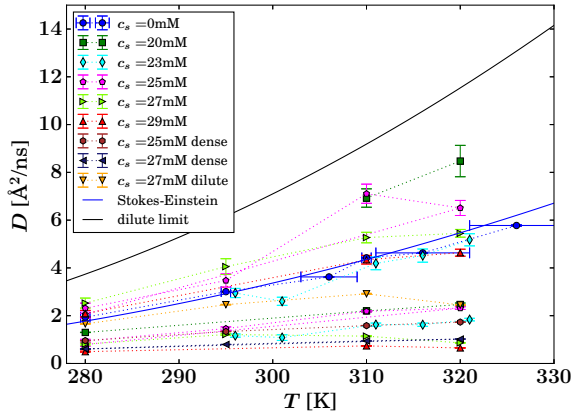

Fig. 7.17. Summary of the apparent center-of-mass diffusion coefficients, i.e. observable global diffusion coefficients, $D = D(D_t, D_r)$ arising from the superposition of translational D_t and rotational D_r diffusion versus temperature for the different salt concentrations explored (symbols). For $c_s = 27$ mM, the dense and dilute phases (cf. figure 7.2), for $c_s = 29$ mM the dense phase were also measured separately after centrifuging. The upper black solid line denotes the theoretical apparent diffusion coefficient in the limit of infinite dilution $D(\varphi \longrightarrow 0)$, the lower blue solid line represents the Stokes-Einstein relation for the BSA sample without salt. The measurements on the BSA solution without salt was subject to temperature stability issues notably at the most elevated temperatures, indicated by the error bars. For all other spectra, the temperature error was smaller than the symbols.

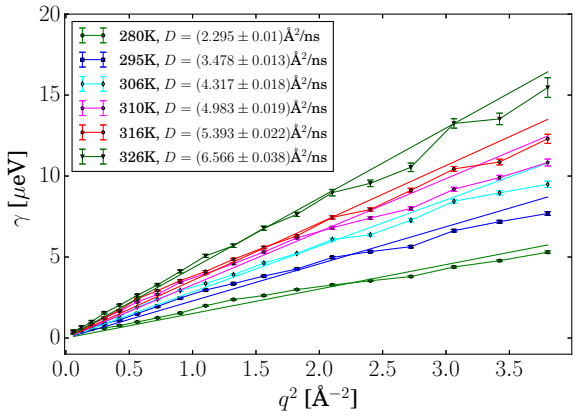

Fig. 7.18. Fits for each q individually of the QENS spectra of the salt-free sample. Linewidth of the first, i.e., narrowest, Lorentzian $\gamma(q)$, attributed to the apparent center-of-mass diffusion, plotted versus q^2, obtained by performing a q-wise fit of the QENS spectra of the pure BSA sample ($c_p = 240$ mg/mL), not imposing Fickian diffusion. In this case only one additional diffusion coefficient was allowed in the fit to account for the internal diffusion, as well as one solvent Lorentzian. The lines denote fits of the Fickian diffusion model $\gamma = Dq^2$. Due to the lack of a second Lorentzian accounting for internal diffusion, the thus obtained diffusion coefficients overestimate the actual diffusion.

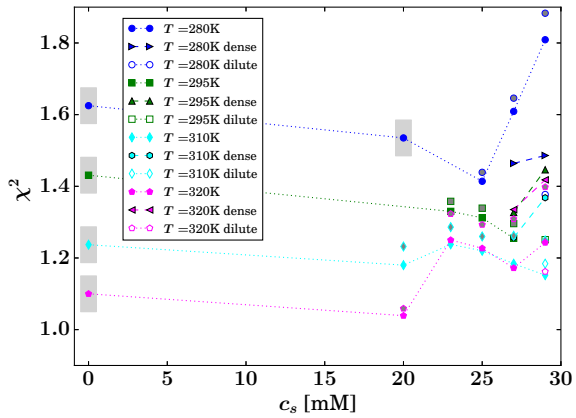

Fig. 7.19. Summary of the goodness-of-fit χ^2 obtained from the global fits for all samples. For the dense and dilute phases separated by a centrifuge (marked as "dense" and "dilute", respectively, in the legend) as well as for the samples marked by a grey shaded area under the respective symbol, only one center-of-mass diffusion coefficient was permitted in the fit. For the fits where two center-of-mass diffusion coefficients were employed, χ^2 for the alternative situation of one center-of-mass diffusion coefficient is in addition displayed by the corresponding grey-filled symbols with identical shape and edge color, that are always located above the associated fit with two center-of-mass diffusion coefficients. All spectra were acquired with the same integral incident neutron flux on the sample. Therefore, the systematic temperature-dependence of this error-weighted χ^2 can be attributed to the higher total spectral signal at lower T, and, thus, lower statistical error.

Figure 7.19 summarizes the reduced goodness-of-fit,

$$\chi^2 := \frac{1}{N_d - N_p} \sum_{i=1}^{N_d} \frac{(y_i - f(x_i, \mathbf{p}))^2}{\sigma_i^2}, \tag{7.10}$$

where y_i are the spectral intensities at points x_i along the spectral axis, f the model function evaluated at the fit parameters $\mathbf{p}$, σ_i the errors on y_i, N_d the number of data points and N_p the number of fit parameters, for all global fits in this work. From figure 7.19 its can be seen that the fits allowing for two separate apparent center-of-mass diffusion coefficients result in a better fit than when only allowing for one center-of-mass diffusion coefficients for non-centrifuged samples at elevated salt concentrations. The residuals reported in figure 7.20 confirm that the central region near $\hbar\omega = 0$ is, however slightly, better fitted with two global diffusion coefficients for samples undergoing LLPS.

Figure 7.21 confirms the consistency of the present with previous results [538, 542]. Figures 7.22 and 7.23 summarize additional parameters from the model used to fit the QENS data described in the previous section.

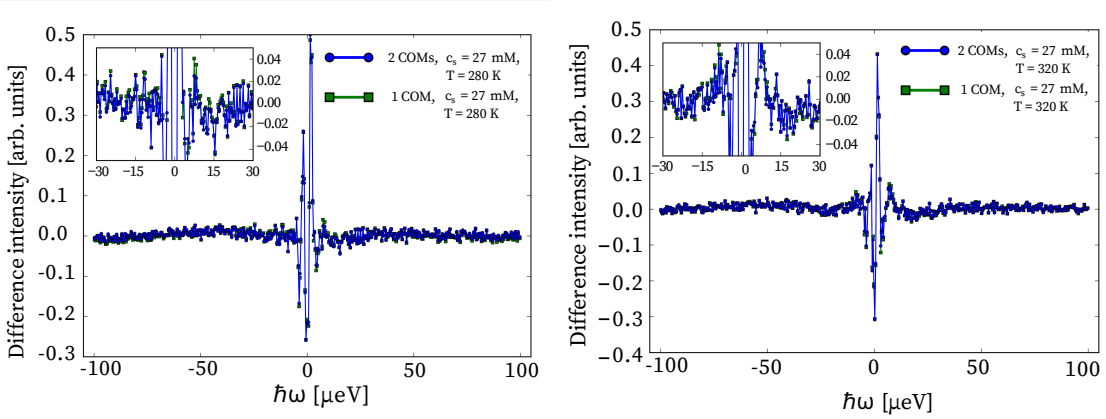

Fig. 7.20. Comparison of the residuals of the fits (difference between data and fit function per energy channel), summed over all q, for the model with one and two effective apparent center-of-mass diffusion (COM) coefficients. Mixed sample (i.e., without external separation by centrifuging) of BSA at 240 mg/ml in D_2O with 27 mM $LaCl_3$, at $T = 280$ K (left), and $T = 320$ K (right). The insets represent a zoom to the main part emphasizing the region near zero energy transfer. The model with two COMs results in a very slightly but noticeably better fit (cf. figure 7.19).

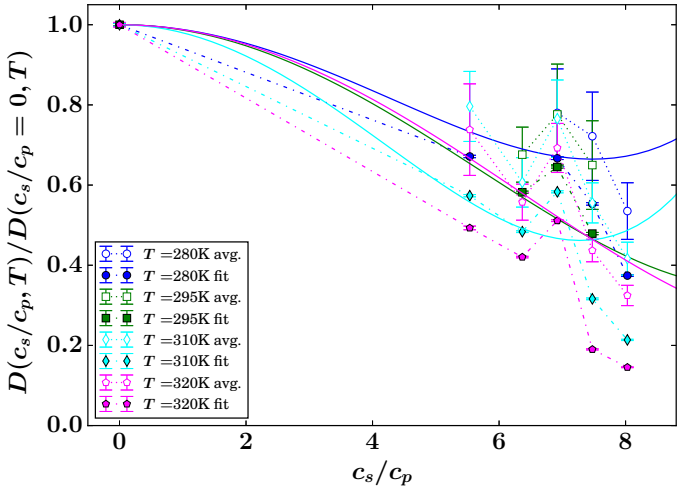

Fig. 7.21. Comparison of the fit result for the center-of mass diffusion coefficients (symbols) with parametrized master curves (solid lines) from previous works [538, 542]. Full symbols represent fits accounting for one single apparent center-of-mass diffusion coefficient for all samples. Open symbols represent the weighted average $[\, r D_{\text{dense}} + (1-r)\, D_{\text{dilute}}\,]$ for the samples where two center-of-mass diffusion coefficients were allowed. The dotted and dash-dotted lines are guides to the eye. It is emphasized that the exact location of LLPS in terms of optical turbidity strongly depends on the protein batch employed. Results from past work are, therefore, not directly comparable.

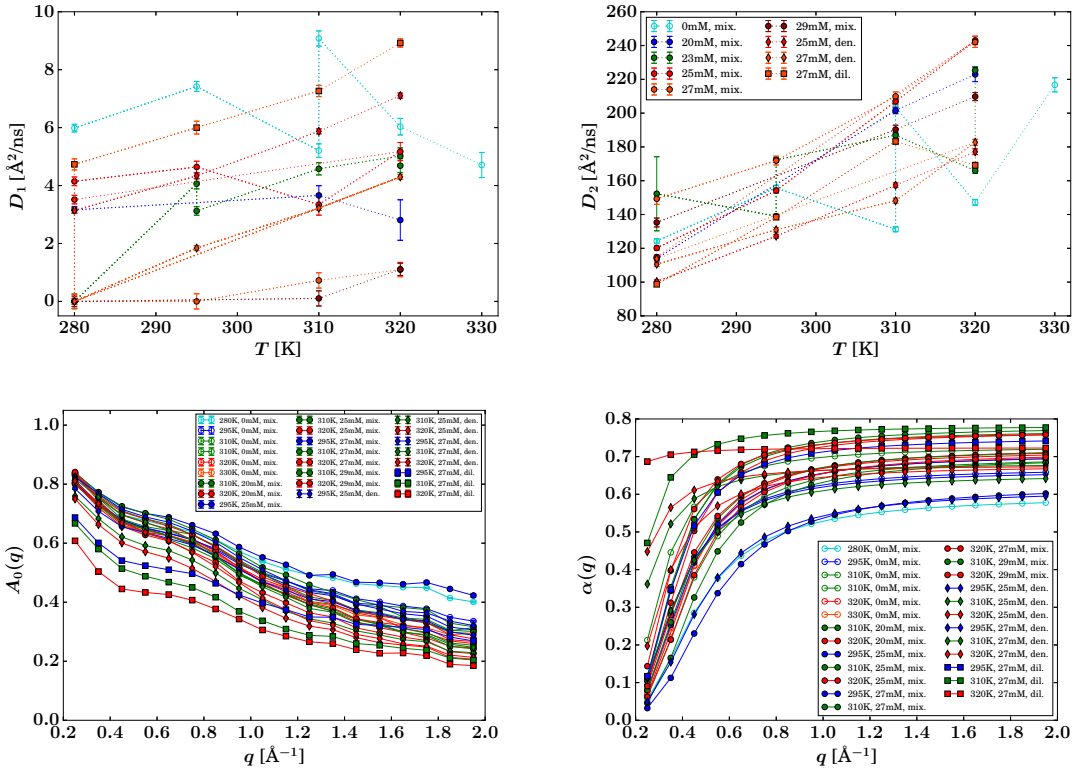

Fig. 7.22. Internal diffusion coefficients D_1 (top left) and D_2 (top right) of the two-diffusive states model defined in equation 7.5 (symbols), attributed to the protein backbone and side chain fluctuations, respectively. The lines are guides to the eye. Elastic incoherent structure factor $A_0(q)$ (bottom left) and coupling parameter $\alpha(q)$ (bottom right) of the two diffusion processes contributing to the internal dynamics of the proteins, each with a corresponding diffusion coefficient D_1 and D_2 (cf. figure 7.22). Its is noted that α is not a fit parameter itself, but calculated from the model function.

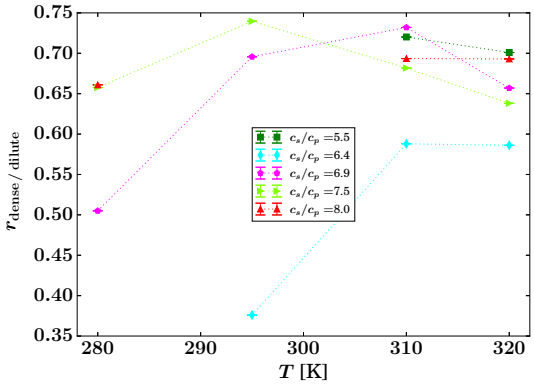

Fig. 7.23. Relative weight r of the apparent center-of-mass diffusion coefficient attributed to the dense and dilute phase, respectively, according to equation 7.5, in the fits allowing two center-of-mass diffusion coefficients.

7.5.4 Additional interpretation in terms of absolute volumes

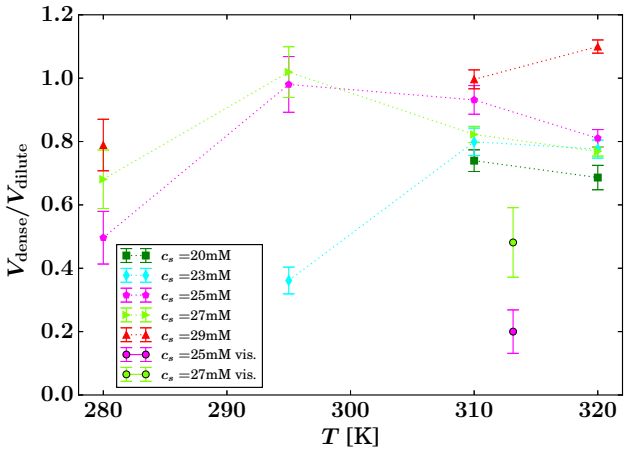

Fig. 7.24. Ratio of the volumes in the dense and dilute phase, respectively, calculated from the fit parameter r of the QENS spectra using equation 7.11 and equation 7.13 with $g(c_s/c_p) \equiv 1$ (symbols with edges). The circle symbols denote the ratios calculated from visual inspection.

From the implementation in the fit algorithm we have:

$$\frac{r_{\text{dense/dilute}}}{1 - r_{\text{dense/dilute}}} = \frac{c_{\text{dense}}\, V_{\text{dense}}}{c_{\text{dilute}}\, V_{\text{dilute}}}, \tag{7.11}$$

thus,

$$c_{\text{total}} V_{\text{total}} = \frac{1}{1 - r_{\text{dense/dilute}}} \cdot c_{\text{dilute}} V_{\text{dilute}}\,. \tag{7.12}$$

This implementation, along with the central hypothesis from the previous section, results in the following expected ratio of the splitting volumes:

$$\frac{c_{p,\text{dense}}\, V_{\text{dense}}}{c_{p,\text{dilute}}\, V_{\text{dilute}}} = \frac{\varphi_{\text{dense}}\, V_{\text{dense}}}{\varphi_{\text{dilute}}\, V_{\text{dilute}}} = \frac{f^{-1}(D_{\text{dense}} \,/\, g(c_s/c_p))\, V_{\text{dense}}}{f^{-1}(D_{\text{dilute}} \,/\, g(c_s/c_p))\, V_{\text{dilute}}}, \tag{7.13}$$

where f^{-1} is the inverse of the monomeric hard-sphere colloidal crowding function $f(\varphi)$ and $g(c_s/c_p)$ the salt-induced master curve presented earlier. In contrast to equation 7.5, the above equation 7.13 requires an explicit assumption on $g(c_s/c_p)$ in the two separated phases, since due to the inversion f^{-1}, it no longer cancels out.

An attempt to estimate the volumes in the two phases was done by visual inspection, comparing the photograph of the centrifuged sample with an empty 15 mL Falcon tube. The empty Falcon was put in front of the photograph of the BSA samples with 25 and 27 mM $LaCl_3$ ($c_s/c_p = 6.9$ and 7.5, respectively; see figure 7.10) to adjust the zoom of the latter based on the size of the real tube and then placed next to it to estimate the position of the meniscus between the dense (bottom) and the dilute phase. Using this approach, for the sample with $c_s/c_p = 7.5$ (right tube, figure 7.10) we estimated that the amount of the dense phase on the total 1 mL sample is $\sim$ 0.3-0.35 mL, resulting in $\sim$ 0.7-0.65 mL of the dilute phase and corresponding to the 30-35 and the 70-65% on the total, respectively. For the sample with $c_s/c_p = 6.9$ (left tube in figure 7.10), we estimated a volume of 0.85-0.9 mL for

the dense phase and 0.1-0.15 mL for the dilute one, with corresponding percentage values of 85-90 and the 10-15%, respectively.

By inverting equation 7.12, the protein concentration in the dilute phase can be calculated as

$$c_{\mathrm{dilute}} = c_{\mathrm{total}} \left(1 - r_{\mathrm{dense/dilute}}\right) \frac{V_{\mathrm{total}}}{V_{\mathrm{dilute}}}\,, \tag{7.14}$$

where $c_{\mathrm{total}} = 240$ mg/mL, $V_{\mathrm{total}} = 1$ mL, V_{dilute} is estimated from the photographs and $r_{\mathrm{dense/dilute}}$ are the values in figure 7.23. For example, we can consider the BSA sample with 27 mM $LaCl_3$. If one estimates $V_{\mathrm{dilute}} \approx 0.65$ mL as explained above and takes $r_{\mathrm{dense/dilute}} \approx 0.68$ from figure 7.23, $c_{\mathrm{dilute}} \approx 240$ mg/ml$\cdot\,(1 - 0.68)/0.65 \approx 118$ mg/mL is obtained, corresponding to a dilution factor of ~ 2. If instead from figure 7.10 (right) one estimates a splitting in two approximately equal volumes, $c_{\mathrm{dilute}} \approx 240$ mg/ml$\cdot\,(1 - 0.68)/0.5 \approx 153.6$ mg/ml, corresponding to a dilution by a factor of 1.56, closer to the value of 1.6 found by Da Vela et al. [530]. Results of these calculations for the 27 mM salt sample with different splitting volumes are reported in Table 7.2.

It has to be stressed that for figure 7.24, $g(c_s/c_p) \equiv 1$ was assumed in the above equation 7.13. It is at present not clear why this assumption results in reasonable volume ratios, whereas including $g(c_s/c_p)$ of the average slowing-down – which was determined for $c_s < c^*$, assuming no LLPS, i.e., a single apparent global diffusion Lorentzian – does not give reasonable results. One may speculate that the polydispersity, i.e., cluster size distribution, giving rise to $g(c_s/c_p)$, causes an average speeding up and slowing down, respectively, in the different phases, resulting in an apparent approximate compensation of the salt-induced deviation from momomeric diffusion.

$\mathbf{c_s/c_p}$	$\mathbf{V_{dense}}$ **(mL)**	$\mathbf{V_{dilute}}$ **(mL)**	$\mathbf{r_{dense/dilute}}$	$\mathbf{c_{dilute}}$ **(mg/mL)**	**dilution factor**
7.5	0.30	0.70	≈ 0.68	109.7	~ 2.19
	0.35	0.65		118.1	~ 2.03
	0.40	0.60		128	~ 1.88
	0.50	0.50		153.6	~ 1.56 [530]

Table 7.2. Protein concentration in the dilute phase c_{dilute} calculated using equation 7.14 and dilution factor $c_{\mathrm{total}}/c_{\mathrm{dilute}}$ for the BSA sample with 27 mM salt, assuming different splitting volumes for the two phases and $\mathrm{r}_{\mathrm{dense/dilute}}$ taken from the fit results in figure 7.23.

Chapter 8

Summary and outlook

8.1 Summary and conclusions

Neutron spectroscopy plays a crucial role in understanding the microscopic diffusion properties in soft and biological matter, due to the non-destructiveness of the probe. Cold or slow neutrons in fact match the time and length scales of diffusive motions and relaxations occurring in protein solutions.

In this thesis, a multi-technique approach was employed to investigate the microscopic properties of blood serum protein solutions, with a particular focus on a series of pharmaceutically relevant monoclonal antibodies (mAbs). Neutron spectroscopy allowed to probe the short-time diffusion on multiple scales. In particular, neutron backscattering (NBS) and neutron spin-echo (NSE) experiments were carried out to shed light onto collective and self-diffusion phenomena in highly-concentrated solutions of a series of different mAb variants. The interpretation of the data using diffusion models borrowed from colloid physics enabled a comprehensive understanding of the effects of crowding on protein aggregation mechanisms, such as reversible self-association (RSA) and liquid-liquid phase separation (LLPS). The nanosecond time window accessible by NBS and NSE techniques sheds lights on transient, short-lived clusters, which gradually dissociate at physiological temperature. Such transient clustering is essential for understanding the viscosity behaviour of the studied mAbs. In fact, we observed that in the most viscous solutions, clusters are typically small (mainly dimers and trimers), hypothetically formed in a nucleation dominated (ND) mechanism.

The pharmaceutically relevant mAbs studied in this thesis mostly differ in the final parts of their Fab arms, in the so called complementarity-determining regions (CDRs) of the Fv domain. These differences in their primary sequences result in a network of protein-protein interactions (PPIs) mediated by either charged or hydrophobic patches on the protein surface. The combined spectroscopic techniques allowed a detailed analysis of diffusion behaviour on the nanosecond timescale, revealing distinct clustering tendencies for different mAbs. At the same time, a static technique like SANS confirmed the aggregation behaviour and probed the different intermolecular interactions in the solutions. The consistency of the results across different techniques, including NBS, NSE, SANS and MD simulations, strengthens the reliability of the findings and demonstrates the utility of an interdisciplinary approach.

A QENS study was also conducted on a well-established protein-salt model system – BSA in solution with different $LaCl_3$ concentrations) to elucidate the role of short-time dynamics upon entering the LLPS regime. The significant observation is that the microscopic environment in the nanosecond scale remains highly dynamic, even while crossing the LLPS phase transition, so even when the

solution divides macroscopically into a dense and a dilute phase.

8.2 Importance of industrial participation in basic research

Industrial involvement in basic research can help bridge the gap between fundamental scientific discoveries and practical applications. This collaboration often leads to a faster translation of scientific findings into commercial products and technologies and to the development of new research tools and methodologies that benefit both academia and industry.

In the specific case of this work, thanks to Lonza we had access to an extraordinary amount of different mAbs engineered for specific scopes that we could investigate with large-scale facility techniques, espcially with neutrons that are well-known to require high amount of material. The access to these kind of experiments is not straightforward and the collaboration with scientists working in those is certainly a great opportunity for the companies. At the same time, the company offered the possibility to perform complementary characterization of the samples with specific instruments also used in their daily industrial research and to spend several months at their headquarters in Basel.

8.3 Outlook

This work contributes to extending the general knowledge on protein solution behaviour on both macroscopic and microscopic level, with a focus on two mechanisms of protein aggregation: reversible self-association (RSA) and liquid-liquid phase separation (LLPS), which is a proper phase transition. Both processes can result in high viscosities and unwanted behaviours in solution. By exploring the short-time self- and collective diffusion in highly concentrated protein solutions, we provided insights on those mechanisms at a molecular level, relying on the fact that these will be useful in the future in formulation development and drug production.

By studying the antibodies in a formulation buffer in actually commercialized biologics, this thesis provides the ground/the references for a systematic analysis on how some viscosity-reducing excipients and/or solution stabilizers, such as Arg-HCl, NaCl, or trehalose, affect the short-time self- and collective diffusion, the intermolecular interactions and solution structure of the same antibody variants. Moreover, the UCST-LLPS mechanism observed in some of the mAbs in solution can be investigated in a more extensive and systematic way, e.g. following the strategy used for the model system BSA-$LaCl_3$ in this work.

Furthermore, the conducted research again re-affirms the validity of neutron scattering as a powerful and versatile tool to probe structural and dynamic features in biologic molecules, and its applicability onto research areas of major interest in society, such as pharmaceutical and medical sciences. The realisation of this project would not have been possible without the integration of experimental techniques in large-scale facilities, laboratory experiments and computational studies, resulting in a comprehensive approach to the initial research question.

Despite the presence of unanswered questions in the domains of protein and formulation science, a significant knowledge gap has been addressed in this field, with the results obtained serving as a foundational basis for subsequent research endeavours.

Appendix:
List of experiments performed at large scale facilities

This chapter lists all the experiments carried out during the time of the thesis at different large scale facilities. Some of the data collected directly entered this work, while some other are out of the scope of the manuscript and will be part of future works. For each experiment performed, the scientific case investigated is reported, along with the facility, the beam line, the dates of the experiments, the DOI for the data and the role that this author has played during the experiment. The experiments are listed from the most recent to the furthest in time.

1. **Diffusive and structural properties of BLG during fibril formation**
   Facility: ILL
   Exp. number: 8-04-987
   Time allocated: 4 days (28 Jun-2 Jul 2024)
   Instrument: IN16B
   DOI: 10.5291/ILL-DATA.8-04-987
   Role: co-proposer, experimenter

2. **Role of a non-ionic surfactant in the adsorption of different therapeutically relevant IgG1 and IgG4 monoclonal antibodies (mAbs) on siliconized surfaces**
   Facility: ILL
   Exp. number: 8-04-978
   Time allocated: 3 days (13-16 Mar 2024)
   Instrument: fluid and interface grazing-angle reflectometer (FIGARO)
   DOI: 10.5291/ILL-DATA.8-04-978
   Role: main proposer, experimenter

3. **Casein micelle formation as result of liquid-liquid phase separation (LLPS) in an IDP solution**
   Facility: ILL
   Exp. number: 9-13-1076
   Allocated time: 2 days (31 Oct-2 Nov) + 3 days (3-6 Nov 2023)
   Instruments: wide-angle spin-echo spectrometer (WASP), IN15
   DOI: 10.5291/ILL-DATA.9-13-1076
   Role: co-proposer, experimenter

4. **Revealing the diffusive properties of non-classical protein crystallization pathways**
   Facility: ILL
   Exp. number: 8-04-940
   Allocated time: 4 days (30 Oct-3 Nov) + 3 days (7-10 Nov 2023)
   Instruments: WASP, IN16B
   DOI: 10.5291/ILL-DATA.8-04-940
   Role: main proposer, experimenter

5. **Structure and dynamics approaching the arrested states for different monoclonal antibodies (mAbs)**
   with PEG
   Facility: ILL
   Exp. number: 8-04-951, 936
   Allocated time: 6 days (7-13 Sept) + 3 days (15-18 Sept 2023)
   Instruments: IN15, IN16B
   DOI: 10.5291/ILL-DATA.8-04-951, 10.5291/ILL-DATA.8-04-936
   Role: main proposer, experimenter

6. **Systematic investigation of the diffusive properties of macromolecules in bovine milk**
   Facility: ILL
   Exp. number: INTER-588
   Allocated time: 3 days (25-28 Aug 2023)
   Instrument: IN16B
   DOI: 10.5291/ILL-DATA.INTER-588
   Role: co-proposer, experimenter

7. **Internal diffusive dynamics in solution on the ns-nm-scale of polymers during thermal and chemical induced network formation**
   Facility: ILL
   Exp. number: 9-13-1077
   Allocated time: 2 days (1-3 Jul 2023)
   Instrument: IN16B
   DOI: 10.5291/ILL-DATA.9-13-1077
   Role: co-proposer, experimenter

8. **Differences between monoclonal antibodies (mAbs): viscosity, diffusion, and transient cluster formation**
   Facility: ILL
   Exp. 8-04-932
   Allocated time: 4 days at (3-7 Jun) + 1 day (11-12 Jun 2023)
   Instruments: IN15, D22
   DOI: 10.5291/ILL-DATA.8-04-932
   Role: main proposer, experimenter

9. **Structural and diffusive properties of an IDPin a polydisperse environment**
   Facility: ILL
   Exp. number: 8-04-953
   Allocated time: 6 days (26 May-1 Jun) + 2 days (8-10 Sept 2023)

Instruments: IN16B, massive dynamic q-range small-angle diffractometer (D33)
DOI: 10.5291/ILL-DATA.8-04-953
Role: main proposer, experimenter

10. **Casein as a model IDP: impact of salt on the internal diffusive dynamics in solution**
Facility: ILL
Exp. number: 9-13-1046
Allocated time: 4 days (7-11 Apr 2023)
Instrument: IN16B
DOI: 10.5291/ILL-DATA.9-13-1046
Role: co-proposer, experimenter

11. **Influence of antibody type, temperature and additives on the viscosity of monoclonal antibody solutions**
Facility: ESRF
Exp. number: MD-1368
Allocated time: 3 days (2-5 Dec 2022)
Instrument: ID-02
DOI: 10.15151/ESRF-ES-970991476
Role: main proposer, experimenter

12. **Accessing the dynamic origin of phase separation in a charge-tuned protein solutions**
Facility: SNS (ORNL)
Exp. number: IPTS 23886
Allocated time: 6 days (19-25 Jul 2022)
Instrument: BL-02 BASIS
DOI: No DOI, data curated by the SNS and accessible upon request
Role: experimenter

13. **Tunable equilibrium monoclonal antibody nanocluster dispersions at high concentrations**
Facility: ILL
Exp. number: 8-04-923
Allocated time: 3 days at IN16B (6-9 Sept), 1 day at D11 (10-11 Sept 2021)
Instruments: IN16B, D11
DOI: 10.5291/ILL-DATA.8-04-923
Role: experimenter

14. **Dynamic cluster formation, viscosity, and diffusion in monoclonal antibody (mAb) solutions depending on antibody type and crowding**
Facility: ILL
Exp. number: 8-04-908
Allocated time: 5 days at IN16B (20-25 May 2021)
Instrument: IN16B
DOI: 10.5291/ILL-DATA.8-04-908
Role: data analysis

Glossary

The next list describes all the abbreviations and acronyms used within the body of the document.

ADH	alcol dehydrogenase
ANNs	artificial neural networks
BASIS	BAckscattering SIlicon Spectrometer
BATS	Backscattering Time-of-flight Spectrometer
BLG	β-lactoglobulin
BSA	bovine serum albumin
CC	clustering coefficient
CDR	complementarity determining region
CDRs	complementarity determining regions
CDR-H1/H2/H3	CDR loop 1/2/3 in the heavy chain
CDR-L1/L2/L3	CDR loop 1/2/3 in the light chain
CHO	chinese hamster ovary
CSNS	China Spallation Neutron Source
COM	center-of-mass
DGV	double gene vectors
DLS	dynamic light scattering
DWF	Debye-Waller factor
D11	lowest momentum transfer and lowest background small-angle neutron scattering instrument
D22	large dynamic range small-angle diffractometer
D33	massive dynamic q-range small-angle diffractometer
EISF	elastic incoherent structure factor
EFWS	elastic fixed window scan

ESRF	European Synchrotron Radiation Facility
ESS	European Spallation Source
Fab	antigen-binding fragment
Fc	crystallisable fragment/domain
FcRn	neonatal Fc receptor
FDA	Food and Drug Administration
FDT	fluctuation-dissipation theorem
FEL	free-electron laser
FIGARO	fluid and interface grazing-angle reflectometer
FRM-II	Forschungsreaktor München II
Fv	variable fragment/domain
FWHM	full width at half maximum
GRASP	Graphical Reduction and Analysis SANS Program
GRAVY	grand average of hydropathy
GSE	generalized Stokes-Einstein
GS-KO	glutamine synthetase knockout
HC	heavy chain
HDX	hydrogen-deuterium exchange
HFIR	high flux isotope reactor
HIC	hydrophobic interaction column
HS	hard-sphere
HSA	human serum albumin
HWHM	half width at half maximum
ID	intradermal
IDP	intrinsically disordered protein
IDPs	intrinsically disordered proteins
IFWS	inelastic fixed window scan
Ig	immunoglobulin
Igs	immunoglobulins
ILL	Institut Laue-Langevin

ID	intradermal
IM	intramuscular
IN13	thermal neutron backscattering spectrometer
IN15	high resolution spin-echo spectrometer
IN16B	cold neutron high-flux backscattering spectrometer
ISF	intermediate scattering function
IV	intravenous
JPARC	Japan Proton Accelerator Research Complex
LANSCE	Los Alamos Neutron Science Center
LC	light chain
LCST	lower critical solution temperature
LLPS	liquid-liquid phase separation
LYS	lysozyme
mAb	monoclonal antibody
mAbs	monoclonal antibodies
MBP	myelin basic protein
MD	molecular dynamics
ML	machine learning
MSD	mean squared displacement
MSDs	mean squared displacements
MW	molecular-weight
MWCO	molecular weight cutoff
NBS	neutron backscattering spectroscopy
NCNR	National Center for Neutron Research
ND	nucleation dominated
NHERF1	mammalian Na^+/H^+ exchange regulatory factor 1
NIST	National Institute of Standards and Technology
NM	normal mode
NMR	nuclear magnetic resonance
NSE	neutron spin-echo

NTU	nephelometric turbidity units
ORNL	Oak Ridge National Laboratory
pAbs	polyclonal antibodies
PCA	principal component analysis
PDB	Protein Data Bank
PDI	polydispersity index
PFG	pulsed-field gradient
PGK	phosphoglycerate kinase
PNC	Patches of Negative Charge
PPC	Patches of Positive Charge
PPIs	protein-protein interactions
PSCM	Partnership for Soft Condensed Matter
PSD	position-sensitive detector
PSH	Patches of Surface Hydrophobicity
PSI	Paul Scherrer Institute
PST	phase-space transformation
QENS	quasielastic neutron scattering
RMSD	root mean square deviation
RSA	reversible self-association
SAbDab	Structural Antibody Database
SAbPred	Antibody Prediction Toolbox
SALR	short-range attraction long-range repulsion
SANS	small angle neutron scattering
SAXS	small angle X-ray scattering
SC	subcutaneous
SE	Stokes-Einstein
SEC	size-exclusion chromatography
SED	Stokes-Einstein-Debye
SE-HPLC	Size exclusion-high-performance liquid chromatography
SFvCSP	structural Fv charge symmetry parameter

SHS	sticky hard sphere
SINQ	Swiss Spallation Neutron Source
SLD	scattering length density
SLS	static light scattering
SNS	Spallation Neutron Source
SST	system suitability test
TAP	Therapeutic Antibody Profiler
TOF	time-of-flight
UCST	upper critical solution temperature
UV-Vis	ultraviolet-visible
USANS	ultra-small angle neutron scattering
VH/VL	variable domain of the heavy/light chain
VMD	Visual Molecular Dynamics
VROC	viscometer / rheometer-on-a-chip
XPCS	X-ray photon-correlation spectroscopy
WASP	wide-angle spin-echo spectrometer

List of Symbols

The next list describes several symbols that are used within the body of the document.

Chemical compounds

Al aluminium

Ala alanine (amino acid, A)

Arg, Arg-HCl arginine (amino acid, R), arginine-monohydrochloride

Asn, Asp aspartic acid (amino acid, P), asparagine (amino acid, N)

Cl, C chlorine, carbon

Cys cysteine (amino acid, C)

Gln, Glu, Gly glutamine (amino acid, Q), glutamic acid (amino acid, E), glycine (amino acid, G)

H_2O, D_2O normal water, deuterated/heavy water

H, D, He hydrogen, deuterium, helium

His, His-HCl histidine (amino acid, H), histidine-monohydrochloride

Ile, Leu isoleucine (amino acid, I), leucine (amino acid, L)

K, P potassium, phosphorus

$LaCl_3$ lantanum chloride

Lys, Lys-HCl lysine (K), lysine-monohydrochloride

Met methionine (amino acid, M)

Na, N sodium, nitrogen

NaCl, NaOAc, Na_2SO_4 sodium chloride, sodium acetate, sodium solphate

Phe, Pro phenylalanine (amino acid, F), proline (amino acid, P)

Sec, Ser selenocysteine (amino acid, U), serine (amino acid, S)

Thr, Trp, Tyr threonine (amino acid, T), tryptophan (amino acid, W), tyrosine (amino acid, Y)

V vanadium

Val valine (amino acid, V)

Other symbols

$\beta(q)$ scaling factor in QENS fit models, in general the DWF

η, η_0 solution viscosity, solvent viscosity

$\Gamma(q)$ HWHM of the 2^{nd} narrowest Lorentzian of the QENS fit model, related to internal diffusion

$\gamma(q)$ HWHM of the narrowest Lorentzian of the QENS fit model, associated to COM diffusion

ε_{280} extinction coefficient at 280 nm

$\mathrm{A_2}$ second virial coefficient from SLS

$\mathrm{B_2}$, $\mathrm{B_2^{HS}}$ second virial coefficient from SANS/SAXS, second virial coefficient for hard spheres

$\mathrm{k_D}$ diffusion-interaction parameter from DLS

pH logarithmic scale for the acidity or basicity of aqueous solutions

pI isoelectric point

pKa (logarithm of) acid dissociation constant

ν, ω frequency, angular velocity

φ protein volume fraction

$\vec{q}$, $\vec{Q}$ scattering vector / momentum ($\vec{Q}$ used in theoretical introduction for consistency with textbooks, $\vec{q}$ used in publications)

$A_0(q)$ EISF

c_p, c_s protein concentration, salt concentration

D, D_{app} short-time apparent COM self-diffusion coefficient

D_c^{long} long-time collective diffusion coefficient from DLS

D_{dense}, D_{dilute} short-time self-diffusion coefficient of the dense phase and the dilute phase

D_{r0}, D_{t0} rotational and translational short-time self-diffusion coefficient at the dilute limit

Physics constants

$\hbar$ reduced Planck constant

ν_e electron neutrino

μ_B Bohr's magneton (electron magnetic moment)

μ_N neutron magnetic moment

e^-, e^+ electron, positron

k_B Boltzmann constant

n neutron

List of Figures

2.1 Different classes of human immunoglobulins . . . 21
2.2 Structure of an IgG1 antibody monomer . . . 23
2.3 Percutaneous routes of drug administration . . . 25

3.1 Geometry of a neutron scattering experiment . . . 39
3.2 Density of final scattering states per unit energy range . . . 40
3.3 Scattered wave as a superposition of an incident plane wave and an outgoing spherical wave . . . 44
3.4 Self and collective dynamics within the same group of particles . . . 47
3.5 Scattering function of elastic, quasi-elastic and inelastic neutron scattering . . . 56
3.6 Operation principles of a backscattering spectrometer . . . 60
3.7 Sketch of a spin-echo spectrometer . . . 63
3.8 Schematic setup of a SANS instrument. . . . 68
3.9 Accessible length- and time-scales of typical scattering techniques . . . 69

4.1 Graphical representation of the dialysis method used . . . 77
4.2 Graphical representation of the concentration via centrifugation method used . . . 78
4.3 Schematic of a RheoSense VROC® Initium rheometer . . . 80
4.4 Sketch of the rectangular slit of a viscometer-rheometer on a chip (VROC®) . . . 80
4.5 Full chain alignment of IgG1 mAbs . . . 81
4.6 Sequence identity matrix for the full chains and Fv of the mAbs . . . 82
4.7 Variable domain alignments depicted on all mAb structures . . . 83
4.8 Amino-acidic composition of Fv of the mAbs . . . 84
4.9 Single-amino acid abundance in the Fv of the mAbs . . . 85
4.10 Molecular weight and total number of residues of the mAbs (full chains and Fv) . . . 88

5.1 Structure and sequence similarity of the mAbs . . . 93
5.2 Relative viscosity $\eta_r = \eta/\eta_0$ of H_2O solutions of the mAbs vs concentration . . . 100
5.3 Model-free comparison of QENS spectra from two mAbs at the same conditions . . . 102
5.4 Example QENS spectrum from a mAb with its fit components . . . 102
5.5 Apparent diffusion coefficients D from QENS vs antibody concentration at three temperatures . . . 105
5.6 Time-evolution of mAb inter-domain angle deviations from MD simulations . . . 106
5.7 Simulation-derived diffusive MSD $\langle u^2 \rangle$ along the residues of both HC and LC . . . 107
5.8 Viscosity correlation with parameters derived from protein sequence and MD simulations . . . 108

5.9 Separation of mAbs using PCA on computed features . . . 109
5.10 Protein network graphs from the simulations at high concentration . . . 110
5.11 Temperature dependence of mAb-mAb interactions probed using SANS . . . 112
5.12 mAb-variant dependence of protein-protein interactions probed through SANS . . . 112
5.13 Reduced second virial coefficient B_2/B_2^{HS} derived from SANS *vs* temperature . . . 113
5.14 Viscosity of a subset of mAbs in deuterated formulation buffer . . . 116
5.15 Temperature dependence of model-free QENS spectra . . . 117
5.16 Hydrogen radial distributions of the antibodies . . . 119
5.17 Product of diffusion and relative viscosity *vs* crowding . . . 119
5.18 Example of $\beta(\mathbf{q})$ obtained from QENS fits . . . 120
5.19 Crowding and temperature dependence of vibrational MSDs in mAb solutions . . . 120
5.20 Block average method to determine sampling time threshold in MD simulations . . . 121
5.21 Hydrogen bond network relaxation of mAbs in solution from MD simulations . . . 122
5.22 Structure factor from SANS fits and Kratky plot of SANS data for a subset of mAbs . . . 123

6.1 Stucture of an IgG4 mAb and sequence similarity with IgG1 mAbs. . . . 128
6.2 Viscosity *vs* protein volume fraction of the mAbs . . . 134
6.3 Second virial coefficient A_2 from SLS and diffusion-interaction parameter $\mathrm{k_D}$ from DLS 135
6.4 Intermediate scattering function $I(q,t)/I(q,0)$ of mAb5 at 50 mg/mL and 37°C . . . 137
6.5 Collective diffusion function of the mAbs from NSE . . . 139
6.6 Effective diffusion of the mAbs calculated via Jscatter using their normal modes . . . 141
6.7 SANS profiles of all mAbs at 20 mg/mL at 37°C and 21°C . . . 142
6.8 SANS profiles of mAb4* (IgG4) at 37°C at c_p = 50, 20, 10, 5, 2 mg/mL . . . 143
6.9 Collective relaxation time of the mAbs from NSE at 37 and 7°C . . . 145
6.10 Polydispersity index of the mAbs from NSE fits at 37 and 7°C . . . 145
6.11 Visual appearance of mAb solutions after NSE measurements . . . 146
6.12 Slowing down of the diffusion while cooling down . . . 147
6.13 Correlation functions $g_2(t)$ obtained by DLS at 90° during NSE acquisitions . . . 149
6.14 Guinier representation of SANS data from all the mAbs (1) . . . 150
6.15 Guinier representation of SANS data from all the mAbs (2) . . . 151
6.16 Kratky representation of SANS data from all the mAbs . . . 152
6.17 Aromaticity, aliphatic index, GRAVY, isoelectric point and charge at pH 6 of the mAbs . 154
6.18 Hydrophobic and charged residues in Fc domain. . . . 156
6.19 Estimation of mAb intra-molecular distances . . . 156

7.1 Graphical abstract: cluster distribution calculated with the Flory-Stockmayer theory . . 158
7.2 Visual appearance and phase-diagram for LLPS in BSA at $c_p = 240$ mg/ml with 27 mM $LaCl_3$ . . . 160
7.3 Example QENS spectrum of a sample undergoing LLPS with fit components . . . 161
7.4 Reduced apparent COM diffusion coefficients *vs* temperature for all the samples . . . 163
7.5 Ratio $D_{\mathrm{dense}}(c_s/c_p,T)/D_{\mathrm{dilute}}(c_s/c_p,T)$ *vs* T measured with QENS and calculated using UV-Vis . . . 164
7.6 BSA solutions with increasing $LaCl_3$ concentration at room temperature . . . 170
7.7 Visual appearance of reversible LCST behaviour . . . 170
7.8 Snapshots of temperature-driven changes in a sample undergoing LLPS . . . 171
7.9 BSA solutions at 27 mM $LaCl_3$ after cold and hot baths . . . 171

7.10 Centrifuge-aided phase-splitting of solutions in the LLPS regime 172
7.11 Normalized averaged absorption measured with UV-Vis 173
7.13 Increasing macroscopic turbidity of the samples with increasing salt concentration . . . 173
7.12 Critical temperature T_0 from UV-Vis data as a function of c_s 174
7.14 Protein concentration in the dense and dilute phase *vs* salt concentration 174
7.15 BASIS resolution function 176
7.16 Additional example QENS spectra 176
7.17 Apparent center-of-mass diffusion coefficients *vs* temperature for different salt contents 177
7.18 $\gamma(q)$ *vs* q^2, obtained from a q-wise fit of the pure protein QENS spectra 177
7.19 Summary of the χ^2 obtained from the global fits for all samples 178
7.20 Residuals of the fits for the model with one and two apparent COM diffusion coefficients 179
7.21 Comparison of the fit result for the COM diffusion coefficients with parametrized master curves from previous works 179
7.22 D_1, D_2, $A_0(q)$ and $\alpha(q)$ of the two internal diffusion processes of the protein 180
7.23 Ratio r of the apparent COM diffusion coefficients from dense and dilute phase *vs* temperature 180
7.24 Ratio of the volumes in the dense and dilute phase calculated from the ratio r *vs* temperature 181

List of Tables

3.1 Energy, temperature, wavelength and velocity ranges for different neutron sources . . . 37
3.2 Coherent and incoherent neutron scattering cross-sections of relevant elements 50

4.1 Physico-chemical properties of the mAbs (full chains) 87
4.2 Physico-chemical properties of the mAb Fv domains 88
4.3 Antibody CDR prediction and scores by TAP 89

5.1 Second virial coefficient A_2 and diffusion-interaction parameter k_D of the mAbs 101
5.2 Biophysical properties and computed parameters of the mAbs 115
5.3 Structural and diffusion parameters for the mAbs calculated from their structures . . . 118
5.4 Parameters obtained from SANS data fitting 122

6.1 Differences in set-point and measured temperatures of the sample changer rack during the SANS experiment 133
6.2 Viscosities of the mAbs at 50 mg/mL and 25°C 133
6.3 Second virial coefficient A_2 and diffusion-interaction parameter k_D of the mAbs 155

7.1 Calculation of the number of salt counterions per protein c_s/c_p 173
7.2 c_p in the dilute phase for BSA with 27 mM salt, assuming different splitting volumes . . 182

Bibliography

[1] Grimaldo, M.; Roosen-Runge, F.; Zhang, F.; Schreiber, F.; Seydel, T. Dynamics of Proteins in Solution *Quarterly Reviews of Biophysics* **2019** *52*, 1–63.

[2] Beenakker, C.; Mazur, P. Diffusion of spheres in a concentrated suspension II *Physica A: Statistical Mechanics and its Applications* **1984** *126*, 349–370.

[3] Nägele, G. On the dynamics and structure of charge-stabilized suspensions *Physics Reports* **1996** *272*, 215–372.

[4] Banchio, A. J.; Nägele, G. Short-Time Transport Properties in Dense Suspensions: from Neutral to Charge-Stabilized Colloidal Spheres *the Journal of Chemical Physics* **2008** *128*, 104903.

[5] Minton, A. P. Excluded volume as a determinant of protein structure and stability *Biophysical Journal* **1980** *32*, 77.

[6] Minton, A. P. The influence of macromolecular crowding and macromolecular confinement on biochemical reactions in physiological media *Journal of Biological Chemistry* **2001** *276*, 10577–10580.

[7] Minton, A. P. Macromolecular crowding *Current Biology* **2006** *16*, R269–R271.

[8] Pastore, A.; Rivas Caballero, G.; Temussi, P. A. Introduction: Molecular Crowding *Chemical Reviews* **2024** *124*, 6697–6699.

[9] Alfano, C.; Fichou, Y.; Huber, K.; Weiss, M.; Spruijt, E.; Ebbinghaus, S.; De Luca, G.; Morando, M. A.; Vetri, V.; Temussi, P. A.; et al. Molecular crowding: the history and development of a scientific paradigm *Chemical Reviews* **2024** *124*, 3186–3219.

[10] Monterroso, B.; Margolin, W.; Boersma, A. J.; Rivas, G.; Poolman, B.; Zorrilla, S. Macromolecular crowding, phase separation, and homeostasis in the orchestration of bacterial cellular functions *Chemical Reviews* **2024** *124*, 1899–1949.

[11] Di Bari, D.; Timr, S.; Guiral, M.; Giudici-Orticoni, M.-T.; Seydel, T.; Beck, C.; Petrillo, C.; Derreumaux, P.; Melchionna, S.; Sterpone, F.; et al. Diffusive dynamics of bacterial proteome as a proxy of cell death *ACS Central Science* **2023** *9*, 93–102.

[12] Caviglia, B.; Di Bari, D.; Timr, S.; Guiral, M.; Giudici-Orticoni, M.-T.; Petrillo, C.; Peters, J.; Sterpone, F.; Paciaroni, A. Decoding the Role of the Global Proteome Dynamics for Cellular Thermal Stability *The Journal of Physical Chemistry Letters* **2024** *15*, 1435–1441.

[13] Arora, S.; Ainavarapu, S. R. K. Crowding-induced effects on the stability of ubiquitin-family proteins *Biophysical Journal* **2024** *123*, 193a–194a.

[14] Xu, G.; Cheng, K.; Liu, M.; Li, C. Studying protein stability in crowded environments by NMR *Progress in Nuclear Magnetic Resonance Spectroscopy* **2024**.

[15] Brzezinski, M.; Argudo, P.; Michels, J.; Parekh, S. H. Crowding accelerates molecular aging in protein condensates *Biophysical Journal* **2024** *123*, 445a.

[16] Szymański, J.; Patkowski, A.; Wilk, A.; Garstecki, P.; Holyst, R. Diffusion and viscosity in a crowded environment: from nano-to macroscale *The Journal of Physical Chemistry B* **2006** *110*, 25593–25597.

[17] Kompella, V. P. S.; Romano, M. C.; Stansfield, I.; Mancera, R. L. What determines sub-diffusive behavior in crowded protein solutions? *Biophysical Journal* **2024** *123*, 134–146.

[18] Schnell, S.; Turner, T. Reaction kinetics in intracellular environments with macromolecular crowding: simulations and rate laws *Progress in Biophysics and Molecular Biology* **2004** *85*, 235–260.

[19] Kim, J. S.; Yethiraj, A. Effect of macromolecular crowding on reaction rates: a computational and theoretical study *Biophysical Journal* **2009** *96*, 1333–1340.

[20] Minton, A. P. Models for excluded volume interaction between an unfolded protein and rigid macromolecular cosolutes: macromolecular crowding and protein stability revisited *Biophysical Journal* **2005** *88*, 971–985.

[21] Patel, S. P.; Nikam, T.; Sreepathi, B.; Karankar, V. S.; Jaiswal, A.; Vardhan, S. V.; Rana, A.; Toga, V.; Srivastava, N.; Saraf, S. A.; et al. Unraveling the Molecular Jam: How Crowding Shapes Protein Aggregation in Neurodegenerative Disorders *ACS Chemical Biology* **2024**.

[22] Miklos, A. C.; Li, C.; Sharaf, N. G.; Pielak, G. J. Volume exclusion and soft interaction effects on protein stability under crowded conditions *Biochemistry* **2010** *49*, 6984–6991.

[23] Kuznetsova, I. M.; Zaslavsky, B. Y.; Breydo, L.; Turoverov, K. K.; Uversky, V. N. Beyond the excluded volume effects: mechanistic complexity of the crowded milieu *Molecules* **2015** *20*, 1377–1409.

[24] Majumdar, S.; Rastogi, H.; Chowdhury, P. K. Bridging Soft Interaction and Excluded Volume in Crowded Milieu through Subtle Protein Dynamics *The Journal of Physical Chemistry B* **2024** *128*, 716–730.

[25] Kuznetsova, I. M.; Turoverov, K. K.; Uversky, V. N. What macromolecular crowding can do to a protein *International Journal of Molecular Sciences* **2014** *15*, 23090–23140.

[26] Kim, Y. C.; Best, R. B.; Mittal, J. Macromolecular crowding effects on protein–protein binding affinity and specificity *The Journal of Chemical Physics* **2010** *133*.

[27] Zimmerman, S. B.; Trach, S. O. Effects of macromolecular crowding on the association of E. coli ribosomal particles *Nucleic Acids Research* **1988** *16*, 6309–6326.

[28] Walter, H.; Brooks, D. E. Phase separation in cytoplasm, due to macromolecular crowding, is the basis for microcompartmentation *FEBS Letters* **1995** *361*, 135–139.

[29] Julius, K.; Weine, J.; Gao, M.; Latarius, J.; Elbers, M.; Paulus, M.; Tolan, M.; Winter, R. Impact of macromolecular crowding and compression on protein–protein interactions and liquid–liquid phase separation phenomena *Macromolecules* **2019** *52*, 1772–1784.

[30] André, A. A.; Spruijt, E. Liquid–liquid phase separation in crowded environments *International Journal of Molecular Sciences* **2020** *21*, 5908.

[31] Iborra, F. J. Can visco-elastic phase separation, macromolecular crowding and colloidal physics explain nuclear organisation? *Theoretical Biology and Medical Modelling* **2007** *4*, 1–11.

[32] Dix, J. A.; Verkman, A. Crowding effects on diffusion in solutions and cells *Annu. Rev. Biophys.* **2008** *37*, 247–263.

[33] Smith, S.; Cianci, C.; Grima, R. Macromolecular crowding directs the motion of small molecules inside cells *Journal of the Royal Society Interface* **2017** *14*, 20170047.

[34] Grimaldo, M.; Lopez, H.; Beck, C.; Roosen-Runge, F.; Moulin, M.; Devos, J. M.; Laux, V.; Härtlein, M.; Da Vela, S.; Schweins, R.; et al. Protein Short-Time Diffusion in a Naturally Crowded Environment *The Journal of Physical Chemistry Letters* **2019** *10*, 1709–1715.

[35] Skóra, T.; Vaghefikia, F.; Fitter, J.; Kondrat, S. Macromolecular crowding: how shape and interactions affect diffusion *The Journal of Physical Chemistry B* **2020** *124*, 7537–7543.

[36] Raczyłło, E.; Gołowicz, D.; Skóra, T.; Kazimierczuk, K.; Kondrat, S. Size Sensitivity of Metabolite Diffusion in Macromolecular Crowds *Nano Letters* **2024** *24*, 4801–4809.

[37] Kondrat, S.; Zimmermann, O.; Wiechert, W.; von Lieres, E. The effect of composition on diffusion of macromolecules in a crowded environment *Physical Biology* **2015** *12*, 046003.

[38] Beck, C.; Grimaldo, M.; Lopez, H.; Da Vela, S.; Sohmen, B.; Zhang, F.; Oettel, M.; Barrat, J.-L.; Roosen-Runge, F.; Schreiber, F.; et al. Short-time transport properties of bidisperse suspensions of immunoglobulins and serum albumins consistent with a colloid physics picture *The Journal of Physical Chemistry B* **2022** *126*, 7400–7408.

[39] Singh, A.; Kundrotas, P. J.; Vakser, I. A. Diffusion of proteins in crowded solutions studied by docking-based modeling *The Journal of Chemical Physics* **2024** *161*.

[40] Basak, S.; Sengupta, S.; Chattopadhyay, K. Understanding biochemical processes in the presence of sub-diffusive behavior of biomolecules in solution and living cells *Biophysical Reviews* **2019** *11*, 851–872.

[41] Banks, D. S.; Fradin, C. Anomalous diffusion of proteins due to molecular crowding *Biophysical Journal* **2005** *89*, 2960–2971.

[42] Horton, M. R.; Höfling, F.; Rädler, J. O.; Franosch, T. Development of anomalous diffusion among crowding proteins *Soft Matter* **2010** *6*, 2648–2656.

[43] Kumar, G.; Ardekani, A. M. Concentration-Dependent Diffusion of Monoclonal Antibodies: Underlying Mechanisms of Anomalous Diffusion *Molecular Pharmaceutics* **2024** *21*, 2212–2222.

[44] Rashid, R.; Chee, S. M. L.; Raghunath, M.; Wohland, T. Macromolecular crowding gives rise to microviscosity, anomalous diffusion and accelerated actin polymerization *Physical Biology* **2015** *12*, 034001.

[45] Golkaram, M.; Hellander, S.; Drawert, B.; Petzold, L. R. Macromolecular crowding regulates the gene expression profile by limiting diffusion *PLoS computational Biology* **2016** *12*, e1005122.

[46] Vibhute, M. A.; Schaap, M. H.; Maas, R. J.; Nelissen, F. H.; Spruijt, E.; Heus, H. A.; Hansen, M. M.; Huck, W. T. Transcription and translation in cytomimetic protocells perform most efficiently at distinct macromolecular crowding conditions *ACS Synthetic Biology* **2020** *9*, 2797–2807.

[47] Singh, D.; Singh, L. A Pioneering Review on Quantitative Analysis of the Effect of Macromolecular Crowding on Drug Transport and Release: Current Implications *Journal of Macromolecular Science, Part B* **2024** pages 1–15.

[48] Riera Romo, M.; Pérez-Martínez, D.; Castillo Ferrer, C. Innate immunity in vertebrates: an overview *Immunology* **2016** *148*, 125–139.

[49] Vaillant, A. A. J.; Sabir, S.; Jan, A. Physiology, immune response in *StatPearls* StatPearls Publishing **2022**.

[50] Vaillant, A. A. J.; Jamal, Z.; Patel, P.; Ramphul, K. Immunoglobulin in *StatPearls [Internet]* StatPearls Publishing **2023**.

[51] Boes, M. Role of natural and immune IgM antibodies in immune responses *Molecular Immunology* **2000** *37*, 1141–1149.

[52] Palmeira, P.; Quinello, C.; Silveira-Lessa, A. L.; Zago, C. A.; Carneiro-Sampaio, M. IgG placental transfer in healthy and pathological pregnancies *Journal of Immunology Research* **2012** *2012*, 985646.

[53] Kerr, M. The structure and function of human IgA. *Biochemical Journal* **1990** *271*, 285.

[54] Woof, J. M.; Kerr, M. A. IgA function–variations on a theme *Immunology* **2004** *113*, 175.

[55] Godwin, L.; Sinawe, H.; Crane, J. S. Biochemistry, Immunoglobulin E *Biochemistry, Genetics, and Molecular Biology* **2019**.

[56] Kawakami, T.; Galli, S. J. Regulation of mast-cell and basophil function and survival by IgE *Nature Reviews Immunology* **2002** *2*, 773–786.

[57] Gutzeit, C.; Chen, K.; Cerutti, A. The enigmatic function of IgD: some answers at last *European Journal of Immunology* **2018** *48*, 1101–1113.

[58] Daëron, M. The function of antibodies *Immunological Reviews* **2024** *328*, 113–125.

[59] Cohen, S. Antibody structure. *Journal of Clinical Pathology. Supplement (Ass. Clin. Path.)* **1975** *6*, 1.

[60] Janeway Jr, C. A.; Travers, P.; Walport, M.; Shlomchik, M. J. The distribution and functions of immunoglobulin isotypes in *Immunobiology: The Immune System in Health and Disease. 5th edition* Garland Science **2001**.

[61] Aziz, M.; Iheanacho, F.; Hashmi, M. F. Physiology, Antibody in *StatPearls [Internet]* StatPearls Publishing **2019**.

[62] Metzger, H.; Kinet, J.-P. How antibodies work: focus on Fc receptors *The FASEB Journal* **1988** *2*, 3–11.

[63] Bowman, K. A.; Kaplonek, P.; McNamara, R. P. Understanding Fc function for rational vaccine design against pathogens *Mbio* **2024** *15*, e03036–23.

[64] Ritter, M. A. Polyclonal and monoclonal antibodies *Diagnostic and Therapeutic Antibodies* **2000** pages 23–34.

[65] Hendriksen, C.; Hau, J. Production of polyclonal and monoclonal antibodies *Handbook of laboratory Animal science* **2002** *2*, 391–411.

[66] S. Lipman, N.; R. Jackson, L.; J. Trudel, L.; Weis-Garcia, F. Monoclonal Versus Polyclonal Antibodies: Distinguishing Characteristics, Applications, and Information Resources *ILAR Journal* **2005** *46*, 258–268.

[67] Mitra, S.; Tomar, P. C. Hybridoma technology; advancements, clinical significance, and future aspects *Journal of Genetic Engineering and Biotechnology* **2021** *19*, 1–12.

[68] Ascoli, C. A.; Aggeler, B. Overlooked benefits of using polyclonal antibodies *Biotechniques* **2018** *65*, 127–136.

[69] Köhler, G.; Milstein, C. Continuous Cultures of Fused Cells Secreting Antibody of Predefined Specificity *Nature* **1975** *256*, 495–497.

[70] Ecker, D. M.; Jones, S. D.; Levine, H. L. The therapeutic monoclonal antibody market in *mAbs* volume 7, 1 Taylor & Francis **2015** pages 9–14.

[71] Mullard, A. 2023 FDA approvals. *Nature Reviews. Drug Discovery* **2024**.

[72] Crescioli, S.; Kaplon, H.; Chenoweth, A.; Wang, L.; Visweswaraiah, J.; Reichert, J. M. Antibodies to watch in 2024 in *Mabs* volume 16, 1 Taylor & Francis **2024** page 2297450.

[73] Crescioli, S.; Kaplon, H.; Wang, L.; Visweswaraiah, J.; Kapoor, V.; Reichert, J. M. Antibodies to watch in 2025 in *mAbs* volume 17, 1 Taylor & Francis **2025** page 2443538.

[74] Scott, A. M.; Allison, J. P.; Wolchok, J. D. Monoclonal Antibodies in Cancer Therapy *Cancer Immunity Archive* **2012** *12*.

[75] Saini, S.; Gulati, N.; Awasthi, R.; Arora, V.; Singh, S. K.; Kumar, S.; Gupta, G.; Dua, K.; Pahwa, R.; Dureja, H. Monoclonal antibodies and antibody-drug conjugates as emerging therapeutics for breast cancer treatment *Current Drug Delivery* **2024**.

[76] Das, R. T Cell Receptor-Engaging Monoclonal Antibodies Mobilize the Anti-Tumor Functions of Invariant Natural Killer T Cells *Critical Reviews™ in Oncogenesis* **2024** *29*.

[77] Flego, M.; Ascione, A.; Cianfriglia, M.; Vella, S. Clinical Development of Monoclonal Antibody-Based Drugs in HIV and HCV Diseases *BMC Medicine* **2013** *11*, 1–17.

[78] Bruno, V.; Battaglia, G.; Nicoletti, F. The Advent of Monoclonal Antibodies in the Treatment of Chronic Autoimmune Diseases *Neurological Sciences* **2011** *31*, 283–288.

[79] Voge, N. V.; Alvarez, E. Monoclonal Antibodies in Multiple Slerosis: Present and Future. *Biomedicines* **2019** page 20.

[80] Pour-Reza-Gholi, F.; Assadiasl, S. Eculizumab in kidney diseases *Journal of Nephropharmacology* **2024** *13*.

[81] Raffaelli, B.; Neeb, L.; Reuter, U. Monoclonal antibodies for the prevention of migraine *Expert Opinion on Biological therapy* **2019** *19*, 1307–1317.

[82] Mínguez-Olaondo, A.; López-Bravo, A.; Quintas, S.; Nieves-Castellanos, C.; Layos-Romero, A.; Belvís, R.; Irimia, P.; Díaz-Insa, S. New therapeutic era for migraine attacks with recently approved monoclonal antibodies, ditans and gepants *Revista de Neurologia* **2024** *78*, 47–57.

[83] Van Dyck, C. H. Anti-amyloid-β monoclonal antibodies for Alzheimer's disease: pitfalls and promise *Biological Psychiatry* **2018** *83*, 311–319.

[84] Lacorte, E.; Ancidoni, A.; Zaccaria, V.; Remoli, G.; Tariciotti, L.; Bellomo, G.; Sciancalepore, F.; Corbo, M.; Lombardo, F. L.; Bacigalupo, I.; et al. Safety and efficacy of monoclonal antibodies for Alzheimer's disease: a systematic review and meta-analysis of published and unpublished clinical trials *Journal of Alzheimer's Disease* **2022** *87*, 101–129.

[85] Perneczky, R.; Dom, G.; Chan, A.; Falkai, P.; Bassetti, C. Anti-amyloid antibody treatments for Alzheimer's disease *European Journal of neurology* **2024** *31*, e16049.

[86] Ebell, M. H.; Barry, H. C.; Baduni, K.; Grasso, G. Clinically Important Benefits and Harms of Monoclonal Antibodies Targeting Amyloid for the Treatment of Alzheimer Disease: A Systematic Review and Meta-Analysis *The Annals of Family Medicine* **2024** *22*, 50–62.

[87] Digma, L. A.; Winer, J. R.; Greicius, M. D. Substantial Doubt Remains about the Efficacy of Anti-Amyloid Antibodies *Journal of Alzheimer's Disease* **2024** *97*, 567–572.

[88] Viola, M.; Sequeira, J.; Seiça, R.; Veiga, F.; Serra, J.; Santos, A. C.; Ribeiro, A. J. Subcutaneous Delivery of Monoclonal Antibodies: How Do We Get There? *Journal of Controlled Release* **2018** *286*, 301–314.

[89] Zhong, X.; Liu, Y.; Ardekani, A. M. A compartment model for subcutaneous injection of monoclonal antibodies *International Journal of Pharmaceutics* **2024** *650*, 123687.

[90] Stoner, K. L.; Harder, H.; Fallowfield, L. J.; Jenkins, V. A. Intravenous versus subcutaneous drug administration. Which do patients prefer? A systematic review *The Patient-Patient-Centered Outcomes Research* **2015** *8*, 145–153.

[91] Hilley, P.; Wong, D.; Ma, R.; Peterson, A.; De Cruz, P. Transitioning patients from intravenous to subcutaneous infliximab and vedolizumab for inflammatory bowel disease: what is the opportunity cost of improving access to healthcare? *Internal Medicine Journal* **2024**.

[92] Napolitano, D.; Settanni, C. R.; Parisio, L.; Orgiana, N.; Poscia, A.; Schiavoni, E.; Turchini, L.; Cascio, A. L.; Germini, F.; Sblendorio, E.; et al. Transition from intravenous to subcutaneous biological therapies in inflammatory bowel disease: An online survey of patients *Indian Journal of Gastroenterology* **2024** pages 1–11.

[93] Berteau, C.; Filipe-Santos, O.; Wang, T.; Rojas, H. E.; Granger, C.; Schwarzenbach, F. Evaluation of the Impact of Viscosity, Injection Volume, and Injection Flow Rate on Subcutaneous Injection Tolerance *Medical Devices (Auckland, NZ)* **2015** *8*, 473.

[94] Deokar, V.; Sharma, A.; Mody, R.; Volety, S. M. Comparison of Strategies in Development and Manufacturing of Low Viscosity, Ultra-High Concentration Formulation for IgG1 Antibody *Journal of Pharmaceutical Sciences* **2020** *109*, 3579–3589.

[95] Shire, S. J.; Shahrokh, Z.; Liu, J. Challenges in the Development of High Protein Concentration Formulations *Current Trends in Monoclonal Antibody Development and Manufacturing* **2010** pages 131–147.

[96] Garidel, P.; Kuhn, A. B.; Schäfer, L. V.; Karow-Zwick, A. R.; Blech, M. High-Concentration Protein Formulations: How High is High? *European Journal of Pharmaceutics and Biopharmaceutics* **2017** *119*, 353–360.

[97] Badkar, A.; Gandhi, R.; Davis, S.; LaBarre, M. Subcutaneous Delivery of High-Dose/Volume Biologics: Current Status and Prospect for Future Advancements *Drug Design, Development and Therapy* **2021** *Volume 15*, 159–170.

[98] Le Basle, Y.; Chennell, P.; Tokhadze, N.; Astier, A.; Sautou, V. Physicochemical Stability of Monoclonal Antibodies: A Review. *Journal of Pharmaceutical Sciences* **2020** *109*, 169–190.

[99] Jiskoot, W.; Hawe, A.; Menzen, T.; Volkin, D. B.; Crommelin, D. J. Ongoing Challenges to Develop High Concentration Monoclonal Antibody-Based Formulations for Subcutaneous Administration: Quo Vadis? *Journal of Pharmaceutical Sciences* **2022** *111*, 861–867.

[100] Liu, J.; Nguyen, M. D.; Andya, J. D.; Shire, S. J. Reversible Self-Association Increases the Viscosity of a Concentrated Monoclonal Antibody in Aqueous Solution *Journal of Pharmaceutical Sciences* **2005** *94*, 1928–1940.

[101] Kanai, S.; Liu, J.; Patapoff, T. W.; Shire, S. J. Reversible Self-Association of a Concentrated Monoclonal Antibody Solution Mediated by Fab–Fab Interaction that Impacts Solution Viscosity *Journal of Pharmaceutical Sciences* **2008** *97*, 4219–4227.

[102] Yadav, S.; Liu, J.; Shire, S. J.; Kalonia, D. S. Specific Interactions in High Concentration Antibody Solutions Resulting in High Viscosity *Journal of Pharmaceutical Sciences* **2010** *99*, 1152–1168.

[103] Binabaji, E.; Ma, J.; Zydney, A. L. Intermolecular Interactions and the Viscosity of Highly Concentrated Monoclonal Antibody Solutions *Pharmaceutical Research* **2015** *32*, 3102–3109.

[104] Esfandiary, R.; Parupudi, A.; Casas-Finet, D., J. Gadre; Sathish, H. Mechanism of Reversible Self-Association of a Monoclonal Antibody: Role of Electrostatic and Hydrophobic Interactions *Journal of Pharmaceutical Science* **2015** *104(2)*, 577–586.

[105] Tian, Z.; Jiang, X.; Chen, Z.; Huang, C.; Qian, F. Quantifying Protein Shape to Elucidate Its Influence on Solution Viscosity in High-Concentration Electrolyte Solutions *Molecular Pharmaceutics* **2024**.

[106] Tashima, T. Delivery of orally administered digestible antibodies using nanoparticles *International Journal of Molecular Sciences* **2021** *22*, 3349.

[107] Pitiot, A.; Heuzé-Vourc'h, N.; Sécher, T. Alternative routes of administration for therapeutic antibodies – state of the art *Antibodies* **2022** *11*, 56.

[108] Ajeeb, R.; Clegg, J. R. Intrathecal delivery of Macromolecules: Clinical status and emerging technologies *Advanced Drug Delivery Reviews* **2023** *199*, 114949.

[109] Courtenay, A. J.; McCrudden, M. T.; McAvoy, K. J.; McCarthy, H. O.; Donnelly, R. F. Microneedle-mediated transdermal delivery of bevacizumab *Molecular Pharmaceutics* **2018** *15*, 3545–3556.

[110] Kirkby, M.; Hutton, A. R.; Donnelly, R. F. Microneedle mediated transdermal delivery of protein, peptide and antibody based therapeutics: current status and future considerations *Pharmaceutical Research* **2020** *37*, 117.

[111] Tran, K. T.; Le, T. T.; Agrahari, V.; Peet, M. M.; Ouattara, L. A.; Anderson, S. M.; Le-Kim, T. H.; Singh, O. N.; Doncel, G. F.; Nguyen, T. D. Single-administration long-acting microarray patch with ultrahigh loading capacity and multiple releases of thermally stable antibodies *Molecular Pharmaceutics* **2023** *20*, 2352–2361.

[112] Tucak-Smajić, A. **2023** Biorender templates: parenteral-routes of drug administration.

[113] Kivitz, A.; Segurado, O. G. HUMIRA® Pen: a novel autoinjection device for subcutaneous injection of the fully human monoclonal antibody adalimumab *Expert Review of Medical Devices* **2007** *4*, 109–116.

[114] Davis, J. D.; Bravo Padros, M.; Conrado, D. J.; Ganguly, S.; Guan, X.; Hassan, H. E.; Hazra, A.; Irvin, S. C.; Jayachandran, P.; Kosloski, M. P.; et al. Subcutaneous administration of monoclonal antibodies: pharmacology, delivery, immunogenicity, and learnings from applications to clinical development *Clinical Pharmacology & Therapeutics* **2024** *115*, 422–439.

[115] Homšek, A.; Spasić, J.; Nikolić, N.; Stanojković, T.; Jovanović, M.; Miljković, B.; Vučićević, K. M. Pharmacokinetic characterization, benefits and barriers of subcutaneous administration of monoclonal antibodies in oncology *Journal of Oncology Pharmacy Practice* **2023** *29*, 431–440.

[116] Bittner, B.; Richter, W.; Schmidt, J. Subcutaneous administration of biotherapeutics: an overview of current challenges and opportunities *BioDrugs* **2018** *32*, 425–440.

[117] Matucci, A.; Vultaggio, A.; Danesi, R. The use of intravenous versus subcutaneous monoclonal antibodies in the treatment of severe asthma: a review *Respiratory Research* **2018** *19*, 1–10.

[118] Inoue, Y. Subcutaneous delivery of immune checkpoint inhibitors: new route replacing intravenous administration? *Translational Lung Cancer Research* **2024** *13*, 947.

[119] Moreau, P.; Coiteux, V.; Hulin, C.; Leleu, X.; van de Velde, H.; Acharya, M.; Harousseau, J.-L. Prospective comparison of subcutaneous versus intravenous administration of bortezomib in patients with multiple myeloma *Haematologica* **2008** *93*, 1908–1911.

[120] Van den Nest, M.; Glechner, A.; Gold, M.; Gartlehner, G. The comparative efficacy and risk of harms of the intravenous and subcutaneous formulations of trastuzumab in patients with HER2-positive breast cancer: a rapid review *Systematic Reviews* **2019** *8*, 1–8.

[121] Elford, A. T.; Heldt, R.; Kamal, S.; Christensen, B.; Segal, J. P. Systematic review with meta-analysis of the effectiveness of subcutaneous biologics versus intravenous biologics in inflammatory bowel diseases *European Journal of Gastroenterology & Hepatology* **2024** pages 10–1097.

[122] Mathias, N.; Huille, S.; Picci, M.; Mahoney, R. P.; Pettis, R. J.; Case, B.; Helk, B.; Kang, D.; Shah, R.; Ma, J.; et al. Towards more tolerable subcutaneous administration: Review of contributing factors for improving combination product design *Advanced Drug Delivery Reviews* **2024** page 115301.

[123] Kumar, S.; Sanap, S. N.; Vasoya, M.; Handa, M.; Pandey, P.; Khopade, A.; Sawant, K. K. USFDA-approved parenteral peptide formulations and excipients: Industrial perspective *Journal of Drug Delivery Science and Technology* **2024** page 105589.

[124] King, T. E.; Humphrey, J. R.; Laughton, C. A.; Thomas, N. R.; Hirst, J. D. Optimizing Excipient Properties to Prevent Aggregation in Biopharmaceutical Formulations *Journal of Chemical Information and Modeling* **2023** *64*, 265–275.

[125] Wang, S.; Zhang, N.; Hu, T.; Dai, W.; Feng, X.; Zhang, X.; Qian, F. Viscosity-lowering effect of amino acids and salts on highly concentrated solutions of two IgG1 monoclonal antibodies *Molecular Pharmaceutics* **2015** *12*, 4478–4487.

[126] Prašnikar, M.; Proj, M.; Žiberna, M. B.; Lebar, B.; Knez, B.; Kržišnik, N.; Roškar, R.; Gobec, S.; Grabnar, I.; Žula, A.; et al. The search for novel proline analogs for viscosity reduction and stabilization of highly concentrated monoclonal antibody solutions *International Journal of Pharmaceutics* **2024** *655*, 124055.

[127] Dear, B. J.; Hung, J. J.; Truskett, T. M.; Johnston, K. P. Contrasting the influence of cationic amino acids on the viscosity and stability of a highly concentrated monoclonal antibody *Pharmaceutical Research* **2017** *34*, 193–207.

[128] Dear, B. J.; Hung, J. J.; Laber, J. R.; Wilks, L. R.; Sharma, A.; Truskett, T. M.; Johnston, K. P. Enhancing Stability and Reducing Viscosity of a Monoclonal Antibody With Cosolutes by Weakening Protein-Protein Interactions *Journal of Pharmaceutical Sciences* **2019** *108*, 2517–2526.

[129] Tilegenova, C.; Izadi, S.; Yin, J.; Huang, C. S.; Wu, J.; Ellerman, D.; Hymowitz, S. G.; Walters, B.; Salisbury, C.; Carter, P. J. Dissecting the Molecular Basis of High Viscosity of Monospecific and Bispecific IgG Antibodies *mAbs* **2020** *12*, 1692764.

[130] Ye, Y.; Huo, X.; Yin, Z. Protein-protein interactions at high concentrations: Effects of ArgHCl and NaCl on the stability, viscosity and aggregation mechanisms of protein solution *International Journal of Pharmaceutics* **2021** *601*, 120535.

[131] Braun, S.; Banik, N.; Widera, J. J.; Brandenburg, J. G.; Rosenkranz, T. The Viscosity Reduction Platform: Viscosity-reducing excipients for protein formulation *MilliporeSigma White Paper* **2021**.

[132] Prass, T. M.; Garidel, P.; Schäfer, L. V.; Blech, M. Residue-resolved insights into the stabilization of therapeutic proteins by excipients: A case study of two monoclonal antibodies with arginine and glutamate in *mAbs* volume 16, 1 Taylor & Francis **2024** page 2427771.

[133] Ren, S. Effects of arginine in therapeutic protein formulations: a decade review and perspectives *Antibody Therapeutics* **2023** *6*, 265–276.

[134] Guo, Z.; Chen, A.; Nassar, R. a. Structure-Activity Relationship for Hydrophobic Salts as Viscosity-Lowering Excipients for Concentrated Solutions of Monoclonal Antibodies *Pharmaceutical Research* **2012** *29*, 3102–3109.

[135] Zeng, Y.; Tran, T.; Wuthrich, P.; Naik, S.; Davagnino, J.; Greene, D. G.; Mahoney, R. P.; S., S. D. Caffeine as a Viscosity Reducer for Highly Concentrated Monoclonal Antibody Solutions *Journal of Pharmaceutical Sciences* **2021** *110*, 3594–3604.

[136] Srivastava, A.; O'Dell, C.; Bolessa, E.; McLinden, S.; Fortin, L.; Deorkar, N. Viscosity Reduction and Stability Enhancement of Monoclonal Antibody Formulations Using Derivatives of Amino Acids. *Journal of Pharmaceutical Sciences* **2022** *111*, 2848–2856.

[137] Lapenna, A.; Dagallier, C.; Huille, S.; Tribet, C. Poly (glutamic acid)-Based Viscosity Reducers for Concentrated Formulations of a Monoclonal IgG Antibody *Molecular Pharmaceutics* **2024**.

[138] Bauer, K. C.; Suhm, S.; Wöll, A. K.; Hubbuch, J. Impact of Additives on the Formation of Protein Aggregates and Viscosity in Concentrated Protein Solutions *International Journal of Pharmaceutics* **2017** *516*, 82–90.

[139] Hong, T.; Iwashita, K.; Shiraki, K. Viscosity Control of Protein Solution by Small Solutes: A Review *Current Protein & Peptide Science* **2018** *19(8)*.

[140] Proj, M.; Zidar, M.; Lebar, B.; Strašek, N.; Miličić, G.; Žula, A.; Gobec, S. Discovery of Compounds with Viscosity-Reducing Effects on Biopharmaceutical Formulations with Monoclonal Antibodies *Computational and Structural Biotechnology Journal* **2022** *20*, 5420–5429.

[141] Yadav, P.; Singh, Y.; Chauhan, D.; Yadav, P. K.; Kedar, A. S.; Tiwari, A. K.; Shah, A. A.; Gayen, J. R.; Chourasia, M. K. Development and approval of novel injectables: enhancing therapeutic innovations *Expert Opinion on Drug Delivery* **2024** *21*, 639–662.

[142] Jones, M. T.; Mahler, H.-C.; Yadav, S.; Bindra, D.; Corvari, V.; Fesinmeyer, R. M.; Gupta, K.; Harmon, A. M.; Hinds, K. D.; Koulov, A.; et al. Considerations for the use of polysorbates in biopharmaceuticals *Pharmaceutical Research* **2018** *35*, 1–8.

[143] Khan, T. A.; Mahler, H.-C.; Kishore, R. S. Key interactions of surfactants in therapeutic protein formulations: a review *European Journal of Pharmaceutics and Biopharmaceutics* **2015** *97*, 60–67.

[144] Klich, J. H.; Kasse, C. M.; Mann, J. L.; Huang, Y.; d'Aquino, A. I.; Grosskopf, A. K.; Baillet, J.; Fuller, G. G.; Appel, E. A. Stable High-Concentration Monoclonal Antibody Formulations Enabled by an Amphiphilic Copolymer Excipient *Advanced therapeutics* **2023** *6*, 2200102.

[145] Zhang, C.; Gossert, S. T.; Williams, J.; Little, M.; Barros, M.; Dear, B.; Falk, B.; Kanthe, A. D.; Garmise, R.; Mueller, L.; et al. Ranking mAb–excipient interactions in biologics formulations by NMR spectroscopy and computational approaches in *Mabs* volume 15, 1 Taylor & Francis **2023** page 2212416.

[146] Lv, J.-Y.; Ingle, R. G.; Wu, H.; Liu, C.; Fang, W.-J. Histidine as a versatile excipient in the protein-based biopharmaceutical formulations *International Journal of Pharmaceutics* **2024** page 124472.

[147] Baek, Y.; Emami, P.; Singh, N.; Ilott, A.; Sahin, E.; Zydney, A. Stereospecific interactions between histidine and monoclonal antibodies *Biotechnology and bioengineering* **2019** *116*, 2632–2639.

[148] Saurabh, S.; Kalonia, C.; Li, Z.; Hollowell, P.; Waigh, T.; Li, P.; Webster, J.; Seddon, J. M.; Lu, J. R.; Bresme, F. Understanding the stabilizing effect of histidine on mAb aggregation: a molecular dynamics study *Molecular Pharmaceutics* **2022** *19*, 3288–3303.

[149] Callaway, D. J.; Farago, B.; Bu, Z. Nanoscale protein dynamics: A new frontier for neutron spin echo spectroscopy *The European Physical Journal E* **2013** *36*, 1–8.

[150] Trucillo, P. Drug carriers: A review on the most used mathematical models for drug release *Processes* **2022** *10*, 1094.

[151] Stradner, A.; Schurtenberger, P. Potential and limits of a colloid approach to protein solutions *Soft Matter* **2020** *16*, 307–323.

[152] Nägele, G.; Medina-Noyola, M.; Klein, R.; Arauz-Lara, J. Time-dependent self-diffusion in model suspensions of highly charged brownian particles *Physica A: Statistical Mechanics and its Applications* **1988** *149*, 123–163.

[153] Nägele, G.; Bergenholtz, J.; Dhont, J. Cooperative diffusion in colloidal mixtures *The Journal of Chemical Physics* **1999** *110*, 7037–7052.

[154] Nägele, G. Viscoelasticity and diffusional properties of colloidal model dispersions *Journal of Physics: Condensed Matter* **2002** *15*, S407.

[155] Banchio, A. J.; Heinen, M.; Holmqvist, P.; Nägele, G. Short-and long-time diffusion and dynamic scaling in suspensions of charged colloidal particles *The Journal of Chemical Physics* **2018** *148*.

[156] Einstein, A. Über die von der molekularkinetischen Theorie der Wärme geforderte Bewegung von in ruhenden Füssigkeiten suspendierten Teilchen *Annalen der Physik (Leipzig)* **1905** *17*, 549–560.

[157] Fick, A. Ueber diffusion *Annalen der physik* **1855** *170*, 59–86.

[158] Chang, Q. *Colloid and Interface Chemistry for water quality control* Academic Press **2016**.

[159] de la Torre, J. G.; Huertas, M. L.; Carrasco, B. Calculation of hydrodynamic properties of globular proteins from their atomic-level structure *Biophysical Journal* **2000** *78*, 719–730.

[160] Ortega, A.; Amorós, D.; De La Torre, J. G. Prediction of Hydrodynamic and other Solution Properties of rigid Proteins from Atomic-and Residue-Level Models *Biophysical Journal* **2011** *101*, 892–898.

[161] Tokuyama, M.; Oppenheim, I. On The Theory of Concentrated Hard-Sphere Suspensions *Physica A: Statistical Mechanics and its Applications* **1995** *216*, 85–119.

[162] Myung, J. S.; Roosen-Runge, F.; Winkler, R. G.; Gompper, G.; Schurtenberger, P.; Stradner, A. Weak shape anisotropy leads to a nonmonotonic contribution to crowding, impacting protein dynamics under physiologically relevant conditions *The Journal of Physical Chemistry B* **2018** *122*, 12396–12402.

[163] Grimaldo, M.; Roosen-Runge, F.; Jalarvo, N.; Zamponi, M.; Zanini, F.; Hennig, M.; Zhang, F.; Schreiber, F.; Seydel, T. High-resolution neutron spectroscopy on protein solution samples in *EPJ Web of Conferences* volume 83 EDP Sciences **2015** page 02005.

[164] Banchio, A. J.; Nägele, G.; Bergenholtz, J. Viscoelasticity and generalized Stokes–Einstein relations of colloidal dispersions *The Journal of Chemical Physics* **1999** *111*, 8721–8740.

[165] Callen, H. B.; Welton, T. A. Irreversibility and generalized noise *Physical Review* **1951** *83*, 34.

[166] Kubo, R. The fluctuation-dissipation theorem *Reports on Progress in Physics* **1966** *29*, 255.

[167] Bonn, D.; Kegel, W. K. Stokes–Einstein relations and the fluctuation-dissipation theorem in a supercooled colloidal fluid *The Journal of Chemical Physics* **2003** *118*, 2005–2009.

[168] Zwanzig, R. *Nonequilibrium statistical mechanics* Oxford university press **2001**.

[169] Koenderink, G. H.; Zhang, H.; Aarts, D. G.; Lettinga, M. P.; Philipse, A. P.; Nägele, G. On the validity of Stokes–Einstein–Debye relations for rotational diffusion in colloidal suspensions *Faraday discussions* **2003** *123*, 335–354.

[170] Rothe, M.; Gruber, T.; Gröger, S.; Balbach, J.; Saalwächter, K.; Roos, M. Transient binding accounts for apparent violation of the generalized Stokes–Einstein relation in crowded protein solutions *Physical Chemistry Chemical Physics* **2016** *18*, 18006–18014.

[171] Skar-Gislinge, N.; Camerin, F.; Stradner, A.; Zaccarelli, E.; Schurtenberger, P. Cluster Formation and The Link to Viscosity in Antibody Solutions *arXiv preprint arXiv:2209.05182* **2022** https://arxiv.org/abs/2209.05182v1 (accessed 2023-07-18).

[172] Skar-Gislinge, N.; Camerin, F.; Stradner, A.; Zaccarelli, E.; Schurtenberger, P. Using Cluster Theory to Calculate the Experimental Structure Factors of Antibody Solutions *Molecular Pharmaceutics* **2023** *20*, 2738–2753.

[173] Gentiluomo, L.; Roessner, D.; Streicher, W.; Mahapatra, S.; Harris, P.; Frieß, W. Characterization of Native Reversible Self-Association of a Monoclonal Antibody Mediated by Fab-Fab Interaction *Journal of Pharmaceutical Sciences* **2020** *109*, 2517–2526.

[174] Chowdhury, A.; Manohar, N.; Guruprasad, G.; Chen, A. T.; Lanzaro, A.; Blanco, M.; Johnston, K. P.; Truskett, T. M. Characterizing Experimental Monoclonal Antibody Interactions and Clustering Using a Coarse-Grained Simulation Library and a Viscosity Model *The Journal of Physical Chemistry B* **2023** *127*, 1120–1137 pMID: 36716270.

[175] Saurabh, S.; Lei, L.; Li, Z.; Seddon, J. M.; Lu, J. R.; Kalonia, C.; Bresme, F. Adsorption of monoclonal antibody fragments at the water–oil interface: A coarse-grained molecular dynamics study *APL bioengineering* **2024** *8*.

[176] Prass, T. M.; Garidel, P.; Blech, M.; Schäfer, L. V. Viscosity prediction of high-concentration antibody solutions with atomistic simulations *Journal of Chemical Information and Modeling* **2023** *63*, 6129–6140.

[177] Castellanos, M. M.; Howell, S. C.; Gallagher, D. T.; Curtis, J. E. Characterization of the NISTmAb Reference Material using small-angle scattering and molecular simulation: part I: dilute protein solutions *Analytical and bioanalytical Chemistry* **2018** *410*, 2141–2159.

[178] Janke, J. J.; Starr, C. G.; Kingsbury, J. S.; Furtmann, N.; Roberts, C. J.; Calero-Rubio, C. Computational Screening for mAb Colloidal Stability with Coarse-Grained, Molecular-Scale Simulations *The Journal of Physical Chemistry B* **2024** *128*, 1515–1526.

[179] Hatch, H. W.; Bergonzo, C.; Blanco, M. A.; Yuan, G.; Grudinin, S.; Lund, M.; Curtis, J. E.; Grishaev, A. V.; Liu, Y.; Shen, V. K. Anisotropic coarse-grain Monte Carlo simulations of lysozyme, lactoferrin, and NISTmAb by precomputing atomistic models *The Journal of Chemical Physics* **2024** *161*.

[180] Dai, J.; Izadi, S.; Zarzar, J.; Wu, P.; Oh, A.; Carter, P. J. Variable domain mutational analysis to probe the molecular mechanisms of high viscosity of an IgG1 antibody in *mAbs* volume 16, 1 Taylor & Francis **2024** page 2304282.

[181] Kastelic, M.; Dill, K. A.; Kalyuzhnyi, Y. V.; Vlachy, V. Controlling the viscosities of antibody solutions through control of their binding sites *Journal of Molecular Liquids* **2018** *270*, 234–242.

[182] Makowski, E. K.; Chen, H.-T.; Tessier, P. M. Simplifying complex antibody engineering using machine learning *Cell Systems* **2023** *14*, 667–675.

[183] Makowski, E. K.; Chen, H.-T.; Wang, T.; Wu, L.; Huang, J.; Mock, M.; Underhill, P.; Pelegri-O'Day, E.; Maglalang, E.; Winters, D.; et al. Reduction of monoclonal antibody viscosity using interpretable machine learning in *mAbs* volume 16, 1 Taylor & Francis **2024** page 2303781.

[184] Schmitt, J.; Razvi, A.; Grapentin, C. Predictive Modeling of Concentration-Dependent Viscosity Behavior of Monoclonal Antibody Solutions Using Artificial Neural Networks *Mabs* **2023** *15*, 2169440.

[185] Armstrong, G. B.; Shah, V.; Sanches, P.; Patel, M.; Casey, R.; Jamieson, C.; Burley, G. A.; Lewis, W.; Rattray, Z. A framework for the biophysical screening of antibody mutations targeting solvent-accessible hydrophobic and electrostatic patches for enhanced viscosity profiles *Computational and Structural Biotechnology Journal* **2024** *23*, 2345–2357.

[186] Bansal, R.; Gupta, S.; Rathore, A. S. Analytical platform for monitoring aggregation of monoclonal antibody therapeutics *Pharmaceutical Research* **2019** *36*, 1–11.

[187] Nobbmann, U.; Connah, M.; Fish, B.; Varley, P.; Gee, C.; Mulot, S.; Chen, J.; Zhou, L.; Lu, Y.; Sheng, F.; et al. Dynamic light scattering as a relative tool for assessing the molecular integrity and stability of monoclonal antibodies *Biotechnology and Genetic Engineering Reviews* **2007** *24*, 117–128.

[188] Scherer, T. M.; Liu, J.; Shire, S. J.; Minton, A. P. Intermolecular interactions of IgG1 monoclonal antibodies at high concentrations characterized by light scattering *The Journal of physical Chemistry B* **2010** *114*, 12948–12957.

[189] Woods, J. M.; Nesta, D. Formulation effects on opalescence of a high-concentration MAb *BioProcess Int* **2010** *8*, 48–59.

[190] Arzenšek, D.; Kuzman, D.; Podgornik, R. Colloidal interactions between monoclonal antibodies in aqueous solutions *Journal of Colloid and Interface Science* **2012** *384*, 207–216.

[191] Lai, Y. H.; Koo, S.; Oh, S. H.; Driskell, E. A.; Driskell, J. D. Rapid screening of antibody–antigen binding using dynamic light scattering (DLS) and gold nanoparticles *Analytical Methods* **2015** *7*, 7249–7255.

[192] Hung, J. J.; Dear, B. J.; Karouta, C. A.; Chowdhury, A. A.; Godfrin, P. D.; Bollinger, J. A.; Nieto, M. P.; Wilks, L. R.; Shay, T. Y.; Ramachandran, K.; et al. Protein–protein interactions of highly concentrated monoclonal antibody solutions via static light scattering and influence on the viscosity *The Journal of Physical Chemistry B* **2019** *123*, 739–755.

[193] Arzensek, D.; Kuzman, D.; Podgornik, R. Hofmeister effects in monoclonal antibody solution interactions *The Journal of Physical Chemistry B* **2015** *119*, 10375–10389.

[194] Mosca, I.; Pounot, K.; Beck, C.; Colin, L.; Matsarskaia, O.; Grapentin, C.; Seydel, T.; Schreiber, F. Biophysical determinants for the viscosity of concentrated monoclonal antibody solutions *Molecular Pharmaceutics* **2023** *20*, 4698–4713.

[195] Saito, S.; Hasegawa, J.; Kobayashi, N.; Kishi, N.; Uchiyama, S.; Fukui, K. Behavior of monoclonal antibodies: relation between the second virial coefficient (B 2) at low concentrations and aggregation propensity and viscosity at high concentrations *Pharmaceutical Research* **2012** *29*, 397–410.

[196] Raut, A. S.; Kalonia, D. S. Opalescence in monoclonal antibody solutions and its correlation with intermolecular interactions in dilute and concentrated solutions *Journal of Pharmaceutical Sciences* **2015** *104*, 1263–1274.

[197] Calero-Rubio, C.; Ghosh, R.; Saluja, A.; Roberts, C. J. Predicting protein-protein interactions of concentrated antibody solutions using dilute solution data and coarse-grained molecular models *Journal of Pharmaceutical Sciences* **2018** *107*, 1269–1281.

[198] Finet, S.; Skouri-Panet, F.; Casselyn, M.; Bonnete, F.; Tardieu, A. The Hofmeister effect as seen by SAXS in protein solutions *Current Opinion in Colloid & Interface Science* **2004** *9*, 112–116.

[199] Zhang, F.; Skoda, M. W.; Jacobs, R. M.; Martin, R. A.; Martin, C. M.; Schreiber, F. Protein interactions studied by SAXS: effect of ionic strength and protein concentration for BSA in aqueous solutions *The Journal of Physical Chemistry B* **2007** *111*, 251–259.

[200] Molodenskiy, D.; Shirshin, E.; Tikhonova, T.; Gruzinov, A.; Peters, G.; Spinozzi, F. Thermally induced conformational changes and protein–protein interactions of bovine serum albumin in aqueous solution under different pH and ionic strengths as revealed by SAXS measurements *Physical Chemistry Chemical Physics* **2017** *19*, 17143–17155.

[201] Skou, S.; Gillilan, R. E.; Ando, N. Synchrotron-based small-angle X-ray scattering of proteins in solution *Nature protocols* **2014** *9*, 1727–1739.

[202] Chowdhury, A.; Bollinger, J. A.; Dear, B. J.; Cheung, J. K.; Johnston, K. P.; Truskett, T. M. Coarse-grained molecular dynamics simulations for understanding the impact of short-range anisotropic attractions on structure and viscosity of concentrated monoclonal antibody solutions *Molecular Pharmaceutics* **2020** *17*, 1748–1756.

[203] Polimeni, M.; Zaccarelli, E.; Gulotta, A.; Lund, M.; Stradner, A.; Schurtenberger, P. A multi-scale numerical approach to study monoclonal antibodies in solution *APL Bioengineering* **2024** *8*.

[204] Lilyestrom, W. G.; Shire, S. J.; Scherer, T. M. Influence of the cosolute environment on IgG solution structure analyzed by small-angle X-ray scattering *The Journal of Physical Chemistry B* **2012** *116*, 9611–9618.

[205] Lilyestrom, W. G.; Yadav, S.; Shire, S. J.; Scherer, T. M. Monoclonal Antibody Self-Association, Cluster Formation, and Rheology at High Concentrations *The Journal of Physical Chemistry B* **2013** *117*, 6373–6384.

[206] Mosbæk, C. R.; Konarev, P. V.; Svergun, D. I.; Rischel, C.; Vestergaard, B. High concentration formulation studies of an IgG2 antibody using small angle X-ray scattering *Pharmaceutical Research* **2012** *29*, 2225–2235.

[207] Tian, X.; Langkilde, A. E.; Thorolfsson, M.; Rasmussen, H. B.; Vestergaard, B. Small-angle x-ray scattering screening complements conventional biophysical analysis: comparative structural and biophysical analysis of monoclonal antibodies IgG1, IgG2, and IgG4 *Journal of Pharmaceutical Sciences* **2014** *103*, 1701–1710.

[208] Fukuda, M.; Moriyama, C.; Yamazaki, T.; Imaeda, Y.; Koga, A. Quantitative correlation between viscosity of concentrated MAb solutions and particle size parameters obtained from small-angle X-ray scattering *Pharmaceutical Research* **2015** *32*, 3803–3812.

[209] Inouye, H.; Houde, D.; Temel, D. B.; Makowski, L. Utility of solution x-ray scattering for the development of antibody biopharmaceuticals *Journal of Pharmaceutical Sciences* **2016** *105*, 3278–3289.

[210] Fukuda, M.; Watanabe, A.; Hayasaka, A.; Muraoka, M.; Hori, Y.; Yamazaki, T.; Imaeda, Y.; Koga, A. Small-scale screening method for low-viscosity antibody solutions using small-angle X-ray scattering *European Journal of Pharmaceutics and Biopharmaceutics* **2017** *112*, 132–137.

[211] Xu, A. Y.; Castellanos, M. M.; Mattison, K.; Krueger, S.; Curtis, J. E. Studying excipient modulated physical stability and viscosity of monoclonal antibody formulations using small-angle scattering *Molecular Pharmaceutics* **2019** *16*, 4319–4338.

[212] Narvekar, A.; Gawali, S. L.; Hassan, P. A.; Jain, R.; Dandekar, P. pH dependent aggregation and conformation changes of rituximab using SAXS and its comparison with the standard regulatory approach of biophysical characterization *International Journal of Biological Macromolecules* **2020** *164*, 3084–3097.

[213] Xu, A. Y.; Blanco, M. A.; Castellanos, M. M.; Meuse, C. W.; Mattison, K.; Karageorgos, I.; Hatch, H. W.; Shen, V. K.; Curtis, J. E. Role of Domain–Domain Interactions on the Self-Association and Physical Stability of Monoclonal Antibodies: Effect of pH and Salt *The Journal of Physical Chemistry B* **2023** *127*, 8344–8357.

[214] Imamura, H.; Honda, S. Cue to Acid-Induced Long-Range Conformational Changes in an Antibody Preceding Aggregation: The Structural Origins of the Subpeaks in Kratky Plots of Small-Angle X-ray Scattering *International Journal of Molecular Sciences* **2023** *24*.

[215] Imamura, H.; Ooishi, A.; Honda, S. Getting smaller by denaturation: Acid-induced compaction of antibodies *The Journal of Physical Chemistry Letters* **2023** *14*, 3898–3906.

[216] Zhang, Z.; Woys, A. M.; Hong, K.; Grapentin, C.; Khan, T. A.; Zarraga, I. E.; Wagner, N. J.; Liu, Y. Adsorption of non-ionic surfactant and monoclonal antibody on siliconized surface studied by neutron reflectometry *Journal of Colloid and Interface Science* **2021** *584*, 429–438.

[217] Krueger, S. Small-angle neutron scattering contrast variation studies of biological complexes: Challenges and triumphs *Current Opinion in Structural Biology* **2022** *74*, 102375.

[218] Donnelly, R. B.; Pingali, S. V.; Heroux, L.; Brinson, R. G.; Wagner, N. J.; Liu, Y. Hydrogen–Deuterium Exchange Dynamics of NISTmAb Measured by Small Angle Neutron Scattering *Molecular Pharmaceutics* **2023** *20*, 6358–6367.

[219] Zhou, H.-X.; Bilsel, O. SAXS/SANS probe of intermolecular interactions in concentrated protein solutions *Biophysical Journal* **2014** *106*, 771–773.

[220] Barnett, G. V.; Qi, W.; Amin, S.; Lewis, E. N.; Razinkov, V. I.; Kerwin, B. A.; Liu, Y.; Roberts, C. J. Structural changes and aggregation mechanisms for anti-streptavidin IgG1 at elevated concentration *The Journal of Physical Chemistry B* **2015** *119*, 15150–15163.

[221] Barnett, G. V.; Razinkov, V. I.; Kerwin, B. A.; Laue, T. M.; Woodka, A. H.; Butler, P. D.; Perevozchikova, T.; Roberts, C. J. Specific-ion effects on the aggregation mechanisms and protein–protein interactions for anti-streptavidin immunoglobulin gamma-1 *The Journal of Physical Chemistry B* **2015** *119*, 5793–5804.

[222] Xu, A. Y.; Clark, N. J.; Pollastrini, J.; Espinoza, M.; Kim, H.-J.; Kanapuram, S.; Kerwin, B.; Treuheit, M. J.; Krueger, S.; McAuley, A.; et al. Effects of Monovalent Salt on Protein-Protein Interactions of Dilute and Concentrated Monoclonal Antibody Formulations *Antibodies* **2022** *11*, 24.

[223] Castellanos, M. M.; Pathak, J. A.; Leach, W.; Bishop, S. M.; Colby, R. H. Explaining the non-Newtonian character of aggregating monoclonal antibody solutions using small-angle neutron scattering *Biophysical Journal* **2014** *107*, 469–476.

[224] Clark, N. J.; Zhang, H.; Krueger, S.; Lee, H. J.; Ketchem, R. R.; Kerwin, B.; Kanapuram, S. R.; Treuheit, M. J.; McAuley, A.; Curtis, J. E. Small-angle neutron scattering study of a monoclonal antibody using free-energy constraints *The Journal of Physical Chemistry B* **2013** *117*, 14029–14038.

[225] Papachristodoulou, M.; Doutch, J.; Leung, H. S. B.; Church, A.; Charleston, T.; Clifton, L. A.; Butler, P. D.; Roberts, C. J.; Bracewell, D. G. In situ neutron scattering of antibody adsorption during protein A chromatography *Journal of Chromatography A* **2020** *1617*, 460842.

[226] Sato, N.; Yogo, R.; Yanaka, S.; Martel, A.; Porcar, L.; Morishima, K.; Inoue, R.; Tominaga, T.; Arimori, T.; Takagi, J.; et al. A feasibility study of inverse contrast-matching small-angle neutron scattering method combined with size exclusion chromatography using antibody interactions as model systems *The Journal of Biochemistry* **2021** *169*, 701–708.

[227] Yearley, E. J.; Zarraga, I. E.; Shire, S. J.; Scherer, T. M.; Gokarn, Y.; Wagner, N. J.; Liu, Y. Small-angle neutron scattering characterization of monoclonal antibody conformations and interactions at high concentrations *Biophysical Journal* **2013** *105*, 720–731.

[228] Castellanos, M. M.; Pathak, J.; Colby, R. Aggregation of concentrated monoclonal antibody solutions studied by rheology and neutron scattering in *APS March Meeting Abstracts* volume 2013 **2013** pages G45–006.

[229] Godfrin, P. D.; Zarraga, I. E.; Zarzar, J.; Porcar, L.; Falus, P.; Wagner, N. J.; Liu, Y. Effect of Hierarchical Cluster Formation on The Viscosity of Concentrated Monoclonal Antibody Formulations Studied by Neutron Scattering *The Journal of Physical Chemistry B* **2016** *120*, 278–291.

[230] Wang, G.; Varga, Z.; Hofmann, J.; Zarraga, I. E.; Swan, J. W. Structure and relaxation in solutions of monoclonal antibodies *The Journal of Physical Chemistry B* **2018** *122*, 2867–2880.

[231] Castellanos, M. M.; Clark, N. J.; Watson, M. C.; Krueger, S.; McAuley, A.; Curtis, J. E. Role of molecular flexibility and colloidal descriptions of proteins in crowded environments from small-angle scattering *The Journal of Physical Chemistry B* **2016** *120*, 12511–12518.

[232] Gulotta, A.; Polimeni, M.; Lenton, S.; Starr, C. G.; Stradner, A.; Zaccarelli, E.; Schurtenberger, P. Combining scattering experiments and colloid theory to characterize charge effects in concentrated antibody solutions *Molecular Pharmaceutics* **2023**.

[233] Alpert, Y.; Cser, L.; Faragó, B.; Franěk, F.; Mezei, F.; Ostanevich, Y. M. Segmental flexibility in pig immunoglobulin G studied by neutron spin-echo technique *Biopolymers: Original Research on Biomolecules* **1985** *24*, 1769–1784.

[234] Yearley, E. J.; Godfrin, P. D.; Perevozchikova, T.; Zhang, H.; Falus, P.; Porcar, L.; Nagao, M.; Curtis, J. E.; Gawande, P.; Taing, R.; et al. Observation of Small Cluster Formation in Concentrated Monoclonal Antibody Solutions and Its Implications to Solution Viscosity *Biophysical Journal* **2014** *106*, 1763–1770.

[235] Stingaciu, L. R.; Ivanova, O.; Ohl, M.; Biehl, R.; Richter, D. Fast antibody fragment motion: flexible linkers act as entropic spring *Scientific Reports* **2016** *6*, 22148.

[236] Wang, T.; Chen, J.; Du, X.; Feng, G.; Dai, T.; Li, X.; Liu, D. How Neutron Scattering Techniques benefit investigating Structures and Dynamics of Monoclonal Antibody *Biochimica et Biophysica Acta (BBA) - General Subjects* **2022** *1866*, 130206.

[237] Fleischer, G.; Fujara, F. NMR as a generalized incoherent scattering experiment in *Solid-State NMR I Methods* pages 159–207 Springer **1994**.

[238] Song, J.; Taraban, M.; Yu, Y. B.; Lu, L.; Biswas, P. G.; Xu, W.; Xi, H.; Bhambhani, A.; Hu, G.; Su, Y. In-situ biophysical characterization of high-concentration protein formulations using w NMR in *Mabs* volume 16, 1 Taylor & Francis **2024** page 2304624.

[239] Poppe, L.; Jordan, J. B.; Lawson, K.; Jerums, M.; Apostol, I.; Schnier, P. D. Profiling formulated monoclonal antibodies by 1H NMR spectroscopy *Analytical Chemistry* **2013** *85*, 9623–9629.

[240] Kheddo, P.; Cliff, M. J.; Uddin, S.; van der Walle, C. F.; Golovanov, A. P. Characterizing monoclonal antibody formulations in arginine glutamate solutions using 1H NMR spectroscopy *mAbs* **2016** *8, 7*, 1245–1258.

[241] Majumder, S.; Bhattacharya, D. S.; Langford, A.; Ignatius, A. A. Utility of high resolution 2D NMR fingerprinting in assessing viscosity of therapeutic monoclonal antibodies *Pharmaceutical Research* **2022** *39*, 529–539.

[242] Panchal, J.; Falk, B. T.; Antochshuk, V.; McCoy, M. A. Investigating protein–excipient interactions of a multivalent VHH therapeutic protein using NMR spectroscopy in *Mabs* volume 14, 1 Taylor & Francis **2022** page 2124902.

[243] Kheddo, P.; Bramham, J. E.; Dearman, R. J.; Uddin, S.; Van Der Walle, C. F.; Golovanov, A. P. Investigating liquid–liquid phase separation of a monoclonal antibody using solution-state NMR spectroscopy: Effect of Arg· Glu and Arg· HCl *Molecular Pharmaceutics* **2017** *14*, 2852–2860.

[244] Narayanan, T. Recent advances in synchrotron scattering methods for probing the structure and dynamics of colloids *Advances in Colloid and Interface Science* **2024** page 103114.

[245] Reiser, M.; Girelli, A.; Ragulskaya, A.; Das, S.; Berkowicz, S.; Bin, M.; Ladd-Parada, M.; Filianina, M.; Poggemann, H.-F.; Begam, N.; et al. Resolving molecular diffusion and aggregation of

antibody proteins with megahertz X-ray free-electron laser pulses *Nature Communications* **2022** *13*, 5528.

[246] Ragulskaya, A.; Begam, N.; Girelli, A.; Rahmann, H.; Reiser, M.; Westermeier, F.; Sprung, M.; Zhang, F.; Gutt, C.; Schreiber, F. Interplay between kinetics and dynamics of liquid–liquid phase separation in a protein solution revealed by coherent X-ray Spectroscopy *The Journal of Physical Chemistry Letters* **2021** *12*, 7085–7090.

[247] Moron, M.; Al-Masoodi, A.; Lovato, C.; Reiser, M.; Randolph, L.; Surmeier, G.; Bolle, J.; Westermeier, F.; Sprung, M.; Winter, R.; et al. Gelation dynamics upon pressure-induced liquid–liquid phase separation in a water–lysozyme solution *The Journal of Physical Chemistry B* **2022** *126*, 4160–4167.

[248] Chushkin, Y.; Gulotta, A.; Roosen-Runge, F.; Pal, A.; Stradner, A.; Schurtenberger, P. Probing cage relaxation in concentrated protein solutions by X-ray photon correlation spectroscopy *Physical Review Letters* **2022** *129*, 238001.

[249] Girelli, A.; Bin, M.; Filianina, M.; Dargasz, M.; Anthuparambil, N. D.; Möller, J.; Zozulya, A.; Andronis, I.; Timmermann, S.; Berkowicz, S.; et al. Coherent X-rays reveal anomalous molecular diffusion and cage effects in crowded protein solutions *arXiv preprint arXiv:2410.08873* **2024**.

[250] Vodnala, P.; Karunaratne, N.; Bera, S.; Lurio, L.; Thurston, G. M.; Karonis, N.; Winans, J.; Sandy, A.; Narayanan, S.; Yasui, L.; et al. Radiation damage limits to XPCS studies of protein dynamics in *AIP Conf. Proc* volume 1741, 050026 **2016** pages 10–1063.

[251] Lurio, L. B.; Thurston, G. M.; Zhang, Q.; Narayanan, S.; Dufresne, E. M. Use of continuous sample translation to reduce radiation damage for XPCS studies of protein diffusion *Journal of Synchrotron Radiation* **2021** *28*, 490–498.

[252] Vineyard, G. H. Scattering of slow neutrons by a liquid *Physical Review* **1958** *110*, 999.

[253] Singwi, K.; Sjölander, A. Diffusive Motions in Water and Cold Neutron Scattering *Physical Review* **1960** *119*, 863.

[254] Gähler, R.; Golub, R.; Habicht, K.; Keller, T.; Felber, J. Space-time description of neutron spin echo spectrometry *Physica B: Condensed Matter* **1996** *229*, 1–17.

[255] Keller, T.; Besenböck, W.; Feller, J.; Gähler, R.; Golub, R.; Hank, P.; Köppe, M. A comparison of spin echo and conventional neutron instruments by the coherence properties of the neutrons *Physica B: Condensed Matter* **1997** *234*, 1120–1125.

[256] Felber, J.; Gähler, R.; Golub, R.; Prechtel, K. Coherence volumes and neutron scattering *Physica B: Condensed Matter* **1998** *252*, 34–43.

[257] Liu, Y. Intermediate scattering function for macromolecules in solutions probed by neutron spin echo *Physical Review E* **2017** *95*, 020501.

[258] Liu, Y. Short-time dynamics of proteins in solutions studied by neutron spin echo *Current Opinion in Colloid & Interface Science* **2019** *42*, 147–156.

[259] Callaway, D. J.; Bu, Z. Visualizing the nanoscale: protein internal dynamics and neutron spin echo spectroscopy *Current Opinion in Structural Biology* **2017** *42*, 1–5.

[260] Bu, Z.; Biehl, R.; Monkenbusch, M.; Richter, D.; Callaway, D. J. Coupled protein domain motion in Taq polymerase revealed by neutron spin-echo spectroscopy *Proceedings of the National Academy of Sciences* **2005** *102*, 17646–17651.

[261] Häussler, W. Neutron spin echo studies on ferritin: free-particle diffusion and interacting solutions *European Biophysics Journal* **2008** *37*, 563–571.

[262] Le Coeur, C.; Longeville, S. Microscopic protein diffusion at high concentration by neutron spin-echo spectroscopy *Chemical Physics* **2008** *345*, 298–304.

[263] Lal, J.; Fouquet, P.; Maccarini, M.; Makowski, L. Neutron spin-echo studies of hemoglobin and myoglobin: multiscale internal dynamics *Journal of Molecular Biology* **2010** *397*, 423–435.

[264] Farago, B.; Li, J.; Cornilescu, G.; Callaway, D. J.; Bu, Z. Activation of nanoscale allosteric protein domain motion revealed by neutron spin echo spectroscopy *Biophysical Journal* **2010** *99*, 3473–3482.

[265] Yoshida, K.; Yamaguchi, T.; Osaka, N.; Endo, H.; Shibayama, M. A study of alcohol-induced gelation of β-lactoglobulin with small-angle neutron scattering, neutron spin echo, and dynamic light scattering measurements *Physical Chemistry Chemical Physics* **2010** *12*, 3260–3269.

[266] Smolin, N.; Biehl, R.; Kneller, G.; Richter, D.; Smith, J. C. Functional domain motions in proteins on the 1–100 ns timescale: comparison of neutron spin-echo spectroscopy of phosphoglycerate kinase with molecular-dynamics simulation *Biophysical Journal* **2012** *102*, 1108–1117.

[267] Biehl, R.; Monkenbusch, M.; Richter, D. Exploring internal protein dynamics by neutron spin echo spectroscopy *Soft Matter* **2011** *7*, 1299–1307.

[268] Stadler, A.; Monkenbusch, M.; Biehl, R.; Richter, D.; Ollivier, J. Neutron spin-echo and TOF reveals protein dynamics in solution *Journal of the Physical Society of Japan* **2013** *82*, SA016.

[269] Inoue, R.; Oroguchi, T.; Oda, T.; Farago, B.; Martel, A.; Porcar, L.; Sato, M.; Sugiyama, M. Internal dynamics of multidomain protein as revealed by an optimized neutron spin echo measurement and all-atom molecular dynamics simulation *Physical Review Research* **2023** *5*, 043154.

[270] Zhe-Xin, S.; Teng-Fei, C.; Xiang-Qiang, C. Neutron spin echo spectrometer: advanced in studying protein domain motions *PHYSICS* **2024** *53*, 174–184.

[271] Ameseder, F.; Stingaciu, L. R.; Radulescu, A.; Holderer, O.; Falus, P.; Monkenbusch, M.; Biehl, R.; Richter, D.; Stadler, A. M. Structure and Dynamics of Intrinsically Disordered and Unfolded Proteins: Investigations using Small-Angle Scattering and Neutron Spin-Echo Spectroscopy *Biophysical Journal* **2019** *116*, 490a–491a.

[272] Callaway, D. J.; Nicholl, I. D.; Shi, B.; Reyes, G.; Farago, B.; Bu, Z. Nanoscale dynamics of the cadherin–catenin complex bound to vinculin revealed by neutron spin echo spectroscopy *Proceedings of the National Academy of Sciences* **2024** *121*, e2408459121.

[273] Girelli, A.; Beck, C.; Bäuerle, F.; Matsarskaia, O.; Maier, R.; Zhang, F.; Wu, B.; Lang, C.; Czakkel, O.; Seydel, T.; Schreiber, F.; Roosen-Runge, F. Molecular Flexibility of Antibodies Preserved Even in the Dense Phase After Macroscopic Phase Separation *Molecular Pharmaceutics* **2021** *18*, 4162–4169 pMID: 34637319.

[274] Stingaciu, L.-R. Study of protein dynamics via neutron spin echo spectroscopy *Journal of Visualized Experiments* **2022** *182*.

[275] Beck, C.; Appel, M.; Grimaldo, M.; Roosen-Runge, F.; Zhang, F.; Frick, B.; Schreiber, F.; Seydel, T. Neutron spectroscopy on protein solutions employing backscattering with an increased energy range *Physica B: Condensed Matter* **2019** *562*, 31–35.

[276] Matsarskaia, O.; Bühl, L.; Beck, C.; Grimaldo, M.; Schweins, R.; Zhang, F.; Seydel, T.; Schreiber, F.; Roosen-Runge, F. Evolution of the structure and dynamics of bovine serum albumin induced by thermal denaturation *Physical Chemistry Chemical Physics* **2020** *22*, 18507–18517.

[277] Shou, K.; Sarter, M.; De Souza, N. R.; De Campo, L.; Whitten, A. E.; Kuchel, P. W.; Garvey, C. J.; Stadler, A. M. Effect of red blood cell shape changes on haemoglobin interactions and dynamics: a neutron scattering study *Royal Society open science* **2020** *7*, 201507.

[278] Hassani, A. N.; Haris, L.; Appel, M.; Seydel, T.; Stadler, A. M.; Kneller, G. R. Multiscale relaxation dynamics and diffusion of myelin basic protein in solution studied by quasielastic neutron scattering *The Journal of Chemical Physics* **2022** *156*.

[279] Pounot, K.; Chaaban, H.; Fodera, V.; Schiro, G.; Weik, M.; Seydel, T. Tracking internal and global diffusive dynamics during protein aggregation by high-resolution neutron spectroscopy *The Journal of Physical Chemistry Letters* **2020** *11*, 6299–6304.

[280] Pounot, K.; Appel, M.; Beck, C.; Weik, M.; Schirò, G.; Fichou, Y.; Seydel, T.; Schreiber, F. High-resolution Neutron Spectroscopy to Study Picosecond-nanosecond Dynamics of Proteins and Hydration Water *Journal of visualized experiments: JoVE* **2022**.

[281] Fagerberg, E.; Lenton, S.; Nylander, T.; Seydel, T.; Skepo, M. Self-diffusive properties of the intrinsically disordered protein histatin 5 and the impact of crowding thereon: a combined neutron spectroscopy and molecular dynamics simulation study *The Journal of Physical Chemistry B* **2022** *126*, 789–801.

[282] Matsuo, T.; Peters, J. Sub-Nanosecond dynamics of pathologically relevant bio-macromolecules observed by incoherent neutron scattering *Life* **2022** *12*, 1259.

[283] Fujiwara, S. Dynamical Behavior of Disordered Regions in Disease-Related Proteins Revealed by Quasielastic Neutron Scattering *Medicina* **2022** *58*, 795.

[284] Pena-Francesch, A.; Jung, H.; Tyagi, M.; Demirel, M. C. Diffusive dynamic modes of recombinant squid ring teeth proteins by neutron spectroscopy *Biomacromolecules* **2022** *23*, 3165–3173.

[285] Cisse, A.; Schachner-Nedherer, A.-L.; Appel, M.; Beck, C.; Ollivier, J.; Leitinger, G.; Prassl, R.; Kornmueller, K.; Peters, J. Dynamics of apolipoprotein B-100 in interaction with detergent probed by incoherent neutron scattering *The Journal of Physical Chemistry Letters* **2021** *12*, 12402–12410.

[286] Han, Q.; Veríssimo, N. V.; Bryant, S. J.; Martin, A. V.; Huang, Y.; Pereira, J. F.; Santos-Ebinuma, V. C.; Zhai, J.; Bryant, G.; Drummond, C. J.; et al. Scattering approaches to unravel protein solution behaviors in ionic liquids and deep eutectic solvents: From basic principles to recent developments *Advances in Colloid and Interface Science* **2024** page 103242.

[287] Beck, C.; Grimaldo, M.; Braun, M. K.; Bühl, L.; Matsarskaia, O.; Jalarvo, N. H.; Zhang, F.; Roosen-Runge, F.; Schreiber, F.; Seydel, T. Temperature and salt controlled tuning of protein clusters *Soft Matter* **2021** *17*, 8506–8516.

[288] Mosca, I.; Beck, C.; Jalarvo, N. H.; Matsarskaia, O.; Roosen-Runge, F.; Schreiber, F.; Seydel, T. Continuity of Short-Time Dynamics Crossing the Liquid–Liquid Phase Separation in Charge-Tuned Protein Solutions *The Journal of Physical Chemistry Letters* **2024** *15*, 12051–12059.

[289] Tominaga, T.; Nakagawa, H.; Sahara, M.; Oda, T.; Inoue, R.; Sugiyama, M. Data Collection for Dilute Protein Solutions via a Neutron Backscattering Spectrometer *Life* **2022** *12*, 675.

[290] Beck, C.; Pounot, K.; Mosca, I.; Jalarvo, N. H.; Roosen-Runge, F.; Schreiber, F.; Seydel, T. Notes on Fitting and Analysis Frameworks for QENS Spectra of (Soft) Colloid Suspensions in *EPJ Web of Conferences* volume 272 EDP Sciences **2022** page 01004.

[291] Matsuo, T. An improved analytical model of protein dynamics at the sub-nanosecond timescale *Physical Chemistry Chemical Physics* **2023** *25*, 11586–11600.

[292] Sarter, M.; Stewart, J. R.; Nilsen, G. J.; Devonport, M.; Nemkovski, K. Data Analysis of Dynamics in Protein Solutions Using Quasi-Elastic Neutron Scattering: Important Insights from Polarized Neutrons *Journal of the American Chemical Society* **2024** *146*, 28023–28033.

[293] Lovesey, S. W. *Theory of neutron scattering from condensed matter* Clarendon Press; Oxford (UK) **1984**.

[294] Squires, G. L. *Introduction to the Theory of Thermal Neutron Scattering* Cambridge University Press 3 edition **2012**.

[295] Fernandez-Alonso, F.; Price, D. L. *Neutron Scattering* Academic Press **2013**.

[296] Mosca, I. *Nanosecond timescale confined dynamics of G-Quadruplex DNA as affected by anticancer drugs* (Master's thesis), Università degli Studi di Perugia **2021**.

[297] Watanabe, N. Neutronics of pulsed spallation neutron sources *Reports on Progress in Physics* **2003** *66*, 339.

[298] Mezei, F. The raison d'être of long pulse spallation sources *Journal of Neutron Research* **1997** *6*, 3–32.

[299] Haines, J.; McManamy, T.; Gabriel, T.; Battle, R.; Chipley, K.; Crabtree, J.; Jacobs, L.; Lousteau, D.; Rennich, M.; Riemer, B. Spallation neutron source target station design, development, and commissioning *Nuclear Instruments and Methods in Physics Research Section A: Accelerators, Spectrometers, Detectors and Associated Equipment* **2014** *764*, 94–115.

[300] Ageron, P. Cold neutron sources at ILL *Nuclear Instruments and Methods in Physics Research Section A: Accelerators, Spectrometers, Detectors and Associated Equipment* **1989** *284*, 197–199.

[301] Kirch, K.; Lauss, B.; Schmidt-Wellenburg, P.; Zsigmond, G. Ultracold neutrons—physics and production *Nuclear Physics News* **2010** *20*, 17–23.

[302] Pynn, R. Neutron scattering—a non-destructive microscope for seeing inside matter *Neutron applications in earth, energy and environmental Sciences* **2009** pages 15–36.

[303] Sakai, V. G.; Arbe, A. Quasielastic neutron scattering in soft matter *Current Opinion in Colloid & Interface Science* **2009** *14*, 381–390.

[304] Lechner, R. E. II Instrumentation II. 3 Quasielastic and Inelastic Neutron Scattering *Neutrons in Soft Matter* **2011** *203*.

[305] Bée, M. *Quasielastic neutron scattering* Adam Hilger; Bristol (UK); ISBN 0-85274-371-8 **1988**.

[306] Roosen-Runge, F.; Hennig, M.; Zhang, F.; Jacobs, R. M. J.; Sztucki, M.; Schober, H.; Seydel, T.; Schreiber, F. Protein Self-Diffusion in Crowded Solutions *Proceedings of the National Academy of Sciences* **2011** *108*, 11815—-11820.

[307] Grimaldo, M.; Roosen-Runge, F.; Zhang, F.; Seydel, T.; Schreiber, F. Diffusion and Dynamics of γ-Globulin in Crowded Aqueous Solutions *The Journal of Physical Chemistry B* **2014** *118*, 7203–7209.

[308] Bée, M. A Physical Insight into the Elastic Incoherent Structure Factor *Physica B: Condensed Matter* **1992** *182*, 323–336.

[309] Berrod, Q.; Lagrené, K.; Ollivier, J.; Zanotti, J.-M. Inelastic and quasi-elastic neutron scattering. Application to soft-matter in *EPJ Web of Conferences* volume 188 EDP Sciences **2018** page 05001.

[310] Francesca, N.; Peters, J.; Russo, D.; Barbieri, S.; Chiapponi, C.; Cupane, A.; Deriu, A.; Di Bari, M.; Farhi, E.; Gerelli, Y.; et al. IN13 backscattering spectrometer at ILL: looking for motions in biological macromolecules and organisms *Neutron News* **2008** *19*, 14–18.

[311] Frick, B. Neutron backscattering spectroscopy in *Neutron and X-ray Spectroscopy* pages 483–527 Springer **2006**.

[312] Mamontov, E.; Herwig, K. W. A Time-of-flight Backscattering Spectrometer at the Spallation Neutron Source, BASIS *Review Scientific Instruments* **2011** *82*.

[313] Hennig, M.; Frick, B.; Seydel, T. Optimum velocity of a phase-space transformer for cold-neutron backscattering spectroscopy *Journal of Applied Crystallography* **2011** *44*, 467–472.

[314] Hennig, M. *Dynamics of Globular Proteins in Crowded Electrolyte Solutions. Studied by Neutron Scattering* Ph.D. thesis Universität Tübingen **2011**.

[315] Frick, B.; Mamontov, E.; Van Eijck, L.; Seydel, T. Recent Backscattering Instrument Developments at the ILL and SNS *Zeitschrift für Physikalische Chemie* **2010** *224*, 33–60.

[316] Appel, M.; Frick, B.; Magerl, A. First Results with the Neutron Backscattering and TOF Spectrometer Option BATS on IN16B *Physica B: Condensed Matter* **2019** *562*, 6–8.

[317] Osti, N. C.; Jalarvo, N.; Mamontov, E. Backscattering silicon spectrometer (BASIS): sixteen years in advanced materials characterization *Materials Horizons* **2024** *11*, 4535–4572.

[318] Mezei, F. Neutron spin echo: A new concept in polarized thermal neutron techniques *Zeitschrift für Physik A Hadrons and nuclei* **1972** *255*, 146–160.

[319] Mezei, F.; Pappas, C.; Gutberlet, T. *Neutron spin echo spectroscopy: Basics, trends and applications* volume 601 Springer Science & Business Media **2002**.

[320] Mezei, F. The principles of neutron spin echo in *Neutron Spin Echo: Proceedings of a Laue-Langevin Institut Workshop Grenoble, October 15–16, 1979* Springer **2005** pages 1–26.

[321] Williams, W. G. *Polarized neutrons* 1 Clarendon Press Oxford **1988**.

[322] Farago, B.; Falus, P.; Hoffmann, I.; Gradzielski, M.; Thomas, F.; Gomez, C. The IN15 upgrade *Neutron News* **2015** *26*, 15–17.

[323] Schleger, P.; Alefeld, B.; Barthelemy, J.; Ehlers, G.; Farago, B.; Giraud, P.; Hayes, C.; Kollmar, A.; Lartigue, C.; Mezei, F.; et al. The long-wavelength neutron spin-echo spectrometer IN15 at the Institut Laue-Langevin *Physica B: Condensed Matter* **1997** *241*, 164–165.

[324] Farago, B. Recent neutron spin-echo developments at the ILL (IN11 and IN15) *Physica B: Condensed Matter* **1999** *267*, 270–276.

[325] Feigin, L. A.; Svergun, D. I. *Structure Analysis by Small-Angle X-Ray and Neutron Scattering* Plenum Press, New York **1987**.

[326] Pedersen, J. S. Analysis of Small-Angle Scattering Data from Colloids and Polymer Solutions: Modeling and Least-Squares Fitting *Advances in Colloid and Interface Science* **1997** *70*, 171–210.

[327] Guinier, A.; Fournet, G. *Small-Angle Scattering of X-rays* volume 14 Wiley New York **1955**.

[328] Porod, G. Die Röntgenkleinwinkelstreuung von dichtgepackten kolloiden Systemen - I. Teil *Kolloid-Zeitschrift* **1951** *124*, 83 – 114 cited by: 1627.

[329] Baruchel, J.; Hodeau, J.-L.; Lehmann, M. S.; Regnard, J.-R.; Schlenker, C. *Neutron and synchrotron radiation for condensed matter studies. Volume 1: theory, instruments and methods* Springer-Verlag, Les Editions de Physique **1993**.

[330] Kline, S. R. Reduction and Analysis of SANS and USANS Data Using IGOR Pro *Journal of Applied Crystallography* **2006** *39*, 895–900.

[331] Beck, C. *Protein Dynamics Studied with Neutron Spectroscopy* Ph.D. thesis Universität Tübingen **2020**.

[332] Malcolm, S.; Barton, P.; Murphy, C.; Ferguson-Smith, M.; Bentley, D.; Rabbitts, T. Localization of human immunoglobulin kappa light chain variable region genes to the short arm of chromosome 2 by in situ hybridization. *Proceedings of the National Academy of Sciences* **1982** *79*, 4957–4961.

[333] Erikson, J.; Martinis, J.; Croce, C. M. Assignment of the genes for human λ immunoglobulin chains to chromosome 22 *Nature* **1981** *294*, 173–175.

[334] Molé, C. M.; Béné, M. C.; Montagne, P. M.; Seilles, E.; Faure, G. C. Light chains of immunoglobulins in human secretions *Clinica chimica acta* **1994** *224*, 191–197.

[335] Bräuninger, A.; Goossens, T.; Rajewsky, K.; Küppers, R. Regulation of immunoglobulin light chain gene rearrangements during early B cell development in the human *European Journal of Immunology* **2001** *31*, 3631–3637.

[336] Montaño, R. F.; Morrison, S. L. Influence of the isotype of the light chain on the properties of IgG *The Journal of Immunology* **2002** *168*, 224–231.

[337] Forconi, F.; Sozzi, E.; Rossi, D.; SS, S.; Amato, T.; Raspadori, D.; Trentin, L.; Leoncini, L.; Gaidano, G.; Lauria, F.; et al. Selective influences in the expressed immunoglobulin heavy and light chain gene repertoire in hairy cell leukemia. *haematologica* **2008** *93*, 697–705.

[338] Townsend, C. L.; Laffy, J. M.; Wu, Y.-C. B.; Silva O'Hare, J.; Martin, V.; Kipling, D.; Fraternali, F.; Dunn-Walters, D. K. Significant differences in physicochemical properties of human immunoglobulin kappa and lambda CDR3 regions *Frontiers in Immunology* **2016** *7*, 388.

[339] Raybould, M. I.; Turnbull, O. M.; Suter, A.; Guloglu, B.; Deane, C. M. Contextualising the developability risk of antibodies with lambda light chains using enhanced therapeutic antibody profiling *Communications Biology* **2024** *7*, 62.

[340] Topală, T.; Bodoki, A.; Oprean, L.; Oprean, R. Bovine serum albumin interactions with metal complexes *Clujul medical* **2014** *87*, 215.

[341] Hill, P.; MacMillan, R. C.; Lee, V. A fundamental equation of state for heavy water *Journal of Physical and Chemical Reference Data* **1982** *11*, 1–14.

[342] Cho, C. H.; Urquidi, J.; Singh, S.; Robinson, G. W. Thermal Offset Viscosities of Liquid H2O, D2O, and T2O *The Journal of Physical Chemistry B* **1999** *103*, 1991–1994.

[343] Susi, H.; Timasheff, S. N.; Stevens, L. Infrared spectra and protein conformations in aqueous solutions: I. The amide I band in H2O and D2O solutions *Journal of Biological Chemistry* **1967** *242*, 5460–5466.

[344] Efimova, Y.; Haemers, S.; Wierczinski, B.; Norde, W.; Well, A. v. Stability of globular proteins in H2O and D2O *Biopolymers: Original Research on Biomolecules* **2007** *85*, 264–273.

[345] Giubertoni, G.; Bonn, M.; Woutersen, S. D2O as an imperfect replacement for H2O: Problem or opportunity for protein research? *The Journal of Physical Chemistry B* **2023** *127*, 8086–8094.

[346] Braun, M. K.; Wolf, M.; Matsarskaia, O.; Da Vela, S.; Roosen-Runge, F.; Sztucki, M.; Roth, R.; Zhang, F.; Schreiber, F. Strong Isotope Effects on Effective Interactions and Phase Behavior in Protein Solutions in the Presence of Multivalent Ions *J. Phys. Chem. B* **2017** *121*, 1731–1739.

[347] Zbacnik, T. J.; Holcomb, R. E.; Katayama, D. S.; Murphy, B. M.; Payne, R. W.; Coccaro, R. C.; Evans, G. J.; Matsuura, J. E.; Henry, C. S.; Manning, M. C. Role of buffers in protein formulations *Journal of Pharmaceutical Sciences* **2017** *106*, 713–733.

[348] Wang, S. S.; Yan, Y. S.; Ho, K. US FDA-Approved Therapeutic Antibodies with High-Concentration Formulation: Summaries and Perspectives *Antibody Therapeutics* **2021** *4*, 262–272.

[349] Cock, P. J. A.; Antao, T.; Chang, J. T.; Chapman, B. A.; Cox, C. J.; Dalke, A.; Friedberg, I.; Hamelryck, T.; Kauff, F.; Wilczynski, B.; de Hoon, M. J. L. Biopython: freely available Python tools for computational molecular biology and bioinformatics *Bioinformatics* **2009** *25*, 1422–1423.

[350] Gasteiger, E.; Hoogland, C.; Gattiker, A.; Duvaud, S.; Wilkins, M. R.; Appel, R. D.; Bairoch, A. *Protein Identification and Analysis Tools on the Expasy Server", in "The Proteomics Protocols Handbook* John M. Walker, Humana Press **2005**.

[351] Lobry, J.; Gautier, C. Hydrophobicity, expressivity and aromaticity are the major trends of amino-acid usage in 999 Escherichia coli chromosome-encoded genes *Nucleic Acids Research* **1994** *22*, 3174–3180.

[352] Kyte, J.; Doolittle, R. F. A simple method for displaying the hydropathic character of a protein *Journal of Molecular Biology* **1982** *157*, 105–132.

[353] Guruprasad, K.; Reddy, B.; Pandit, M. W. Correlation between stability of a protein and its dipeptide composition: a novel approach for predicting in vivo stability of a protein from its primary sequence *Protein Engineering, Design and Selection* **1990** *4*, 155–161.

[354] Consortium, U. UniProt: a hub for protein information *Nucleic acids Research* **2015** *43*, D204–D212.

[355] Humphrey, W.; Dalke, A.; Schulten, K. VMD – Visual Molecular Dynamics *Journal of Molecular Graphics* **1996** *14*, 33–38.

[356] Larkin, M. A.; Blackshields, G.; Brown, N. P.; Chenna, R.; McGettigan, P. A.; McWilliam, H.; Valentin, F.; Wallace, I. M.; Wilm, A.; Lopez, R.; et al. Clustal W and Clustal X version 2.0 *Bioinfformatics* **2007** *23*, 2947–2948.

[357] Dunbar, J.; Krawczyk, K.; Leem, J.; Marks, C.; Nowak, J.; Regep, C.; Georges, G.; Kelm, S.; Popovic, B.; Deane, C. M. SAbPred: a structure-based antibody prediction server *Nucleic Acids Research* **2016** *44*, W474–W478.

[358] Dunbar, J.; Krawczyk, K.; Leem, J.; Baker, T.; Fuchs, A.; Georges, G.; Shi, J.; Deane, C. M. SAbDab: the structural antibody database *Nucleic Acids Research* **2013** *42*, D1140–D1146.

[359] Dunbar, J.; Fuchs, A.; Shi, J.; Deane, C. ABangle: characterising the VH–VL orientation in antibodies *Protein Engineering, Design and Selection* **2013** *26*, 611–620.

[360] Abanades, B.; Georges, G.; Bujotzek, A.; Deane, C. M. ABlooper: fast accurate antibody CDR loop structure prediction with accuracy estimation *Bioinformatics* **2022** *38*, 1877–1880.

[361] Raybould, M. I.; Marks, C.; Lewis, A. P.; Shi, J.; Bujotzek, A.; Taddese, B.; Deane, C. M. Thera-SAbDab: the therapeutic structural antibody database *Nucleic acids Research* **2020** *48*, D383–D388.

[362] Raybould, M. I.; Marks, C.; Krawczyk, K.; Taddese, B.; Nowak, J.; Lewis, A. P.; Bujotzek, A.; Shi, J.; Deane, C. M. Five computational developability guidelines for therapeutic antibody profiling *Proceedings of the National Academy of Sciences* **2019** *116*, 4025–4030.

[363] Acrivos, A. Non-Newtonian Fluids: Rheometry *Science* **1976** *191*, 942–942.

[364] *https://www.rheosense.com/technology*.

[365] Sutera, S. P.; Skalak, R. The History of Poiseuille's Law *Annual Review of Fluid Mechanics* **1993** *25*, 1–20.

[366] Stokes, G. G. On the Theories of the Internal Friction of Fluids in Motion, and of the Equilibrium and Motion of Elastic Solids in *Classics of Elastic Wave Theory* Society of Exploration Geophysicists **2007**.

[367] Macosko, C. W. *Rheology: Principles, Measurements, and Applications* VCH Publishers, Inc. **1994**.

[368] Pipe, C. J.; Majmudar, T. S.; McKinley, G. H. High Shear Rate Viscometry *Rheologica Acta* **2008** *47*, 621–642.

[369] Sievers, F.; Wilm, A.; Dineen, D.; Gibson, T. J.; Karplus, K.; Li, W.; Lopez, R.; McWilliam, H.; Remmert, M.; Söding, J.; et al. Fast, scalable generation of high-quality protein multiple sequence alignments using Clustal Omega *Molecular Systems Biology* **2011** *7*, 539.

[370] Sievers, F.; Higgins, D. G. The clustal omega multiple alignment package *Multiple sequence alignment: Methods and protocols* **2021** pages 3–16.

[371] Cock, P. J.; Antao, T.; Chang, J. T.; Chapman, B. A.; Cox, C. J.; Dalke, A.; Friedberg, I.; Hamelryck, T.; Kauff, F.; Wilczynski, B.; et al. BioPython: Freely Available Python Tools for Computational Molecular Biology and Bioinformatics *Bioinformatics* **2009** *25*, 1422–1423.

[372] Lonberg, N. Human antibodies from transgenic animals *Nature Biotechnology* **2005** *23*, 1117–1125.

[373] Mullard, A. FDA Approves 100th Monoclonal Antibody Product *Nature Reviews Drug Discovery* **2021** *20*, 491–495.

[374] Hongrong Cai, H.; Pandit, A. A. Therapeutic Monoclonal Antibodies Approved by FDA in 2022 (Mini Review). *Journal of Clinical and Experimental Immunology* **2023** *8*, 533–535.

[375] Castelli, M. S.; McGonigle, P.; Hornby, P. J. The Pharmacology and Therapeutic Applications of Monoclonal Antibodies *Pharmacology Research & Perspectives* **2019** *7*, e00535.

[376] Vidarsson, G.; Dekkers, G.; Rispens, T. IgG Subclasses and Allotypes: from Structure to Effector Functions *Frontiers in Immunology* **2014** *5*, 520.

[377] Humphrey, W.; Dalke, A.; Schulten, K. VMD: Visual Molecular Dynamics *Journal of Molecular Graphics* **1996** *14*, 33–38.

[378] Eargle, J.; Wright, D.; Luthey-Schulten, Z. Multiple Alignment of protein structures and sequences for VMD *Bioinformatics* **2006** *22*, 504–506.

[379] Huber, R.; Deisenhofer, J.; Colman, P. M.; Matsushima, M.; Palm, W. Crystallographic Structure Studies of an IgG Molecule and an Fc Fragment *Nature* **1976** *264*, 415–420.

[380] Saphire, E. O.; Parren, P. W.; Pantophlet, R.; Zwick, M. B.; Morris, G. M.; Rudd, P. M.; Dwek, R. A.; Stanfield, R. L.; Burton, D. R.; Wilson, I. A. Crystal Structure of a Neutralizing Human IgG Against HIV-1: a Template for Vaccine Design *Science* **2001** *293*, 1155–1159.

[381] Keizer, R. J.; Huitema, A. D.; Schellens, J. H.; Beijnen, J. H. Clinical Pharmacokinetics of Therapeutic Monoclonal Antibodies *Clinical Pharmacokinetics* **2010** *49*, 493–507.

[382] Dear, B. J.; Hung, J. J.; Laber, J. R.; Wilks, L. R.; Sharma, A.; Truskett, T. M.; Johnston, K. P. Enhancing Stability and Reducing Viscosity of a Monoclonal Antibody With Cosolutes by Weakening Protein-Protein Interactions *Journal of Pharmaceutical Sciences* **2019** *108*, 2517–2526.

[383] Li, L.; Kumar, S.; Buck, P. M.; Burns, C.; Lavoie, J.; Singh, S. K.; Warne, N. W.; Nichols, P.; Luksha, N.; Boardman, D. Concentration dependent Viscosity of Monoclonal Antibody Solutions: Explaining Experimental Behavior in terms of Molecular Properties *Pharmaceutical Research* **2014** *31*, 3161–3178.

[384] Tomar, D. S.; Li, L.; Broulidakis, M. P.; Luksha, N. G.; Burns, C. T.; Singh, S. K.; Kumar, S. In-Silico Prediction of Concentration-Dependent Viscosity Curves for Monoclonal Antibody Solutions *mAbs* **2017** *9*, 476–489.

[385] Apgar, J. R.; Tam, A. S.; Sorm, R.; Moesta, S.; King, A. C.; Yang, H.; Kelleher, K.; Murphy, D.; D'Antona, A. M.; Yan, G.; et al. Modeling and Mitigation of High-Concentration Antibody Viscosity through Structure-Based Computer-Aided Protein Design *Public Library of Science one* **2020** *15*, e0232713.

[386] Sharma, V. K.; Patapoff, T. W.; Kabakoff, B.; Pai, S.; Hilario, E.; Zhang, B.; Li, C.; Borisov, O.; Kelley, R. F.; Chorny, I.; Zhou, J. Z.; Dill, K. A.; Swartz, T. E. In Silico Selection of Therapeutic Antibodies for Development: Viscosity, Clearance, and Chemical Stability *Proceedings of the National Academy of Sciences* **2014** *111*, 18601–18606.

[387] Lai, P.-K.; Swan, J. W.; Trout, B. L. Calculation of Therapeutic Antibody Viscosity with Coarse-Grained Models, Hydrodynamic Calculations and Machine Learning-Based Parameters *Mabs* **2021** *13*, 1907882 pMID: 33834944.

[388] Lai, P.-K.; Gallegos, A.; Mody, N.; Sathish, H. A.; Trout, B. L. Machine Learning Prediction of Antibody aggregation and Viscosity for High Concentration Formulation Development of Protein Therapeutics *Mabs* **2022** *14*, 2026208 pMID: 35075980.

[389] Blanco, M. A. Computational Models for Studying Physical Instabilities in High Concentration Biotherapeutic Formulations *Mabs* **2022** *14*, 2044744 pMID: 35282775.

[390] Forder, J. K.; Ilott, A. J.; Sahin, E.; Roberts, C. J. Simulation of High-Concentration Self-Interactions for Monoclonal Antibodies from Well-Behaved to Poorly-Behaved Systems *AIChE Journal* **2023** *69*, e17965.

[391] Da Vela, S.; Roosen-Runge, F.; Skoda, M. W.; Jacobs, R. M.; Seydel, T.; Frielinghaus, H.; Sztucki, M.; Schweins, R.; Zhang, F.; Schreiber, F. Effective Interactions and Colloidal Stability of Bovine γ-Globulin in Solution *The Journal of Physical Chemistry B* **2017** *121*, 5759–5769.

[392] Girelli, A.; Rahmann, H.; Begam, N.; Ragulskaya, A.; Reiser, M.; Chandran, S.; Westermeier, F.; Sprung, M.; Zhang, F.; Gutt, C.; Schreiber, F. Microscopic Dynamics of Liquid-Liquid Phase Separation and Domain Coarsening in a Protein Solution Revealed by X-Ray Photon Correlation Spectroscopy *Physical Review Letters* **2021** *126*.

[393] Ruane, S.; Li, Z.; Hollowell, P.; Hughes, A.; Warwicker, J.; Webster, J. R. P.; van der Walle, C. F.; Kalonia, C.; Lu, J. R. Investigating the Orientation of an Interfacially Adsorbed Monoclonal Antibody and Its Fragments Using Neutron Reflection *Molecular Pharmaceutics* **2023** *20*, 1643–1656 pMID: 36795985.

[394] Scarcelli, J. J.; Shang, T. Q.; Iskra, T.; Allen, M. J.; Zhang, L. Strategic Deployment of CHO Expression Platforms to Deliver Pfizer's Monoclonal Antibody Portfolio *Biotechnology Progress* **2017** *33*, 1463–1467.

[395] L. Colin; C. Beck; A. Girelli; C. Grapentin; O. Matsarskaia; K. Pounot; F. Schreiber; T. Seydel Dynamic Cluster Formation, Viscosity, and Diffusion in Monoclonal Antibody Solutions Depending on Antibody Type and Crowding **2021** ILL data, DOI: 10.5291/ILL-DATA.8-04-908.

[396] Arnold, O.; Bilheux, J.-C.; Borreguero, J.; Buts, A.; Campbell, S. I.; Chapon, L.; Doucet, M.; Draper, N.; Leal, R. F.; Gigg, M.; et al. Mantid—Data Analysis and Visualization Package for Neutron Scattering and μ SR Experiments *Nuclear instruments and Methods in Physics Research section A: accelerators, spectrometers, detectors and associated equipment* **2014** *764*, 156–166.

[397] Beck, C.; Pounot, K.; Mosca, I.; Jalarvo, N. H.; Roosen-Runge, F.; Schreiber, F.; Seydel, T. Notes on Fitting and Analysis Frameworks for QENS Spectra of (Soft) Colloid Suspensions *EPJ Web of Conferences* **2022** *272*, 01004.

[398] Beck, C.; Grimaldo, M.; Roosen-Runge, F.; Braun, M. K.; Zhang, F.; Schreiber, F.; Seydel, T. Nanosecond Tracer Diffusion as a Probe of The Solution Structure and Molecular Mobility of Protein Assemblies: The Case of Ovalbumin *The Journal of Physical Chemistry B* **2018** *122*, 8343–8350.

[399] Fitter, J. Confined Molecular Motions of Globular Proteins Studied in Powder Samples and in Solution *Le Journal de Physique IV* **2000** *10*, Pr7–265.

[400] Lindner, P.; Schweins, R. The D11 Small-Angle Scattering Instrument: A New Benchmark for SANS *Neutron News* **2010** *21*, 15–18.

[401] Klosowski, P.; Könnecke, M.; Tischler, J.; Osborn, R. NeXus: A Common Format for the Exchange of Neutron and Synchrotron Data *Physica B: Condensed Matter* **1997** *241-243*, 151–153 Proceedings of the International Conference on Neutron Scattering.

[402] Könnecke, M.; Akeroyd, F. A.; Bernstein, H. J.; Brewster, A. S.; Campbell, S. I.; Clausen, B.; Cottrell, S.; Hoffmann, J. U.; Jemian, P. R.; Männicke, D.; et al. The NeXus Data Format *Journal of Applied Crystallography* **2015** *48*, 301–305.

[403] L. Colin; C. Beck; C. Buchholz; C. Grapentin; O. Matsarskaia; I. Mosca; K. Pounot; L. Reichart; F. Schreiber; T. Seydel Tunable Equilibrium Monoclonal Antibody Nanocluster Dispersions at High Concentrations **2021** ILL data, DOI: 10.5291/ILL-DATA.8-04-923.

[404] Phillips, J. C.; Braun, R.; Wang, W.; Gumbart, J.; Tajkhorshid, E.; Villa, E.; Chipot, C.; Skeel, R. D.; Kale, L.; Schulten, K. Scalable Molecular Dynamics with NAMD *Journal of Computational Chemistry* **2005** *26*, 1781–1802.

[405] Huang, J.; MacKerell Jr, A. D. CHARMM36 All-Atom Additive Protein Force Field: Validation Based on Comparison to NMR data *Journal of Computational Chemistry* **2013** *34*, 2135–2145.

[406] Huang, J.; Rauscher, S.; Nawrocki, G.; Ran, T.; Feig, M.; De Groot, B. L.; Grubmüller, H.; MacKerell, A. D. CHARMM36m: An Improved Force Field for Folded and Intrinsically Disordered Proteins *Nature Methods* **2017** *14*, 71–73.

[407] Mark, P.; Nilsson, L. Structure and Dynamics of the TIP3P, SPC, and SPC/E Water Models at 298 K *The Journal of Physical Chemistry A* **2001** *105*, 9954–9960.

[408] Martyna, G. J.; Tobias, D. J.; Klein, M. L. Constant Pressure Molecular Dynamics Algorithms *The Journal of Chemical Physics* **1994** *101*, 4177–4189.

[409] Ryckaert, J.-P.; Ciccotti, G.; Berendsen, H. J. Numerical Integration of the Cartesian Equations of Motion of A System With Constraints: Molecular Dynamics of N-Alkanes *Journal of Computational Physics* **1977** *23*, 327–341.

[410] Grubmüller, H.; Heller, H.; Windemuth, A.; Schulten, K. Generalized Verlet algorithm for Efficient Molecular Dynamics Simulations with long-range Interactions *Molecular Simulation* **1991** *6*, 121–142.

[411] Tuckerman, M.; Berne, B. J.; Martyna, G. J. Reversible Multiple Time scale Molecular Dynamics *the Journal of Chemical Physics* **1992** *97*, 1990–2001.

[412] Essmann, U.; Perera, L.; Berkowitz, M. L.; Darden, T.; Lee, H.; Pedersen, L. G. A smooth particle mesh Ewald method *The Journal of Chemical Physics* **1995** *103*, 8577–8593.

[413] Wells, B. A.; Chaffee, A. L. Ewald Summation for Molecular Simulations *Journal of Chemical Theory and Computation* **2015** *11*, 3684–3695.

[414] Grossfield, A.; Patrone, P. N.; Roe, D. R.; Schultz, A. J.; Siderius, D. W.; Zuckerman, D. M. Best Practices for Quantification of Uncertainty and Sampling Quality in Molecular Simulations [Article v1. 0] *Living Journal of Computational Molecular Science* **2018** *1*.

[415] Jurrus, E.; Engel, D.; Star, K.; Monson, K.; Brandi, J.; Felberg, L. E.; Brookes, D. H.; Wilson, L.; Chen, J.; Liles, K.; et al. Improvements to The APBS Biomolecular Solvation Software Suite *Protein Science* **2018** *27*, 112–128.

[416] Olsson, M. H.; Søndergaard, C. R.; Rostkowski, M.; Jensen, J. H. PROPKA3: Consistent Treatment of Internal and Surface Residues in Empirical pKa Predictions *Journal of Chemical Theory and Computation* **2011** *7*, 525–537.

[417] Abraham, M. J.; Murtola, T.; Schulz, R.; Páll, S.; Smith, J. C.; Hess, B.; Lindahl, E. GROMACS: High Performance Molecular Simulations through Multi-Level Parallelism from Laptops to Supercomputers *SoftwareX* **2015** *1–2*, 19–25.

[418] Páll, S.; Abraham, M. J.; Kutzner, C.; Hess, B.; Lindahl, E. Tackling Exascale Software Challenges in Molecular Dynamics Simulations with GROMACS in S. Markidis; E. Laure, editors, *Solving Software Challenges for Exascale* Lecture Notes in Computer Science Springer International Publishing, Cham **2015** pages 3–27.

[419] Chen, P.-c.; Hub, J. S. Validating Solution Ensembles from Molecular Dynamics Simulation by Wide-Angle X-Ray Scattering Data *Biophysical Journal* **2014** *107*, 435–447.

[420] Michaud-Agrawal, N.; Denning, E. J.; Woolf, T. B.; Beckstein, O. MDAnalysis: A Toolkit for the Analysis of Molecular Dynamics Simulations *Journal of Computational Chemistry* **2011** *32*, 2319–2327.

[421] Gowers, R. J.; Linke, M.; Barnoud, J.; Reddy, T. J. E.; Melo, M. N.; Seyler, S. L.; Domański, J.; Dotson, D. L.; Buchoux, S.; Kenney, I. M.; Beckstein, O. MDAnalysis: A Python Package for the Rapid Analysis of Molecular Dynamics Simulations *Proceedings of the 15th Python in Science Conference* **2016** pages 98–105.

[422] Hagberg, A. A.; Schult, D. A.; Swart, P. J. Exploring Network Structure, Dynamics, and Function Using NetworkX in G. Varoquaux; T. Vaught; J. Millman, editors, *Proceedings of the 7th Python in Science Conference* Pasadena, CA USA **2008** pages 11–15.

[423] Roosen-Runge, F.; Schurtenberger, P.; Stradner, A. Self-Diffusion of Nonspherical Particles Fundamentally Conflicts With Effective Sphere Models *Journal of Physics: Condensed Matter* **2021** *33*, 154002.

[424] Harris, L. J.; Larson, S. B.; Hasel, K. W.; McPherson, A. Refined Structure of an Intact IgG2a Monoclonal Antibody, *Biochemistry* **1997** *36*, 1581–1597.

[425] Bonner, A.; Furtado, P. B.; Almogren, A.; Kerr, M. A.; Perkins, S. J. Implications of the Near-Planar Solution Structure of Human Myeloma Dimeric IgA1 for Mucosal Immunity and IgA Nephropathy *The Journal of Immunology* **2008** *180*, 1008–1018.

[426] Pedregosa, F.; Varoquaux, G.; Gramfort, A.; Michel, V.; Thirion, B.; Grisel, O.; Blondel, M.; Prettenhofer, P.; Weiss, R.; Dubourg, V.; Vanderplas, J.; Passos, A.; Cournapeau, D.; Brucher, M.; Perrot, M.; Duchesnay, E. Scikit-learn: Machine Learning in Python *Journal of Machine Learning Research* **2011** *12*, 2825–2830.

[427] Lindner, P.; Zemb, T. *Neutrons, X-rays, and Light: Scattering Methods Applied to Soft Condensed Matter* Elsevier North-Holland **2002**.

[428] Debye, P. Zerstreuung von Röntgenstrahlen *Ann. Phys.* **1915** *351*, 809–823.

[429] Hansen, J.-P.; McDonald, I. R. *Theory of simple liquids* Academic Press Amsterdam 3rd edition **2006**.

[430] Svergun, D. I.; Koch, M. H. J. Small-Angle Scattering Studies of Biological Macromolecules in Solution *Rep. Prog. Phys.* **2003** *66*, 1735–1782.

[431] Gunton, J.; Shiryayev, A.; Pagan, D. *Protein Condensation: Kinetic Pathways to Crystallization and Disease* Cambridge University Press **2007**.

[432] Schärtl, W. *Light Scattering from Polymer Solutions and Nanoparticle Dispersions* Springer **2007**.

[433] Noro, M. G.; Frenkel, D. Extended corresponding-states behavior for particles with variable range attractions *Journal of Chemical Physics* **2000** *113*, 2941–2944.

[434] Bonneté, F.; Vivarès, D. Interest of the Normalized Second Virial Coefficient and Interaction Potentials for Crystallizing Large Macromolecules *Acta Crystallographica D* **2002** *58*, 1571–1575.

[435] von Bülow, S.; Siggel, M.; Linke, M.; Hummer, G. Dynamic cluster Formation Determines Viscosity and Diffusion in Dense Protein Solutions *Proceedings of the National Academy of Sciences* **2019** *116*, 9843–9852.

[436] Harris, L. J.; Skaletsky, E.; McPherson, A. Crystallographic Structure of an Intact IgG1 Monoclonal Antibody *Journal of Molecular Biology* **1998** *275*, 861–872.

[437] Kayentao, K.; Ongoiba, A.; Preston, A. C.; Healy, S. A.; Hu, Z.; Skinner, J.; Doumbo, S.; Wang, J.; Cisse, H.; Doumtabe, D.; et al. Subcutaneous Administration of a Monoclonal Antibody to Prevent Malaria *New England Journal of Medicine* **2024** *390*, 1549–1559.

[438] Cummings, J.; Osse, A. M. L.; Cammann, D.; Powell, J.; Chen, J. Anti-amyloid monoclonal antibodies for the treatment of Alzheimer's disease *BioDrugs* **2024** *38*, 5–22.

[439] Jogdeo, C. M.; Bhattacharya, D. S.; Lin, V.; Kolhe, P.; Badkar, A. Assessing physicochemical Stability of monoclonal antibodies in a simulated subcutaneous environment *Journal of Pharmaceutical Sciences* **2024**.

[440] Andya, J. D.; Liu, J.; Shire, S. J. Analysis of irreversible aggregation, reversible self-association and fragmentation of monoclonal antibodies by analytical ultracentrifugation *Current Trends in monoclonal antibody development and manufacturing* **2010** pages 207–227.

[441] Pang, K. T.; Yang, Y. S.; Zhang, W.; Ho, Y. S.; Sormanni, P.; Michaels, T. C.; Walsh, I.; Chia, S. Understanding and controlling the molecular mechanisms of protein aggregation in mAb therapeutics *Biotechnology Advances* **2023** *67*, 108192.

[442] Lao, Z.; Tang, Y.; Dong, X.; Tan, Y.; Li, X.; Liu, X.; Li, L.; Guo, C.; Wei, G. Elucidating the reversible and irreversible self-assembly mechanisms of low-complexity aromatic-rich kinked peptides and steric zipper peptides *Nanoscale* **2024** *16*, 4025–4038.

[443] Sukumar, M.; Doyle, B. L.; Combs, J. L.; Pekar, A. H. Opalescent appearance of an IgG1 antibody at high concentrations and its relationship to noncovalent association *Pharmaceutical Research* **2004** *21*, 1087–1093.

[444] Salinas, B. A.; Sathish, H. A.; Bishop, S. M.; Harn, N.; Carpenter, J. F.; Randolph, T. W. Understanding and modulating opalescence and viscosity in a monoclonal antibody formulation *Journal of Pharmaceutical Sciences* **2010** *99*, 82–93.

[445] Mason, B. D.; Zhang, L.; Remmele Jr, R. L.; Zhang, J. Opalescence of an IgG2 monoclonal antibody solution as it relates to liquid–liquid phase separation *Journal of Pharmaceutical Sciences* **2011** *100*, 4587–4596.

[446] Arora, J.; Hu, Y.; Esfandiary, R.; Sathish, H. A.; Bishop, S. M.; Joshi, S. B.; Middaugh, C. R.; Volkin, D. B.; Weis, D. D. Charge-mediated Fab-Fc interactions in an IgG1 antibody induce reversible self-association, cluster formation, and elevated viscosity in *mAbs* volume 8, 8 Taylor & Francis **2016** pages 1561–1574.

[447] Nakauchi, Y.; Nishinami, S.; Murakami, Y.; Ogura, T.; Kano, H.; Shiraki, K. Opalescence Arising from Network Assembly in Antibody Solution *Molecular Pharmaceutics* **2022** *19*, 1160–1167.

[448] Lai, P.-K.; Ghag, G.; Yu, Y.; Juan, V.; Fayadat-Dilman, L.; Trout, B. L. Differences in human IgG1 and IgG4 S228P monoclonal antibodies viscosity and self-interactions: Experimental assessment and computational predictions of domain interactions in *mAbs* volume 13, 1 Taylor & Francis **2021** page 1991256.

[449] Li, M.; Wang, Y.; Tao, F.; Xu, P.; Zhang, S. QTY code designed antibodies for aggregation prevention: A structural bioinformatic and computational study *Proteins: Structure, Function, and Bioinfformatics* **2024** *92*, 206–218.

[450] Saurabh, S.; Zhang, Q.; Seddon, J. M.; Lu, J. R.; Kalonia, C.; Bresme, F. Unraveling the Microscopic Mechanism of Molecular Ion Interaction with Monoclonal Antibodies: Impact on Protein Aggregation *Molecular Pharmaceutics* **2024** *21*, 1285–1299.

[451] Brudar, S.; Breydo, L.; Chung, E.; Dill, K. A.; Ehterami, N.; Phadnis, K.; Senapati, S.; Shameem, M.; Tang, X.; Tayyab, M.; et al. Antibody association in solution: cluster distributions and mechanisms in *mAbs* volume 16, 1 Taylor & Francis **2024** page 2339582.

[452] Zhai, Y.; Martys, N. S.; George, W. L.; Curtis, J. E.; Nayem, J.; Liu, Y.; et al. Intermediate scattering functions of a rigid body monoclonal antibody protein in solution studied by dissipative particle dynamic simulation *Structural Dynamics* **2021** *8*.

[453] Sohmen, B.; Beck, C.; Frank, V.; Seydel, T.; Hoffmann, I.; Hermann, B.; Nüesch, M.; Grimaldo, M.; Schreiber, F.; Wolf, S.; et al. The Onset of Molecule-Spanning Dynamics in Heat Shock Protein Hsp90 *Advanced Science* **2023** *10*, 2304262.

[454] Aalberse, R. C.; Schuurman, J. IgG4 breaking the rules *Immunology* **2002** *105*, 9–19.

[455] Newman, R.; Hariharan, K.; Reff, M.; Anderson, D. R.; Braslawsky, G.; Santoro, D.; Hanna, N.; Bugelski, P. J.; Brigham-Burke, M.; Crysler, C.; et al. Modification of the Fc region of a primatized IgG antibody to human CD4 retains its ability to modulate CD4 receptors but does not deplete CD4+ T cells in chimpanzees *Clinical Immunology* **2001** *98*, 164–174.

[456] Roux, K. H.; Strelets, L.; Michaelsen, T. E. Flexibility of human IgG subclasses. *Journal of Immunology (Baltimore, Md.: 1950)* **1997** *159*, 3372–3382.

[457] Shambesh, M.; Craig, P.; Wen, H.; Rogan, M.; Paolillo, E. IgG1 and IgG4 serum antibody responses in asymptomatic and clinically expressed cystic echinococcosis patients *Acta tropica* **1997** *64*, 53–63.

[458] Neergaard, M. S.; Kalonia, D. S.; Parshad, H.; Nielsen, A. D.; Møller, E. H.; Van De Weert, M. Viscosity of high concentration protein formulations of monoclonal antibodies of the IgG1 and IgG4 subclass–Prediction of viscosity through protein–protein interaction measurements *European Journal of Pharmaceutical Sciences* **2013** *49*, 400–410.

[459] Covington, A. K.; Paabo, M.; Robinson, R. A.; Bates, R. G. Use of the glass electrode in deuterium oxide and the relation between the standardized pd (pad) scale and the operational ph in heavy water *Analytical Chemistry* **1968** *40*, 700–706.

[460] Hoffmann, I. Data Analysis and Background Subtraction in Neutron Spin Echo Spectroscopy *Frontiers in Physics* **2021** *8*.

[461] Dewhurst, C. D. Graphical reduction and analysis small-angle neutron scattering program: *GRASP Journal of Applied Crystallography* **2023** *56*, 1595–1609.

[462] Kingsbury, J. S.; Saini, A.; Auclair, S. M.; Fu, L.; Lantz, M. M.; Halloran, K. T.; Calero-Rubio, C.; Schwenger, W.; Airiau, C. Y.; Zhang, J.; Gokarn, Y. R. A single Molecular descriptor to predict solution behavior of therapeutic antibodies *Science Advances* **2020** *6*, eabb0372.

[463] Biehl, R. Jscatter, a program for evaluation and analysis of experimental data *PLoS One* **2019** *14*, e0218789.

[464] Raut, A. S.; Kalonia, D. S. Liquid–Liquid phase separation in a dual variable domain immunoglobulin protein solution: effect of formulation factors and protein–protein interactions *Molecular Pharmaceutics* **2015** *12*, 3261–3271.

[465] Yang, T.-C.; Langford, A. J.; Kumar, S.; Ruesch, J. C.; Wang, W. Trimerization dictates solution opalescence of a monoclonal antibody *Journal of Pharmaceutical Sciences* **2016** *105*, 2328–2337.

[466] Natesan, R.; Agrawal, N. J. Non-covalent Fc-Fab interactions significantly alter internal dynamics of an IgG1 antibody *Scientific Reports* **2022** *12*, 9321.

[467] Ragheb, R.; Nobbmann, U. Multiple scattering effects on intercept, size, polydispersity index, and intensity for parallel (VV) and perpendicular (VH) polarization detection in photon correlation spectroscopy *Scientific Reports* **2020** *10*, 21768.

[468] Odhner, H.; Jacobs, D. Refractive index of liquid D2O for visible wavelengths *Journal of Chemical & Engineering Data* **2012** *57*, 166–168.

[469] Bhandari, K.; Wei, Y.; Amer, B. R.; Pelegri-O'Day, E. M.; Huh, J.; Schmit, J. D. Prediction of Antibody Viscosity from Dilute Solution Measurements *Antibodies* **2023** *12*.

[470] Mosca, I.; Beck, C.; Grapentin, C.; Grundel, A.; Hoffmann, I.; Matsarskaia, O.; Nasro, R.; Pounot, K.; Schreiber, F.; Seydel, T. Differences between monoclonal antibodies: Viscosity, diffusion, and transient cluster formation. **2023** dOI: 10.5291/ILL-DATA.8-04-932.

[471] Nishi, H.; Miyajima, M.; Nakagami, H.; Noda, M.; Uchiyama, S.; Fukui, K. Phase separation of an IgG1 antibody solution under a low ionic strength condition *Pharmaceutical Research* **2010** *27*, 1348–1360.

[472] Reiche, K.; Hartl, J.; Blume, A.; Garidel, P. Liquid-liquid phase separation of a monoclonal antibody at low ionic strength: Influence of anion charge and concentration *Biophysical Chemistry* **2017** *220*, 7–19.

[473] Mason, B. D.; Zhang-van Enk, J.; Zhang, L.; Remmele, R. L.; Zhang, J. Liquid-Liquid Phase Separation of a Monoclonal Antibody and Nonmonotonic Influence of Hofmeister Anions *Biophysical Journal* **2010** *99*, 3792–3800.

[474] Wang, Y.; Lomakin, A.; Latypov, R. F.; Benedek, G. B. Phase Separation in Solutions of Monoclonal Antibodies and the Effect of Human Serum Albumin *Proceedings of the National Academy of Sciences* **2011** *108*, 16606–16611.

[475] Rogers, B. A.; Rembert, K. B.; Poyton, M. F.; Okur, H. I.; Kale, A. R.; Yang, T.; Zhang, J.; Cremer, P. S. A stepwise mechanism for aqueous two-phase system formation in concentrated antibody solutions *Proceedings of the National Academy of Sciences* **2019** *116*, 15784–15791.

[476] Rehman, S. U.; Nadeem, A.; Javed, M.; Hassan, F.-u.; Luo, X.; Khalid, R. B.; Liu, Q. Genomic identification, evolution and sequence analysis of the heat-shock protein gene family in buffalo *Genes* **2020** *11*, 1388.

[477] Schrödinger, L.; DeLano, W. PyMOL.

[478] ten Wolde, P. R.; Frenkel, D. Enhancement of Protein Crystal Nucleation by Critical Density Fluctuations *Science* **1997** *277*, 1975–1978.

[479] Anderson, V. J.; Lekkerkerker, H. N. Insights Into Phase Transition Kinetics from Colloid Science *Nature* **2002** *416*, 811–815.

[480] Benedek, G. B. Cataract as a Protein Condensation Disease: the Proctor Lecture *Investigative Ophthalmology & Visual Science* **1997** *38*, 1911–1921.

[481] Chen, Z.; Huai, Y.; Mao, W.; Wang, X.; Ru, K.; Qian, A.; Yang, H. Liquid–liquid Phase Separation of Biomacromolecules and Its Roles in Metabolic Diseases *Cells* **2022** *11*, 3023.

[482] Yu, S.; Chen, W.; Liu, G.; Flores, B.; DeWolf, E. L.; Fan, B.; Xiang, Y.; Webber, M. J. Glucose-Driven Droplet Formation in Complexes of a Supramolecular Peptide and Therapeutic Protein *J. Am. Chem. Society* **2024** *146*, 7498–7505.

[483] Boyko, S.; Surewicz, W. K. Tau Liquid–liquid Phase Separation in Neurodegenerative Diseases *Trends Cell Biology* **2022** *32*, 611–623.

[484] Dong, X.; Bera, S.; Qiao, Q.; Tang, Y.; Lao, Z.; Luo, Y.; Gazit, E.; Wei, G. Liquid–liquid Phase Separation of Tau Protein Is Encoded at the Monomeric Level *J. Phys. Chem. Lett.* **2021** *12*, 2576–2586.

[485] Case, L. B.; Zhang, X.; Ditlev, J. A.; Rosen, M. K. Stoichiometry Controls Activity of Phase-separated Clusters of Actin Signaling Proteins *Science* **2019** *363*, 1093–1097.

[486] Banani, S. F.; Lee, H. O.; Hyman, A. A.; Rosen, M. K. Biomolecular Condensates: Organizers of Cellular Biochemistry *Nature Reviews Mol. Cell Biology* **2017** *18*, 285–298.

[487] Shin, Y.; Brangwynne, C. P. Liquid Phase Condensation in Cell Physiology and Disease *Science* **2017** *357*, eaaf4382.

[488] Banerjee, P. R.; Milin, A. N.; Moosa, M. M.; Onuchic, P. L.; Deniz, A. A. Reentrant Phase Transition Drives Dynamic Substructure Formation in Ribonucleoprotein Droplets *Angewandte Chemie International Edition* **2017** *56*, 11354–11359.

[489] Li, P.; Banjade, S.; Cheng, H.-C.; Kim, S.; Chen, B.; Guo, L.; Llaguno, M.; Hollingsworth, J. V.; King, D. S.; Banani, S. F.; et al. Phase Transitions in the Assembly of Multivalent Signalling Proteins *Nature* **2012** *483*, 336–340.

[490] Banani, S. F.; Rice, A. M.; Peeples, W. B.; Lin, Y.; Jain, S.; Parker, R.; Rosen, M. K. Compositional Control of Phase-separated Cellular Bodies *Cell* **2016** *166*, 651–663.

[491] Zeng, X.; Pappu, R. V. Developments in Describing Equilibrium Phase Transitions of Multivalent Associative Macromolecules *Current Opinion Structural Biology* **2023** *79*, 102540.

[492] Chattaraj, A.; Blinov, M. L.; Loew, L. M. The Solubility Product Extends the Buffering Concept To Heterotypic Biomolecular Condensates *eLife* **2021** *10*, e67176.

[493] Saini, B.; Mukherjee, T. K. Biomolecular Condensates Regulate Enzymatic Activity Under a Crowded Milieu: Synchronization of Liquid–Liquid Phase Separation and Enzymatic Transformation *J. Phys. Chem. B* **2023** *127*, 180–193.

[494] Geng, X.; Zhang, Y. 53BP1 Regulates Heterochromatin Through Liquid-liquid Phase Separation (LLPS) *Cancer Research* **2024** *84*, 1720–1720.

[495] Jung, J.-H.; Barbosa, A. D.; Hutin, S.; Kumita, J. R.; Gao, M.; Derwort, D.; Silva, C. S.; Lai, X.; Pierre, E.; Geng, F.; et al. A Prion-like Domain in ELF3 Functions as a Thermosensor in Arabidopsis *Nature* **2020** *585*, 256–260.

[496] Kang, W.; Ma, X.; Liu, C.; Wang, S.; Zhou, Y.; Xue, C.; Xu, Y.; Li, B. Liquid-liquid Phase Separation (LLPS) in Synthetic Biosystems *Materials Science Engineering: R: Reports* **2024** *157*, 100762.

[497] Chen, F.; Li, X.; Guo, W.; Wang, Y.; Guo, M.; Shum, H. C. Size Scaling of Condensates in Multicomponent Phase Separation *J. Am. Chem. Society* **2024**.

[498] van Vliet, R. E.; Dreischor, M. W.; Hoefsloot, H. C.; Iedema, P. D. Dynamics of Liquid–liquid Demixing: Mesoscopic Simulations of Polymer Solutions *Fluid phase equilibria* **2002** *201*, 67–78.

[499] Lin, Y.-H.; Forman-Kay, J. D.; Chan, H. S. Sequence-specific Polyampholyte Phase Separation in Membraneless Organelles *Phys. Rev. Lett.* **2016** *117*, 178101.

[500] Lin, Y.; McCarty, J.; Rauch, J. N.; Delaney, K. T.; Kosik, K. S.; Fredrickson, G. H.; Shea, J.-E.; Han, S. Narrow Equilibrium Window for Complex Coacervation of Tau and RNA Under Cellular Conditions *eLife* **2019** *8*, e42571.

[501] Uversky, V. N.; Kuznetsova, I. M.; Turoverov, K. K.; Zaslavsky, B. Intrinsically Disordered Proteins as Crucial Constituents of Cellular Aqueous Two Phase Systems and Coacervates *FEBS Lett.* **2015** *589*, 15–22.

[502] Ranganathan, S.; Shakhnovich, E. I. Dynamic Metastable Long-living Droplets Formed by Sticker-spacer Proteins *eLife* **2020** *9*, e56159.

[503] Sear, R. P.; Cuesta, J. A. Instabilities in Complex Mixtures with a Large Number of Components *Phys. Rev. Lett.* **2003** *91*, 245701.

[504] Rana, U.; Brangwynne, C. P.; Panagiotopoulos, A. Z. Phase Separation Vs Aggregation Behavior for Model Disordered Proteins *J. Chem. Phys.* **2021** *155*, 125101.

[505] Takae, K.; Tanaka, H. Role of Hydrodynamics in Liquid–liquid Transition of a Single-component Substance *Proceedings National Academy Sciences* **2020** *117*, 4471–4479.

[506] Möller, J.; Grobelny, S.; Schulze, J.; Bieder, S.; Steffen, A.; Erlkamp, M.; Paulus, M.; Tolan, M.; Winter, R. Reentrant Liquid-Liquid Phase Separation in Protein Solutions at Elevated Hydrostatic Pressures *Phys. Rev. Lett.* **2014** *112*, 028101.

[507] Girelli, A.; Rahmann, H.; Begam, N.; Ragulskaya, A.; Reiser, M.; Chandran, S.; Westermeier, F.; Sprung, M.; Zhang, F.; Gutt, C.; et al. Microscopic Dynamics of Liquid-liquid Phase Separation and Domain Coarsening in a Protein Solution Revealed by X-ray Photon Correlation Spectroscopy *Phys. Rev. Lett.* **2021** *126*, 138004.

[508] Bartels, J.; Lembke, U.; Pascova, R.; Schmelzer, J.; Gutzow, I. Evolution of Cluster Size Distribution in Nucleation and Growth Processes *Journal of Non-Crystalline Solids* **1991** *136*, 181–197.

[509] Miller, M. A.; Frenkel, D. Competition of Percolation and Phase Separation in a Fluid of Adhesive Hard Spheres *Phys. Rev. Lett.* **2003** *90*, 135702.

[510] Miller, M. A.; Frenkel, D. Phase Diagram of the Adhesive Hard Sphere Fluid *J. Chem. Phys.* **2004** *121*, 535–545.

[511] Valadez-Pérez, N. E.; Liu, Y.; Eberle, A. P.; Wagner, N. J.; Castaneda-Priego, R. Dynamical Arrest in Adhesive Hard-sphere Dispersions Driven by Rigidity Percolation *Phys. Rev. E* **2013** *88*, 060302.

[512] Roosen-Runge, F.; Zhang, F.; Schreiber, F.; Roth, R. Ion-activated Attractive Patches as a Mechanism for Controlled Protein Interactions *Scientific Reports* **2014** *4*, 1–5.

[513] Surfaro, F.; Maier, R.; Pastryk, K.-F.; Zhang, F.; Schreiber, F.; Roth, R. An Alternative Approach To the Osmotic Second Virial Coefficient of Protein Solutions and Its Application To Liquid-liquid Phase Separation *J. Chem. Phys.* **2023** *158*, 164902.

[514] Farshad, M.; DelloStritto, M. J.; Suma, A.; Carnevale, V. Detecting Liquid–Liquid Phase Separations Using Molecular Dynamics Simulations and Spectral Clustering *J. Phys. Chem. B* **2023** *127*, 3682–3689.

[515] Agarwal, A.; Arora, L.; Rai, S. K.; Avni, A.; Mukhopadhyay, S. Spatiotemporal Modulations in Heterotypic Condensates of Prion and α-synuclein Control Phase Transitions and Amyloid Conversion *Nature Communications* **2022** *13*, 1154.

[516] Hansen, J.; Egelhaaf, S. U.; Platten, F. Protein Solutions Close To Liquid–liquid Phase Separation Exhibit a Universal Osmotic Equation of State and Dynamical Behavior *Phys. Chem. Chem. Phys.* **2023** *25*, 3031–3041.

[517] Noro, M. G.; Frenkel, D. Extended Corresponding-states Behavior for Particles with Variable Range Attractions *J. Chem. Phys.* **2000** *113*, 2941–2944.

[518] Hansen, J.; Pedersen, J. N.; Pedersen, J. S.; Egelhaaf, S. U.; Platten, F. Universal Effective Interactions of Globular Proteins Close To Liquid–liquid Phase Separation: Corresponding-states Behavior Reflected in the Structure Factor *J. Chem. Phys.* **2022** *156*.

[519] Hansen, J.; Moll, C. J.; López Flores, L.; Castañeda-Priego, R.; Medina-Noyola, M.; Egelhaaf, S. U.; Platten, F. Phase Separation and Dynamical Arrest of Protein Solutions Dominated by Short-range Attractions *J. Chem. Phys.* **2023** *158*.

[520] Valadez-Pérez, N. E.; Liu, Y.; Castañeda-Priego, R. Reversible Aggregation and Colloidal Cluster Morphology: the Importance of the Extended Law of Corresponding States *Phys. Rev. Lett.* **2018** *120*, 248004.

[521] Zhang, F.; Roosen-Runge, F.; Sauter, A.; Wolf, M.; Jacobs, R. M.; Schreiber, F. Reentrant Condensation, Liquid–liquid Phase Separation and Crystallization in Protein Solutions Induced by Multivalent Metal Ions *Pure Appl. Chem.* **2014** *86*, 191–202.

[522] Matsarskaia, O.; Roosen-Runge, F.; Lotze, G.; Möller, J.; Mariani, A.; Zhang, F.; Schreiber, F. Tuning Phase Transitions of Aqueous Protein Solutions by Multivalent Cations *Phys. Chem. Chem. Phys.* **2018** *20*, 27214–27225.

[523] Saha, R.; Mitra, R. K. Trivalent Cation-induced Phase Separation in Proteins: Ion Specific Contribution in Hydration Also Counts *Phys. Chem. Chem. Phys.* **2022** *24*, 23661–23668.

[524] Saha, R.; Mitra, R. K. Thermo-Resistive Phase Behavior of Trivalent Ion-Induced Microscopic Protein-Rich Phases: Correlating with Ion-Specific Protein Hydration *Langmuir* **2023** *39*, 4601–4610.

[525] Matsarskaia, O.; Braun, M. K.; Roosen-Runge, F.; Wolf, M.; Zhang, F.; Roth, R.; Schreiber, F. Cation-induced Hydration Effects Cause Lower Critical Solution Temperature Behavior in Protein Solutions *J. Phys. Chem. B* **2016** *120*, 7731–7736.

[526] Matsarskaia, O.; Roosen-Runge, F.; Schreiber, F. Multivalent Ions and Biomolecules: Attempting a Comprehensive Perspective *ChemPhysChem.* **2020** *21*, 1742–1767.

[527] Fries, M. R.; Conzelmann, N. F.; Günter, L.; Matsarskaia, O.; Skoda, M. W.; Jacobs, R. M.; Zhang, F.; Schreiber, F. Bulk phase behavior vs interface adsorption: Specific multivalent cation and anion effects on bsa interactions *Langmuir* **2021** *37*, 139–150.

[528] Soraruf, D.; Roosen-Runge, F.; Grimaldo, M.; Zanini, F.; Schweins, R.; Seydel, T.; Zhang, F.; Roth, R.; Oettel, M.; Schreiber, F. Protein Cluster Formation in Aqueous Solution in the Presence of Multivalent Metal Ions–a Light Scattering Study *Soft Matter* **2014** *10*, 894–902.

[529] Matsarskaia, O.; Roosen-Runge, F.; Lotze, G.; Möller, J.; Mariani, A.; Zhang, F.; Schreiber, F. Tuning Phase Transitions of Aqueous Protein Solutions by Multivalent Cations *Phys. Chem. Chem. Phys.* **2018** *20*, 27214–27225.

[530] Da Vela, S.; Braun, M. K.; Dörr, A.; Greco, A.; Möller, J.; Fu, Z.; Zhang, F.; Schreiber, F. Kinetics of Liquid–liquid Phase Separation in Protein Solutions Exhibiting LCST Phase Behavior Studied by Time-resolved USAXS and VSANS *Soft Matter* **2016** *12*, 9334–9341.

[531] Bramham, J. E.; Golovanov, A. P. Temporal and Spatial Characterisation of Protein Liquid-liquid Phase Separation Using NMR Spectroscopy *Nature Communications* **2022** *13*, 1767.

[532] Bleibel, J.; Habiger, M.; Lütje, M.; Hirschmann, F.; Roosen-Runge, F.; Seydel, T.; Zhang, F.; Schreiber, F.; Oettel, M. Two Time Scales for Self and Collective Diffusion Near the Critical Point in a Simple Patchy Model for Proteins with Floating Bonds *Soft Matter* **2018** *14*, 8006–8016.

[533] Surfaro, F.; Zhang, F.; Schreiber, F.; Roth, R. The Ion-activated Attractive Patchy Particle Model and Its Application To the Liquid–vapor Phase Transitions *J. Chem. Phys.* **2024** *161*.

[534] Ronceray, P.; Zhang, Y.; Liu, X.; Wingreen, N. S. Stoichiometry Controls the Dynamics of Liquid Condensates of Associative Proteins *Phys. Rev. Lett.* **2022** *128*, 038102.

[535] Xiang, Y.-X.; Shan, Y.; Lei, Q.-L.; Ren, C.-L.; Ma, Y.-Q. Dynamics of Protein Condensates in Weak-binding Regime *Phys. Rev. E* **2022** *106*, 044403.

[536] Galvanetto, N.; Ivanović, M. T.; Chowdhury, A.; Sottini, A.; Nüesch, M. F.; Nettels, D.; Best, R. B.; Schuler, B. Extreme Dynamics in a Biomolecular Condensate *Nature* **2023** pages 1–8.

[537] Riest, J.; Nägele, G. Short-time Dynamics in Dispersions with Competing Short-range Attraction and Long-range Repulsion *Soft Matter* **2015** *11*, 9273–9280.

[538] Grimaldo, M.; Roosen-Runge, F.; Hennig, M.; Zanini, F.; Zhang, F.; Zamponi, M.; Jalarvo, N.; Schreiber, F.; Seydel, T. Salt-Induced Universal Slowing Down of the Short-Time Self-Diffusion of a Globular Protein in Aqueous Solution *J. Phys. Chem. Lett.* **2015** *6*, 2577–2582.

[539] Grimaldo, M.; Roosen-Runge, F.; Hennig, M.; Zanini, F.; Zhang, F.; Jalarvo, N.; Zamponi, M.; Schreiber, F.; Seydel, T. Hierarchical Molecular Dynamics of Bovine Serum Albumin in Concentrated Aqueous Solution Below and Above Thermal Denaturation *Phys. Chem. Chem. Phys.* **2015** *17*, 4645–4655.

[540] Lee, J. C.; Timasheff, S. N. Partial Specific Volumes and Interactions with Solvent Components of Proteins in Guanidine Hydrochloride *Biochemistry* **1974** *13*, 257–265.

[541] Qvist, J.; Schober, H.; Halle, B. Structural Dynamics of Supercooled Water from Quasielastic Neutron Scattering and Molecular Simulations *J. Chem. Phys.* **2011** *134*.

[542] Beck, C.; Grimaldo, M.; Braun, M. K.; Bühl, L.; Matsarskaia, O.; Jalarvo, N. H.; Zhang, F.; Roosen-Runge, F.; Schreiber, F.; Seydel, T. Temperature and Salt Controlled Tuning of Protein Clusters *Soft Matter* **2021** *17*, 8506–8516.

[543] Roosen-Runge, F.; Bicout, D. J.; Barrat, J.-L. Analytical Correlation Functions for Motion Through Diffusivity Landscapes *J. Chem. Phys.* **2016** *144*.

[544] Beck, C.; Grimaldo, M.; Lopez, H.; Da Vela, S.; Sohmen, B.; Zhang, F.; Oettel, M.; Barrat, J.-L.; Roosen-Runge, F.; Schreiber, F.; Seydel, T. Short-Time Transport Properties of Bidisperse Suspensions of Immunoglobulins and Serum Albumins Consistent with a Colloid Physics Picture *J. Phys. Chem. B* **2022** *126*, 7400–7408.

[545] Flory, P. J. Molecular Size Distribution in Three Dimensional Polymers. I. Gelation *J. Am. Chem. Society* **1941** *63*, 3083–3090.

[546] Stockmayer, W. H. Theory of Molecular Size Distribution and Gel Formation in Branched Polymers II. General Cross Linking *J. Chem. Phys.* **1944** *12*, 125–131.

[547] Bianchi, E.; Tartaglia, P.; Zaccarelli, E.; Sciortino, F. Theoretical and Numerical Study of the Phase Diagram of Patchy Colloids: Ordered and Disordered Patch Arrangements *J. Chem. Phys.* **2008** *128*.

[548] Villois, A.; Capasso Palmiero, U.; Mathur, P.; Perone, G.; Schneider, T.; Li, L.; Salvalaglio, M.; deMello, A.; Stavrakis, S.; Arosio, P. Droplet Microfluidics for the Label-Free Extraction of Complete Phase Diagrams and Kinetics of Liquid–Liquid Phase Separation in Finite Volumes *Small* **2022** *18*, 2202606.

[549] Bucciarelli, S.; Casal-Dujat, L.; De Michele, C.; Sciortino, F.; Dhont, J.; Bergenholtz, J.; Farago, B.; Schurtenberger, P.; Stradner, A. Unusual Dynamics of Concentration Fluctuations in Solutions of Weakly Attractive Globular Proteins *J. Phys. Chem. Lett.* **2015** *6*, 4470–4474.

[550] Bucciarelli, S.; Myung, J. S.; Farago, B.; Das, S.; Vliegenthart, G. A.; Holderer, O.; Winkler, R. G.; Schurtenberger, P.; Gompper, G.; Stradner, A. Dramatic Influence of Patchy Attractions on Short-time Protein Diffusion Under Crowded Conditions *Science Advances* **2016** *2*, e1601432.

[551] Paalman, H.; Pings, C. Numerical Evaluation of X-Ray Absorption Factors for Cylindrical Samples and Annular Sample Cells *J. Appl. Phys.* **1962** *33*, 2635–2639.

[552] Hulse, W. L.; Gray, J.; Forbes, R. T. Evaluating the Inter and Intra Batch Variability of Protein Aggregation Behaviour Using Taylor Dispersion Analysis and Dynamic Light Scattering *International Journal Pharmaceutics* **2013** *453*, 351–357.

[553] Matsarskaia, O.; Braun, M. K.; Roosen-Runge, F.; Wolf, M.; Zhang, F.; Roth, R.; Schreiber, F. Cation-Induced Hydration Effects Cause Lower Critical Solution Temperature Behavior in Protein Solutions *J. Phys. Chem. B* **2016** *120*, 7731–7736.

[554] Mittag, T.; Pappu, R. V. A Conceptual Framework for Understanding Phase Separation and Addressing Open Questions and Challenges *Molecular Cell* **2022** *82*, 2201–2214.